Numerical modeling of hydraulic stimulation and induced seismicity in deep geothermal reservoirs

Dac Thuong Ngo

PSL UNIVERSITÉ PARIS

THÈSE DE DOCTORAT
DE L'UNIVERSITÉ PSL

Préparée à MINES ParisTech

Numerical modeling of hydraulic stimulation and induced seismicity in deep geothermal reservoirs

Modélisation numérique de la stimulation hydraulique et de la sismicité induite dans des réservoirs géothermiques profonds

Soutenue par

Dac Thuong NGO

Le 27 juin 2019

Ecole doctorale n° 398

Géosciences, Ressources Naturelles et Environnement

Spécialité

Géosciences et géoingénierie

Composition du jury :

Hervré, CHAURIS Professeur, MINES ParisTech	Président
Patrick, SELVADURAI Professeur, McGill University	*Rapporteur*
Jean, SULEM Professeur, École des Ponts ParisTech	*Rapporteur*
Eva, SCHILL Professeur, University of Darmstadt	*Examinateur*
Michel, GARCIA Docteur, KIDOVA	*Invité*
Frédéric, PELLET Professeur, MINES ParisTech	*Directeur de thèse*
Dominique, BRUEL Docteur, MINES ParisTech	Co-*directeur de thèse*

MINES ParisTech | PSL

Résumé

La géothermie est une source d'énergie renouvelable pouvant servir de base pour la production d'électricité ou le chauffage, sans ou avec une émission limitée de gaz à effet de serre. Cependant, le développement et l'exploitation des réservoirs géothermiques profonds s'accompagnent généralement d'une sismicité induite - un effet secondaire qui peut susciter de vives inquiétudes auprès du public et empêcher une utilisation à grande échelle de l'énergie géothermique. La pièce maîtresse d'une installation géothermique est un échangeur de chaleur, c'est-à-dire un réservoir, situé dans des roches chaudes en profondeur. Ce réservoir de roche est créé en utilisant la technique de la stimulation hydraulique, qui consiste essentiellement à injecter un fluide à des pressions élevées pour créer de nouvelles fractures hydrauliques qui se connecteront au réseau de fractures ou de failles préexistantes. Ce faisant de nouvelles voies pour la circulation du fluide seront créées et la surface d'échange de chaleur sera considérablement augmentée.

Plusieurs processus physiques couplés interviennent lors de la stimulation et de l'exploitation de réservoirs géologiques profonds. Il s'agit essentiellement de la déformation et de la rupture de la roche, de l'écoulement du fluide, et des variations de température. Ces processus couplés et dépendants du temps sont à l'origine de la propagation des fractures et de la réactivation de failles, responsable de la sismicité induite.

Cette thèse de doctorat est axée sur l'utilisation de simulations numériques dans le but de mieux comprendre le comportement thermo-hydro-mécanique des réservoirs géothermiques fracturés et de déterminer le potentiel de sismicité induite. La propagation des fractures hydrauliques et la réactivation de failles préexistantes sont modélisées à l'aide du concept de matériau cohésif en combinaison avec des éléments finis cohésifs et en tenant compte des processus physiques sous-jacents (par exemple, écoulement de fluide, déformation de la roche). Différents facteurs pouvant avoir un impact majeur sur la propagation de la fracture et la réactivation de la faille sont étudiés, tels que le frottement des failles préexistantes, le débit d'injection de fluide et l'orientation des failles. Les variations de température résultant de

l'injection et de la circulation d'un fluide pouvant avoir un effet à long terme sont également étudiées séparément.

La sismicité induite est ensuite étudiée sous l'angle de l'utilisation de la loi de la conservation de l'énergie afin d'expliquer le mécanisme de génération d'ondes élastiques consécutif à la rupture. Le processus de conversion de l'énergie de déformation accumulée dans un système avant la rupture en énergie cinétique pendant la rupture, quelle que soit la vitesse avec laquelle la charge externe est appliquée au système, est clairement démontré. Cette approche permet de bien comprendre les facteurs qui ont un impact majeur sur l'intensité des ondes sismiques induites. Ensuite, une procédure de modélisation est proposée pour calculer les accélérations maximales induites à la surface du sol par le glissement de la faille. Ces accélérations sont utilisées pour évaluer l'intensité du séisme en relation avec la perception humaine des ondes sismiques et l'endommagement causé aux infrastructures, participant ainsi au processus d’acceptation par le public de tout nouveau projet d’exploitation géothermique.

Abstract

Geothermal energy is a renewable resource that can provide base-load energy for electricity production or heating purposes without, or with limited, emission of green house gases. However, the development and the exploitation of deep geothermal power plants is usually accompanied by induced seismicity – a side effect that can raise serious concerns to the public and may prevent large-scale application of geothermal energy. The centerpiece of a deep geothermal power plant is a heat exchanger, i.e., a reservoir, located in hot rocks at depth. This rock reservoir is created using a hydraulic stimulation technique, which essentially consists of injecting fluid at high pressures to create new hydraulic fractures that will connect with pre-existing fractures/faults, thus multiplying possible pathways for fluid circulation. Multiple physical processes are involved during the stimulation and exploitation of the rock reservoir, including fluid flow, rock deformation of the rock, and temperature changes. These processes are the origin of the rock failure (e.g., fracture propagation, fault reactivation) that is responsible for the induced seismicity. In return, the induced seismicity can be regarded as a real-time indicator of the spatial progress of the reservoir during hydraulic stimulation.

This doctoral research focuses on the use of numerical simulations to better understand the behavior of fractured geothermal reservoirs and the potential of induced seismicity. The propagation of hydraulic fractures and the reactivation of pre-existing faults are modeled using the cohesive material concept in combination with finite cohesive elements and taking into account the underlying physical processes (e.g., fluid flow, rock deformation). Various factors that may have a major impact on fracture propagation and fault reactivation are investigated, such as the friction condition of the pre-existing faults, the fluid injection rate, and the fault orientation. Temperature changes resulting from fluid injection and circulation that may have a long term effect are also separately investigated.

The induced seismicity is first studied from the standpoint of using the law of energy conservation in order to explain the mechanism of elastic waves generation due to failure. The process of converting the strain energy accumulated in a system prior to the failure into kinetic

energy during failure, regardless of how slowly the external load is applied to the system, is clearly demonstrated. This approach provides a good understanding of the factors that have a major impact on the intensity of the induced seismic waves. A modeling procedure is then proposed to calculate the peak ground accelerations that are induced by the fault slip. The computed accelerations on the ground surface are used to assess the earthquake intensity, the human perception of the seismic waves, and the damage potential to infrastructures.

Acknowledgement

I am grateful to the many people who participated in different ways in the success of my doctoral research.

First of all, I express my sincere gratitude to my advisors: Prof. Frédéric Pellet and Dr. Dominique Bruel, who entrusted me with this research topic. They gave me a lot of encouragement and guidance during my work at the Center for Geosciences of MINES ParisTech. Their advice was very valuable.

I thank Prof. Patrick Selvadurai from McGill University and Prof. Jean Sulem from Ecole des Ponts ParisTech for their acceptance of being the reviewers of my research work. I greatly appreciated their advice and all the discussions I had with them.

I thank Prof. Hervré Chauris from MINES ParisTech, who accepted to be president of the jury, as well as Prof. Eva Schill from University of Darmstadt and Dr. Michel Garcia from KIDOVA who accepted to participate in the evaluation of this work.

I would like also to thank Prof. Michel Tijani for all the helpful discussions and the tough questions he gave me as well.

My sincere thanks also go to my friends and colleagues: Zezhong, Hao, Xiangdong, Paule, Mejda, Sara, Hafsa, Aurélien, Qinglin and Shuaitao.

Finally, my last thoughts are with my family and all my loved ones for their unconditional support in difficult times. To all, thank you very much.

Fontainebleau, Juin 2019

NGO Dac Thuong

Table of contents

Chapter 1

Introduction

1.1 INTRODUCTION TO GEOTHERMAL ENERGY

1.1.1 Geothermal resources potential

Geothermal energy is the thermal energy contained in the Earth's crust. The sources of geothermal heat are associated with the upward conduction and convection of energy from the Earth's core and mantle, and with the decay of the naturally radioactive isotopes of uranium, thorium and potassium (Barbier, 1997; Boyle, 2004; Brown et al., 2012). These natural processes, which occur over geological time scales, maintain the renewal of the thermal energy content and make geothermal energy practically inexhaustible.

Geothermal energy exists in two major forms: natural hydrothermal systems and heat stored in hot rock formations. In natural hydrothermal systems, an interconnected network of open pores and fractures is present in the rock mass, which allows the flow of fluids. Natural groundwater is abundant in these systems; it is heated by the surrounding hot rock and is carried upward by natural convective circulation. These natural systems can be found in porous and/or naturally fractured rocks and are typically located at depths of 1 – 4 km in a number of locations e.g., New Zealand, Indonesia, Northern Italy, Japan, Mexico, Iceland (DiPippo, 1988; Mock et al., 1997; Tester, 1989). However, natural hydrothermal systems are the exception rather than the rule as heat, natural groundwater and permeability/porosity must be present.

The heat stored in hot rock formations, on the other hand, is in principle available anywhere around the world if one drills deep enough and can appropriately stimulate the rock (i.e., create sufficient permeability) at these depths. The reason is that the temperature of the Earth increases with depth. On average, the geothermal gradient is about 30 °C/km (Banks, 2012; Barbier, 1997; Brown et al., 2012). However, there are many areas where thermal gradients are considerably greater. A thermal gradient of 50 °C/km is commonly available in the Western U.S (Beckers et al., 2014) where the minimum temperature at a depth of 5 km is estimated to be 250 ºC. The same thermal gradient was also found in Southern Australia (Geodynamics, 2015) where temperatures of 273 ºC and 283 ºC have been found at depths of around 5 km. A local geothermal gradient on the order of 65 °C/km was found at the Fenton Hill site in the Jemez Mountains of New Mexico, United States. For regions that have an average geothermal gradient of 30°C/km, a temperature of 150 °C is expected at depths of around 5 km, depths that are accessible with current drilling technology; this temperature is considered to be suitable for efficient heat exploitation (Potter et al., 1974). The rock formations at depths where suitable temperatures can be found have two typical characteristics: low permeability to almost impermeable and essentially dry – the so-called hot dry rocks (HDR). HDRs hold an enormous amount of thermal energy that can be extracted for electricity production. A comparison of geothermal energy output with other energy sources is shown in Figure 1.1.

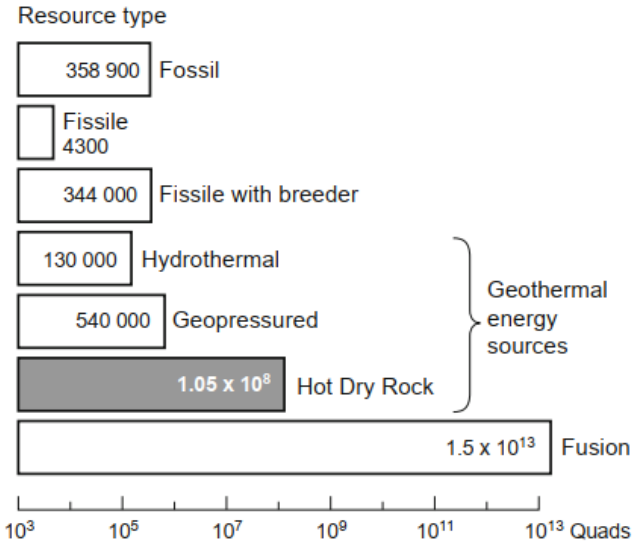

Figure 1.1 Estimates of the worldwide resource base for geothermal and other energy sources (Brown et al., 2012). Note: 1 quad = 293 x 10^9 kWh; world energy consumption in 2010 is 524 quads

It is obvious from Figure 1.1 that the geothermal energy stored in HDRs is second only to fusion energy, a source that is yet to be developed. It has been estimated that the total amount of thermal energy contained in HDR at accessible depths is about 300 times greater than the energy that oil, natural gas and coal combined could provide (Duchane and Brown, 2002; Tester, 1989). This amount of energy is enough to supply all the energy needs of the world for centuries to come (Edwards et al., 1982).

1.1.2 Hot Dry Rock concept

The importance of HDR resources originates not just from its huge quantity but also from its abundant availability throughout the world. However, the low permeability and the absence of natural water in HDRs require that permeability-enhancing operations have to be carried out and a heat transport medium, e.g., water or brine, must be supplied artificially. The first attempts to exploit the heat contained in HDRs were made in the United States by a group of researchers from the Los Alamos National Laboratory (Brown and Duchane, 1999; Smith, 1975), who conceived the HDR concept and began to develop the world's first HDR reservoir at Fenton Hill in New Mexico (USA) between 1974 and 1978 (Murphy et al., 1983). The original HDR concept, as shown in Figure 1.2, was simple (Abé, 1992; Brown et al., 2012; Potter et al., 1974): A well is drilled into the HDR formation. Through this well, water is injected at pressures high enough to create a single plane vertical fracture, perpendicular to the direction of the minimum compressive stress, which is often horizontal at depths greater than 500 – 1000 m. The vertical fracture would grow as a disc to a diameter of several hundred meters, creating a large reservoir of rock with sufficient area for heat exchange between the water and the hot rock. A second well is subsequently drilled to connect with the reservoir at some distance from the first well. Once the stimulation phase and the well completion are finished, water circulation and heat extraction can begin. Cold water is pumped into the reservoir through the first well. The water is heated by contact with the hot rock as it flows across the reservoir. The resulting superheated water is then pumped up to the surface via the second well and begins the power generation phase. After extracting the useful heat, the same water is re-injected back into the reservoir to begin a new circulation circle. Thus, an HDR system operates and recovers the heat from HDRs in a closed-loop circulation, making the

production operations sustainable to some extent, although some water loss from the system may still occur.

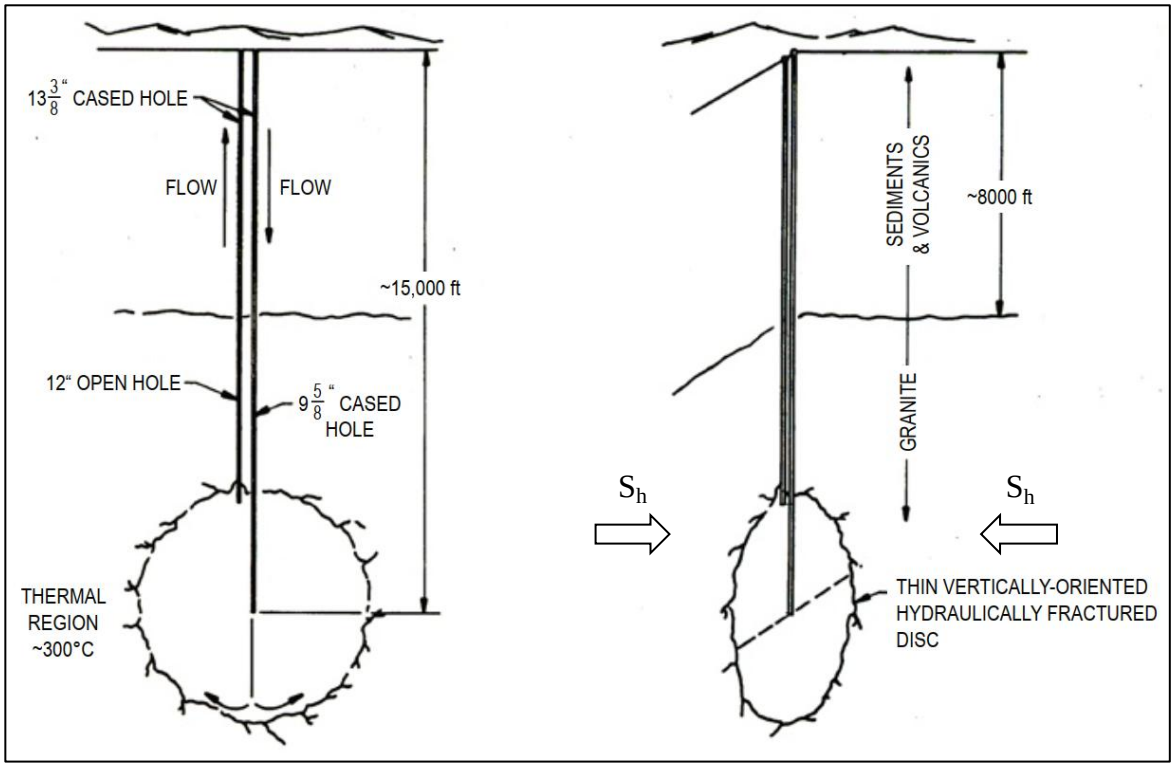

Figure 1.2 Original concept of an HDR geothermal system consisting of two wells and a vertical fracture created by hydraulic stimulation. Left: Front view showing typical dimensions for the wells, depth of the reservoir, and temperature. Right: 3D view showing the orientation of the fracture relative to the minimum stress. (Adapted from (Brown et al., 2012).)

For large HDR systems, larger areas are required for heat exchange. This could be achieved by creating a set of multiple parallel fractures using hydraulic stimulation in open uncased sections of the borehole (Nicol and Robinson, 1990). A schematic of such a system is illustrated in Figure 1.3.

The successful development of an HDR reservoir depends on the choice of a site that provides suitable rock at a depth that is reachable with limited drilling costs. The reservoir created should provide a sufficient area for rapid heat transfer between the rock and water and requires a reasonable amount of energy to pump water through it, i.e., resistance to flow must be relatively small. The reservoir must also operate with minimum water loss from the system and its temperature should not be drawn down too quickly.

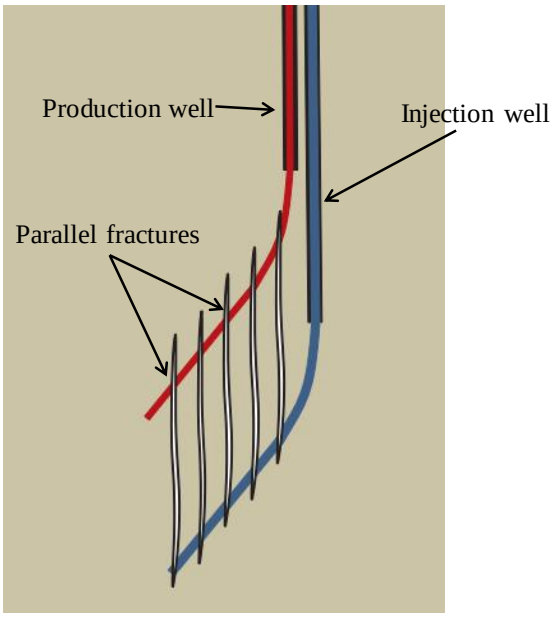

Figure 1.3 HDR concept for large geothermal systems that contains multiple parallel vertical fractures. Two deviated wells connect these fractures to create a closed-loop system (Adapted from (Jung, 2013))

1.1.3 Enhanced Geothermal Systems

This original HDR concept was based on a consideration of the crystalline formation at great depths as an intact and almost impermeable rock mass. However, this consideration was refuted based on further understanding gained from the work at the Fenton Hill HDR project and the Camborne School of Mines (CSM) geothermal project at Rosemanowes, Cornwall, England (Murphy et al., 1983). The existence of natural joints and existing fractures has been confirmed and their influence on the development of the geothermal reservoir is considered to be significant. In fact, high fracture densities can be expected in most deep rock formations, although only a fraction of them are likely to be conductive (Evans et al., 1999). Microseismic evidence at the Fenton Hill project showed that instead of generating a disc-shaped fracture, hydraulic stimulation leads to the opening and/or shearing of the natural joints and existing fractures, and permanently improves the permeability of the formation (Duchane and Brown, 2002; Evans et al., 1999; Murphy et al., 1983; Richards et al., 1994). The shearing and/or opening of existing fractures was also the main permeability enhancement mechanism observed in the CSM project (Baria et al., 1989; Green and Baria, 1989). In fact, the seismic investigations at the CSM project concluded that all detected microseismic activity indicated

shear sources that are consistent with known rock joint orientations and in-situ stress magnitudes and orientations. These observations and further experimental studies prompted the concept of Enhanced Geothermal Systems (EGS) in which natural joints and existing fractures play important role in the development of the rock reservoir (Batchelor, 1989a; Cornet, 1989). Instead of being considered as a continuum medium, the rock is treated as a discrete medium that contains natural joints and fractures. The permeability of this medium could be enhanced by massive water injection in long uncased borehole sections to shear and open the natural fractures. The EGS concept is illustrated in Figure 1.4.

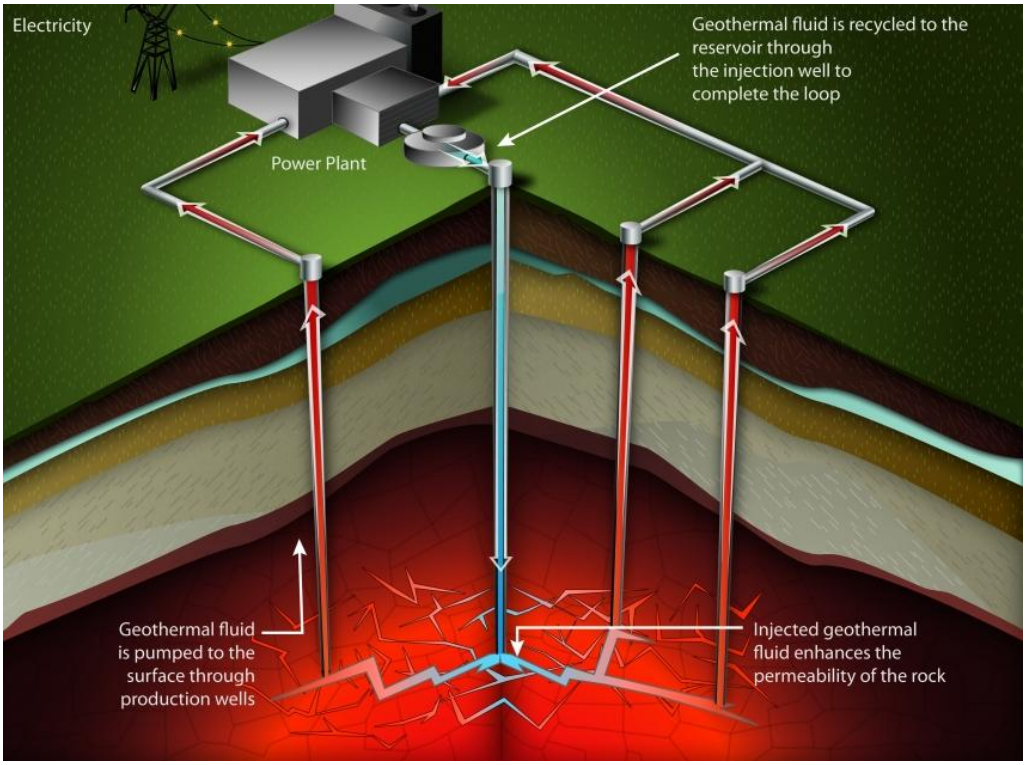

Figure 1.4 Schematic of the EGS concept that contains one injection well and three production wells. The permeability of the rock mass is enhanced by the shearing and opening of existing joints/fractures. Source: DOE (2015).

Generally, an EGS reservoir must have a number of properties in order to be technically feasible and economically viable. These include the total volume, the total heat exchange surface, the flow impedance, and the thermal and stress-field properties. The reference limits for these properties are summarized in Table 1.1.

Table 1.1 Required properties for an EGS reservoir. Source: Rybach (2010)

Property	**Value**
Fluid production rate	50 – 100 L/s
Wellhead temperature	150 – 200 °C
Total effective heat exchange surface	> 2 x 10^6 m^2
Rock volume	> 2 x 108 m^3
Flow impedance	< 0.1 MPa/(L/s)
Water loss	< 10%

1.2 PIONEERING EGS PROJECTS

Since the creation of the world's first HDR reservoirs at Fenton Hill, many EGS projects have been developed in the United States, Europe and elsewhere. These projects have used a more or less similar approach to that used at Fenton Hill HDR reservoir, using the technique of hydraulic fracturing to create the large heat transfer areas necessary in a HDR reservoir. Major pioneering projects are summarized in the following paragraphs.

1.2.1 Fenton Hill HDR project

The first HDR geothermal project at Fenton Hill, New Mexico, United States, was initiated in 1971 by the Los Alamos National Laboratory (LANL). The primary objective of the project was to develop and demonstrate of an economical and commercially viable technology for extracting thermal energy stored in HDR. The site, located just outside of the ring fault structure of the Valles Caldera, was chosen primarily on the basis of favorable heat flow and the simplicity of the geologic structure in the anticipated reservoir rock (Brown and Duchane, 1999). The estimated thermal gradient is on the order of 65 °C/km. The basement rock is at a depth of about 730 m, and contains Precambrian igneous and metamorphic rocks. The rock mass is extremely tight with hydraulic conductivity in the range of nano-darcies (Brown et al., 2012). A geologic cross section of the rock mass with the geothermal gradient is shown in Figure 1.5.

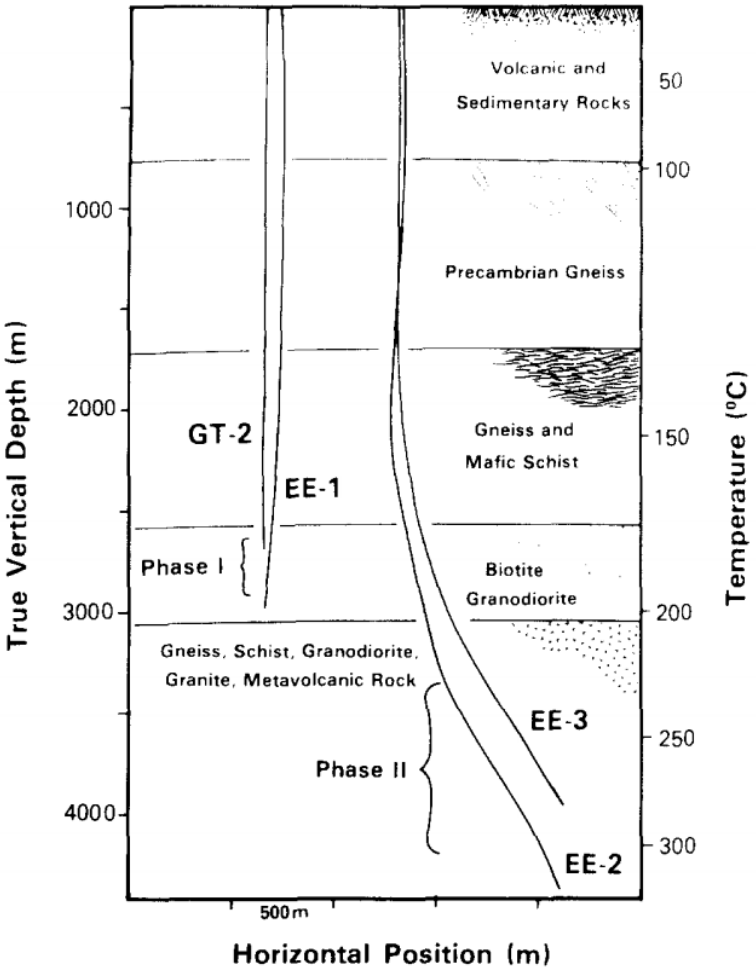

Figure 1.5 Elevation view of the Phase I (GT-2B and EE-1) and Phase II (EE-2 and EE-3) wellbore at the Fenton Hill HDR project (Grigsby et al., 1989)

Two separate, confined HDR reservoirs were created at the Fenton Hill site in hot crystalline rock at different depths and then assessed and flow-tested for almost a year. Work on the shallower reservoir (Phase I reservoir) began in 1974 (Brown et al., 2012). The first borehole, GT-2 (Figure 1.5), was drilled into the granitic rock at a depth of 2900 m at a mean temperature of 195 °C. After a series of water injections to generate a hydraulic fracture from the bottom of the GT-2 borehole, the second borehole, EE-1, was directionally drilled beneath the bottom of the borehole GT-2 to intersect with the created hydraulic fracture. A good connection between the second borehole and the created reservoir was not immediately achieved, and sidetracking was necessary to establish contact with the initial well via a combination of induced and natural fracture pathways. In total, over 2000 m^3 of water was

injected at average pressures of 10 MPa. Later, the reservoir was enlarged due to extensive testing. Using microseismic data, the final volume of the reservoir was estimated at 10 x 10^6 m^3 (Brown, 2009). Circulation tests showed a thermal production power of 3 MW at a flow rate of about 6 L/s.

Development of the second, much larger, deeper, and hotter HDR reservoir began in 1980 (Phase II). The initial intent of this reservoir was to create a series of vertical, disc-shaped fractures connecting two inclined, vertically separated wellbores (Brown and Duchane, 1999). This concept is presented in Figure 1.3. The two boreholes were drilled sequentially, one above the other. The first borehole EE-2 (Figure 1.5) was drilled to a vertical depth of about 4400 m, with the lower 1000 m directionally drilled at an angle of 35° to the vertical. The second borehole EE-3 (Figure 1.5) was then drilled in a similar manner to the first, but with the directionally drilled segment positioned 380 m above the directionally drilled portion of the first borehole. A number of hydraulic stimulations were carried out in an effort to connect these two boreholes by multiple vertical fractures. In total, over 21000 m^3 of water was injected at average pressures of 48 MPa. However, all these stimulations failed to connect the two boreholes. A satisfactory connection between the boreholes was then achieved after sidetracking the upper borehole into the stimulated region, which had been identified using induced microseismic data. The Phase II reservoir operated at a much higher temperature, above 300 °C, than the Phase I reservoir. A circulation test revealed a thermal power production of 10 MW at a circulation flow rate of 12 – 14 L/s. Water loss during circulation was estimated to be extremely low due to the inherent tightness of the surrounding sealed rock mass, combined with the stress cage effect (Brown et al., 2012). However, the resistance to flow was 2.1 MPa/(L/s), which is unacceptably high compared to the reference limit value given in Table 1.1. It was believed that much of the impedance was concentrated in the zones immediately surrounding the boreholes. The Fenton Hill project was terminated in 1995 due to lack of financial support.

1.2.2 Camborne School of Mines Project

The Camborne School of Mines project at Rosemanowes Quarry in Cornwall, England started in 1977 and proceeded in 3 phases (Batchelor, 1989a; Parker, 1989). The Phase 1 of the

project involved preliminary experiments at shallow depths. The objective of this phase was to understand the role of the natural fracture system and find the best way to establish and control flow paths within the fracture system. Four boreholes were drilled to a depth of 300 m; explosives and hydraulic fracturing were used in combination to connect the four boreholes. The circulation test later showed that the impedance was greatly reduced. The lowest impedance achieved was close to 0.1 MPa per L/s. Temperature gradients at the site were estimated at 30 – 40 °C/km, the highest in England (Parker, 1989).

The next phase of the project, Phase 2A, began in 1980 and lasted until 1983. The goal of this phase was to learn how to create and manage a full-size reservoir that has all the parameters necessary for commercial operation, except the depth of the reservoir. During this phase, two boreholes (RH11 and RH12) deviated from the vertical by 30° and spaced by 300 m were drilled to a depth of 2000 m. The reservoir was created by explosive fracturing near the wellbore, followed by hydraulic stimulation of the lower borehole using water injected at flow rates up to 100 L/s to try to open up the existing joints to connect to the upper borehole (Parker, 1989). However, the circulation test, in which water was injected through the lower borehole revealed, that a massive amount of water was lost from the system and the pumping pressure required was too high (Baria et al., 1989). Seismic monitoring showed that during the stimulation and subsequent circulation, the reservoir grew vertically downwards, as shown in Figure 1.6, probably extending to a depth of two kilometers below the two boreholes.

During Phase 2B, a third borehole RH15 was drilled to a depth of 2600 m to access the stimulated zone below the existing two boreholes (Batchelor, 1989b). Its position was selected to penetrate through the microseismic cloud. Stimulation was then performed on RH15 using viscous gel. A substantial thermal drawdown was observed during the first year of a circulation test. Circulation tests later suggested that the optimum hydraulic performance at Rosemanowes would have an injection flow rate of 24 L/s, a flow impedance of 0.6 MPa/(L/s) and water loss of 21%. This is still far from the requirements, as given in Table 1.1, for this EGS reservoir to be considered to be economically viable.

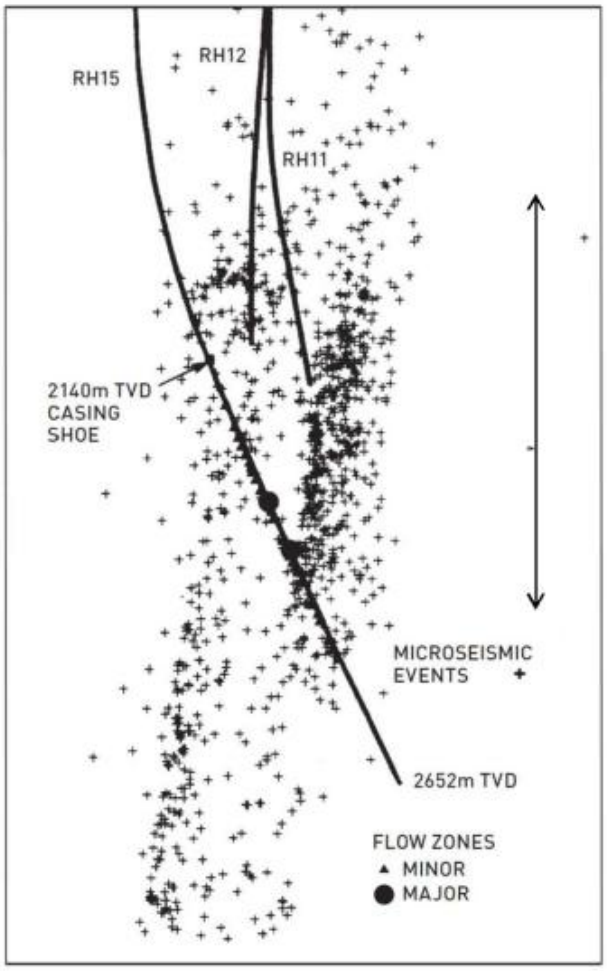

Figure 1.6 Front view of the seismic cloud of the EGS-system at Rosemanowes (Jung, 2013)

1.2.3 Soultz-sous-Forêts project

The Enhanced Geothermal System (EGS) of Soultz-sous-Forêts (France) is a European research program for the extraction of energy from deep hot fractured rocks. The site of Soultz is located in the central part of the Upper Rhine Valley 6 km east of the Western main fault. The Soultz granitic basement lies below 1.4 km of sediments, goes down to 5 km, and is strongly fractured (Genter and Traineau, 1996; Ledésert et al., 1993; Sausse, 2002). The joint systems are clustered, with a high density of joints in the fracture zones and a much lower density in the competent rock. The fracture zones and joints are mainly subvertical at a strike of 160°. The geostatic stress state includes a minimum horizontal stress S_h, which is about 54% of the vertical stress S_v (S_h = 0.54 S_v), and a maximum horizontal stress S_H, which is

almost equal to the vertical stress ($S_H = S_v$) (Cornet et al., 2007; Ledésert et al., 2010; Sausse and Genter, 2005). Temperature anomalies have been documented at the site and in the region around Soultz (Dèzes et al., 2004; Ziegler, 1992), which indicate that some of the faults are permeable, transporting water from great depth up to the cap rock. The temperature at 5 km in the granitic basement is about 200 °C (Freymark et al., 2017; Held et al., 2014; Hettkamp et al., 2004) and the lower part of the temperature profile indicates a conductive heat transfer regime.

In total, five deep boreholes have been drilled at the Soultz site (Hébert et al., 2010). The two initial boreholes (GPK1, 3600 m deep and EPS1, 2200 m deep) were mainly for the purpose of investigating the nature and the structure of the rock mass. The other three boreholes (GPK2, GPK3 and GPK4) are located at depths 4400 to 5000 m. These boreholes form a triplet system in which GPK3 is used for injection of fluids, while GPK2 and GPK4 are dedicated to production. An elevation showing the relative locations of the four boreholes GPK1 to GPK4 is presented in Figure 1.7. All boreholes drilled had open sections of 500 – 750 m in the lowest part that would be stimulated. Each borehole of the triplet system was stimulated by injecting large volumes of water at various flow rates. A volume of 22000 m^3 was injected at 50 L/s into borehole GPK2, which resulted in a wellhead pressure of 14.5 MPa at shut-in. Stimulation of the borehole GPK3 involved pumping of 34000 m^3 of water at a flow rate from 50 to 90 L/s. The maximum wellhead pressure produced was 17.9 MPa. The borehole GPK4 was stimulated by injecting 21500 m^3 of water at a flow rate from 30 to 45 L/s and the peak wellhead pressure was 17.5 MPa (Evans et al., 2012). The permeability of the rock mass was significantly improved after stimulation. Transmissibility of single fractures after the stimulation could exceed 1 d.m and was only slightly pressure dependent (Schill et al., 2017). Several circulation tests were later performed. The production flow rate for the two production boreholes GPK2 and GPK4 reached 30 L/s, which is still far from the requirement of 50 – 100 L/s (Table 1.1). Long term circulation of the triplet system with power production commenced in 2010 (Genter et al., 2010).

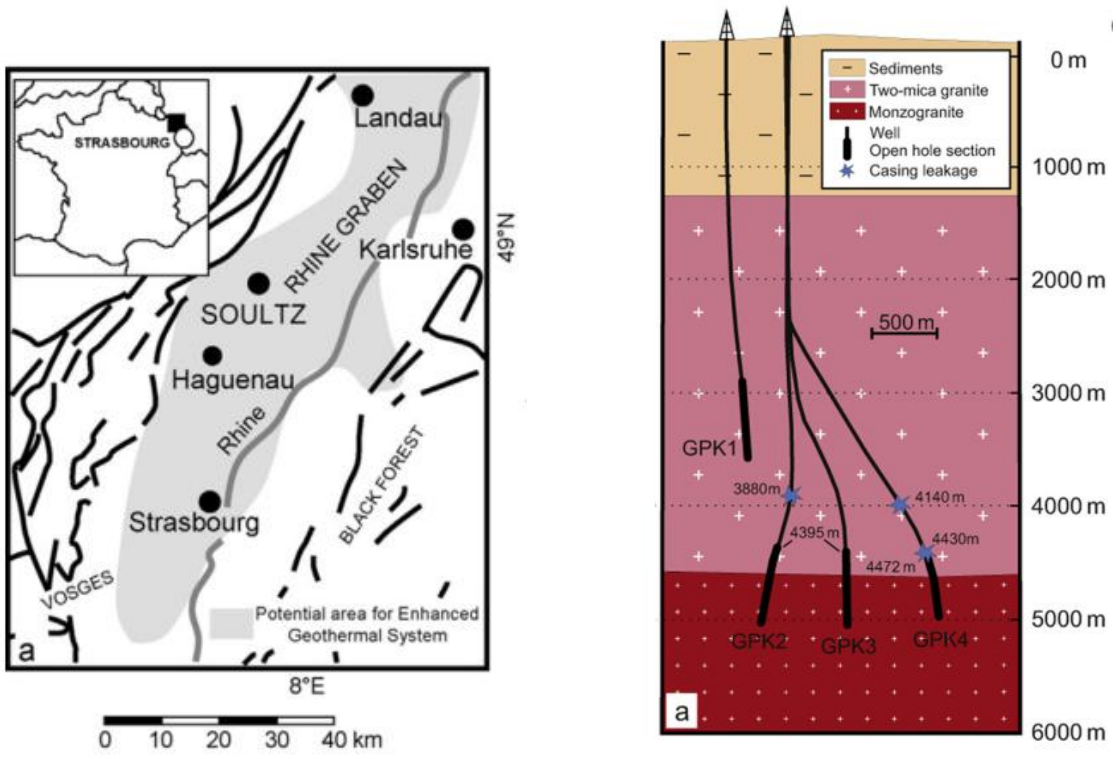

(a) (b)

Figure 1.7 (a) Schematic map of the Rhine graben and location of the Soultz-sous-Forêts EGS site (Calò et al., 2014), (b) Simplified deep geology, well trajectories and location of open sections and leakages in the Soultz-sous-Forêts reservoir (Held et al., 2014)

1.3 INDUCED SEISMICITY IN EGS DEVELOPMENT

The centerpiece of an EGS project is the heat exchanger created in the hot rock at depth. Hydraulic stimulation has become a common technique to achieve this result. Fluid, such as water, is injected at sufficiently high pressure into the rock mass to create new fractures or activate the pre-existing ones. Given the high pressures and the massive amount of water needed in the stimulation, the seismic risk has increasingly become a major concern (Evans et al., 2012; Zang et al., 2014). In fact, one of the main challenges for the development of an EGS is associated with assessing the induced seismicity that may be triggered by hydraulic pressurization during the stimulation and circulation phases (Ellsworth, 2013; Pellet, 2017; Wohlenberg and Keppler, 1987). Thousands of seismic events are generated during the stimulation and exploitation of EGS reservoirs. In some sites, events of high magnitude were induced and could be felt on the ground surface.

At Soultz-sous-Forêts, massive water injections into the boreholes GPK2, GPK3 and GPK4 (located at depths from 4400 to 5000 m) resulted in approximately 90,000 micro-earthquakes. The stimulation of the borehole GPK2 alone triggered over 700 events of magnitude between M_L 1.0 and 2.5 during injection. A large event of magnitude M_L 2.6 occurred after the shut-in (Dorbath et al., 2009; Evans et al., 2012). More than 200 event of magnitude between M_L 1.0 and 2.5 occurred during the stimulation of borehole GPK3; the largest event that had a magnitude M_L 2.9 also occurred after the shut-in. Stimulation of the borehole GPK4 also resulted in multiple seismic events, some reaching a magnitude M_L 2.7; in total, more than 30 events of magnitude above M_L 2.0 were triggered (Rybach, 2010). The circulation tests performed in 2005 and 2008 also induced seismicity with the largest event having a magnitude of M_L 2.3 (Cuenot et al., 2008; Dorbath et al., 2009).

At the Basel EGS site in Switzerland, the stimulation of a 5000 m deep borehole in 2006 triggered multiple seismic events that were clearly perceived by the public. The first event of magnitude M_L 2.6 occurred during fluid injection, followed by two larger events of magnitude M_L 2.7 and 3.4 that occurred during shut-in. After the bleed-off, three aftershocks of $M_L > 3$ were recorded (Deichmann and Giardini, 2009; Häring et al., 2008). These induced seismic events raised concerns among the public, which led to the cancelation of the project by the Basel government at the end of 2009 and the borehole was closed in 2011.

Induced seismicity has also occurred during the development phase of many other EGS projects. For instance, multiple induced seismic events of magnitude approaching M_L 3.7 were recorded at the Cooper Basin EGS project in Australia after the injection of 20,000 m^3 of water (Asanuma et al., 2005; Baisch et al., 2006). As recently as 2017, an earthquake of magnitude M_W 5.5 that struck South Korea in November 2017 was believed to be linked to the stimulation activities at the nearby Pohang EGS project (Grigoli et al., 2018).

Many induced microseismic events have also been reported during the production phases of various EGS projects. At the Hellisheidi geothermal power plant, which is located within the Hengill volcanic system in Iceland, microseismic activity increased immediately after reinjection of geothermal waste water began (Flóvenz et al., 2015; Juncu et al., 2018), with two largest induced seismic events of magnitude 4. Later investigations showed that the fluid reinjection caused an increase in pore pressure which led to increased seismicity and fault slip

(Juncu et al., 2018). Both the pore pressure increase and the fault slip resulted in the observed surface deformation. An induced event of magnitude M_L = 2.7 was also recorded in August 2009 during the circulation phase at the geothermal project in Landau, Germany (Gaucher et al., 2015).

The risk of induced seismicity has to be thoroughly assessed and quantified before an EGS project can begin, especially for projects located near urban areas. Otherwise, this issue can impede the development or even lead to the cancelation of the project as was seen in Basel, Switzerland. Seismicity induced during the injection and withdrawal of fluids is believed to be associated with the slip of pre-existing faults and the propagation of new tensile fractures (Pearson, 1981). Both the fault slip and the fracture propagation are related to the in-situ stress variation, which is induced by thermo-poromechanical processes involved during the injection and withdrawal of fluids (Ghassemi and Tao, 2016; Ghassemi and Tarasovs, 2015; Ghassemi and Zhang, 2004; Segall and Fitzgerald, 1998). The thermo-mechanical coupling (i.e., changes in in-situ stress due to temperature variations) is important on long time scales from months to years (Ghassemi, 2012; Ghassemi and Tarasovs, 2015). While the poro-mechanical effect due to changes in pore pressure affects the deformation of the rock mass more quickly. Consequently, seismic events induced during the fluid injection are usually considered to be caused by the shear slip on natural faults in response to a reduction of the shear strength the faults due to an increase in pore pressure. However, thermoelastic perturbations can cause an increase of the deviatoric stress in the cooled portion of the reservoir, potentially provoking an unstable condition (De Simone et al., 2013). Thus, a comprehensive approach to assess the risk of induced seismicity should take into consideration the effects of both thermo- and poromechanical processes. A schematic of the fault slip due to fluid injection, the propagation of the induced seismic waves and the potential impact on surface structures is illustrated in Figure 1.8. The intensity of induced seismicity can be estimated based on the peak accelerations or peak velocities recorded on the ground surface and using the modified Mercalli intensity scale (Wald et al., 1999; Wood and Neumann, 1931). Figure 1.2 provides a relationship between the peak ground accelerations or peak ground velocities and the seismic intensity, human perception and potential structural damage. The consequences of the induced

seismicity can range from a nuisance to the population to structural damages to the infrastructure.

Table 1.2 Modified Mercalli intensity scale and corresponding peak ground acceleration and peak ground velocity. Source: Wald et al. (1999), Wood and Neumann (1931)

Intensity	Peak acceleration (%g)	Peak velocity (cm/s)	Perceived shaking	Potential damage
I	< 0.17	< 0.1	Not felt	None
II–III	0.17 – 1.4	0.1 – 1.1	Weak	None
IV	1.4 –3.9	1.1 – 3.4	Light	None
V	3.9 – 9.2	3.4 – 8.1	Moderate	Very light
VI	9.2 –18	8.1 – 16	Strong	Light
VII	18 –34	16 – 31	Very strong	Moderate
VIII	34 –65	31 – 60	Severe	Moderate to heavy
IX	65 – 124	60 – 116	Violent	Heavy
X+	> 124	> 116	Extreme	Very heavy

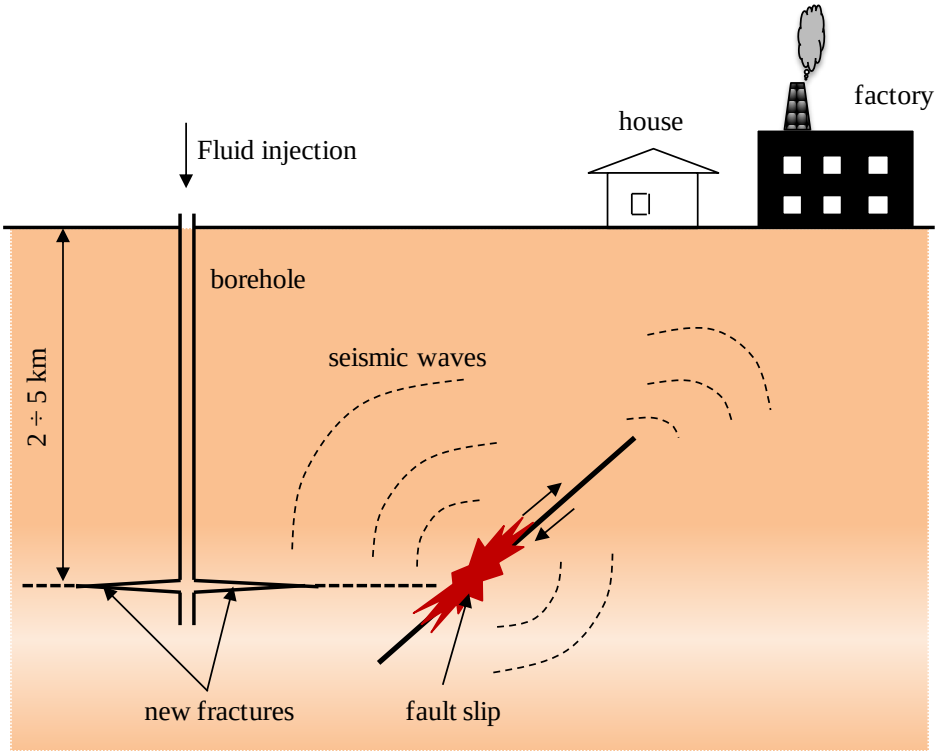

Figure 1.8 Slip of fault due to fluid injection, propagation of induced seismic waves, and potential impact on surface structures and human perception. Adapted from Rutqvist et al. (2014)

1.4 OBJECTIVE OF THIS RESEARCH

This research is a part of the major project GEOTREF – a multidisciplinary platform for innovation and demonstration activities for the exploration and development of high geothermal energy in fractured reservoirs. The project is funded by the *Investissement d'avenir* program of the French government through the *Agence de l'Environnement et de la Maitrise de l'Energie* (ADEME) and the Guadeloupe region. The aim of the project is to improve the understanding of fractured geothermal reservoirs in order to reduce geothermal "geological risk" and to ensure sustainable exploitation of the reservoir during the production phase.

As part of the Research and Development group of the project GEOTREF, this work is mainly concerned with modeling the propagation of new tensile fractures and the slip of pre-existing faults during the stimulation of deep geothermal reservoirs and proposing a numerical procedure to modeling the seismicity induced by fault slip. The following objectives are set for this work:

- Simulate the propagation of hydraulic fractures and their interaction with pre-existing faults during the hydraulic stimulation of deep geothermal reservoirs; study the thermal effects on long term propagation of hydraulic fractures.
- Study the reactivation and the slip of the pre-existing faults to determine parameters that control the fault slip and propose a procedure to estimate the peak ground acceleration that is induced by the fault slip
- Explain and model the dynamic effects induced by the fracture propagation in a rigorous manner using conservation laws

Chapter 2

Theoretical framework and numerical simulation approach

RÉSUMÉ

Ce chapitre décrit d'abord le problème central de cette thèse de doctorat, à savoir la propagation des fractures hydrauliques et leurs interactions avec des failles préexistantes lors de la mise en valeur de réservoirs géothermiques. Ce chapitre fournira ensuite un résumé de la base théorique des processus physiques impliqués. Les équations de la théorie des milieux thermo–poroélastiques saturés en fluide sont présentées en premier. Celles-ci incluent les équations de déformation des milieux poreux, les équations d'écoulement du fluide dans les pores, dans les fractures et les failles, ainsi que celles du transfert de chaleur. Ensuite, les critères de propagation de la rupture basés sur la mécanique de la rupture et sur le concept de matériau cohésif sont présentés. L'aspect dynamique de la propagation de la fracture est également inclus. Puis, le phénomène de réactivation des failles et le critère de réactivation des failles sont passés en revue, l'accent étant mis sur l'utilisation du critère de Coulomb pour évaluer la réactivation de la défaillance. Les équations des modèles de fractures hydrauliques simples sont également présentées. Ces modèles servent de solutions de référence pour la validation des modèles numériques. Enfin, les méthodes numériques de modélisation de la propagation des fractures sont exposées, notamment la méthode des éléments finis étendus et la technique des éléments cohésifs.

SUMMARY

This chapter first describes the central problem of this doctoral research which is the propagation of hydraulic fractures and their interactions with pre-existing faults during the development of geothermal reservoirs. The chapter then provides a summary of the theoretical basis for the physical processes that are involved. The equations of the theory of fluid–saturated thermo–poroelastic media are presented first. These include equations for deformation of porous media, the fluid flow in the pores and in the fractures and faults, and the heat transfer. Next, the criteria for fracture propagation, based on fracture mechanics and the concept of cohesive material, are presented. The dynamic aspect of fracture propagation is also included. The phenomenon of fault reactivation and the criterion for fault reactivation are then reviewed with an emphasis on using the Coulomb friction criterion for assessing fault reactivation. The equations for single hydraulic fracture models are also presented. Those models serve as reference solutions for the validation of the numerical models. Finally, the numerical methods for modeling fracture propagation are presented, which include the extended finite element method and the cohesive element technique.

2.1 INTRODUCTION

This doctoral research is centered on the numerical modeling of the propagation of hydraulic fractures and the potential reactivation of pre-existing faults during hydraulic stimulation of deep geothermal reservoirs. The process of hydraulic stimulation is schematically presented in Figure 2.1. A borehole is drilled into a hot dry rock formation and fluid is injected at pressures high enough to create new hydraulic fractures (Figure 2.1a). As the hydraulic fractures propagate they may intersect pre-existing faults (Figure 2.1b). The fluid then flows into these faults, leading to an increase in the fluid pressure in the faults, which in turn causes the faults to slip. The fault slip is both beneficial and hazardous. On the one hand, the fault slip will improve the fault permeability due to dilatancy effects and fault roughness, thus enhancing the overall permeability of the reservoir which is beneficial. On the other hand, the fault slip may also be unstable, which means that the fault slip may induce seismic waves; if the induced seismic waves are strong enough, they can cause harm to people and damage structures on the ground, which is hazardous.

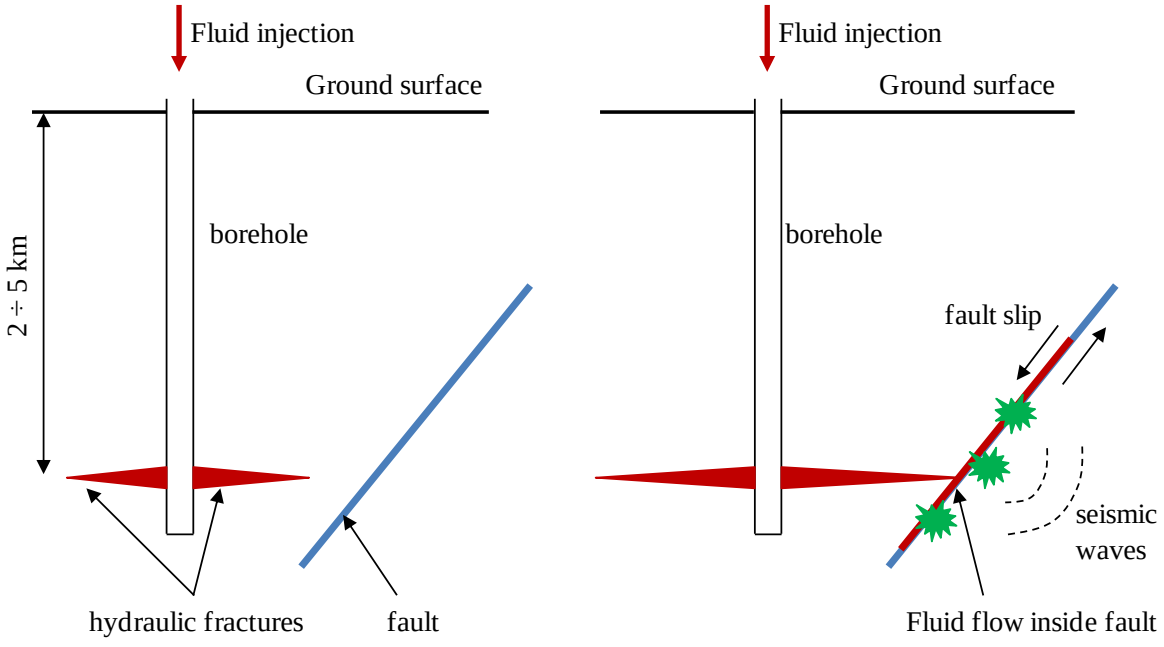

(a) Propagation of hydraulic fractures

(b) Intersection of hydraulic fractures with pre-existing faults

Figure 2.1 Schematic representation of the hydraulic stimulation of geothermal reservoirs

The propagation of hydraulic fractures or the reactivation of pre-existing faults in a permeable porous rock mass that is fully saturated due to the injection of fluid is a coupled problem that involves multiple physical processes:

(i) deformation of the porous rock mass;
(ii) flow of the fluid within the pores;
(iii) flow of the fluid within the hydraulic fractures and the pre-existing faults;
(iv) propagation of the hydraulic fractures or the reactivation of the pre-existing faults;
(v) heat transfer.

In-situ conditions such as the presence of natural fractures, incomplete data regarding the initial conditions (e.g., stresses and pore pressure) or physical properties of the rock mass, may add additional complexities to the problem. Furthermore, the propagation of brittle fractures is inherently a dynamic process that releases energy in the form of elastic waves. The effects of these waves may be significant over a short time period (on the order of seconds) following the sudden propagation of the fracture. Meanwhile, the diffusion of fluid within the pores and the fluid injection operation itself occur over much longer time period (on the order of hours or even days). Thus, coupling the inertial effects with the fluid diffusion is an unrealistic task. A modeling procedure to quantify the induced dynamic effects is presented in Chapter 5. Thermal effects also need to be accounted for since hydraulic stimulation of EGS involves temperature changes of significant orders as cold water is pumped into hot rock formations. The above phenomena and the equations for describing these phenomena are presented in the next sections.

2.2 GENERAL GOVERNING EQUATIONS

2.2.1 Deformation of porous rock mass

The rock mass is macroscopically considered as a homogeneous, isotropic, and poroelastic medium whose constitutive relation is expressed as (Coussy, 2004):

$$\sigma_{ij} - \sigma_{ij,0} = \left(K - \frac{2}{3} G \right) \varepsilon_{kk} \delta_{ij} + 2G\varepsilon_{ij} - 3\alpha K \left(T - T_0 \right) \delta_{ij} - b\left(p - p_0 \right) \delta_{ij} \tag{2.1}$$

where σ_{ij} is the current total stress (compression is negative), $\sigma_{ij,0}$ is the initial stress; ε_{ij} is the current strain of the skeleton, ε_{kk} is the volumetric strain (summation over the repeated indices $\varepsilon_{kk} = \varepsilon_{11} + \varepsilon_{22} + \varepsilon_{33}$); p and p_0 are the current and initial pore pressures, respectively; T and T_0 are the current and initial temperatures, respectively; K and G are the bulk modulus and the shear modulus of the skeleton, respectively; α is the linear thermal expansion coefficient of the skeleton; and b is the Biot's coefficient, which is related to the bulk modulus K of the skeleton and the bulk modulus K_S of the solid phase as:

$$b = 1 - \frac{K}{K_S} \tag{2.2}$$

The bulk modulus K and the shear modulus G are related to the Young's modulus E and the Poisson's ratio ν of the skeleton as:

$$K = \frac{E}{3(1-2\nu)} \qquad\qquad G = \frac{E}{2(1+\nu)} \tag{2.3}$$

Equation (2.1) can be interpreted as follows: on the left hand side is the total stress, while on the right hand side is the stress supported by the skeleton, i.e., the first two terms, and the stress supported by the fluid, which is the last term. Thus, the effective stress, which is the stress supported by the skeleton, is expressed as:

$$\sigma''_{ij} - \sigma''_{ij,0} = \left(K - \frac{2}{3} G \right) \varepsilon_{kk} \delta_{ij} + 2G\varepsilon_{ij} - 3\alpha K \left(T - T_0 \right) \delta_{ij} \tag{2.4}$$

Comparing equation (2.4) with equation (2.1), the effective stress can be expressed as function of the total stress and the pore pressure as:

$$\sigma''_{ij} = \sigma_{ij} + bp\ \delta_{ij} \tag{2.5}$$

Equation (2.5) is the expression for Biot's effective stress, which applies when the solid phase is either compressible or incompressible. For an incompressible solid phase (i.e., $K_S \to \infty$), according to equation (2.2) the Biot's coefficient is $b = 1$, and thus equation (2.5) becomes the familiar expression for Terzaghi's effective stress:

$$\sigma_{ij}^{''} = \sigma_{ij} + p\ \delta_{ij} \tag{2.6}$$

All the field quantities (stresses, strains, pressure, and temperature) in equation (2.1) are functions of coordinates $\mathbf{x}(x_1, x_2, x_3)$ and time *t*. Under conditions of small perturbations, the strain ε_{ij} can be related to the displacement components u_i as:

$$\varepsilon_{ij} = \frac{1}{2}\left(u_{i,j} + u_{j,i}\right) \tag{2.7}$$

where the comma denotes the partial derivative with respect to the spatial variable.

The skeleton of the rock mass must always be in a state of equilibrium. The equilibrium equations under quasi-static conditions and when body forces are absent are:

$$\sigma_{ij,j} = 0 \tag{2.8}$$

Substitution of equation (2.4) into equation (2.8) while taking into account equation (2.7) leads to the equation that governs the kinematics of the skeleton:

$$\left(K + \frac{G}{3}\right)u_{k,ki} + Gu_{i,kk} - 3\alpha K\ T_{,i} - bp_{,i} = 0 \tag{2.9}$$

The unknown variables in equation (2.9) include the displacements u_i, the pore pressure *p* and the temperature *T*.

2.2.2 Pore fluid flow

The continuity equation for the pore fluid under small perturbations conditions is given by, (Coussy, 2004; Selvadurai and Suvorov, 2016):

$$b\frac{\partial \varepsilon_{kk}}{\partial t} + \frac{1}{M}\frac{\partial p}{\partial t} - 3\alpha_m \frac{\partial T}{\partial t} + \nabla.\left(\phi \underline{v}\right) = 0 \tag{2.10}$$

where *M* is the Biot modulus; α_m is a coefficient; $\phi \underline{v}$ is the fluid velocity vector; and $\nabla.()$ is the divergence operator.

The Biot modulus *M* is related to the bulk modulus of the fluid K_f, the bulk modulus of the solid phase K_S, the initial porosity ϕ_0, and the Biot's coefficient *b* as:

$$\frac{1}{M} = \frac{\phi_0}{K_f} + \frac{b - \phi_0}{K_S} \tag{2.11}$$

The coefficient α_m is a function of the linear thermal expansion coefficients α_s and α_f of the fluid and the solid phases (Selvadurai and Suvorov, 2016):

$$\alpha_m = \alpha_f + (b - \phi)\alpha_S \tag{2.12}$$

The fluid flow within the pores is assumed to follow Darcy's law. The velocity vector $\phi \underline{v}$ is expressed as:

$$\phi \underline{v} = -\frac{k}{\eta} \nabla p \tag{2.13}$$

where k is the hydraulic conductivity, in m^2; η is the dynamic viscosity of the fluid, in Pa.s

Substituting equation (2.13) into equation (2.10) leads to the field equation that governs the fluid flow in the pores:

$$b \frac{\partial \varepsilon_{kk}}{\partial t} + \frac{1}{M} \frac{\partial p}{\partial t} = 3\alpha_m \frac{\partial T}{\partial t} + \frac{k}{\eta} \nabla^2 p \tag{2.14}$$

It should be noted from equation (2.14) that the partial derivative with respect to time of the volumetric strain ε_{kk} shows the coupling between the mechanicals response of the skeleton and the fluid diffusion.

2.2.3 Fluid flow in hydraulic fractures and existing fractures

In permeable reservoirs, fluid loss from fractures is considered to be a pressure-independent process. The Carter's leakoff model gives an expression for the infiltration rate of fluid from the fracture as (Carter, 1957):

$$g(\mathbf{x}, t) = \frac{2C_L}{\sqrt{t - t_0}} \tag{2.15}$$

where $g(\mathbf{x}, t)$ is the infiltration rate from both faces of the hydraulic fracture; C_L is the Carter's leakoff coefficient; t_0 is the time at which the hydraulic fracture arrives at the point **x**.

The Carter's model is obtained from the pressure diffusion equation, assuming that the leakoff is one-dimensional. The model is used to describe the physical phenomenon that occurs as the fracturing fluid deposits a thin layer of material on the fracture faces. This phenomenon of material deposition is usually observed in hydraulic stimulation of oil and gas reservoirs where proppants and chemical additives (e.g., polymers) are used. In hydraulic stimulation of deep geothermal reservoirs, fresh water or brine is usually used. Thus, we assume that there is no material deposition on the surfaces of the hydraulic fracture. Therefore, the leakoff flow rate will depend only on the permeability of the rock mass and the difference in pressure between the inside of the fracture and inside of the reservoir, and can be expressed as:

$$g = C_0(p_f - p_r) \tag{2.16}$$

where C_0 is the constant leakoff coefficient; p_f and p_r are the pressure inside the fracture and inside the reservoir (Figure 2.2), respectively.

With leakoff included, the continuity equation for the incompressible fluid flow in the fracture is given by:

$$\frac{\partial w}{\partial t} + \frac{\partial q}{\partial s} + g = 0 \tag{2.17}$$

where w is the fracture aperture; q is the longitudinal fluid flow rate, as shown in Figure 2.2.

When two surfaces of the fracture are considered as parallel and smooth plates and the fluid is Newtonian and incompressible, the longitudinal flow rate q in steady state is related to the pressure gradient as (i.e., the Poiseuille equation):

$$q = -\frac{w^3}{12\eta}\frac{\partial p_f}{\partial s} \tag{2.18}$$

where η is the dynamic viscosity of the fluid. From equation (2.18), the transmissivity of the fracture is defined as:

$$k_t = \frac{w^3}{12\eta} \tag{2.19}$$

Substituting the Poiseuille equation (2.18) into the continuity equation leads to the field equation that governs fluid flow in the fracture, as:

$$\frac{\partial w}{\partial t} + g = \frac{\partial}{\partial s}\left(\frac{w^3}{12\eta} \frac{\partial p_f}{\partial s} \right) \tag{2.20}$$

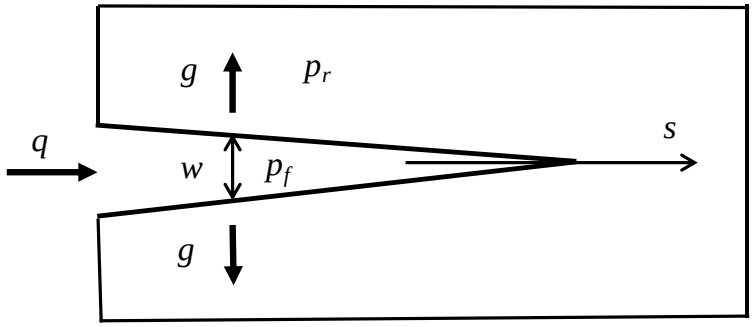

Figure 2.2 Fracture geometry and fluid flow in the fracture. *w* is the fracture aperture, *q* is the longitudinal flow, *g* is the leakoff flow rate

2.2.4 Heat transfer

As stated previously, hydraulic stimulation of EGS reservoirs involves temperature changes of significant magnitudes. Rock formations, e.g., crystalline rock masses, where EGS reservoirs are developed, usually have a very low permeability. In these formations, the predominant mode of heat transfer in the rock mass is conduction. The convective heat transfer associated with the slow diffusion fluid flows is negligible (Selvadurai and Suvorov, 2016). Therefore, Fourier's law of heat conduction can be used to describe the heat transfer in the rock matrix as:

$$\underline{q} = -\lambda \nabla T \tag{2.21}$$

where $\underline{q}$ is the heat flux vector; λ is the thermal conductivity of the rock mass.

The thermal energy conservation equation for the rock mass is given as:

$$C_P \frac{\partial T}{\partial t} + \nabla . \underline{q} = 0 \tag{2.22}$$

where C_P is the overall heat capacity of the rock mass.

The heat equation is obtained by substituting Fourier's heat conduction equation (2.21) into the equation of thermal energy conservation (2.22):

$$C_P \frac{\partial T}{\partial t} - \lambda \nabla^2 T = 0 \tag{2.23}$$

where $\nabla^2()$ is the Laplace operator.

At the interface between a flowing fluid and a solid, such as fluid – rock interface, heat transfer takes place by convection. The basic relationship for heat transfer by convection is:

$$\underline{q} \cdot \underline{n} = h(T - T_a) \tag{2.24}$$

where $\underline{q}$ is the heat flux vector, $\underline{n}$ is the unit normal vector, T_a is the temperature of the fluid, T is the temperature on the surface of the solid, and h is the convective heat transfer coefficient

2.3 FRACTURE PROPAGATION

For brittle rocks such as granite under in-situ conditions of stress, fracture is the main mechanism of failure. Other processes that may lead to failure include corrosion and wear. However, these processes happen slowly over long time periods and are less of a concern, especially for rock masses where EGS rock reservoirs are to be created. In general, the fracture process is divided into three distinct phases (Broberg, 1999): (1) loading without crack growth, (2) stable crack growth, and (3) unstable crack growth. Stable crack growth can be controlled by controlling the applied load and a prescribed slow crack growth may be obtained. This is not possible for unstable crack growth, which occurs spontaneously and is usually accompanied induced dynamic effects such as elastic waves.

In the vicinity of the tip of a crack, two distinctly different zones exist, as shown in Figure 2.3. These include a small zone immediately next to the crack tip known as the *process zone* and a plastic zone outside the process zone. The fracture process always starts from the process zone, where stress and strain concentrations occur. When subjected to high stress, the nucleation and growth of micro-separations takes place in the process zone, i.e., material separation, such as the breakage of atomic bonds. Micro-separations are nucleated at inhomogeneities in the material, e.g., flaws or boundaries between grains. As these micro-separations extend and propagate, voids are created, which in turn propagate and coalesce with other voids and with the main crack, allowing the main crack to grow.

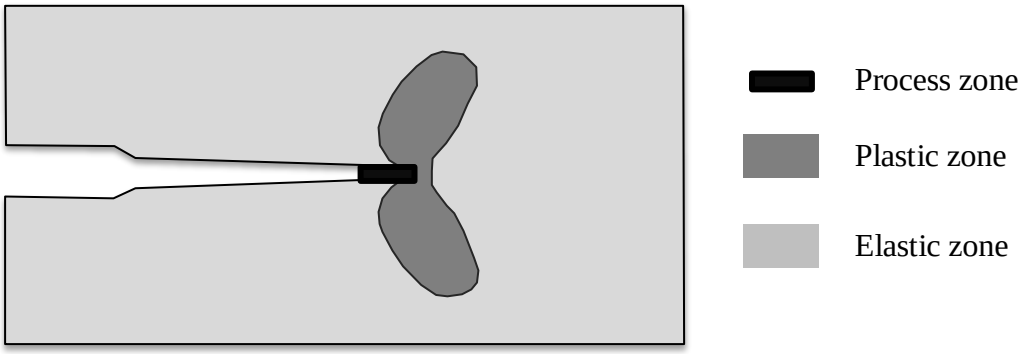

Figure 2.3 Two distinct zones in the vicinity of a crack tip. The nucleation and growth of micro-separations take place in the process zone, leading to the creation of voids. The propagation and coalescence of voids allow the crack to grow. After (Broberg, 1999)

For polycrystalline materials such as rocks, the micro-separations are in the form of micro-cracks. The nucleation and growth of these micro-cracks in the process zone is the kernel for the propagation of macro-crack in these materials. (Atkinson, 1989) used the loading of a blunt notch, as shown in Figure 2.4, to illustrate the formation and propagation of a macro-crack. Several micro-cracks exist in the initial configuration (Figure 2.4-a). As the applied load is increased, more micro-cracks are nucleated in the process zone (Figure 2.4-b) and propagate (Figure 2.4-c). The coalescence of these micro-cracks allows the macro-crack to propagate (Figure 2.4-d,e). A new process zone develops a head of the tip of the macro-crack in parallel with the propagation of the macro-crack. The size of the process zone depends on the nature of the material and its internal structure. For brittle rocks, the size of the process zone is relatively small in comparison with the dimensions of the cracked body and hence a large part of the body remains elastic.

There are three basic modes of crack tip displacement, as illustrated in Figure 2.5. Mode I is the opening mode where the principal load is applied normal to the crack plane and the crack tends to open. Mode II corresponds to the case where the crack faces tend to slide over each other due to in-plane shear. Mode III occurs when out-of-plane shear is the predominant applied load. A cracked body can be loaded in any one of these modes, or a combination of two or three modes.

Fracture propagation can be studied and modeled using either the theory of fracture mechanics or the cohesive zone model. The fundamental elements of these concepts and related issues are presented in the following sections.

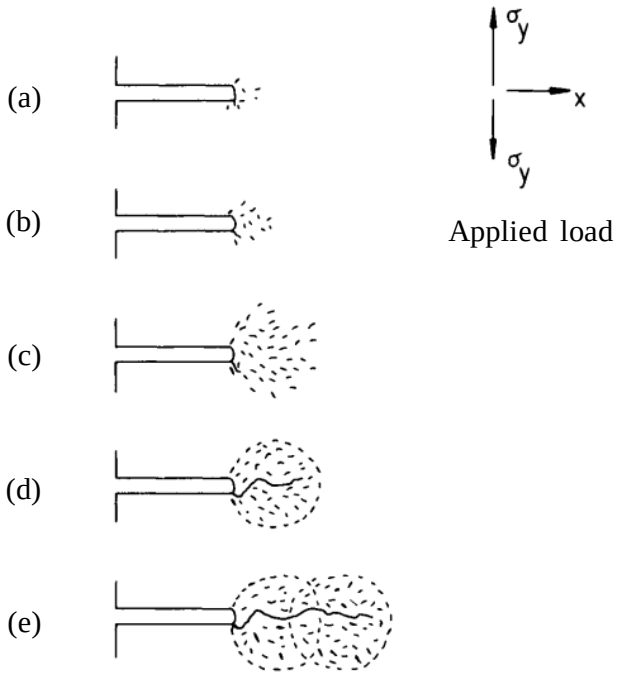

Figure 2.4 Development of a process zones and extension of the macro-crack from the tip of a blunt notch due to applied load σ_y. The applied load increases from drawings (a) to (e). (a) Existing micro-cracks. (b) Nucleation of micro-cracks. (c) Propagation of micro-cracks. (d) Coalescence of micro-cracks. (e) Extension of the macro-crack. Source: adapted from Atkinson (1989)

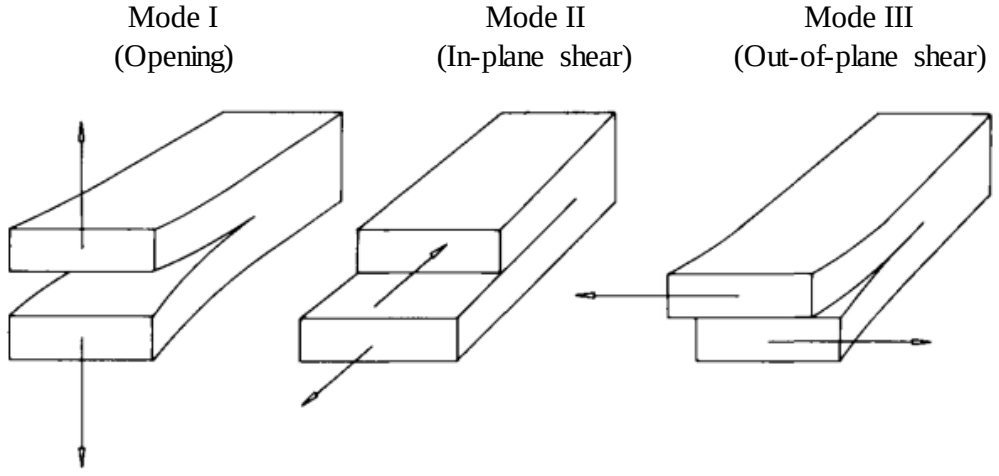

Figure 2.5 Three fundamental modes of fracture: Mode I, tensile or opening mode; Mode II, in-plane shear or sliding mode; Mode III, out-of-plane shear or tearing mode

2.3.1 Fracture mechanics

The theory of fracture mechanics revolves around two major approaches, namely the Griffith energy balance approach, which was developed by Griffith (1920), and the Irwin stress analysis approach, which was introduced by Irwin (1957). These approaches and related issues are presented in detail in the following paragraphs.

2.3.1.1 Griffith energy balance approach

Griffith used thermodynamic arguments to find the criterion for a crack to grow due to an external load. By using the results of stress analyses of a plate containing a crack-like elliptical hole (Inglis, 1913), Griffith showed a quantitative connection between the fracture stress – the applied stress at which the crack starts to propagate, and the crack size (Griffith, 1920). According to the first law of thermodynamics, the total energy of a system remains constant as the system moves from one equilibrium state to another. Griffith argued that the quasi-static propagation of a crack can be seen as occurring under equilibrium conditions. Thus, during the propagation of the crack the decrease in strain energy must be sufficient to overcome the energy necessary to create new crack surfaces.

Consider a Mode I fracture as shown in Figure 2.6, the total energy of the system is composed of the potential energy Π and the total surface energy W_s. Thus:

$$E = \Pi + W_s \tag{2.25}$$

The potential energy Π, which is supplied by the internal strain energy and the work of the external loads, is given by:

$$\Pi = \frac{1}{2}\int_{\Omega} \sigma_{ij}\varepsilon_{ij} d\Omega - \int_{S} \sigma_{ij} n_j dS \tag{2.26}$$

The energy release rate G_I, which is a measure of the energy available for an increment of crack extension in Mode I, is defined as:

$$G_I = -\frac{d\Pi}{dA} \tag{2.27}$$

where A is the crack area

The Mode I fracture energy G_{IC}, which is the energy necessary to create new crack surfaces for the same increment of crack extension, is defined as:

$$G_{IC} = -\frac{dW_s}{dA} \tag{2.28}$$

The Griffith energy balance for an incremental increase in the crack area *dA* can be written as:

$$\frac{dE}{dA} = \frac{d\Pi}{dA} + \frac{dW_s}{dA} = 0 \tag{2.29}$$

Substituting equations (2.27) and (2.28) into equation (2.29) gives the criterion for fracture propagation as:

$$G_I = G_{IC} \tag{2.30}$$

Griffith used the results from the stress analysis of Inglis and showed that for a plate containing a crack subjected to Mode I loading as shown Figure 2.6, the potential energy is given by:

$$\Pi = \Pi_0 - \frac{\pi\sigma^2 a^2 B}{E} \tag{2.31}$$

where Π_0 is the potential energy of the uncracked body, which is independent of the crack length; *B* is the plate thickness. Combining equation (2.27) and equation (2.31) leads to the expression of the energy release rate G_I as:

$$G_I = \frac{\pi\sigma^2 a}{E} \tag{2.32}$$

Since the formation of one crack of length *2a* creates two surfaces of the same area *A = 2aB*, the total surface energy W_s is given by:

$$W_s = 4aB\gamma_s \tag{2.33}$$

where γ_s is the unit surface energy, in J/m^2.

Combining equation (2.28) and equation (2.33) leads to the expression of the fracture energy G_{IC} for the Mode I fracture as:

$$G_{IC} = 2\gamma_s \tag{2.34}$$

The fracture stress, which is the stress at which the crack starts to propagate, can be obtained by combining equations (2.30), (2.32), and (2.34), as:

$$\sigma_f = \sqrt{\frac{2E\gamma_s}{\pi a}} \tag{2.35}$$

The fracture criterion, as in equation (2.35), is obtained through the introduction of the concept of the energy release rate (equation (2.27)), which is the net change in potential energy of the whole system that accompanies an increment of crack extension. Thus, the energy release rate characterizes the global behavior without regard for the local stress concentrations, which is in contrast to the stress analysis approach presented below.

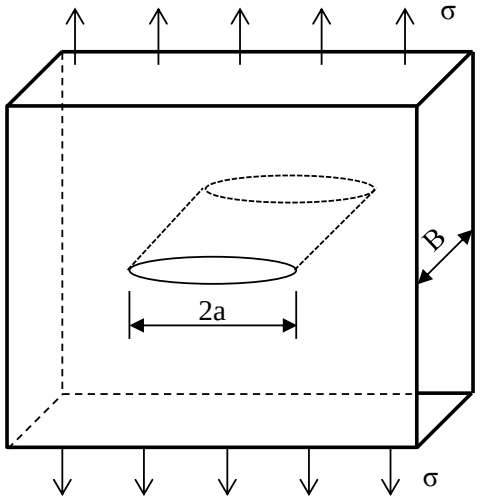

Figure 2.6 Plate with a crack of length *2a* subjected to a remote stress σ

2.3.1.2 Irwin stress analysis approach

This stress analysis-based approach for studying fracture was introduced by Irwin (1957), who recognized that for certain cracked configurations subjected to external loads, it is possible to obtain closed-form expressions for the stresses in the region near the crack tip, assuming that the material is isotropic and linear elastic. The stresses at a point M near the crack tip and located by the polar coordinates (r, θ), as shown Figure 2.7, are given by:

$$\sigma_{ij} = \frac{K}{\sqrt{2\pi r}} f_{ij}(\theta) \tag{2.36}$$

where K is the *stress intensity factor* that depends on the loading mode; $f_{ij}(\theta)$ is a well defined dimensionless function of θ and depends on the loading mode. Functions $f_{ij}(\theta)$ for Modes I and II are given in Table 2.1.

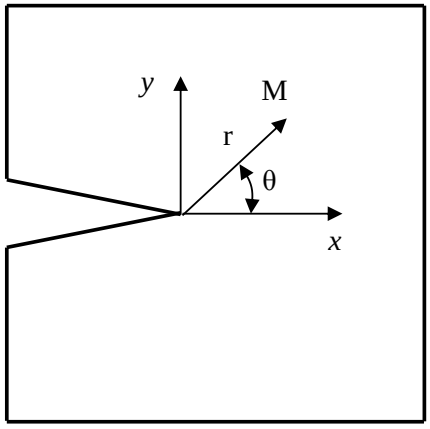

Figure 2.7 Definition of the coordinate axis ahead of a crack tip

Table 2.1 Functions $f_{ij}(\theta)$ for Mode I and II fracture (Anderson, 2005)

$f_{ij}(\theta)$	**Mode I**	**Mode II**
f_{xx}	$\cos\left(\frac{\theta}{2}\right)\left[1-\sin\left(\frac{\theta}{2}\right)\sin\left(\frac{3\theta}{2}\right)\right]$	$-\sin\left(\frac{\theta}{2}\right)\left[2+\cos\left(\frac{\theta}{2}\right)\cos\left(\frac{3\theta}{2}\right)\right]$
f_{yy}	$\cos\left(\frac{\theta}{2}\right)\left[1+\sin\left(\frac{\theta}{2}\right)\sin\left(\frac{3\theta}{2}\right)\right]$	$\sin\left(\frac{\theta}{2}\right)\cos\left(\frac{\theta}{2}\right)\cos\left(\frac{3\theta}{2}\right)$
f_{xy}	$\cos\left(\frac{\theta}{2}\right)\sin\left(\frac{\theta}{2}\right)\cos\left(\frac{3\theta}{2}\right)$	$\cos\left(\frac{\theta}{2}\right)\left[1-\sin\left(\frac{\theta}{2}\right)\sin\left(\frac{3\theta}{2}\right)\right]$

There are three stress intensity factors K_I, K_{II}, and K_{III} that correspond to the three loading modes I, II, and III. In a mixed-mode problem (i.e., when more than one loading mode is present), the principle of linear superposition applies and the stresses are given as:

$$\sigma_{ij} = \sigma_{ij}^{(I)} + \sigma_{ij}^{(II)} + \sigma_{ij}^{(III)} \tag{2.37}$$

where $\sigma_{ij}^{(I)}$, $\sigma_{ij}^{(II)}$, and $\sigma_{ij}^{(III)}$ are the stress contributions of Mode I, II, and III, respectively.

For a given loading condition, the stress intensity factor is the only parameter that characterizes the stress field, and thus the strain field, of the region near a crack tip. The propagation of the crack depends entirely on the stress intensity factor. For instance, under pure Mode I loading, the crack propagation criterion is expressed as:

$$K_I = K_{IC} \tag{2.38}$$

where K_{IC} is the critical stress intensity factor, which is unique to each material and can be obtained through experiments. Expressions similar to equation (2.38) also apply to pure fracture Modes II and III.

2.3.1.3 Relationship between the energy release rate and stress intensity factor

The fracture criterion can be expressed as the energy release rate as in equation (2.30) or as a stress intensity factor as in equation (2.38). Based on the observation that the energy released for an increment of crack extension must be equal to the work required to close the crack, Irwin performed a crack closure analysis and obtained the relationship between the stress intensity factor and the energy release rate for a Mode I fracture as:

$$G_I = \frac{K_I^2}{E'} \tag{2.39}$$

where $E' = E$ for plane stress and $E' = E/(1-\nu^2)$ for plane strain, E is the Young's modulus.

Defining the fracture energy as $G_{IC} = K_{IC}^2 / E'$, the Irwin fracture criterion (equation (2.38)) becomes identical to the Griffith fracture criterion (equation (2.30)) and is repeated here for convenience:

$$G_I = G_{IC} \tag{2.40}$$

The fracture criterion expressed by equation (2.40) can be generalized to apply to mixed-mode loading conditions. The fracture criterion expressed by equation (2.38) is applicable only for an individual loading mode. Pure Mode I fracture propagates when equation (2.38) is satisfied. Pure Mode II fracture propagates when $K_{II} = K_{IIC}$. When multiple loading modes are present,

the use of stress intensity factors to express the fracture criterion becomes complicated and unclear because the stress intensity factors of different modes are not additive. In such cases, the more convenient way is to use the fracture criterion defined in terms of the energy release rate in a generalized form because there exists a relationship between the stress intensity factor and the energy release rate for mixed-mode loading conditions, which is given by, (Anderson, 2005):

$$G = \frac{K_I^2}{E'} + \frac{K_{II}^2}{E'} + \frac{K_{III}^2}{\mu} \tag{2.41}$$

where μ is the shear modulus. Equation (2.41) can be interpreted as: under mixed-mode conditions, the total energy release rate G is equal to the sum of work G_I, G_{II}, and G_{III} necessary to close the crack along the normal, in-plane, and out-of-plane directions, respectively, i.e.,:

$$G = G_I + G_{II} + G_{III} \tag{2.42}$$

where

$$G_I = \frac{K_I^2}{E'} \;;\; G_{II} = \frac{K_{II}^2}{E'} \;;\; G_{III} = \frac{K_{III}^2}{\mu} \tag{2.43}$$

The fracture criterion under mixed-mode loading conditions now becomes:

$$G = G_C \tag{2.44}$$

where G_C is the equivalent fracture energy.

2.3.1.4 Equivalent fracture energy

Equation (2.44) is similar to equation (2.40), except that the equivalent fracture energy G_C is no longer a constant, depending not only on the material as is the case of G_{IC} (or G_{IIC}, G_{IIIC}), but also on the proportions between G_I, G_{II}, and G_{III}. Several formulae have been proposed to compute G_C, including the following:

- The BK law (Benzeggagh and Kenane, 1996)

$$G_C = G_{IC} + \left(G_{IIC} - G_{IC}\right)\left(\frac{G_{II} + G_{III}}{G_I + G_{II} + G_{III}}\right)^m \tag{2.45}$$

where *m* is a material parameter

- The Power law (Wu and Reuter Jr, 1965)

$$\frac{G}{G_C} = \left(\frac{G_I}{G_{IC}}\right)^a + \left(\frac{G_{II}}{G_{IIC}}\right)^b + \left(\frac{G_{III}}{G_{IIIC}}\right)^c \tag{2.46}$$

where *a, b, c* are material parameters

- The Reeder law (Reeder et al., 2002)

$$G_C = G_{IC} + \left[\left(G_{IIC} - G_{IC}\right) + \left(G_{IIIC} - G_{IIC}\right)\left(\frac{G_{III}}{G_{II} + G_{III}}\right)\right]\left(\frac{G_{II} + G_{III}}{G}\right)^m \tag{2.47}$$

where *m* is a material parameter

2.3.1.5 Crack orientation

Under mixed-mode loading conditions, the direction of crack propagation also needs to be determined; several proposals exist in the literature (Erdogan and Sih, 1963; Qian and Fatemi, 1996; Sih and Barthelemy, 1980). The propagation direction determined based on the maximum tangential stress or minimum strain energy is presented below.

- Maximum tangential stress criterion:

This criterion states that the crack will propagate along the radial direction determined by $\theta = \theta_c$ on which the tangential stress σ_θ becomes maximum. Mathematically, θ_c is determined from:

$$\frac{\partial \sigma_\theta}{\partial \theta} = 0 \text{ and } \frac{\partial^2 \sigma_\theta}{\partial \theta^2} < 0 \tag{2.48}$$

- Minimum strain energy criterion

This criterion is based on the local density of the strain energy in the region around the crack tip. The crack is assumed to grow in a direction along which the strain energy density factor *S* reaches a minimum value. Thus the direction of crack growth is determined by:

$$\frac{\partial S}{\partial \theta} = 0 \text{ and } \frac{\partial^2 S}{\partial \theta^2} > 0 \tag{2.49}$$

2.3.1.6 Comments on the Griffith energy and Irwin stress approach

Both the Griffith energy balance and the Irwin stress analysis approaches form the foundation of linear elastic fracture mechanics. Both are based on the assumption that the material is linear elastic and thus singular stresses are allowed to exist at the crack tip. This assumption cannot be true for real materials, which all have a certain stress limit. Therefore, for real materials plastic deformation will always occur in the region around the crack tip where there are high stress concentrations. However, as long as the plastic zone is small in relation to the crack size, its effect is negligible and the above approaches are considered acceptable. This is true for rocks, especially brittle rocks that show very little plastic deformation before fracture occurs, as demonstrated in many experiments (Keshavarz, 2009; Keshavarz et al., 2010).

When plastic deformation is no longer negligible, the fracture criteria proposed by Griffith and Irwin are no longer valid. The energy consumed by plastic deformation has to be taken into consideration. In these cases, the fracture criterion can be formulated based on the concept of the J-integral, a more general concept introduced by Rice (1968) that can be applied to both linear and non-linear materials in monotonic loading conditions. With a crack shown in Figure 2.9, the J-integral is defined as (Rice, 1968):

$$J = \int_{\Gamma} \left(w dy - T_i \frac{\partial u_i}{\partial x} ds \right) \tag{2.50}$$

where w is the strain energy density; T_i are components of the traction vector; u_i are components of the displacement vector; ds is the length increment along the contour Γ.

(Rice, 1968) showed that the value of the J-integral is independent of the path of integration around the crack and is equal to the energy release rate G defined in the previous section.

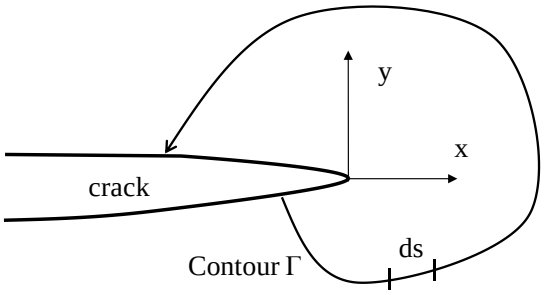

Figure 2.8 Arbitrary contour around the tip of a crack

In fracture problems where poroelastic effects are involved (e.g., fracture propagation due to hydraulic stimulation), the poroelasticity needs to be considered. It was shown by Atkinson and Craster (1991) that when taken into account the poroelastic effects retard the propagation of a fracture as pore pressures reduce the stress intensity factor. Using computational modeling, Selvadurai and Mahyari (1997) and Mahyari and Selvadurai (1998) also showed that the time-dependent variation of stress intensity factors at a propagating fracture can be computed using the transient analysis of the associated hydromechanical problem. For instance, for the problem of fracture propagation due to hydraulic stimulation the transient coupled stress-diffusion analysis is performed first and the effective stresses are then used to compute the stress intensity factors.

2.3.2 Cohesive zone model

An alternative for modeling the fracture is the cohesive zone model (CZM). This model was introduced by Dugdale (1960) and Barenblatt (1962), who tried to find a way to describe the damage zone at the crack tip. The model is based on the observation that there is always a partially damaged zone at the tip of a crack (i.e., the *cohesive zone*) through which stress can continue to be transferred until the separation between the two faces of this cohesive zone reaches a certain value. The cohesive zone (Figure 2.9) at the crack tip is the transition zone between the traction-free crack and the intact material and can be seen as the process zone. For the crack presented in Figure 2.9, the separation reaches a critical displacement δ_f at the tip of the traction-free crack. The tractions are zero at this point, but are equal to the tensile strength R_T at the tip of the cohesive zone.

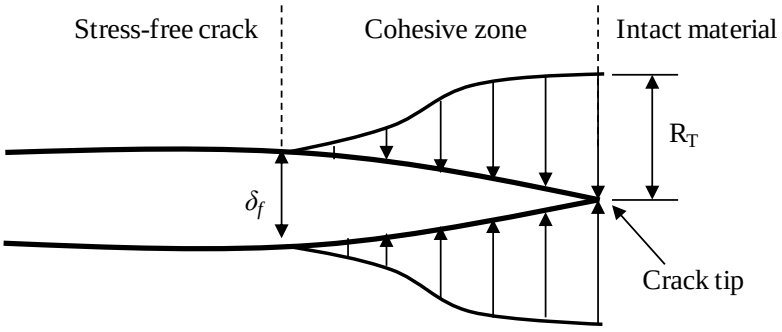

Figure 2.9 Schematic of cohesive zone

The cohesive zone model is defined by a traction – separation law. The damage initiation occurs when the traction reaches the tensile strength of the material. As the external load is increased the separation increases while the traction across this cohesive surface decreases and eventually vanishes. The traction-free crack is thus created and allows the crack to grow. A damage variable is used to track the damage of the cohesive zone during the separation process. The damage variable is zero until damage initiation, monotonically increases during the damage evolution, and reaches one as separation reaches the critical separation.

An example of the cohesive model for Mode I fracture is shown in Figure 2.10. This linear cohesive model can be described by three parameters: the tensile strength R_T, the critical separation δ_f and the initial stiffness K. The energy dissipated during the separation process for a unit increment of crack extension is by definition the fracture energy. It is obvious from Figure 2.10 that:

$$G_{IC} = \frac{1}{2} R_T \delta_f \tag{2.51}$$

The normal traction that can still be transferred across the cohesive zone during the separation process is calculated as:

$$\sigma = (1 - D)\sigma^p \tag{2.52}$$

where D is the damage variable and σ^p is a traction predictor. These two parameters are defined as (with $\delta_0 = R_T / K$)

$$D = \frac{\delta_f (\delta - \delta_0)}{\delta(\delta_f - \delta_0)} \qquad \sigma^p = K\delta \tag{2.53}$$

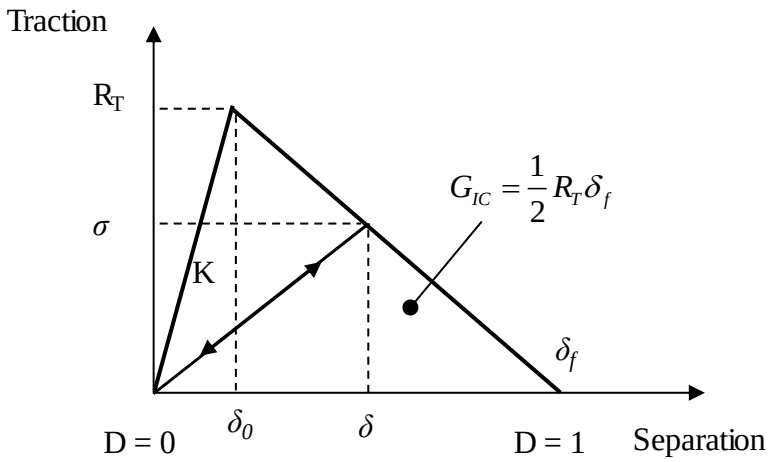

Figure 2.10 Schematic of a linear cohesive law for Mode I fracture. The three parameters of the model are the tensile strength R_T, the critical separation δ_f, and the initial stiffness K. σ and δ are the current normal traction and current normal separation, respectively

2.4 DYNAMIC FRACTURE PROPAGATION AND WAVE PROPAGATION

The propagation of brittle fractures is inherently a dynamic process that involves the release of strain energy in the form of elastic waves (Hardy Jr, 2003; Pollock, 1973; Scholz, 1968). The criterion for Mode I fracture propagation under dynamic conditions is written as follows (Anderson, 2005):

$$K_I(t) = K_{ID} \tag{2.54}$$

where $K_I(t)$ is the instantaneous stress intensity factor, K_{ID} is the dynamic fracture toughness of the material. In the dynamic context, $K_I(t)$ depends not only on the current external loads but also the reflecting stress waves that interact with the local stress field at the crack tip while K_{ID} is a function of the fracture propagation speed V_F. The dependence of K_{ID} on the fracture propagation speed can be expressed by an empirical formula as follows (Anderson, 2005):

$$K_{ID} = K_{IA}\left[1 - \left(\frac{V_F}{V_L}\right)^m\right]^{-1} \tag{2.55}$$

where V_F is the fracture propagation speed, V_L is the limiting fracture propagation speed in the material which is usually taken to be equal to the speed of Rayleigh waves (Freund, 1998), m is a constant, and K_{IA} is the arrest toughness of the material corresponding to $V_F = 0$.

The equation of wave propagation is the equilibrium equation taking into account the inertia forces and is written as:

$$\rho \frac{\partial^2 \mathbf{u}}{\partial t^2} = \nabla . \underline{\underline{\sigma}} + \mathbf{F} \tag{2.56}$$

where **u** is the displacement vector; **F** is the body forces; and $\underline{\underline{\sigma}}$ is the Cauchy stress tensor. Under the condition of small perturbations and a linear elastic material, one has the following relations:

- Kinematic relation between strains and displacements:

$$\underline{\underline{\varepsilon}} = \frac{1}{2}\left(\nabla \mathbf{u} + {}^{T}\nabla \mathbf{u}\right) \tag{2.57}$$

- Linear relation between stresses and strains:

$$\underline{\underline{\sigma}} = \lambda tr(\underline{\underline{\varepsilon}})\underline{\underline{I}} + 2\mu \underline{\underline{\varepsilon}} \tag{2.58}$$

where $\nabla()$ is the gradient operator; λ and μ are the Lamé coefficients.

Combining equations (2.56), (2.57), and (2.58) leads to (without body force, **F** = **0**):

$$\rho \frac{\partial^2 \mathbf{u}}{\partial t^2} = (\lambda + \mu)\nabla(\nabla . \mathbf{u}) + \mu \nabla^2 \mathbf{u} \tag{2.59}$$

Using the Helmholtz decomposition the displacement vector can be decomposed as follows:

$$\mathbf{u} = \mathbf{u}_P + \mathbf{u}_S \quad \text{with} \quad \begin{cases} \mathbf{u}_P = \nabla \varphi \\ \mathbf{u}_S = \mathbf{rot}\, \boldsymbol{\psi} \end{cases} \tag{2.60}$$

where φ is a scalar potential; and **ψ** is vector potential; **rot** () is the rotation operator. It's worth noting that the displacement vector $\mathbf{u}_P$ is irrotational (i.e., **rot** $\mathbf{u}_P$ = 0) and the divergence of $\mathbf{u}_S$

is zero. Using these properties of $\mathbf{u}_P$ and $\mathbf{u}_S$ and equation (2.59), the uncoupled wave equations can be written in terms of $\mathbf{u}_P$ and $\mathbf{u}_S$ as follows:

$$\begin{cases} \dfrac{\partial^2 \mathbf{u}_P}{\partial t^2} - C_P^2 \nabla^2 \mathbf{u}_P = 0 \\ \dfrac{\partial^2 \mathbf{u}_S}{\partial t^2} - C_S^2 \nabla^2 \mathbf{u}_S = 0 \end{cases} \tag{2.61}$$

where C_P and C_S are the speed of dilatational waves (or longitudinal waves) and shear waves (transverse waves), respectively, and are determined by:

$$C_P = \sqrt{\frac{\lambda + 2\mu}{\rho}} \quad \text{and} \quad C_S = \sqrt{\frac{\mu}{\rho}} \tag{2.62}$$

The wave equations can also be written in terms of the two potentials φ and $\boldsymbol{\psi}$ as follows:

$$\begin{cases} \dfrac{\partial^2 \varphi}{\partial t^2} - C_P^2 \nabla^2 \varphi = 0 \\ \dfrac{\partial^2 \boldsymbol{\psi}}{\partial t^2} - C_S^2 \nabla^2 \boldsymbol{\psi} = 0 \end{cases} \tag{2.63}$$

2.5 FAULT REACTIVATION

Faults are shear fractures of rock at geological scales. Depending on the role of the vertical stress relative to the fault shear displacement, faults are classified into three major categories and are illustrated in Figure 2.11. These include (Cornet, 2015; Jaeger et al., 2009; Scholz, 2002):

- Normal fault: the fault shear displacement takes place along the *dip* of the fault, the upper surface of the fault moves *downward* relative to the lower surface, and the vertical stress is the *major* principal stress (Figure 2.11a)
- Thrust fault (or reverse fault): the fault shear displacement also takes place along the *dip* of the fault, the upper surface of the fault moves *upward* relative to the lower surface, and the vertical stress is the *minor* principal stress (Figure 2.11b)
- Strike-slip fault: the fault shear displacement takes place along the *strike* of the fault, the vertical stress is the *intermediate* principal stress (Figure 2.11c)

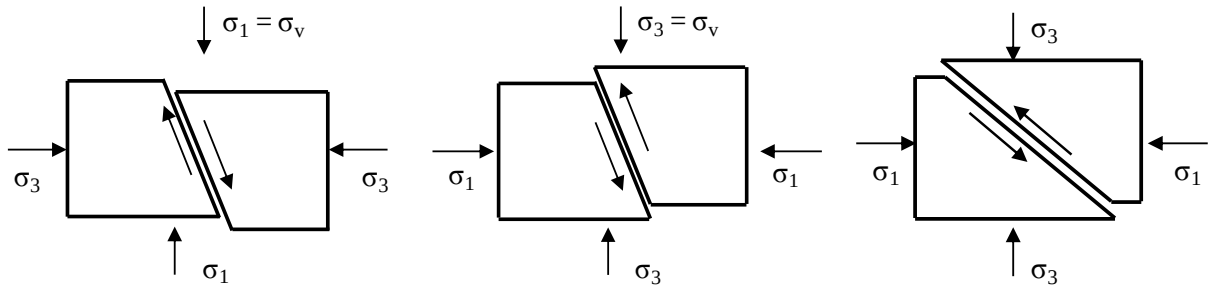

(a) Normal faulting (b) Thrust faulting (c) Strike-slip faulting

Figure 2.11 Different types of faulting. The vertical stress is the major principal stress in normal faulting, the minor principal stress in thrust faulting, and the intermediate principal stress in strike-slip faulting. Adapted from Jaeger et al. (2009)

Since faults are shear fractures, the fault slip or the fault reactivation is merely dependent on the ratio between the fault shear strength and the shear stress acting on the fault. The mechanics of fault reactivation is based on the fundamental law of the mechanics which is Newton's second law of motion. Consider a solid block on a surface as shown in Figure 2.12. The block is subjected to two external forces: a normal force *N* normal to the surface and a shear force *T* parallel to the surface. Two reaction forces (Figure 2.12) appear to counterbalance the applied forces: the normal reaction force *Q* and shear resistance *R*. As long as the shear force *T* does not exceed the shear resistance *R* the solid stay still, or in other word no relative slip between the solid and the surface occurs. Relative slip is initiated when the balance between the shear force *T* and the shear resistance *R* is broken. Experiments showed that the shear resistance *R* is proportional to the normal force *N* via a coefficient called friction coefficient μ (Engelder and Scholz, 1976; Scholz, 1968):

$$R = \mu N \tag{2.64}$$

The slip criterion is expressed as:

$$T = \mu N \tag{2.65}$$

By dividing both sides of equation (2.65) by the effective area of contact, the slip criterion expressed in shear and normal stress τ and σ is obtained as follows:

$$\tau = \mu \sigma \tag{2.66}$$

The right hand side of equation (2.66) can be regarded as the local shear strength. The shear strength determined by equation (2.66) is usually referred to as the Coulomb friction criterion. It's worth noting that when pore pressure is present, the normal stress σ is taken as the effective stress, which wasdefined in equations (2.5) and (2.6), and is repeated here for an incompressible solid phase as:

$$\sigma' = \sigma - p \tag{2.67}$$

Thus the Coulomb friction criterion becomes:

$$\tau = \mu(\sigma - p) \tag{2.68}$$

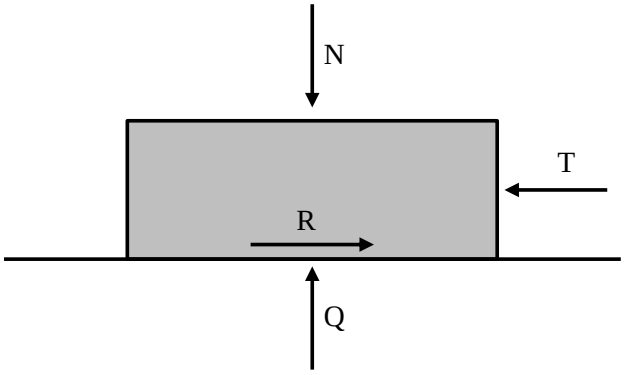

Figure 2.12 Solid block on a horizontal surface, subjected to a force *N* normal to the surface and a force *T* parallel to the surface. *R* is the shear resistance

Equation (2.66) is usually used as a standard criterion for assessing fault reactivation. Equation (2.66) is obtained by considering the global equilibrium of the whole block. However, equation (2.66) itself is expressed in terms of quantities that are defined locally – the shear stress τ and the normal stress σ_n. It is obvious that even though equation (2.66) is satisfied at several locations of the interface, it does not mean that the whole interface will slip. All frictional interfaces, including faults, establish contact through asperities e.g., on several asperities of the interface. Slow slip first initiates locally where resistance to rupture (i.e., shear strength) is the smallest along the interface or where shear stress is locally high. The extension of the local slow slip to a certain state will ignite the global and potentially dynamic slip of the interface (Selvadurai and Glaser, 2015). This phenomenon of slow slip occurring prior to dynamic slip was experimentally observed and investigated in a series of meticulously programmed experiments by Glaser and Selvadurai (2016). It should be noted

that the influence of scale effects on the shear strength of frictional interfaces also needs to be considered when assessing the stability of the interface (Vallier et al., 2010).

In geothermal reservoirs, the slip of pre-existing faults may be induced by the injection of fluid. The fault slip can be seismic, i.e., generating seismic waves or aseismic, i.e., slip without generating seismic waves. Thermo-poro-mechanical couplings play an important role in the stability of faults and the seismic slip (Rattez et al.; Sulem and Stefanou, 2015). Many experiments on rock friction (Byerlee, 1978; Byerlee and Brace, 1968; Hoskins et al., 1968) have shown that for certain types of rock and surface roughness, the relative displacement of a shear fracture can occur in a stick-slip manner, as illustrated in Figure 2.13. Under a constant-held normal load N, as the shear force T applied along a shear fracture increases the shear elastic relative displacement increases, until, at some point, unstable displacement occurs abruptly with a concurrent drop in the shear force. The fracture surfaces subsequently lock together and the shear force can increase and the stick-slip cycle occurs again. The friction of rock is therefore characterized by two different friction coefficients: a coefficient for the *stick* phase, called coefficient of static friction μ, and a coefficient for the *slip* phase, known as the coefficient of dynamic friction μ_d. (Brace and Byerlee, 1966) suggested that the stick-slip phenomenon may provide a mechanism for generation of seismic waves from fault slip.

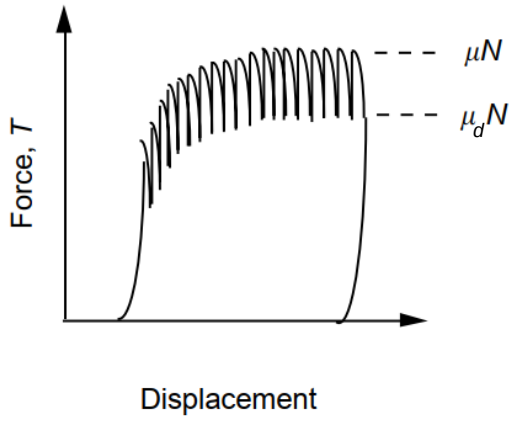

Figure 2.13 Force-displacement for a granite crack surface. T is the shear force, N is the normal force, μ and μ_d are the static and dynamic friction coefficients (Jaeger et al., 2009)

Rock friction is also dependent on time and slip rate, which was experimentally demonstrated by Dieterich (1972) and Jafari et al. (2003). The time- and rate-dependency of the rock friction is expressed through the rate-and-state model as follows:

$$\mu = \mu_0 + a \ln\left(\frac{V}{V_0}\right) + b\Theta$$
$$\frac{d\Theta}{dt} = \frac{V_0}{D_C} e^{-\Theta} - \frac{V}{D_C} \tag{2.69}$$

where V is the slip rate; μ_0 is the steady state friction coefficient at a slip rate $V = V_0$; a and b are friction parameters; D_C is the characteristic slip distance; and Θ is a state variable. The relation between a and b dictates whether the fault is velocity-weakening or velocity strengthening and thus whether the slip is stable or unstable.

The time-dependency of the friction coefficient in the rate-and-state model expressed through the state variable is attributed to the creep effect that causes an increase in the actual area of asperity contact between the two faces of the fault (Engelder and Scholz, 1976). The slip rate-dependency is believed to be caused by the loss and recovery of contact between asperities of the fault as its two faces slip relative to each other.

The rate-and-state friction model has been used to model the slip behavior of a single fault due to direct fluid injection by Cueto-Felgueroso et al. (2017), Dublanchet et al. (2013) and McClure and Horne (2011). The model is able to explain various observational features of earthquake phenomena (Segall, 2010). However, recent laboratory experiments on fault slip due to fluid injection (Scuderi et al., 2017) concluded that slip instabilities can be induced whenever the critical stress state for reactivation is met by an increase in fluid pressure, even if the fault is characterized by velocity strengthening frictional behavior. Moreover, these authors stated that the decrease of shear strength due to the reduction in the effective normal stress largely prevails over the impact of the rate-and-state effects on fault frictional strength. In the current research, the local shear strength of natural fractures or faults is modeled using the Coulomb friction law. This law is implemented in the finite element code ABAQUS using the subroutine USDFLD and the field variable (ABAQUS, 2016).

2.6 HYDRAULIC FRACTURE MODELS AND INTERACTION OF FRACTURES

2.6.1 Hydraulic fracture models

As stated in the previous chapter, the development of a rock reservoir is crucial to the success of a EGS project. Excessive permeability will lead to an unacceptable loss of water from the system, while high impedance (i.e., resistance to flow) will require a large amount of energy to pump water through the reservoir. Thus, in order to estimate the permeability of the reservoir it is necessary to predict the development of fracture geometry based on the stimulation conditions. Three single hydraulic fracture models have been derived to approximately define the development of the fracture geometry. These include two plane strain models – the Khristianovic-Geertsma-de Klerk (KGD) model (Geertsma and de Klerk, 1969) and the Perkins-Kern-Nordgren (PKN) model (Nordgren, 1972), and a three-dimensional axisymmetric model – the radial penny-shaped model (Sneddon, 1946). Figure 2.14 illustrates the geometry of these three fracture models.

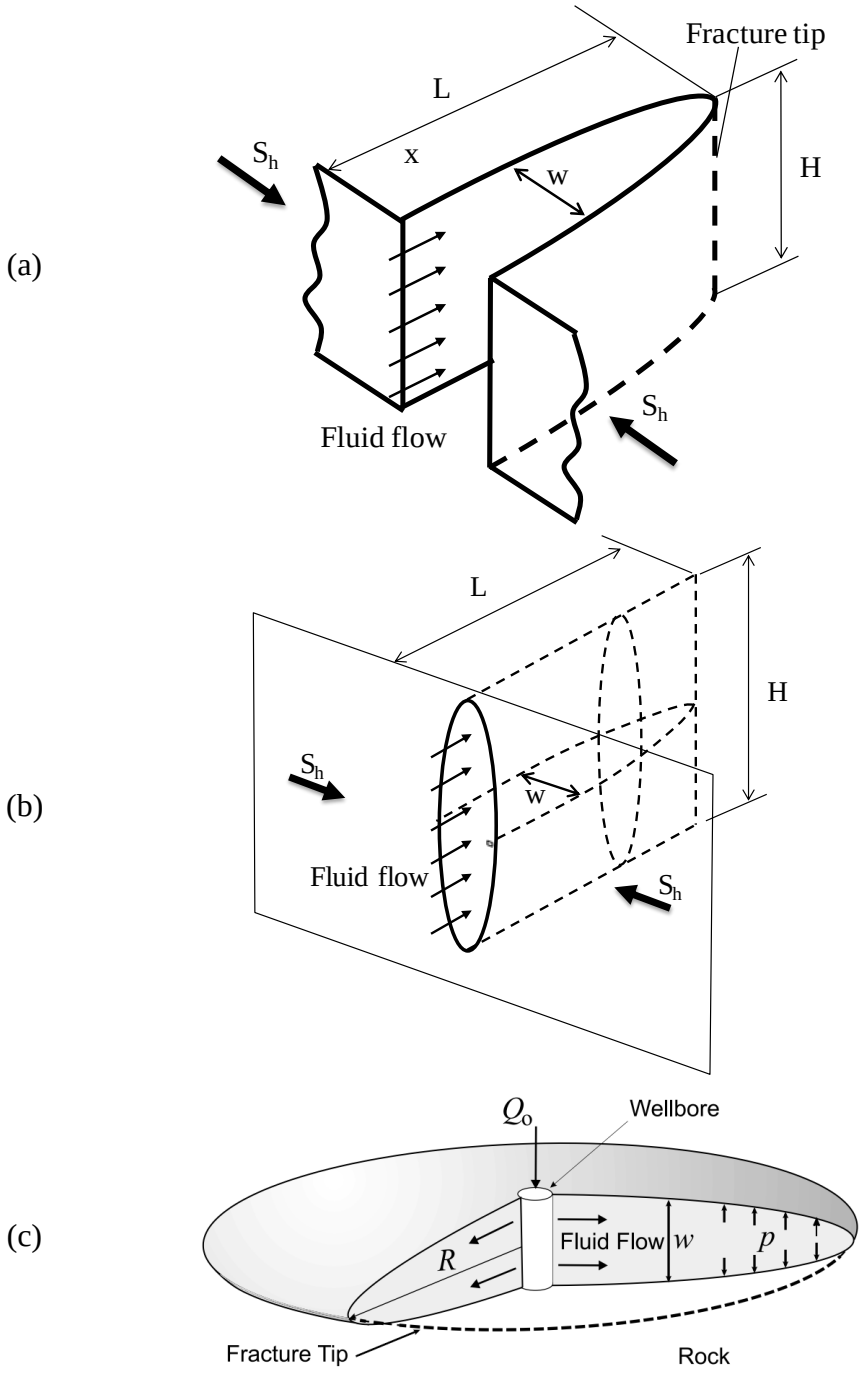

Figure 2.14 Geometry of three single fracture models: (a) KGD model, (b) PKN model, (c) Penny-shaped model (adapted from Savitski and Detournay (2002)). S_h is the minimum compressive stress

Early solutions for the fracture geometry (e.g, fracture length, aperture) and wellbore pressure have been derived for those models by assuming that (i) the material is homogeneous, isotropic, linear elastic, and fully impermeable, (ii) the fluid is Newtonian and its flow within

the fracture is laminar everywhere, (iii) the fluid injection is considered as a line source for the KGD and KPN models and as a point source for the penny-shaped model, and (iv) linear elastic fracture mechanics applies (Geertsma and de Klerk, 1969; Geertsma and Haafkens, 1979). These early solutions have been used by many researchers as a benchmark for comparison with their numerical models. However, it should be noted that several inconsistencies were ignored in order to obtain those solutions. For instance, to obtain solutions of fracture geometry for the KGD and penny-shaped models, a smooth and finite-curvature fracture tip is assumed. This is obviously inconsistent with the linear elastic fracture mechanics, which considers the fracture tip as sharp and having infinite curvature.

More recently, these fracture models (KGD and penny-shaped models) were studied with the incorporation of more consistent considerations for the fracture tip and boundary conditions incorporated (Bunger et al., 2005; Detournay, 2004; Savitski and Detournay, 2002). For instance, the fracture tip is treated as having a zero-aperture with no fluid flow. In these studies, the following assumptions were made: (i) the medium is infinite, (ii) the material is fully impermeable and linear elastic, (iii) linear elastic fracture mechanics applies, and (iv) Carter's leakoff model is used to describe the fluid loss across the walls of the hydraulic fracture. With these assumptions, the governing equations of the problem then reduce to (i) the equilibrium equation for the linear elastic material, which can be given by an integral that relates the hydraulic aperture and the net fluid pressure (Spence and Sharp, 1985), (ii) the local and global mass balance equations for the injected fluid, and (iii) the fracture propagation criterion, which is based on linear elastic fracture mechanics that relates the fluid pressure and the fracture energy. A scaling technique was then used to obtain approximate analytical solutions in the form of regular asymptotic expansions (Bunger et al., 2005; Detournay, 2004; Garagash, 2006; Savitski and Detournay, 2002). It was shown that different regimes of fracture propagation exist, depending on the energy dissipation mechanisms and the fluid balances. Energy can be dissipated either due to the flow of the viscous fluid (viscosity-dominated regime) or the propagation of the fracture (toughness-dominated regime). Meanwhile, the fluid can either be stored in the fracture (storage-dominated regime) or leak into the surrounding medium (leakoff-dominated regime). These four regimes of fracture propagation can be represented in a two dimensional space where each limiting regime has

two coordinates that correspond to an energy dissipation mechanism and a component of global fluid balance, as Figure 2.15 illustrates.

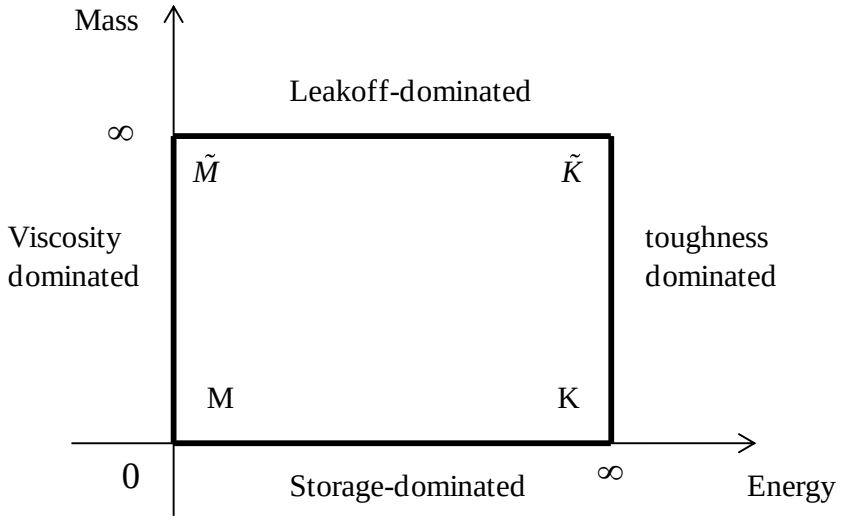

Figure 2.15 Diagram illustrating the four limiting propagation regimes of hydraulic fractures (after (Bunger et al., 2005))

In the following paragraphs, the main results for fracture geometry and injection pressure for the KGD and penny-shaped fracture models near the M and K vertices (viscosity/storage-dominated regime and toughness/storage-dominated regime) are briefly summarized. These regimes were chosen because they correspond to real conditions that could be encountered in deep geothermal reservoirs where the granitic basement has a very low permeability, which corresponds to the storage-dominated regime. Under these conditions, the approximate solutions for the fracture geometry and wellbore pressure for both the KGD and the penny-shaped fracture models are given in a generic form as (Detournay, 2004; Savitski and Detournay, 2002):

- Fracture length:

$$L(t) = \gamma L(t) \tag{2.70}$$

- Fracture aperture:

$$w(x,t) = \varepsilon(t) L(t) \Omega \tag{2.71}$$

- Wellbore pressure:

$$p = \varepsilon(t) E' \Pi \tag{2.72}$$

In the above equations, *L(t)* is the length scale of the same order as the fracture length; expressions for $\varepsilon(t)$, *L(t)*, and the dimensionless numbers γ, Ω, and Π are defined below, dependent on the fracture model and the propagation regime; *E'* is defined as:

$$E' = \frac{E}{1-\nu^2} \tag{2.73}$$

where *E* and *v* are the Young's modulus and Poisson's ratio of the medium, respectively.

The following definitions are also introduced for convenience:

$$\mu' = 12\mu \quad , \quad K' = 4\left(\frac{2}{\pi}\right)^{1/2} K_{IC} \tag{2.74}$$

where μ is the viscosity of the fluid and K_{IC} is the critical Mode I stress intensity factor

2.6.1.1 KGD model

Viscosity-dominated regime (M vertex):

Expressions for $\varepsilon(t)$ and *L(t)* in the viscosity-dominated regime are given by Detournay (2004):

$$\varepsilon_m = \left(\frac{\mu'}{E't}\right)^{1/3} \quad , \quad L_m = \left(\frac{E' Q_0^3 t^4}{\mu'}\right)^{1/6} \tag{2.75}$$

where Q_0 is the injection rate per unit height of the fracture (m^2/s).

By combining equation (2.75) with equations (2.70), (2.71), and (2.72), the expression for the fracture geometry and the wellbore pressure can be obtained as:

$$\begin{aligned} w &= \Omega_{m0}\left(\frac{\mu'^2 Q_0^3}{E'}\right)^{1/6} t^{1/3} \\ L &= \gamma_{m0}\left(\frac{E' Q_0^3}{\mu'}\right)^{1/6} t^{2/3} \\ p &= \Pi_{m0}\left(\mu' E'^2\right)^{1/3} t^{-1/3} \end{aligned} \tag{2.76}$$

where the dimensionless numbers γ_{m0}, Ω_{m0}, and Π_{m0} can be expressed in the form of series expansion and can be found in Adachi and Detournay (2002).

Toughness-dominated regime (K vertex):

Expressions for $\varepsilon(t)$ and $L(t)$ in the toughness-dominated regime are given by Detournay (2004):

$$\varepsilon_k = \left(\frac{K'^4}{E'^4 Q_0 t} \right)^{1/3} \quad , \quad L_k = \left(\frac{E' Q_0 t}{K'} \right)^{2/3} \tag{2.77}$$

By combining equation (2.77) with equations (2.70), (2.71), and (2.72), the expressions for the fracture geometry (aperture and length) and the wellbore pressure are:

$$\begin{aligned} w &= \Omega_{k0} \left(\frac{K'^2 Q_0}{E'^2} \right)^{1/3} t^{1/3} \\ L &= \gamma_{k0} \left(\frac{E' Q_0}{K'} \right)^{2/3} t^{2/3} \\ p &= \Pi_{k0} \left(\frac{K'^4}{E' Q_0} \right)^{1/3} t^{-1/3} \end{aligned} \tag{2.78}$$

where the dimensionless numbers γ, Ω, and Π are given by:

$$\gamma_{k0} = \frac{2}{\pi^{2/3}} \ , \ \Pi_{k0} = \frac{\pi^{1/3}}{8} \ , \ \Omega_{k0} = \frac{1}{\pi^{1/3}} \left(1 - \rho^2\right)^{1/2} \tag{2.79}$$

with $\rho = x/L$, x and L shown in Figure 2.14.

Transition between propagation regimes:

A dimensionless number to distinguish the propagation regimes is defined as (Adachi and Detournay, 2002; Detournay, 2004):

$$K = \frac{K'}{\left(E'^3 \mu' Q_0 \right)^{1/4}} \tag{2.80}$$

Strictly speaking, the viscosity- and toughness-dominated regimes of propagation correspond to $K \ll 1$ and $K \gg 1$, respectively. However, according to (Detournay, 2004), the fracture can

be considered as propagating in the viscosity-dominated regime when K < 1 and in the toughness-dominated regime when K > 4.

2.6.1.2 Penny-shaped fracture model

Two regimes of propagation are also considered for the penny-shaped fracture model: the viscosity- and toughness-dominated regimes.

Viscosity-dominated regime (M vertex):

Expressions for $\varepsilon(t)$ are $L(t)$ in the viscosity-dominated regime are given by Savitski and Detournay (2002):

$$\varepsilon_m = \left(\frac{\mu'}{E't}\right)^{1/3} \quad , \quad L_k = \left(\frac{E'Q_0^3 t^4}{\mu'}\right)^{1/9} \tag{2.81}$$

where Q_0 is the injection rate in m^3/s

By combining equation (2.81) with equations (2.70), (2.71), and (2.72), the expressions for the fracture geometry and the wellbore pressure can be obtained as:

$$\begin{aligned} w &= \Omega_{m0}\left(\frac{\mu'^2 Q_0^3}{E'^2}\right)^{1/9} t^{1/9} \\ L &= \gamma_{m0}\left(\frac{E'Q_0^3}{\mu'}\right)^{1/9} t^{4/9} \\ p &= \Pi_{m0}\left(\mu' E'^2\right)^{1/3} t^{-1/3} \end{aligned} \tag{2.82}$$

where the dimensionless numbers γ_{m0}, Ω_{m0}, and Π_{m0} can be expressed in the form of a series expansion and can be found in O'Keeffe et al. (2018) and Savitski and Detournay (2002).

Toughness-dominated regime (K vertex):

Expressions for $\varepsilon(t)$ and $L(t)$ in the toughness-dominated regime are given by Savitski and Detournay (2002):

$$\varepsilon_k = \left(\frac{K'^6}{E'^6 Q_0 t}\right)^{1/5} \quad , \quad L_k = \left(\frac{E'Q_0 t}{K'}\right)^{2/5} \tag{2.83}$$

By combining equation (2.83) with equations (2.70), (2.71), and (2.72), the expression for the fracture geometry (aperture and length) and the wellbore pressure are:

$$w = \Omega_{k0}\left(\frac{K'^4 Q_0}{E'^4}\right)^{1/5} t^{1/5}$$
$$L = \gamma_{k0}\left(\frac{E' Q_0}{K'}\right)^{2/5} t^{2/5} \qquad (2.84)$$
$$p = \Pi_{k0}\left(\frac{K'^6}{E' Q_0}\right)^{1/5} t^{-1/5}$$

where the dimensionless numbers γ_{k0}, Ω_{k0}, and Π_{k0} are given by:

$$\gamma_{k0} = \left(\frac{3}{\pi\sqrt{2}}\right)^{2/5},\ \Pi_{k0} = \frac{\pi}{8}\left(\frac{\pi}{12}\right)^{1/5},\ \Omega_{k0} = \left(\frac{3}{8\pi}\right)^{1/5}\left(1-\rho^2\right)^{1/2} \qquad (2.85)$$

with $\rho = r/R$, r and R shown in Figure 2.14

Transition between propagation regimes:

A dimensionless number K used to distinguish different propagation regimes is also defined as (Savitski and Detournay, 2002):

$$K = K'\left(\frac{t^2}{\mu'^5 Q_0^3 E'^{13}}\right)^{1/18} \qquad (2.86)$$

The viscosity- and toughness-dominated regimes correspond to K < 1 and K > 3.5, respectively. Unlike the KGD model, the dimensionless number K in this case depends not only on the injection rate and material properties but also on the injection time. From equation (2.86), it is obvious that the fracture propagates in the viscosity-dominated regime at an earlier time (when t is small) and gradually transitions to the toughness-dominated regime at an later time.

2.6.2 Interaction of hydraulic fractures and natural fractures

It has been recognized that natural fractures may have an important impact on the development of EGS reservoirs, especially after the development of the Camborne School of

Mines project, where instead of generating a vertical fracture propagating upwards as predicted the reservoir migrated downwards into the region where there were multiple natural fractures. The interaction between natural fractures and the advancing hydraulic fractures is a key factor that produces complex fracture patterns. Even in rock formations where the natural fractures are sealed or cemented, the natural fractures may still serve as weak pathways to potentially divert advancing hydraulic fractures (Dahi Taleghani and Olson, 2013).

When a hydraulic fracture approaches a natural fracture, two potential scenarios can occur, as Figure 2.16 illustrates: (i) the hydraulic fracture is diverted into the natural fracture, or (ii) the hydraulic fracture crosses the natural fracture. The hydraulic fracture may also be "arrested" by the natural fracture under specific conditions (e.g., frictional strength of the natural fracture). However, as long as the fluid continues to be injected, the hydraulic fracture will eventually continue to propagate, either crossing the natural fracture or being diverted into it. The interaction between hydraulic fracture and natural fracture has been studied using both experimental, theoretical, and numerical simulation approaches. The main objective is to predict under which conditions the hydraulic fracture will cross or divert into the natural fracture.

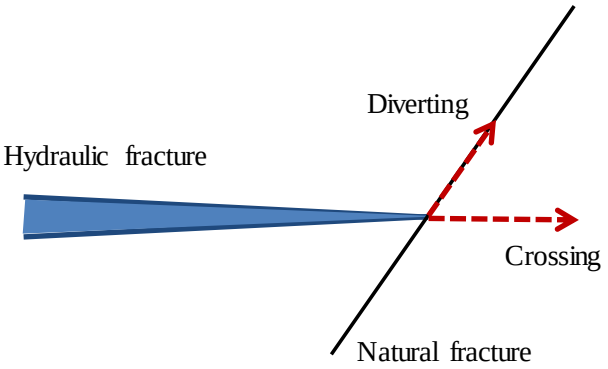

Figure 2.16 Potential scenarios of interaction between a hydraulic fracture and existing fracture

Theoretical studies, primarily based on the theory of linear elastic fracture mechanics, have focused on quantifying the alteration of stress intensity factor at the tip of the hydraulic fracture caused by the stress perturbations due to the presence of the natural fracture in the medium (Gu and Weng, 2010; Taleghani et al., 2016; Thomas et al., 2017; Weng et al., 2016). One such study by Renshaw and Pollard (1995) led to a simple criterion for predicting

whether a hydraulic fracture will propagate across a frictional interface orthogonal to the hydraulic fracture. The Renshaw and Pollard crossing criterion depends on the in-situ stresses, the tensile strength R_T of the medium, and the friction coefficient μ of the interface, and is given as:

$$\frac{-S_H}{R_T - S_h} > \frac{0.35 + \frac{0.35}{\mu}}{1.06} \tag{2.87}$$

Equation (2.87) suggests that the crossing would always occur when the friction coefficient μ is larger than 0.5, which is a typical value for friction coefficient of rocks (Cornet, 2015). However, the interaction of fractures is known to be very sensitive to the intersection angle. (Gu and Weng, 2010) used a similar approach to obtain a crossing criterion for non-orthogonal intersection conditions. They found that as the intersection interaction decreases from 90° (the orthogonal intersection case) the hydraulic fracture is more likely to be diverted into the natural fracture. A plot of their crossing criterion is shown in Figure 2.17. It is obvious from Figure 2.17 that when the fracture intersection angle is smaller than 30°, the diversion of the hydraulic fracture into the natural fracture always occurs in most practical situations.

Experiments on the interaction between hydraulic fractures and natural fractures under different conditions of stress and friction were carried out by Blanton (1982), Renshaw and Pollard (1995), Warpinski and Teufel (1987), and Zhou and Xue (2011). They found that the contrast in in-situ stresses and the angle of intersection are the most important factors that control the intersection behavior. Under normal conditions of stresses found in-situ, the hydraulic fracture tends to divert into the natural fracture; the crossing only occurs in cases of high differential stresses and high intersection angles.

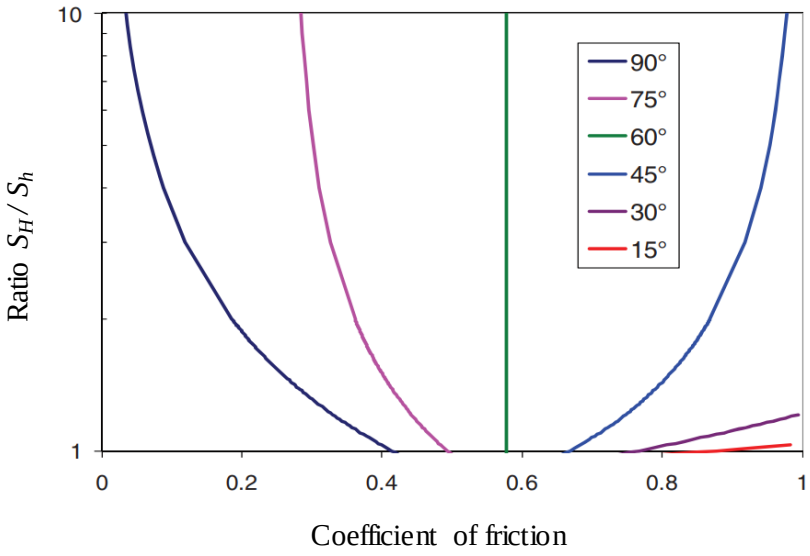

Figure 2.17 Plot of crossing criterion for different intersection angles between 15° and 90°. The region to the right of each curve represents the crossing condition for that intersection angle. Source: Gu et al. (2012)

2.7 NUMERICAL METHODS FOR MODELING FRACTURE PROPAGATION

2.7.1 Extended finite element method

The extended finite element method (XFEM) was introduced by Belytschko and Black (1999) and Moës et al. (1999). The method allows discontinuities such as cracks to be represented independently from the finite element (FE) mesh. Thus, the crack growth is also independent of the FE mesh and remeshing is no longer needed. The central idea in the formulation of this method is that discontinuities are incorporated in a finite element by enriching the traditional finite element approximation with special enriched functions in conjunction with additional degrees of freedom. The enrichment functions typically consist of the near-tip asymptotic functions that capture the singularities around the crack tip and a discontinuous function that represents the jump in displacement across the crack surfaces. The approximation for a displacement vector at any location **x** is given by:

$$\mathbf{u}(\mathbf{x}) = \sum_{I \in N} N_I(\mathbf{x}) \left[\mathbf{u}_I + H(\mathbf{x})\mathbf{a}_I + \sum_{\alpha=1}^{4} F_\alpha(\mathbf{x})\mathbf{b}_I^\alpha \right] \tag{2.88}$$

where $N_I(\mathbf{x})$ are the traditional nodal shape functions associated the finite element mesh, $\mathbf{u}_I$ is the nodal displacement vector, $H(\mathbf{x})$ is the Heaviside function, $\mathbf{a}_I$ is the vector of nodal enriched degrees of freedom associated with discontinuous displacement across the crack surface, $\mathbf{b}_I^{\alpha}$ is the vector of nodal enriched degrees of freedom associated with crack tip singularity, and $F_\alpha(x)$ are asymptotic crack tip functions that are defined in equation (2.89):

$$\{F_\alpha(r,\theta)\} = \left\{\sqrt{r}\sin\frac{\theta}{2}, \sqrt{r}\cos\frac{\theta}{2}, \sqrt{r}\sin\frac{\theta}{2}\sin\theta, \sqrt{r}\sin\frac{\theta}{2}\cos\theta\right\} \tag{2.89}$$

where (r, θ) is a polar coordinate system with its origin at the crack tip and θ = 0 is tangent to the crack at the tip, as Figure 2.**18** illustrates.

The Heaviside function $H(x)$ defined with reference to Figure 2.**18** is:

$$H(\mathbf{x}) = \begin{cases} 1 & \text{if } (\mathbf{x}-\mathbf{x}^*).\mathbf{n} \\ -1 & \text{otherwise} \end{cases} \tag{2.90}$$

where **x** is the location where displacement is currently approximated, and **x*** is the closest projection of **x** on the crack surface, **n** is the unit normal vector at **x***.

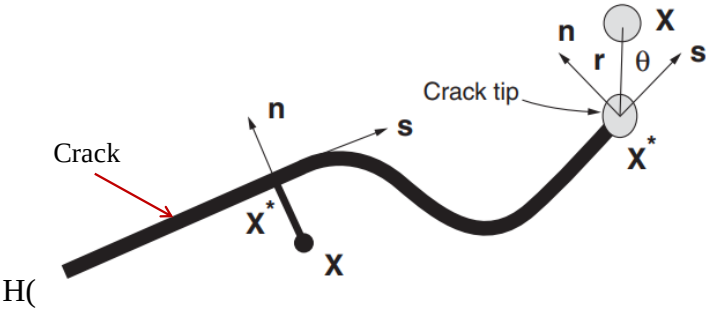

H(

Figure 2.18 Illustration of normal and tangential coordinates for a smooth crack (ABAQUS, 2016)

XFEM was implemented in ABAQUS using the phantom node technique (ABAQUS, 2016). The phantom nodes are added and are superposed on the original real nodes of the enriched elements, as illustrated in Figure 2.19, in which real nodes are represented by full circles and phantom nodes by hollow circles. Before damage initiation, each phantom node is completely constrained to its corresponding real node. Once damage occurs, a crack surface is inserted in the element. The element is split into two parts. Each part of the element is formed by a

combination of some real and phantom nodes. The phantom nodes are now no longer tied to the real nodes but can move apart. If the cohesive zone model is used, the separation between the two faces of the newly created crack is governed by the cohesive law until the cohesive strength of the cracked element becomes zero, after which the phantom and the real nodes move independently. If the linear elastic fracture mechanics approach is used, the real node and the corresponding phantom node will separate when the equivalent energy release rate exceeds the fracture energy release rate and the phantom and the real nodes are also allowed to move independently after the traction has ramped down linearly to zero.

XFEM is very flexible in the sense that it allows cracks to be modeled along arbitrary paths without the need for remeshing. However, it is very difficult to obtain a converged solution, especially when pore fluid pressure is involved and there is intersection of cracks. Unfortunately, these two phenomena (fluid injection and the interaction of fractures) are the main focus of this work. Thus, XFEM is only used for the coupled thermos-mechanical simulations.

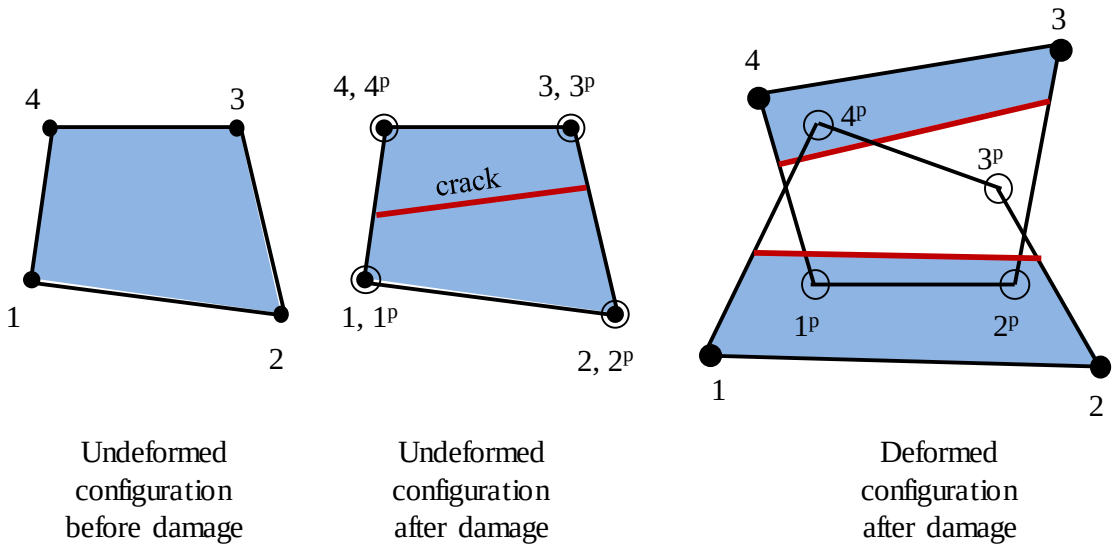

Figure 2.19 A 4-node enriched element in three different configurations: undeformed before damage, undeformed after damage, and deformed after damage. Nodes numbered from 1 to 4 are real nodes and denoted by full circles. Nodes numbered from 1^p to 4^p are phantom nodes that are superposed on the real nodes and become active only after fracture begins. (After (Zielonka et al., 2014))

2.7.2 Cohesive element method

Cohesive elements are an alternative for modeling fracture propagation and the intersection of fractures. For the cohesive element method, the trajectory of the fracture to be modeled is typically defined a priori and cohesive elements are placed only along the fracture trajectory and between finite continuum elements. Cohesive elements can also be inserted between all finite elements of the mesh to model fractures propagating along unknown paths. Another method for unknown fracture paths is to combine cohesive element with remeshing. For each calculation step, the propagation direction is determined based on the stress and strain fields from the previous step. The mesh is then re-generated such that one edge of two continuum elements lies along the propagation path and a cohesive element is inserted between these two continuum elements.

A cohesive law, such as that presented in Section 2.3.2, is necessary to describe the mechanical response of the cohesive element. The cohesive law consists of a damage initiation criterion and a damage evolution criterion. The damage initiation can be based on either stress or strain. For instance, a criterion based on the maximum stress can be expressed as:

$$\max\left\{\frac{\langle\sigma_n\rangle}{R_T}, \frac{\sigma_{s1}}{R_{S1}}, \frac{\sigma_{s2}}{R_{S2}}\right\} = 1 \tag{2.91}$$

where σ_n, σ_{s1}, σ_{s2} are the normal traction and shear tractions in two shear directions; R_T, R_{s1}, R_{s2} are the tensile and shear strengths; the Macaulay brackets are used to signify that a purely compressive stress state does not initiate damage

For the damage evolution, to account for all fracture modes including mixed-mode fracture, an effective separation δ_m is defined as:

$$\delta_m = \sqrt{\langle\delta_n\rangle^2 + \delta_{s1}^2 + \delta_{s2}^2} \tag{2.92}$$

where δ_n, δ_s, δ_t are the separations along the normal, first shear and second shear direction, respectively. Then the damage variable for a linear cohesive law is expressed as:

$$D = \frac{\delta_m^f(\delta_m - \delta_m^0)}{\delta_m(\delta_m^f - \delta_m^0)} \tag{2.93}$$

where δ_m^f is the mixed-mode fracture separation, defined as:

$$\delta_m^f = \frac{2G_C}{R_{eqv}} \tag{2.94}$$

in which G_C is the equivalent fracture energy and can be estimated using, for example, the BK law as presented in Section 2.3.1; R_{eqv} is the equivalent strength, defined as:

$$R_{eqv} = \sqrt{R_T^2 + R_{s1}^2 + R_{s2}^2} \tag{2.95}$$

The actual stress components in the cohesive elements are then calculated via the damage variable D as:

$$t = (1-D)t^p \tag{2.96}$$

where t can be the normal stress σ_n or the shear stresses σ_{s1} or σ_{s2}; t_p is the corresponding predictor which is estimated with the strain as if the material was undamaged (similar to equation **Erreur ! Source du renvoi introuvable.**).

To model the fluid flow, additional fluid pressure degrees of freedom are added to the mid-edge of the cohesive element, as illustrates Figure 2.20. Both tangential and leakoff flows, as presented in Section 2.2.3, can be modeled. The fracture aperture is defined as the change in thickness of the cohesive element as:

$$w = h - H \tag{2.97}$$

where h and H are the initial and current thickness (Figure 2.20)

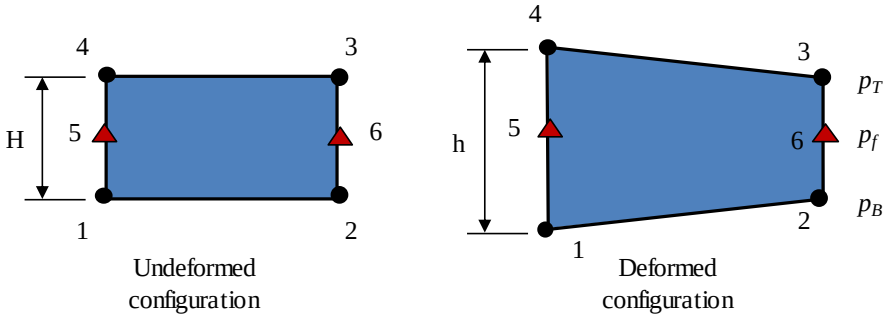

Figure 2.20 Coupled pressure/displacement cohesive element. Corner nodes are denoted by black circles and have both displacement and fluid pressure degrees of freedom (DOF). Mid-edge nodes denoted by red triangles have only fluid pressure DOF (after (Zielonka et al., 2014))

Leakoff can occur through the top and bottom faces of the fracture. Using the assumption of no material deposition as stated in Section 2.2.3, the leakoff flow rates are related to the pressure difference and a constant coefficient that depends only on the permeability of the rock mass:

$$\begin{aligned} V_T &= C_T\left(p_f - p_T\right) \\ V_B &= C_B\left(p_f - p_B\right) \end{aligned} \tag{2.98}$$

where V_T and V_B are the leakoff flow rates of fluid that leaks into the surrounding rock mass through the top and the bottom faces of the fracture, respectively; C_T and C_B are constant leakoff coefficients. A schematic of fluid flow in the fracture is presented in Figure 2.21.

The relation between the leakoff coefficients and the permeability of the rock mass can be obtained by writing Darcy's equation for fluid flow rate across the fracture surfaces as:

$$V_T = V_B = 2\frac{k}{\eta}\frac{p_f - p_T}{H} \tag{2.99}$$

where H is the thickness of the cohesive elements. Comparing equation (2.98) and equation (2.99), one obtains an expression for the leakoff coefficients as:

$$C_T = C_B = \frac{2k}{\eta H} \tag{2.100}$$

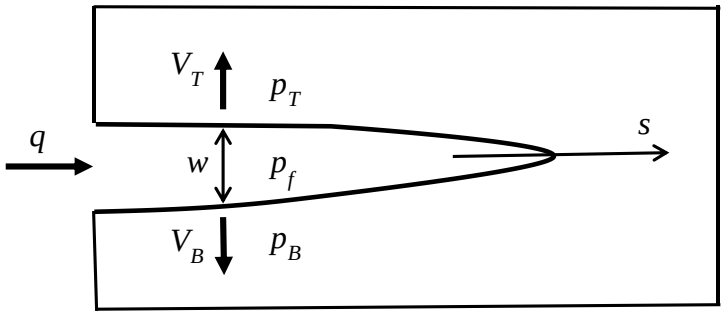

Figure 2.21 Fracture geometry and fluid flows in the fracture. q is the longitudinal fluid flow rate, V_T and V_B are the leakoff velocities. p_T, p_f, p_B are the fluid pressure at the top, inside, and the bottom surfaces of the fracture, respectively

Intersection of multiple fractures can also be modeled by cohesive elements. Each fracture is modeled by a layer of cohesive elements. At the intersection of these layers, a mid-edge node

is shared by all elements to support fluid flow continuity. An example of the intersection of a horizontal fracture with a vertical fracture modeled by cohesive elements is shown in Figure 2.22. At the intersection point, the cohesive elements 10, 20, 30 and 40 share the same mid-edge node 100.

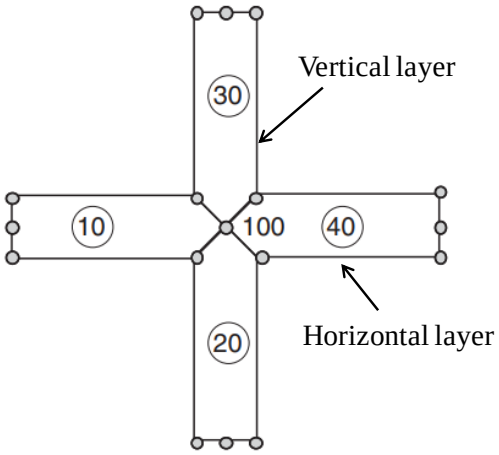

Figure 2.22 Intersection of two fractures (horizontal and vertical) modeled by two cohesive layers. The mid-edge node 100 is shared by all four cohesive elements 10, 20, 30 and 40.(modified from (ABAQUS, 2016))

Chapter 3

Thermal fracture

RÉSUMÉ

Dans ce chapitre, les effets thermiques sur la fracturation des roches sont étudiés. Des simulations numériques sont utilisées pour modéliser l'initiation et la propagation d'une fracture due à des cycles de changements de température imposés. Tout d'abord, la fracturation du sel gemme observée dans une expérience de refroidissement à l'échelle métrique grâce à un dispositif expérimental déployé in-situ est modélisée à l'aide de la méthode des éléments finis étendus (Ngo and Pellet, 2018). Cette méthode permet une représentation de la géométrie de la fracture indépendante du maillage d'éléments finis, tout en permettant de prédire l'orientation de la propagation de la fracture en fonction de l'état de contrainte autour de l'extrémité de la fracture. Les résultats numériques montrent un bon accord avec les observations et les résultats expérimentaux.

Vient ensuite l'étude de propagation des fractures due à l'injection de fluide à partir d'un puits de forage. Le problème est simplifié et seul l'effet thermique est pris en compte. Les simulations montrent que les changements de température peuvent provoquer la fracturation de la roche, même dans des conditions de confinement élevé. Il a été démontré que la contrainte initiale avait un impact significatif sur la croissance des fractures d'origine thermiques.

SUMMARY

Thermal effect on the fracture of rock is studied in this chapter. Numerical simulations are used to model the initiation and propagation of a fracture due to cycles of temperature changes. First, the fracturing of rock salt in an in-situ cooling experiment is modeled using the extended finite element method (Ngo and Pellet, 2018). This method allows a representation of the fracture geometry independent of the finite element mesh while still being able to predict the orientation of fracture propagation based on the stress state around the fracture tip. The numerical results show good agreement with the experimental data.

Second, the fracture propagation from a wellbore due to fluid injection is studied. The problem is simplified and only thermal effects are considered. The simulations show that temperature changes are able to cause the rock to fracture, even under high compressive confinement. The initial stress has been shown to have a significant effect on the growth of the thermal fractures.

3.1 INTRODUCTION

Thermal fracturing can play an important role in the development of geothermal reservoirs. The injection of cold water into the geothermal reservoir during the stimulation and circulation phase will lead to significant temperature decreases in the rock. In response to these temperature decreases, the rock will contract but is refrained by the surrounding rock. Thus, tensile stresses are induced in the rock close to the wellbore. The thermally-induced tensile stresses in the rock, whose amplitude is proportional to the temperature gradient, may exceed the in-situ stresses of the reservoir and result in the formation of fractures. Thermal fractures can be initiated in the vicinity of a wellbore where the rock is in direct contact with the injected cold water and high temperature gradients exist. Secondary thermal fractures can also be initiated from the walls of a major fracture through which cold water is circulated during the heat extraction phase (Bruel, 1995). The thermal fractures initiated near the wellbore can contribute to a reduction of the the peak hydraulic pressure required to initiate fracture in the rock during the hydraulic stimulation (Cha et al., 2017; Zhao et al., 2017; Zhou et al., 2018). While the secondary fractures initiated from the walls of the major hydraulic fractures may enhance the permeability of the reservoir, which in turn can contribute to facilitating the fluid circulation or increasing water loss from the reservoir (Bruel, 2002; Ghassemi, 2012; Huang and Ghassemi, 2016). Thermal effects as a result thermal fracturing have been suggested as a means for the so-called "soft stimulation" of geothermal reservoirs.

The effect of temperature has been shown to "soften" the fracturing of rock (Zhang et al., 2018a; Zhang et al., 2018b; Zhou et al., 2018). (Zhou et al., 2018) conducted laboratory experiments in which rock specimens were heated before performing hydraulic fracturing, showed that the initiation pressure of hydraulic fracturing decreases gradually with an increase in the temperature of the specimens. (Cha et al., 2017) utilized liquid nitrogen at temperature of nearly -200 °C to create a thermal shock to stimulate rock specimens. The thermally-stimulated specimens were then used in hydraulic stimulation tests. The results showed a significantly lower initiation pressure for the specimens that had been thermally stimulated compared to normal specimens. A series of experiments by Keshavarz et al. (2010) in which rock specimens were heated to high temperatures also showed a drastic decrease in rock strength. In all of these experiments, microcracking that originated from temperature changes

was the main cause of the reduced initiation pressure of hydraulic fracturing. Crystalline rocks are composed of multiple minerals that have different thermal expansion characteristics. When subjected to temperature changes, either increasing or decreasing, these minerals deform differently, leading to microcracking at the mineral interface. This microcracking significantly weakens the rock and shifts the fracturing mode of the rock from brittle fracturing to continuous fracturing during fluid injection.

The effect of the temperature on the fracturing of rock is numerically investigated in this chapter and is presented in the next sections. Different numerical techniques are used, including the extended finite element method in combination with fracture mechanics and the cohesive element technique based on the cohesive material concept.

3.2 SIMULATION OF ROCK FRACTURE IN A THERMAL COOLING EXPERIMENT

In this section, the extended finite element method is used to model an experiment of cooling effect on the fracturing of rock salt performed in an underground gallery. The results of this analysis were published in a journal article (Ngo and Pellet, 2018).

The main outcomes of the experiment are summarized, followed by the numerical modeling. The modeling of thermal fracturing of the rock salt consists of two sequential simulations. A heat transfer simulation is first carried out and then, the temperature field obtained from the heat transfer simulation is exported and used as the loading for the fracture propagation simulation.

3.2.1 Summary of the cooling experiment

The primary objective of this cooling experiment was to verify whether a temperature drop is capable of generating fractures in the walls of salt caverns. If so, the secondary objective was to quantify the characteristics of the fractures (e.g. depth, aperture) in order to assess the actual consequences for a gas storage facility during exploitation with a fast cycle of storage and withdrawal, pressure drawdown and associated temperature drops (Hévin et al., 2016).

Test setup:

The experiment was conducted in a 120-meter deep salt mine located in a thick layer of rock salt from the Keuper lithostratigraphic unit. In the main gallery (Figure 3.1) a niche was purposely excavated to house the experiment. The dimensions of the niche are 17.5 m in length, 12 m in width, and 4.5 m in height. The salt block used for the cooling experiment was left unexcavated and has a thickness of 1.5 m (Figure 3.1b). A section of the niche floor (dimensions 3.6 m x 3.6 m) was isolated by a chamber (Figure 3.1a, b and Figure 3.2a), in which the temperature can be regulated by a refrigeration system and fans.

In order to relax the initial horizontal stresses in the salt block, two parallel slots were dug close to the niche wall (Figure 3.1a). Before starting the cooling test, these two slots (1.5 m in depth) were backfilled with salt powder that has a porosity of about 30%.

Testing procedure:

During the experiment, three cooling-warming cycles were performed using the refrigeration system and the four fans installed in the cooling chamber. Each cycle consisted of a 28 day cooling stage, during which air temperature inside the cooling chamber was decreased from 14.5 °C (initial temperature in the gallery) to around -9 °C, followed by a 28 day warming phase. A fourth cooling phase, which also lasted 28 days, followed the first 3 cycles, and the air temperature was decreased to -25 °C. The time evolution of the air temperature inside the cooling chamber during the first cooling phase is shown in Figure 3.2b. The temperature decreased to -9 °C within one hour of starting the experiment. The peaks in temperature observed on days 6, 7, and 15 were due to unexpected opening of the cooling chamber's doors and power supply failures.

To minimize heat losses by convection, the floor around the cooling chamber was covered with an insulating material. A view of the cooling chamber including the layout of the insulation is shown in Figure 3.2a.

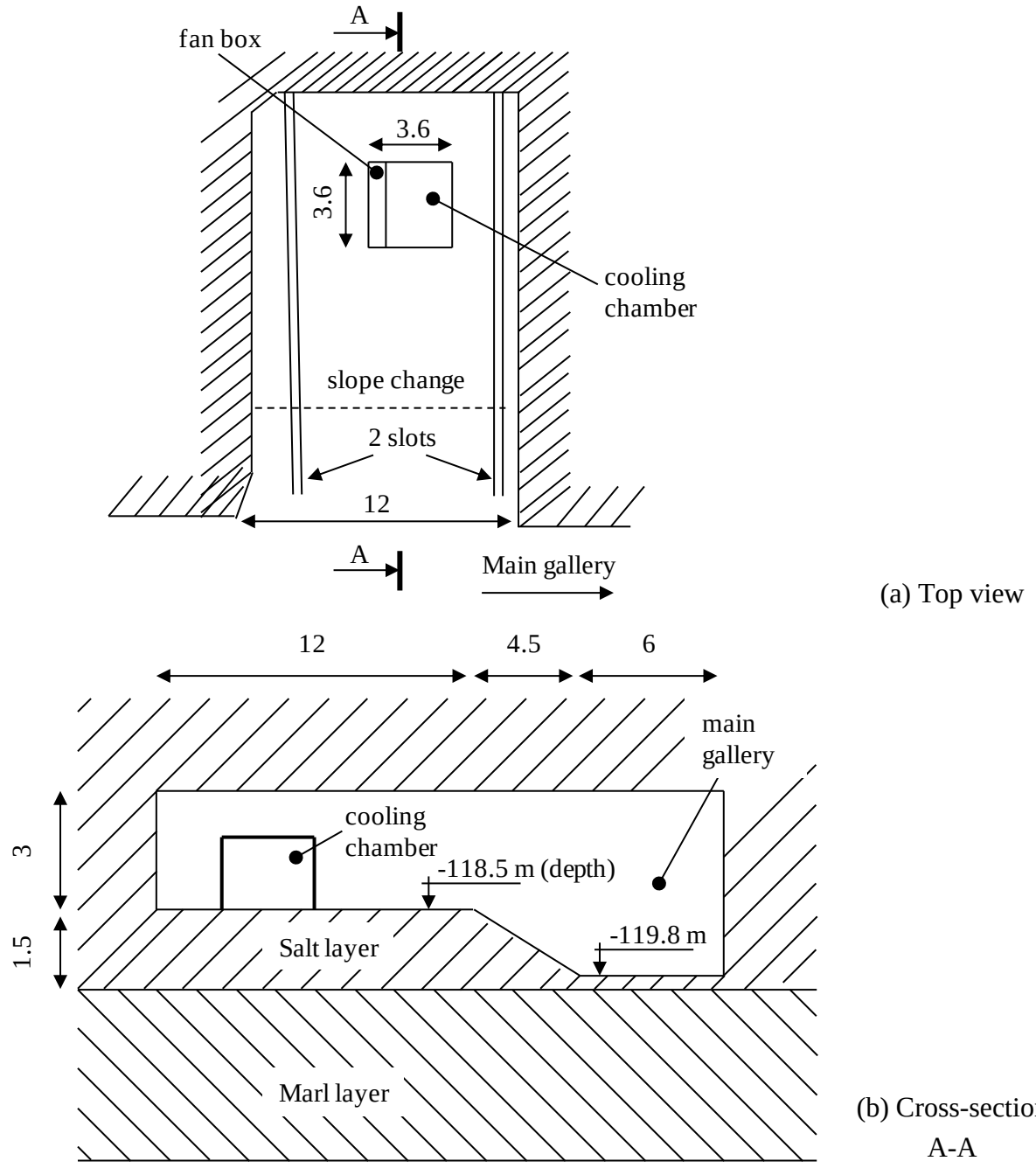

Figure 3.1 Geometry of the gallery and position of the cooling chamber (adapted from Hévin et al. (2016)). Dimensions are given in meters

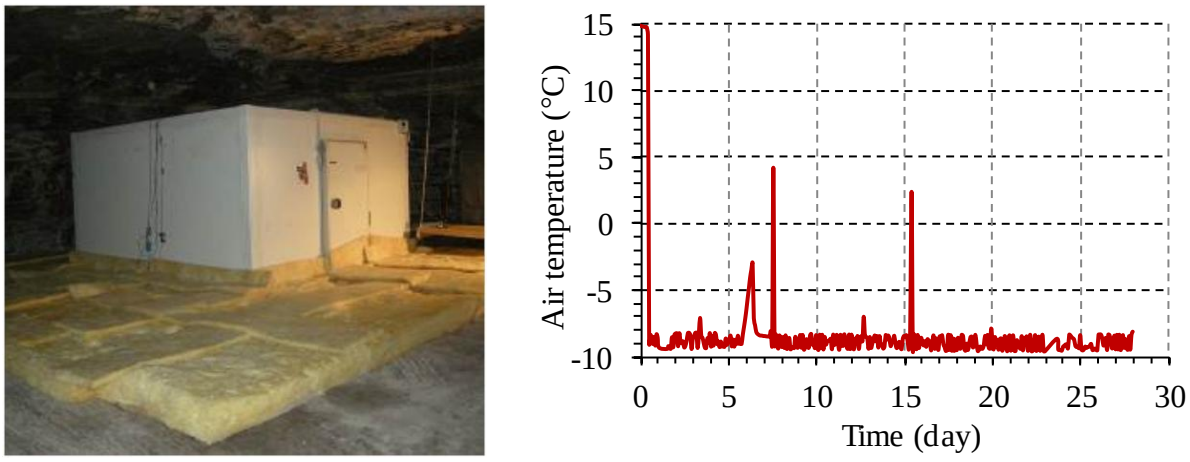

(a) (b)

Figure 3.2 (a) View of the cooling chamber (Hévin et al., 2016); (b) Time evolution of air temperature inside the cooling chamber during the first cooling stage

Temperature monitoring:

Extensive monitoring was carried out during the test. Thermocouples were installed to monitor the temperature on the floor both inside and outside the chamber, and at different depths inside the chamber. Additionally, optical and infrared images were shot at different times to follow the initiation of cracks and their propagation. Figure 3.3 shows the layout of the thermocouples and a view from inside the cooling chamber. The main thermocouples of interest include the ones on the floor, designated by K and S, located along the lines x = 2.3 m (referred to as the main profile) and y = 1.4 m (the transverse profile); and the ones at depths of 0.2 m, 0.4 m, and 0.8 m from the floor's surface, respectively designated T3, T4, T5.

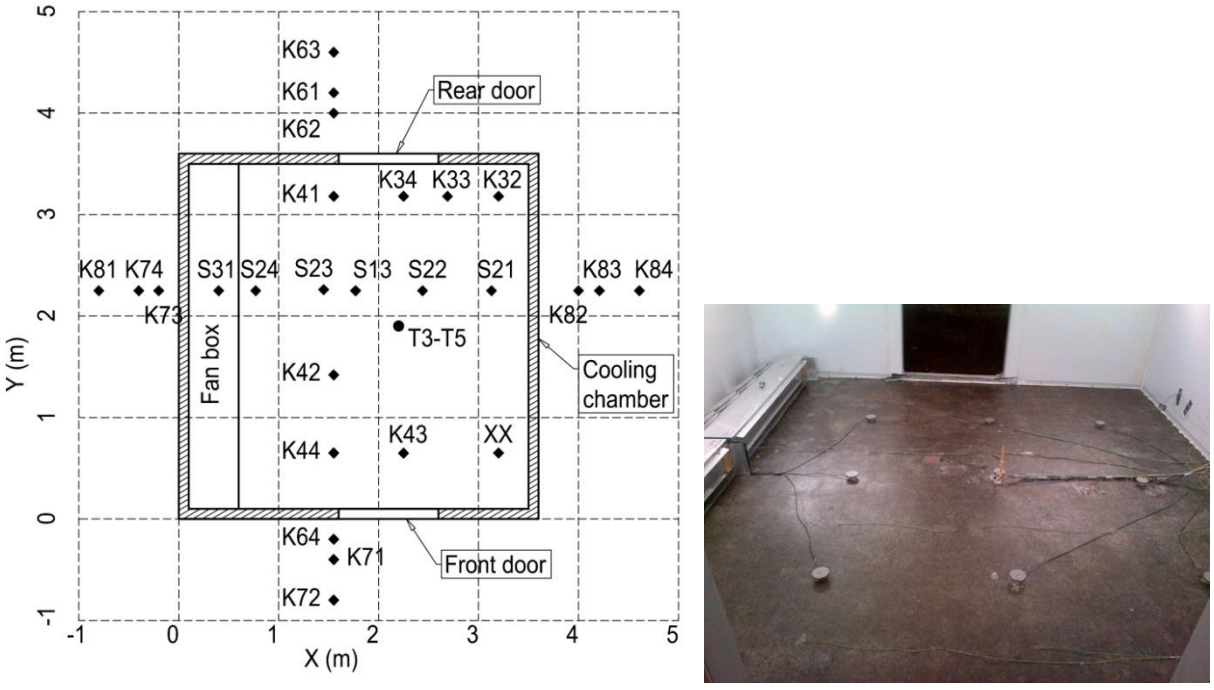

(a) (b)

Figure 3.3 (a) Layout of thermocouples: thermocouples K and S measured temperatures on the floor; thermocouples T3, T4, T5 measured temperatures at depths 0.2 m, 0.4 m, and 0.8 from floor's surface, respectively. (b) View from inside the chamber with sensors on the floor and fans on the left (Hévin et al., 2016)

3.2.2 Heat transfer simulation

The modeling was performed for the first cooling stage since the fracturing process due to temperature changes (both fracture initiation and propagation) occurred mainly during this stage of the experiment. The temperatures measured at different locations were used to calibrate the heat transfer model. The temperature field obtained from the heat transfer model was then introduced in the mechanical model for simulating the fracture initiation and propagation. Both heat transfer and mechanical simulations use the same geometric domain and were performed using the finite element code ABAQUS. Instead of modeling the whole formation from the ground surface to the depth of the gallery, a sub-domain was chosen, as displayed in Figure 3.4. The sub-domain consists of the tested 1.5 m thick salt block and a 5 m thick layer of marl. These dimensions were chosen to satisfy the boundary conditions used for the heat transfer simulation and will be justified later.

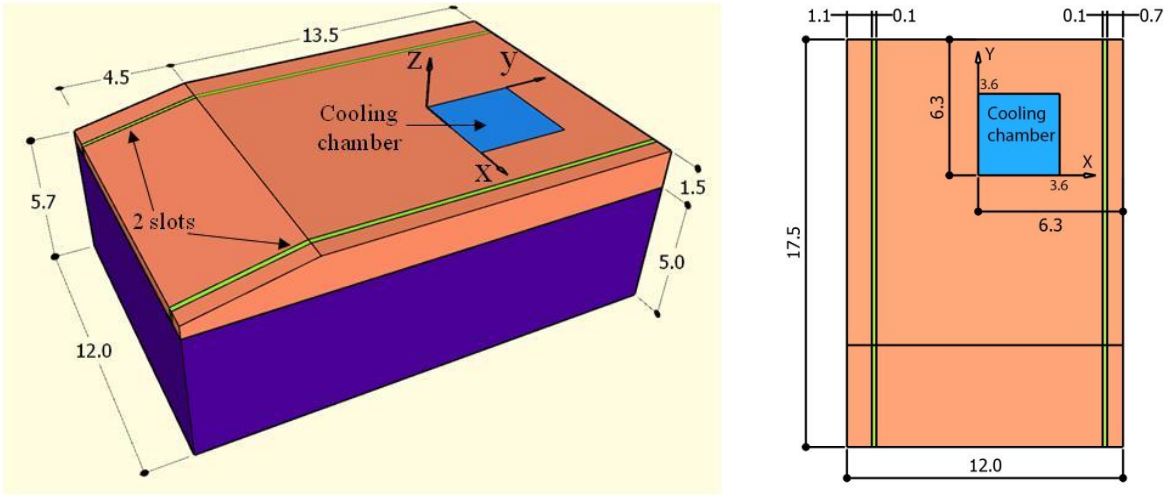

(a) 3D view (b) Top view

Figure 3.4 Sub-domain used for heat transfer and fracture propagation simulations. Dimensions are given in meters (Ngo and Pellet, 2018)

Two types of heat transfer took place in the experiment, namely conduction inside the rock mass and convection at the air – rock mass interface. The different convection zones, which are represented in Figure 3.5, are characterized by different values of the heat transfer coefficient h measured in $W.m^{-2}.C^{-1}$ (see equation (2.24) for coefficient h) as follows (Hévin et al., 2016): $h = 2$ for the 2 slots, $h = 20$ for the floor under the fan box, $h = 3.2x^2 – 1.6x + 19$ for the floor inside the cooling chamber with x in meter, $h = 0.2$ for the insulated zone, and $h = 10$ for the uncovered zone. These values of h were determined by calibrating the temperature at the monitoring points on the floor and at different depths of the testing block. Other physical and thermal properties required for the simulation are given in Table 3.1.

For the simulation, the initial temperature in the whole domain was considered to be 14.5°C. The temperature was held constant at 14.5°C at all boundary planes: $x = -5.7$ m, $x = 6.3$ m, $y = 6$ m, $y = -11.5$ m, and $z = -6.5$ m (see Figure 3.4 for the coordinate system).

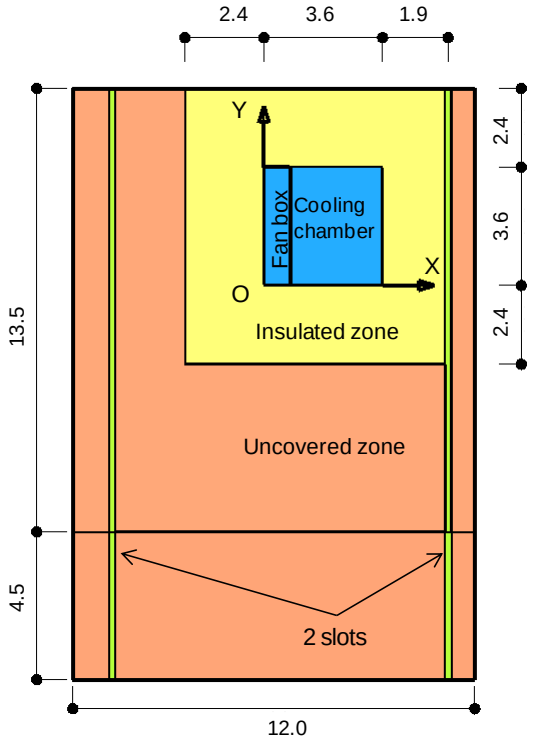

Figure 3.5 Convection zones for heat transfer simulation with different values of the heat transfer coefficient (measured in $W.m^{-2}.C^{-1}$) as follows: $h = 2$ for the 2 slots, $h = 20$ for the floor under the fan box, $h = 3.2x^2 - 1.6x + 19$ for the floor inside the cooling chamber, $h = 0.2$ for the insulated zone, and $h = 10$ for the uncovered zone

Table 3.1 Physical and thermal properties of the rock salt and marl

Parameter	**Unit**	**Salt**	**Marl**
Density ρ	kg/m^3	2200	2300
Heat capacity C_p	J(kg.C)	850	900
Heat conductivity λ	W/(m.C)	6.5	2.9

Results of heat transfer simulation:

Temperatures along the main profile (along *x*-axis) and along the transverse profile (along *y*-axis) are shown in Figure 3.6. As it can be seen, the simulation results agree reasonably well with the test measurements. The temperatures inside the cooling chamber decreased quickly during the first few hours. Along the main profile, the average temperature decrease was about 4 °C after 10 minutes and approximately 9 °C after 1 hour. Temperatures tended to stabilize

after 5 days. Some discrepancies were observed in the first few minutes after the start of the cooling. This can be explained by the phase changes of fluid in the pore space that are not accounted for in the current numerical model. However, after 1 hour the temperature difference between the simulation and test measurements was less than 1°C, except for the thermocouple below the fan box. In fact, the convection condition under the fan box is difficult to control and a constant value of the heat transfer coefficient may not be sufficient to describe the real convective conditions.

Time evolution of the computed temperature was also compared, for different depths, with the experimental values measured by thermocouples T3, T4 and T5, as displayed in Figure 3.7; similar agreements between numerical results and test measurements were obtained.

A 3D view of the spatial distribution of the temperature at the end of the first cooling stage (day 28) is shown in Figure 3.8. Note that the cold fronts (surfaces with low temperatures) did not reach the boundaries of the model. This justifies the dimensions chosen for the model and the constant temperature boundary condition used. Therefore, the computed temperature field is considered to be close to the real temperature observed in the rock mass and will be introduced into the mechanical model

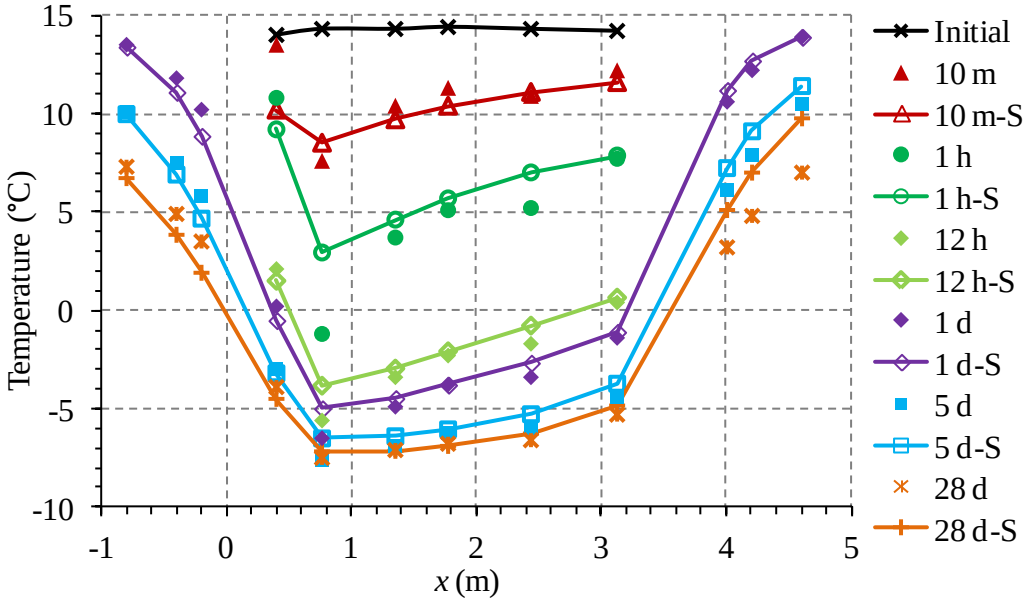

(a) Main profile

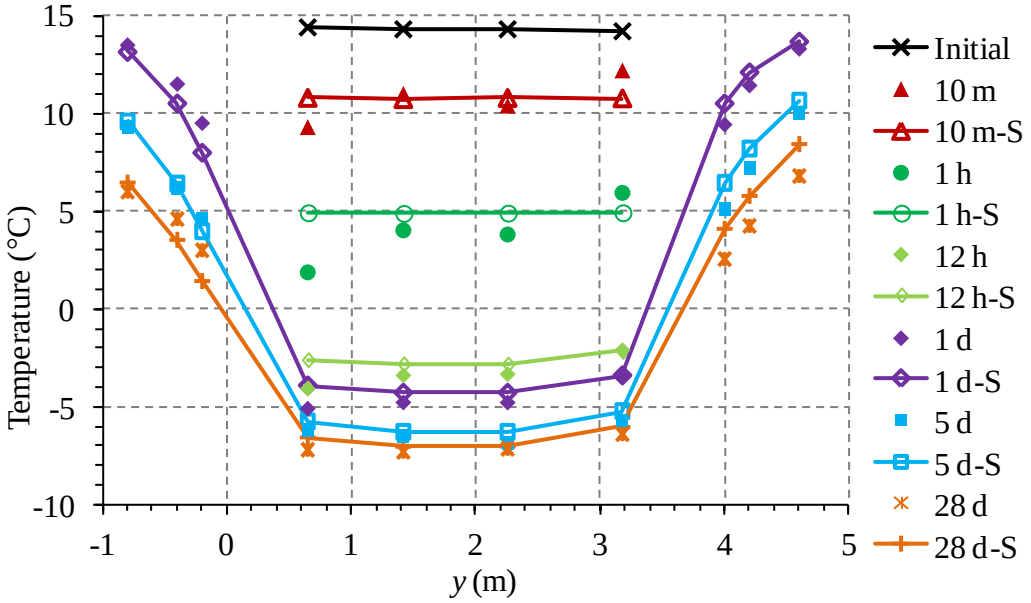

(b) Transverse profile

Figure 3.6 Comparison between simulation and measurement for temperatures along (a) the main profile and (b) the transverse profile. Legends followed by an "S" represent computed results while those without "S" represent the measurements. The cooling chamber is located in $0 \le x \le 3.6$ m and $0 \le y \le 3.6$ m.

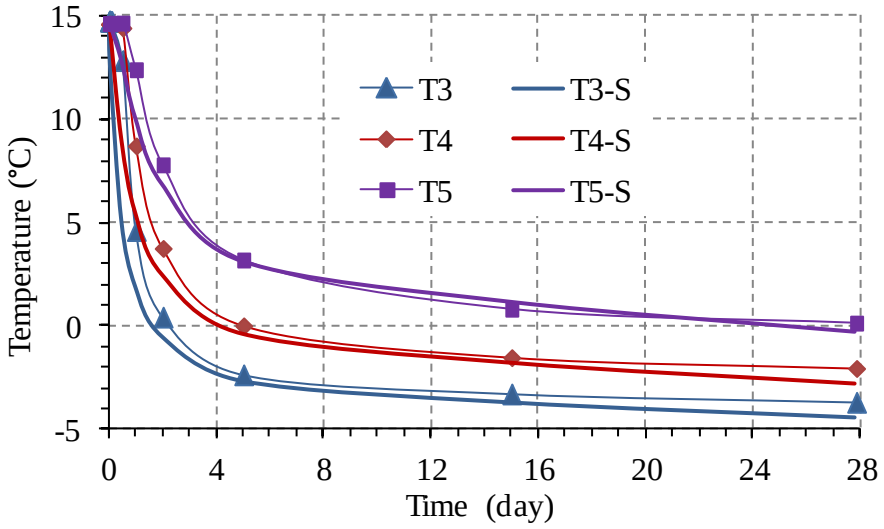

Figure 3.7 Time evolution of the temperature at depths 0.2 m, 0.4 m, and 0.8 m measured by thermocouple T3, T4, and T5, respectively. Legends followed by an "S" represent computed results while those without "S" represent the measurements.

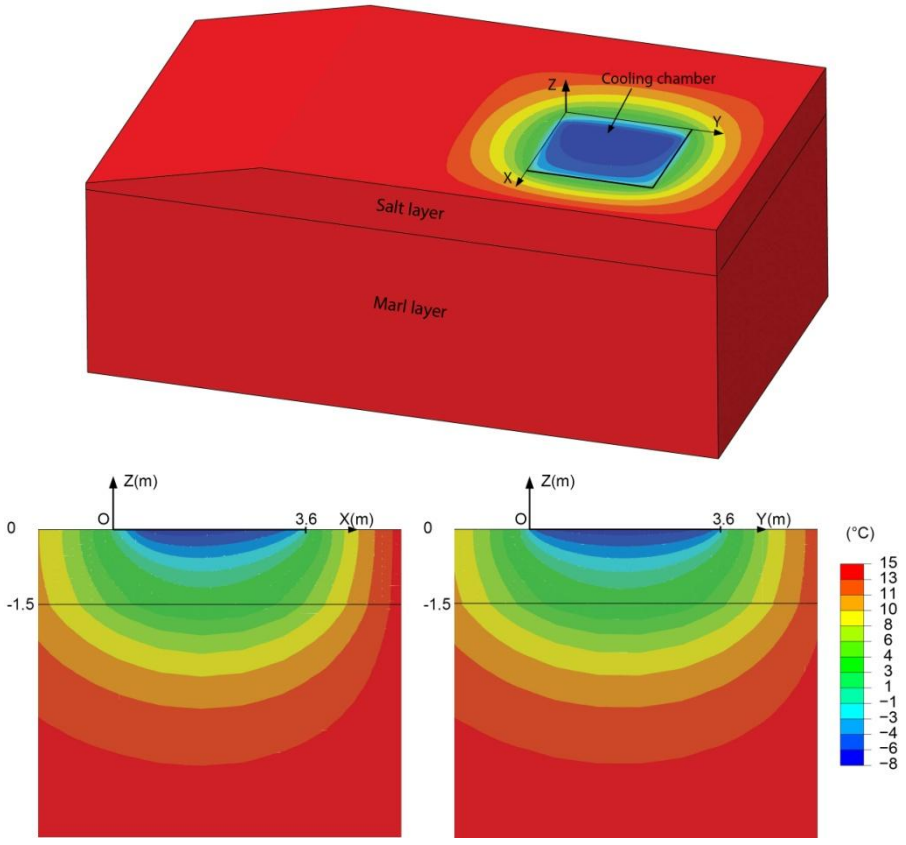

Figure 3.8 Temperature distribution at the end of the first cooling stage. (a) 3D view; (b) Cross sections along the main profile (left) and the transverse profile (right)

3.2.3 Fracture propagation simulation

The fracture propagation simulation consists of two steps. The first step is to initialize the initial stress conditions in the rock mass surrounding the salt block where the cooling experiment was performed. The second step is to model the fracture propagation; the extended finite element method (XFEM) is used for this purpose. XFEM does not require pre-defining the fracture trajectory. Instead, the fracture trajectory is determined based on the stress condition at the fracture tip. Here the fracture propagation direction is supposed to be perpendicular to the maximum tangential stress at the fracture tip, while the fracture propagation criterion is based on a comparison between the strain energy release rate G and the fracture energy G_C as presented in equation (2.44), which is repeated here for convenience:

$$G = G_C \tag{3.1}$$

The strain energy release rate G can be estimated using the Virtual Crack Closure Technique (VCCT) (ABAQUS, 2016), which is based on the assumption that the strain energy released when a crack is extended by a certain amount is the same as the energy required to close the crack by the same amount. Figure 3.9 illustrates the principle of VCCT. In Figure 3.9a, the fracture extends from node *m* to node *n*, accompanied by the release of a certain amount of strain energy. This amount of energy is supposed to be equal to the work necessary to close the fracture from node *n* to node *m* in Figure 3.9b.

For a pure Mode I fracture with the fracture tip located at node 2 (or node 5) as shown in Figure 3.10, the energy release rate when the fracture propagates from node 2 is calculated as follows:

$$G_I = \frac{1}{2}\frac{F_{v,25} \times v_{16}}{bd} \tag{3.2}$$

where $F_{v,25}$ is the nodal force at nodes 2 and 5; v_{16} is the displacement between nodes 1 and 6; d is the length of the element at the crack front; and b is the thickness of the element (not presented in Figure 3.10). The fracture will begin to propagate when $G_I = G_{IC}$ where G_{IC} is the Mode I fracture energy.

The mixed-mode fracture energy G_C in equation (3.1) can be estimated using different laws presented in subsection 2.3.1.4. In this simulation the BK law is used and is repeated in the equation below:

$$G_C = G_{IC} + \left(G_{IIC} - G_{IC}\right)\left(\frac{G_{II} + G_{III}}{G_I + G_{II} + G_{III}}\right)^m \tag{3.3}$$

The three parameters needed to define this law include the Mode I and Mode II fracture energy G_{IC} and G_{IIC} and the material parameter m.

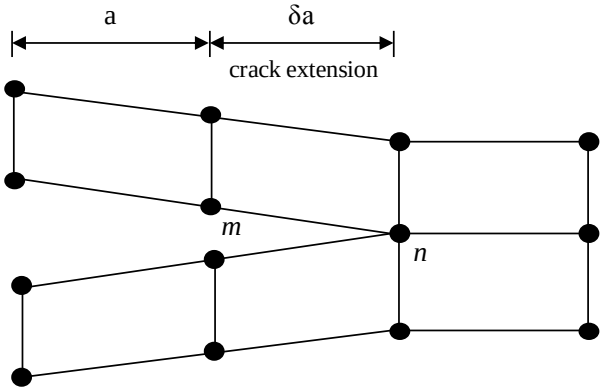

(a) Crack extension from node *m* to node *n*

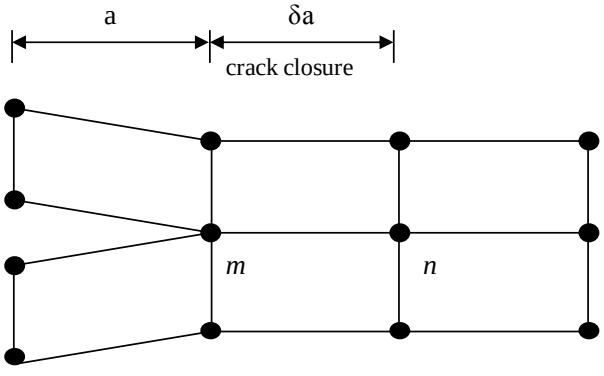

(b) Crack closure a node *m*

Figure 3.9 Extension and closure of Mode I fracture. The energy released when a crack extends by a distance *δa* is the same as the energy required to close the crack by a distance *δa*. Black dots represent the nodes of finite elements. Source: adapted from ABAQUS (2016)

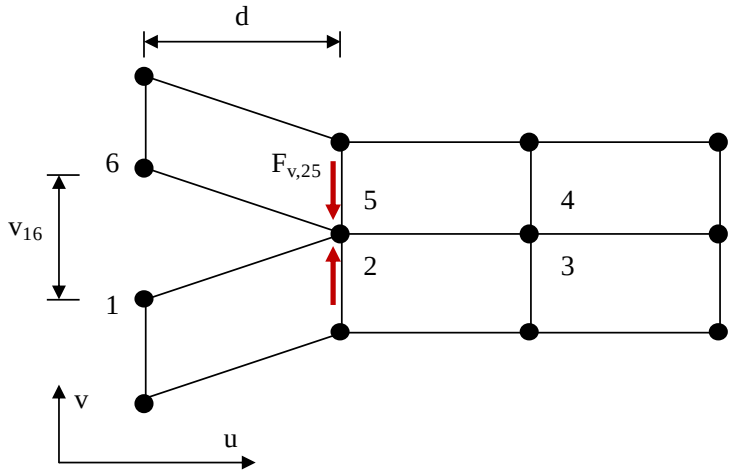

Figure 3.10 Pure Mode I fracture. The fracture tip is at node 2 (or node 5). $F_{v,25}$ is the nodal force at nodes 2 and 5. $v_{v,16}$ is the vertical displacement between nodes 1 and 6

Initial stress initialization:

As explained above, the mechanical simulation of the fracture propagation was performed using the same sub-domain as in the heat transfer simulation. However, the initial stress state was first reproduced using a full model with dimensions of 180 m x 180 m x 180 m (Figure 3.11) and consisting of three layers, which are, from the top: a 40 m thick sandstone layer, an 80 m thick rock salt layer, and a 60 m thick marl layer. All lateral faces and the bottom face of the domain are constrained. The simulation has 3 steps: In the first step, the geostatic stress is applied. The geostatic stress is the lithostatic stress and is supposed to be isotropic. The second step simulates the excavation of the main gallery and the niche. In the third step, the two slots are excavated. The density of the salt and marl were presented in Table 3.1. The density of the upper layer of sandstone is 2500 $kg.m^{-3}$. The thermo-mechanical properties of all 3 rocks are listed in Table 3.2. The stresses computed in the domain of interest will be extracted and used as initial stresses in the sub-model for fracture propagation using the submodeling technique in ABAQUS (ABAQUS, 2016).

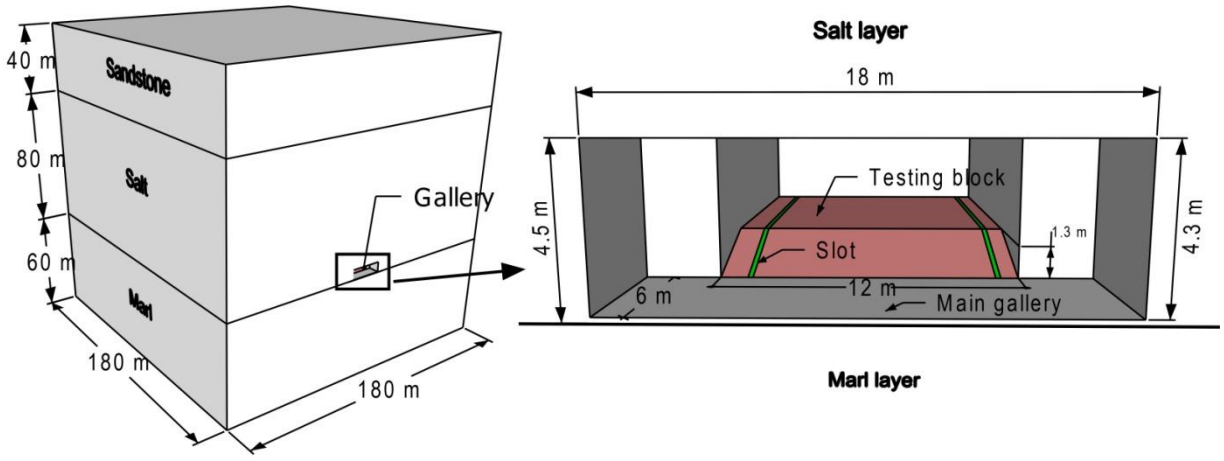

Figure 3.11 Geometric domain used for reproduction of the initial stress state

Table 3.2 Thermo-mechanical properties of the rock salt, marl, and sandstone

Property	**Sandstone**	**Salt**	**Marl**
Young's modulus (GPa)	15	20	15
Poisson ratio (-)	0.25	0.25	0.2
Linear thermal expansion coefficient (C^{-1})	$1.5x10^{-5}$	$2.5x10^{-5}$	10^{-5}

The distributions of stresses σ_x and σ_y on the floor of the cooling chamber at different times are shown in Figure 3.12. Note that the excavation of the niche has the same effect on both σ_x and σ_y as they both decrease from -2.85 MPa to about -2.0 MPa (compression is negative). Conversely, the excavation of the 2 slots modifies σ_x and σ_y differently. As it can be seen in Figure 3.12c, the stress σ_x was more relaxed than σ_y, decreasing from -2.0 MPa before excavation of the slots to about -1.4 MPa afterwards. This is due to the direction of the slots, which are normal to the *x*-axis.

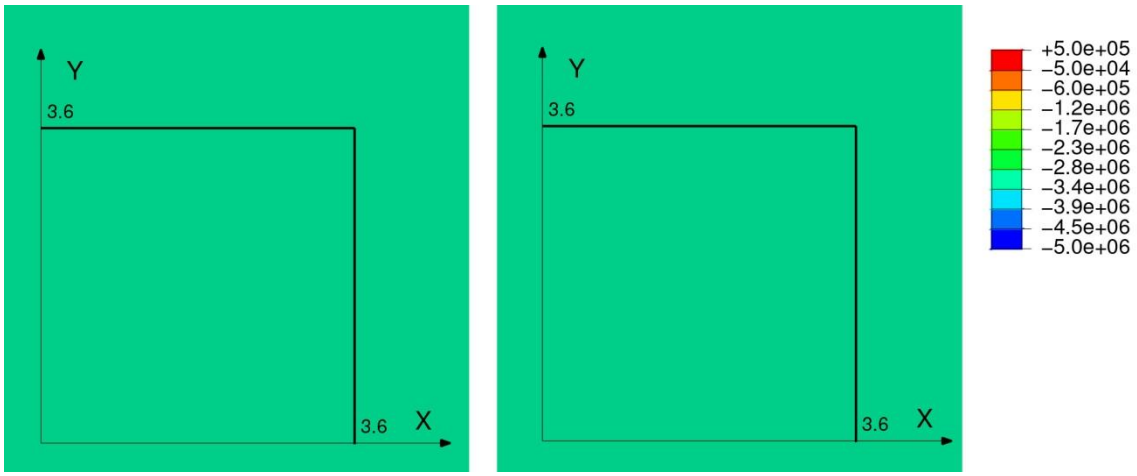

(a) Initial lithostatic state

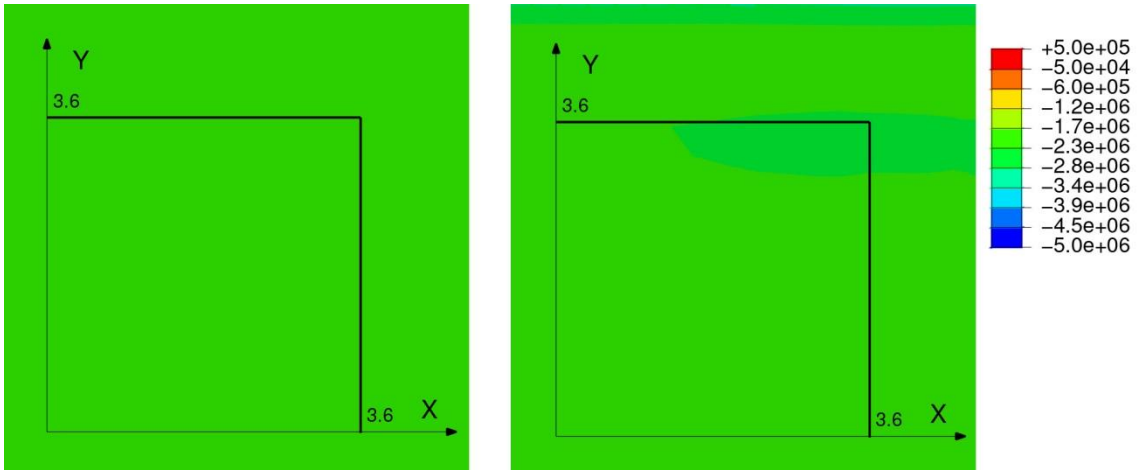

(b) After the excavation of the niche

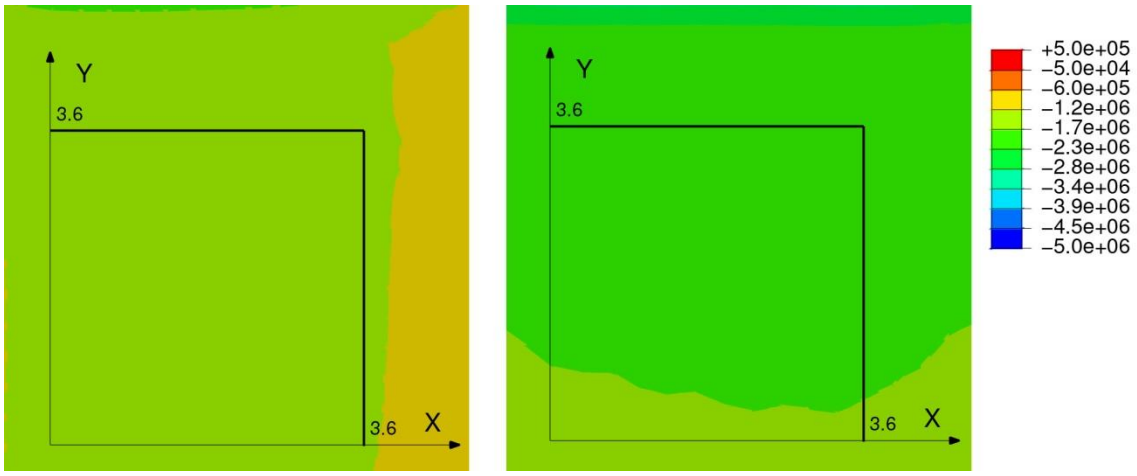

(c) After the excavation of the slots

Figure 3.12 Stresses (σ_x on the left and σ_y on the right) on the floor of the cooling chamber at different steps of excavation. Stresses are given in Pa

Fracture propagation simulation:

For fracture propagation modeling, a sub-model is used (Figure 3.4). All the lateral faces and the bottom face are displacement-constrained. This boundary condition is justified because its effects on the salt block, which is the region of interest, are limited due to the presence of the two slots. Indeed, the two parallel slots isolated the salt block from lateral contact with the walls of the niche. The initial stress state used in the current simulation was taken from the initial stress state initialization model above, for the corresponding geometric domain. The mechanical properties of the salt required for the fracture propagation modeling are typical of those found in the literature. A tensile strength for salt of 2.75 MPa, and fracture toughness $G_{IC} = G_{IIC} = 22$ J/m^2 were used (Wang et al., 2016).

Figure 3.13 shows the stresses in the directions x and y (σ_x on the left, σ_y in the middle) and the temperature (on the right) on the floor of the cooling chamber at different times during the first cooling stage. Note that stress σ_x inside the chamber, which is compressive prior the cooling, changes to tension 1h after the start of cooling. It is also greater than σ_y and increases upon further cooling. At about 4h30, when σ_x exceeds the tensile strength of the rock salt, two cracks are initiated in two locations at a distance of about 1.1 m from the fan box (i.e. x = 1.1 + 0.5 = 1.6 m, with the width of the fan box is 0.5 m), as shown in Figure 3.13b. The locations of the two cracks are immediately in front of the fans where temperature is the most reduced. The cracks then propagated rapidly and coalesced into one crack across the chamber after 5h, as shown in Figure 3.13c. The location and the time at which the first cracks appeared are consistent with the observations made on site. Indeed, (Hévin et al., 2016) reported that a macro-crack was visible after about 6h of cooling at x = 1.5 m.

Stress relaxation was also noticed around the cracks at 5h (σ_x on the left of Figure 3.13). After 5h, the macro-crack on the floor did not propagate further. The region of maximum tensile stress was shifted farther from the fan box, as can be seen in the contour plot of σ_x in Figure 3.13c,d. At the end of the first cooling stage, the temperature distribution became more homogeneous and steady. This caused a decrease in the amplitude of both σ_x and σ_y at the end

of the first cooling stage. For instance, the maximum σ_x, which was about 2.4 MPa after 5h, reduced to close to 1.0 MPa at 28 days.

Although the crack stopped propagating on the floor of the cooling chamber after 5h, the temperature decreases caused the crack to propagate deeper into the salt block. Figure 3.14 shows the crack area on the plane *y*-*z* at different times. The crack's depth at 5h was approximately 0.3 m. As the cooling continued, the crack gradually penetrated deeper into the rock mass; after 1 day it was about 0.8 m deep. The downward crack penetration slowed and stabilized after 5 days. This evolutionary trend was also observed in the experiment (Hévin et al., 2016). The maximum crack depth at 28 days was approximately 1.15 m, which is consistent with the depth observed on site, about 1.25 m.

The evolution over time of the crack depth and the crack aperture on the floor of the cooling chamber at y = 1.8 m are illustrated in Figure 3.15. Note that both the depth and aperture of the crack increased rapidly during the first few hours, after which the increase rate slowed down and stabilized after 5 days. The crack aperture reached a maximum of 0.65 mm after 2 days. The computed crack aperture is of the same order as that observed experimentally, which was about 1 mm (Hévin et al., 2016). The crack aperture then slightly decreased after 5 days; this crack evolution is consistent with that observed experimentally. The reason for this decrease is that the temperature distribution became more homogeneous after 5 days, causing the stresses (including σ_x) to relax and decrease the aperture.

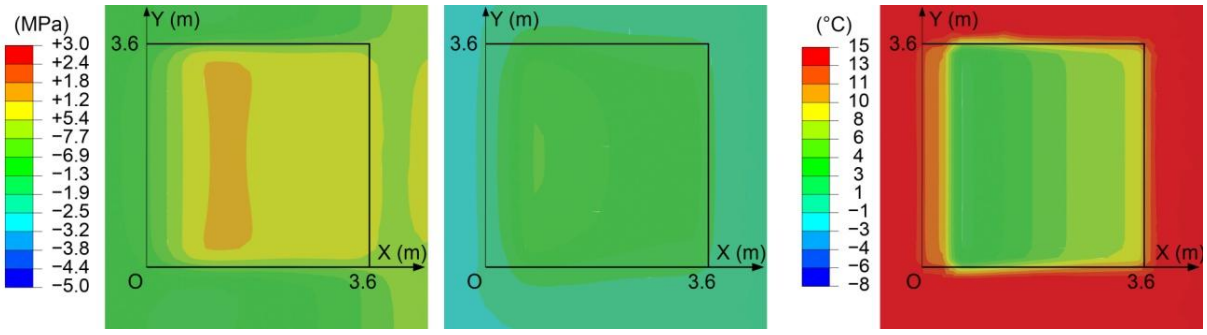

(a) t = 1 h

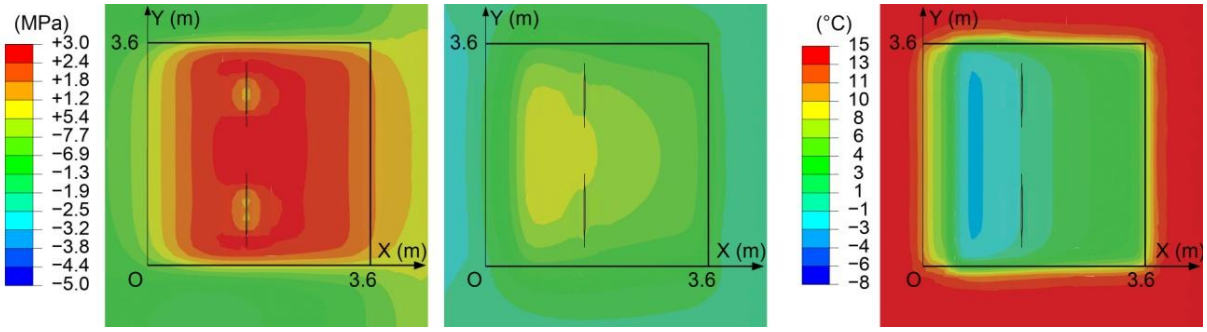

(b) t = 4.5 h

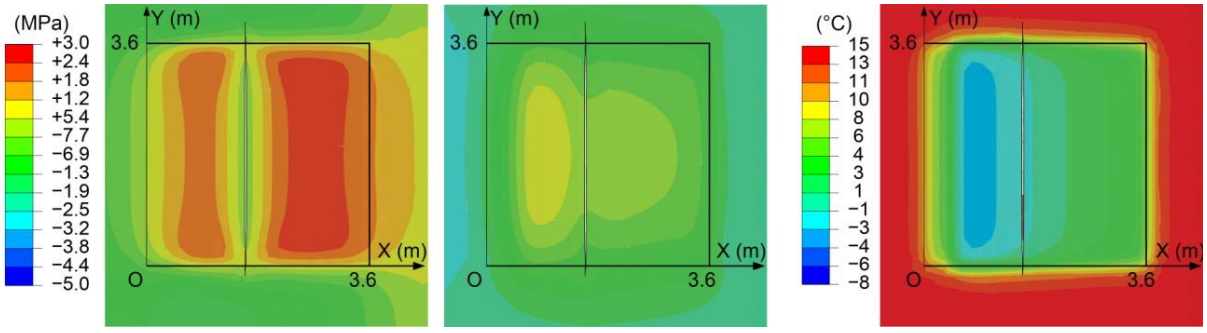

(c) t = 5 h

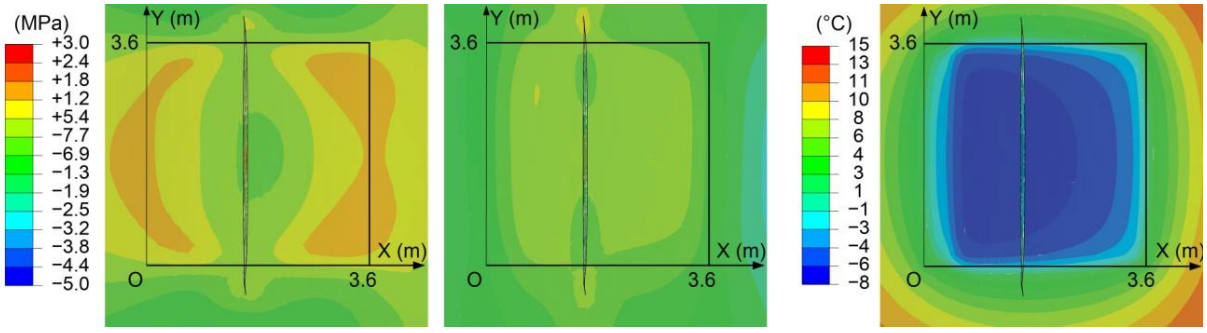

(d) t = 28 d

Figure 3.13 Numerical results (σ_x on the left, σ_y in the middle, temperature on the right) on the floor of the cooling chamber at different times during the cooling stage

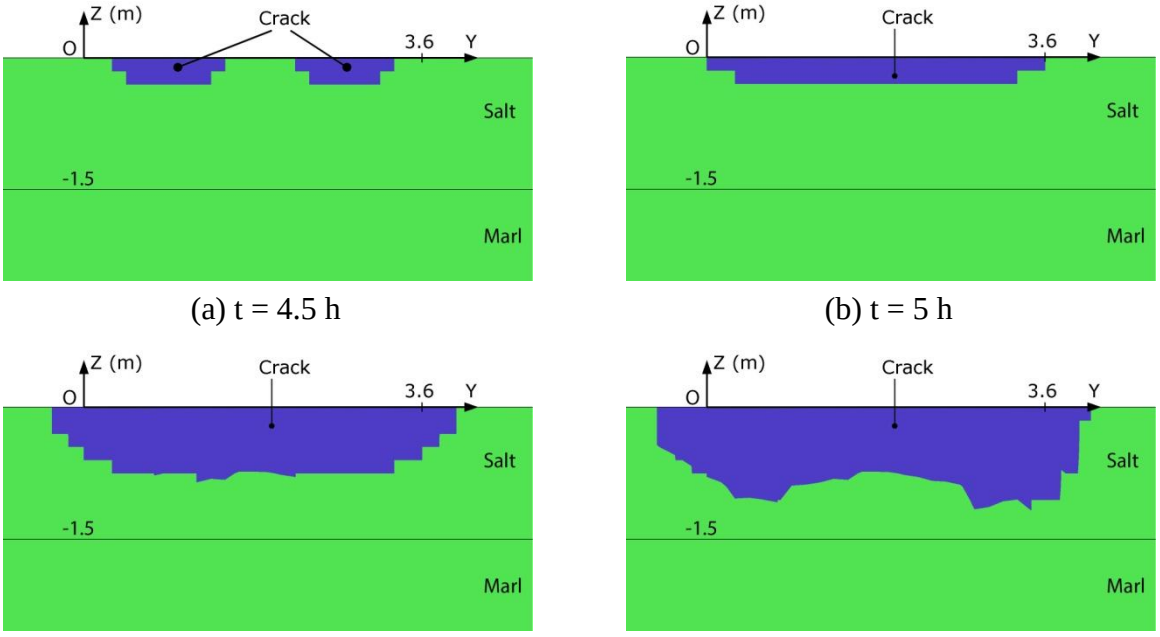

Figure 3.14 Crack area projected on the y-z plane at different times during the cooling stage. The crack area is shaded in blue

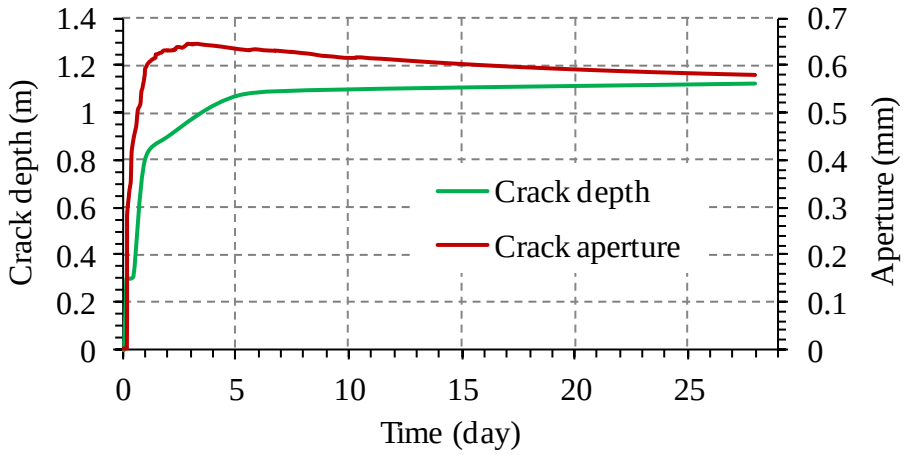

Figure 3.15 Time evolution of crack depth and crack aperture on the floor of the cooling chamber at *y* = 1.8 m

3.3 THERMAL FRACTURE FROM A WELLBORE

As mentioned in the introduction to this chapter, the injection of cold water through a wellbore into a hot rock formation will cause a sudden temperature decreases in the vicinity of the wellbore, which in turn will lead to the contraction of the rock. Tensile stresses will be induced as the rock around the wellbore is refrained from contracting by the surrounding rock.

As a result, fractures can be initiated if the induced tensile stresses exceed the in-situ stress and the tensile strength of the rock. This phenomenon will be studied in this section using 2D simulations.

3.3.1 Model setup

The fracture propagation from a wellbore due to temperature changes was studied using a 2D model presented in Figure 3.16. The 2D rock formation has dimensions of width 10 m and length 10 m. A wellbore of radius 0.15 m is located at the center of the 2D formation. Cold water is injected into the rock formation through the wellbore and potential thermal fractures may initiate from the wellbore. The dimensions of the 2D formation were chosen such that they are still reasonably larger than the length of the expected fractures. The modeling consists of two simulations: a heat transfer simulation and a fracture propagation simulation.

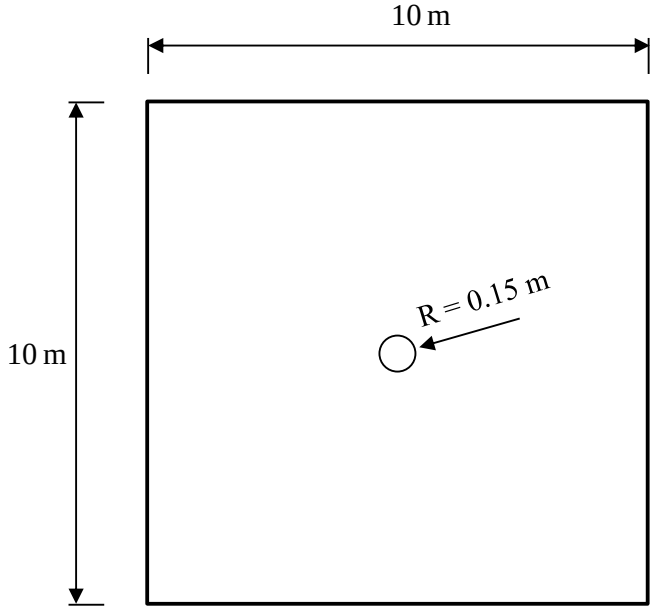

Figure 3.16 Geometry for studying fracture propagation around a wellbore

Heat transfer simulation:

For the heat transfer simulation, the impact of fractures on the temperature field is not considered. The rock mass has an initial temperature of 220 °C and the temperature of the injected water is 20 °C. It is assumed that the temperature of water inside the wellbore remains at its initial temperature (i.e., 20 °C) and the temperature of water inside the fractures is equal

to the temperature of the rock mass. These assumptions mean that only heat transport by fluid diffusion is modeled, while heat transport by fluid flow in the fractures and heat convection between fluid flow and the fracture walls are not taken into account. The heat transfer simulation carried out here is only a rough approximation to the complex conditions occurring in a geothermal wellbore.

For the boundary conditions, the temperature of all outer edges of the 2D domain and of the wellbore is maintained at an initial temperature of 20 °C.

The physical and thermal properties necessary for the heat transfer simulation are summarized in Table 3.3.

Table 3.3 Physical and thermal properties necessary for the heat transfer simulation (Ghassemi and Tarasovs, 2015)

Property	**Unit**	**Value**
Density ρ	kg/m^3	2650
Heat capacity C_p	J/kg °C	790
Heat conductivity λ	W/m °C	10.7

Fracture propagation simulation:

The temperature field obtained from the heat transfer simulation is used as the loading condition for the fracture propagation simulation. The fracture propagation is modeled using the cohesive material concepts in combination with cohesive elements. The plane deformation condition is assumed and the rock mass is supposed to be homogeneous and linear elastic. The temperature field obtained from the heat transfer is symmetric about the center of the wellbore because of the symmetry of the boundary conditions. Therefore, in this fracture propagation simulation only Mode I fractures that propagate radially from the wellbore are expected. For this reason, 24 layers of cohesive material are evenly placed around the wellbore as illustrated in Figure 3.17. The mechanical properties of the rock formation and the initial stresses are given in Table 3.4.

For the boundary conditions, the displacements of all rock surfaces are confined in the direction perpendicular to them. The initial temperature of the rock is 220 °C, which is similar to the initial temperature used in the heat transfer simulation. The temperature of the rock at time t > 0 is imported from the heat transfer simulation. The fracture propagation simulation is also run for 10 days, similar to the time duration of the heat transfer simulation.

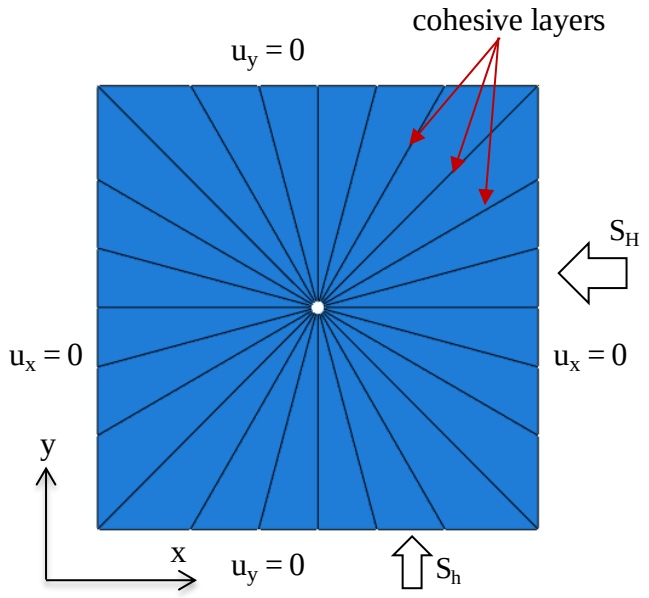

Figure 3.17 Layout of cohesive layers around the wellbore and the boundary condition.

Table 3.4 Parameters used for the fracture propagation simulation

Property	**Value**	**Source / Comment**
Young's modulus	E = 30 GPa	(Keshavarz, 2009)
Poisson's ratio	$\nu = 0.22$	(Keshavarz, 2009)
Linear thermal expansion coefficient	$\alpha = 1.2 \times 10^{-5}$ (1/°C)	Typical value (Wong and Brace, 1979)
Tensile strength	$R_T = 1.25$ MPa	Common value
Fracture energy	$G_{IC} = 62$ N/m ($K_{IC} = 1.4$ MPa.m$^{0.5}$)	Common value (Atkinson, 1989)
Initial stresses	$S_h = -12$, $S_H = -36$ MPa	(Meyer et al., 2017)

3.3.2 Simulation results

3.3.2.1 Results of heat transfer simulation

The contour plots of temperature at different times are presented in Figure 3.18. It can be seen that the temperature field is symmetric about the center of the wellbore as predicted. The cold front spreads away from the wellbore as time increases.

Figure 3.19 shows the temperature along a radius at different times. It should be noted that for one specific curve in Figure 3.19 the temperature gradients, which are a measure of the slope of the curve, are largest near the wellbore and gradually decrease farther away from the wellbore. This indicates that the potential induced tensile stresses are also largest near the wellbore. It is also observed that the temperature gradients in the region near the wellbore decrease over time and the temperature field becomes more homogeneous.

Figure 3.20 represents the time evolution of the temperature at four points A, B, C, and D which are located at 0.25 m, 0.7 m, 1.5 m, and 3.7 m from the center of the wellbore, respectively. The temperature decreases sharply in the hours immediately after the beginning of the simulation, and continues to decrease subsequently but at a much slower rate. The temperature at points closer to the wellbore also decreases more than at points farther away from the wellbore.

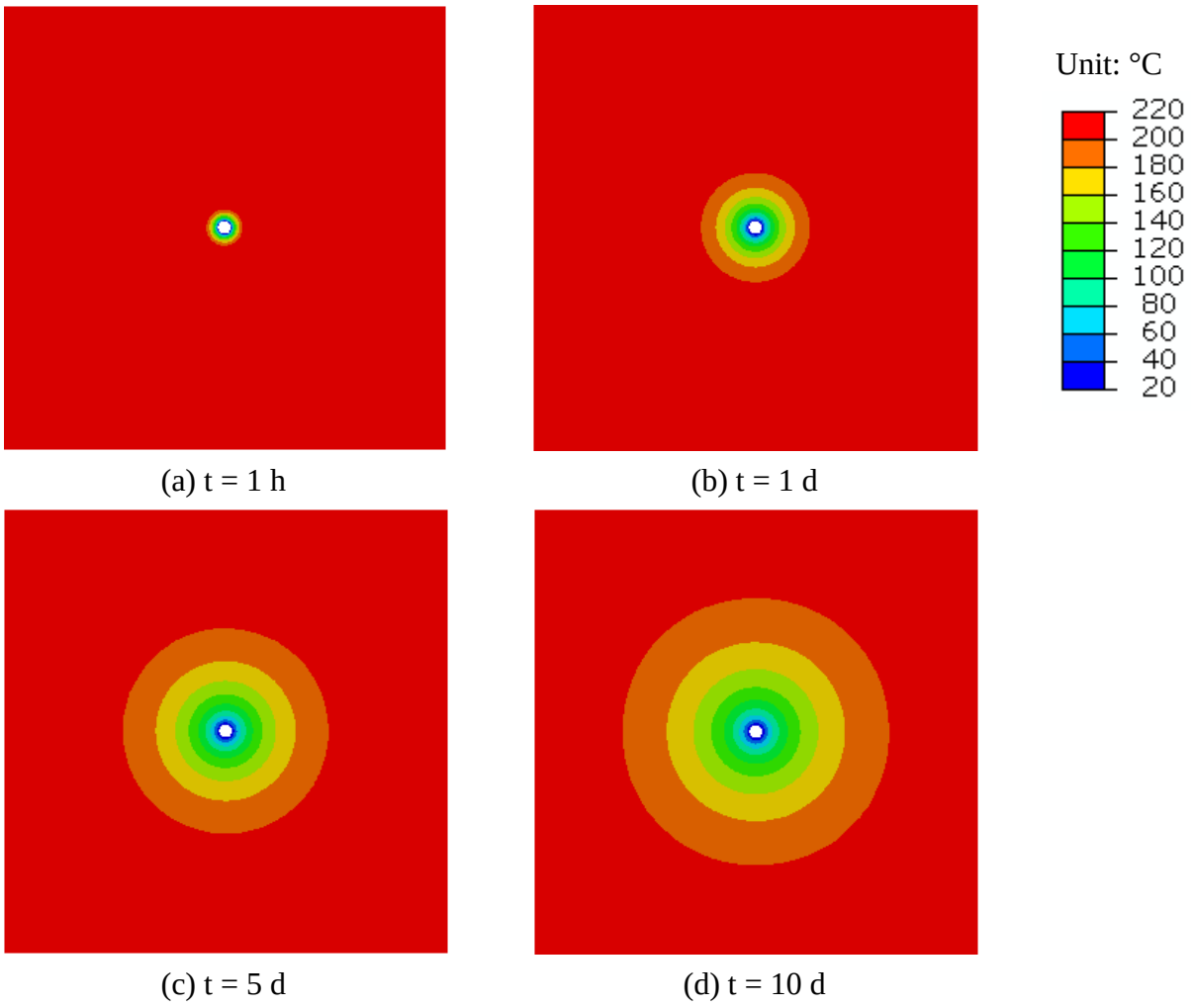

Figure 3.18 Contour plots of temperature at different times

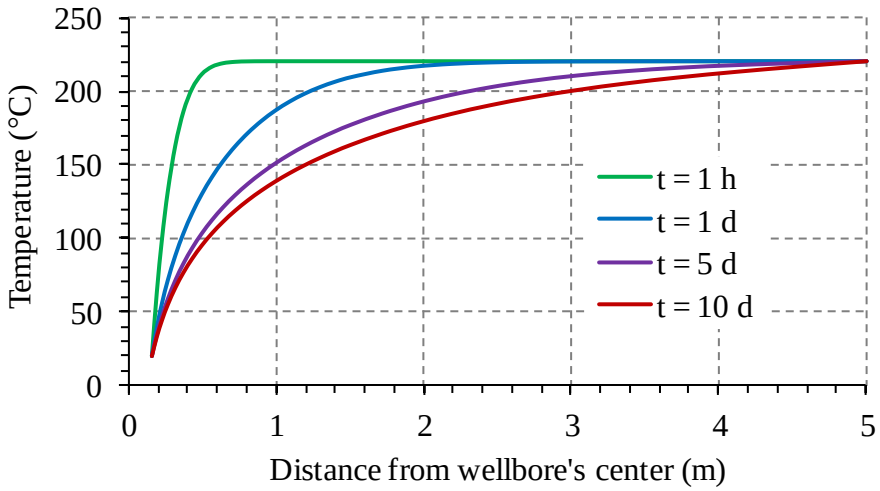

Figure 3.19 Temperature along a radius at different times

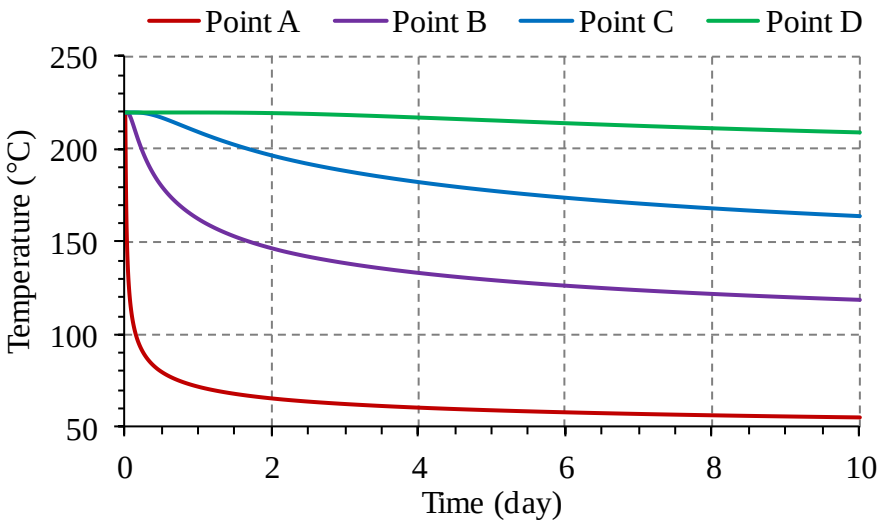

Figure 3.20 Time evolution of temperature at four points A, B, C, and D that are located at 0.25 m, 0.7 m, 1.5 m, and 3.7 m from the center of the wellbore, respectively

3.3.2.2 Results of fracture propagation simulation

The fracture propagation due to temperature changes is presented in Figure 3.21, which shows the contour plots of the damage variable *D*. Since cohesive elements are used to model fractures, the created fractures correspond to $D = 1$. It can be seen that multiple fractures are initiated around the wellbore immediately after the simulation begins. However, only two major fractures dominate and propagate far from the wellbore. These two fractures are perpendicular to the minimum principal stress S_h.

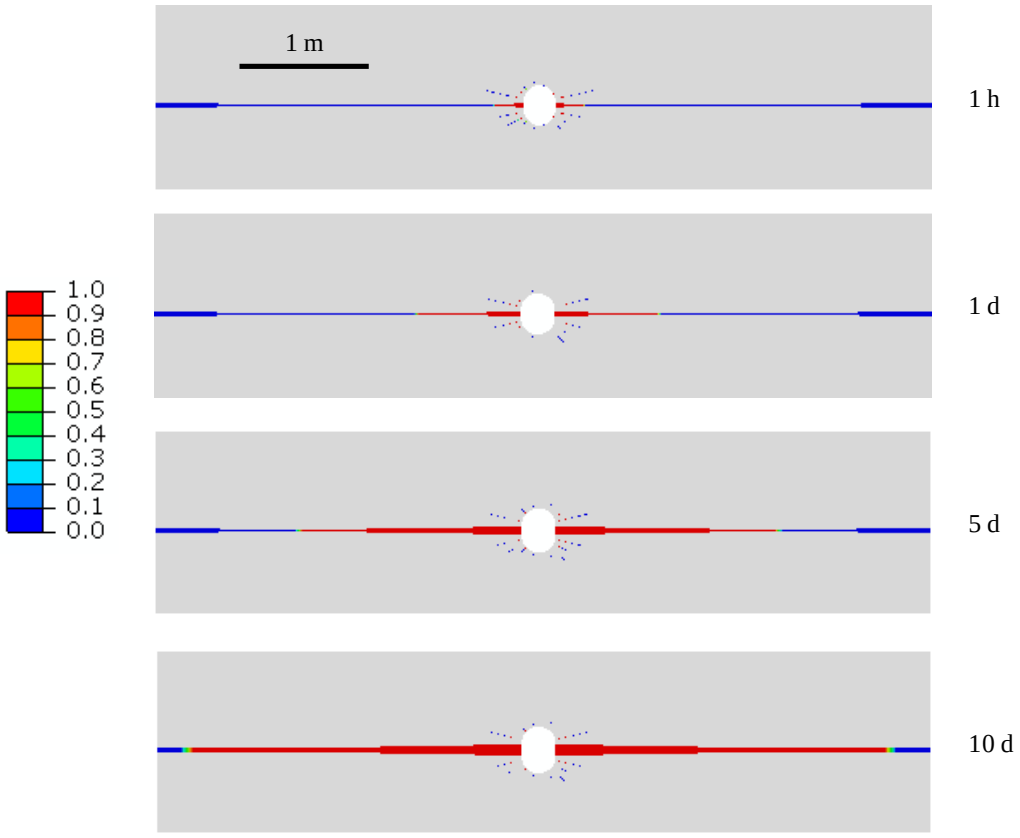

Figure 3.21 Contour plots of damage variable D at different times (when S_h = 12 MPa). Fractured zones correspond to D = 1.

To investigate the influence of the minimum principal stress on the fractures, four different values of the minimum stress S_h were tested: 12 MPa, 18 MPa, 29 MPa, and 36 MPa. Note that the maximum principal stress S_H = 36 MPa.

The fracture pattern at the end of 10 days for all cases is shown in Figure 3.22. In all cases except the case of S_h = 36 MPa, multiple fractures are initiated at first, but only two fractures that are perpendicular to the minimum principal stress S_h continue to propagate further from the wellbore. For the case of S_h = 36 MPa, all the initiated fractures continue to propagate in a symmetrical manner without any preferred direction; this can be observed more clearly in Figure 3.23, which shows the damage variable at the end of 10 days. All the fractures propagate radially and the fracture length is more or less identical in all directions.

The time evolution of the length of the major fracture is shown in Figure 3.24 for all values of S_h. In all cases the fracture length increases rapidly at first and then the rate of increase slows

down. This is because the temperature gradients are largest in the early hours and decrease as time goes on. Another remark is that as the minimum stress S_h increases from 12 MPa to 36 MPa, the length of the major fracture decreases from 2.5 m to 0.3 m.

The fractures induced near the wellbore due to temperature changes resulted from injection of cold fluid may reduce the hydraulic impedance and wellhead pressure (Bruel, 2002; Murphy, 1978; Swenson and Hardeman, 1997) but may also lead to more water loss due creation of new unwanted flow paths. Thermal fractures near the wellbore may also contribute to the instability of wellbore, rendering the wellbore inaccessible as observed at Soultz EGS reservoir (Schill et al., 2017).

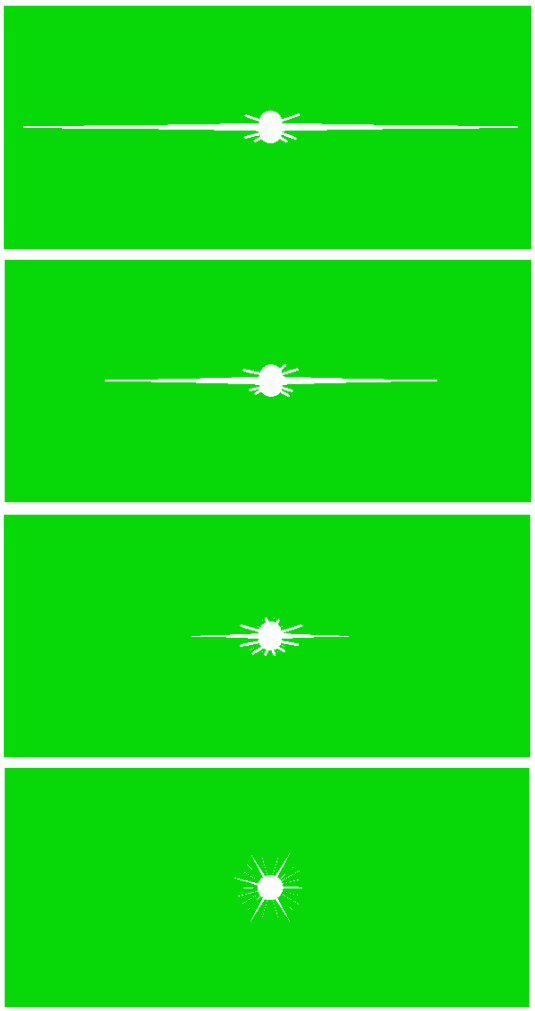

(a) S_h = 12 MPa

(b) S_h = 18 MPa

(c) S_h = 29 MPa

(d) S_h = 36 MPa

Figure 3.22 Deformed shape (amplified 20 times) with fracture pattern at day 10 for different values of the minimum stress S_h. The maximum stress is S_H = 36 MPa

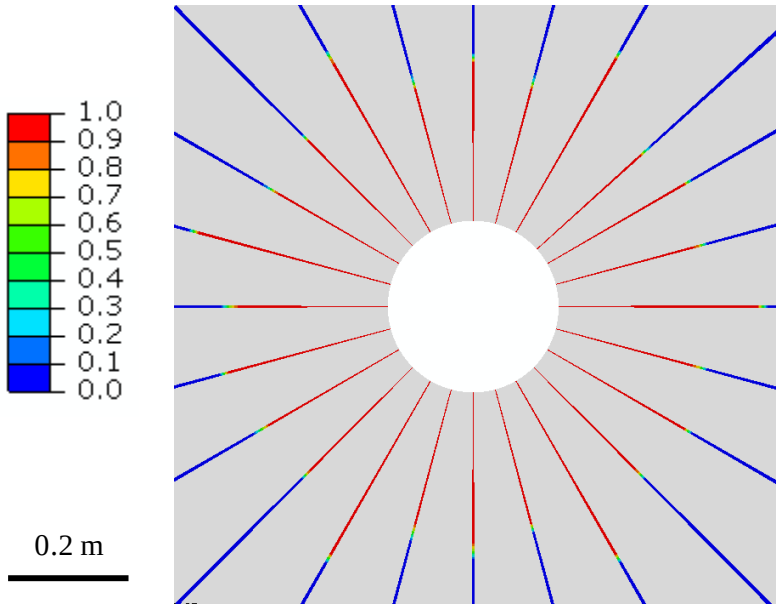

Figure 3.23 Contour plot of damage variable D at time t = 10 d for the isotropic stress case $S_h = S_H$ = 36 MPa. Fractured zones correspond to D = 1

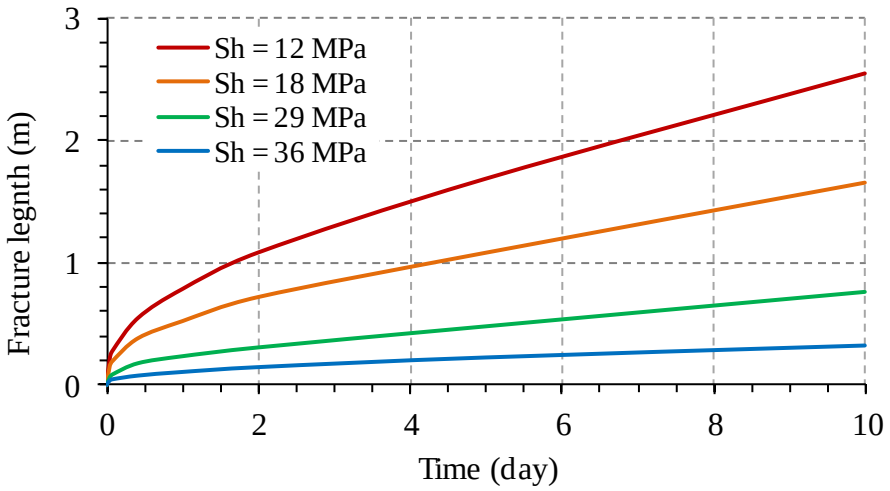

Figure 3.24 Time evolution of the length of the main crack for different cases with different values of the minimum stress S_h. The maximum stress is S_H = 36 MPa

3.3.3 Effect of the temperature of the injected fluid

The effect of the temperature of the injected fluid is numerically investigated here. As demonstrated above the injection of cold fluid can induce fractures near the wellbore and the induced fractures can grow to lengths on the order of meters. It is also known that the peak hydraulic pressure of fracture initiation can be reduced as the length of the initial fracture

increases. Thus, in order to reduce the peak hydraulic pressure, it may be necessary to increase the length of fractures near the wellbore. One way to achieve this is by decreasing the temperature of the injected fluid, which will result in higher temperature gradients and thus induce higher tensile stresses. Many researchers are experimentally investigating an even more "radical" approach by using liquefied nitrogen at temperatures of nearly -200 °C to create thermal fractures (Cha et al., 2017; Zhang et al., 2018a; Zhang et al., 2018b). It is expected that as the temperature of the injected fluid is lowered, the thermal fracture will propagate further. The question is: How effective is the lowering of the temperature of the injected fluid in increasing the length of the thermal fracture? To answer this question, the following simulation scenario was studied. Water at three different temperatures T_0 = 5 °C, 20 °C, and 35 °C is injected into a rock formation that has an initial temperature of 220 °C. The simulation procedure is similar to that described in subsections 3.3.1. The main points are summarized below:

- The modeling of thermal fracturing consists of two simulations: a heat transfer simulation and a fracture propagation simulation
- For the heat transfer simulation, the temperature of the wellbore is assumed to be constant and equal to the temperature of the injected water T_0. The material properties needed for the heat transfer simulation are taken from Table 3.3.
- The fracture propagation simulation uses the temperature field obtained from the heat transfer simulation as the thermal load. The mechanical properties and initial stresses needed for the fracture propagation simulation are taken from Table 3.4.

Simulation results:

The results of the heat transfer simulation for the case T_0 = 20 °C are presented in subsection 3.3.2, while those for the cases T_0 = 5 °C and 35 °C are presented in Figure 3.25. It can be seen from Figure 3.25a and b that the temperature field is symmetric about the center of the wellbore; the temperature in the region near the wellbore (within the radius of 2 m) is lower for T_0 = 5 °C than for T_0 = 35 °C. The temperature in the region farther from the wellbore (out of the radius of 3 m) is nearly identical for all three cases (Figure 3.25c).

Using the obtained temperature fields, the fracture propagation simulations were run and the results for the length of the major fracture are presented in Figure 3.26 and Figure 3.27. The thermal fracture grows rapidly in the early hours, but then the growth rate decreases (Figure 3.26). The effect of the water temperature can be seen clearly in Figure 3.27, which shows that the water temperature has little effect on the final fracture length. Specifically, as the water temperature increases from 5 °C to 35 °C, the final fracture length decreases by 0.4 m from 2.76 m to 2.36 m, about 14 %. This is due to the low heat conductivity of the rock which reduces the penetration of the cold temperature into the rock mass.

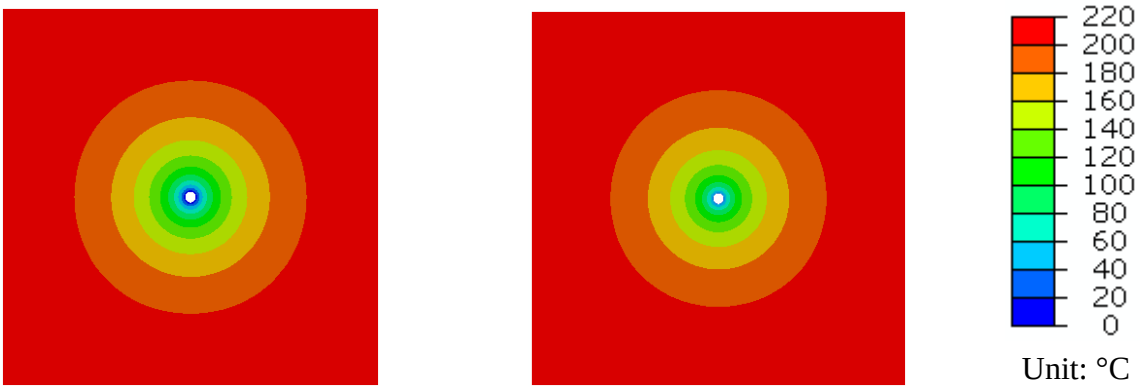

(a) T_0 = 5 °C (b) T_0 = 35 °C

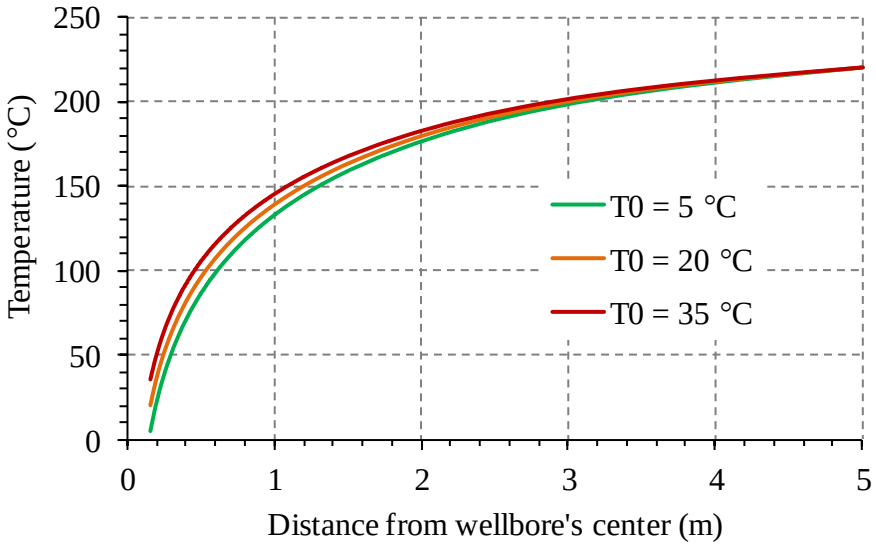

(c) Temperature along a radius at day 10

Figure 3.25 Results of heat transfer simulation for different temperatures of the injected water. (a) and (b) are contour plots of temperature at day 10. (c) is the temperature along a radius at day 10

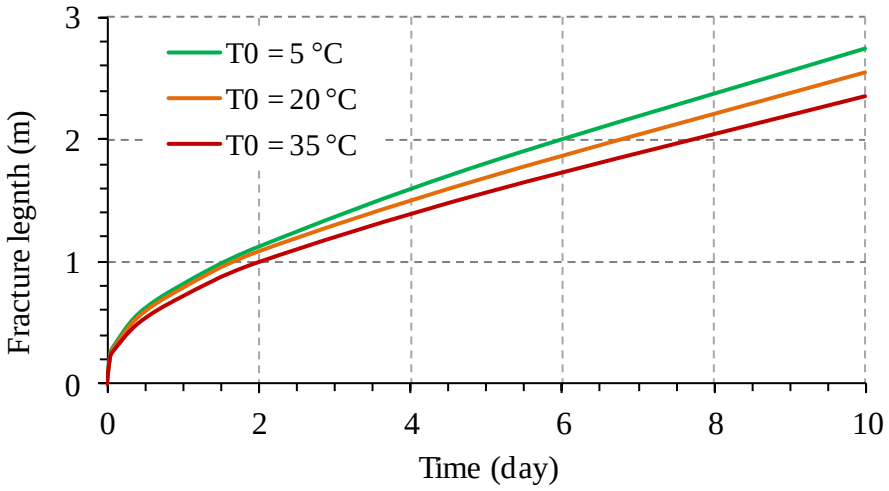

Figure 3.26 Time variation of the length of the major fracture for three cases with different water temperature T_0

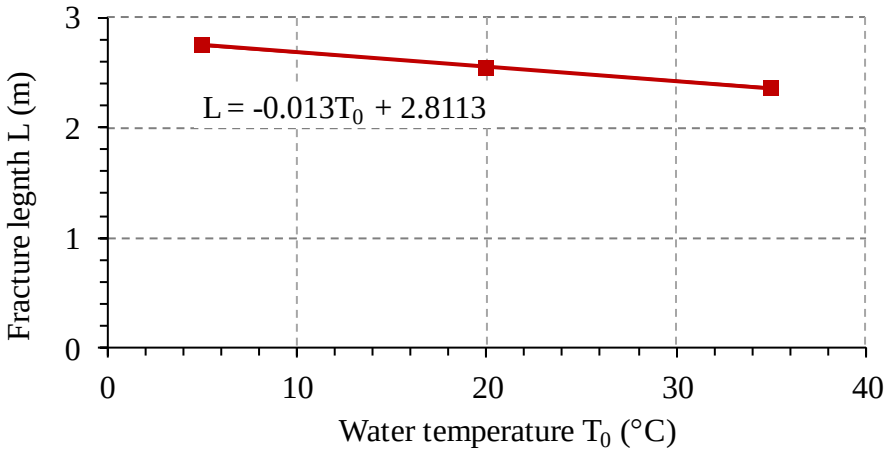

Figure 3.27 Length of the major fracture at day 10 as function of the water temperature T_0

3.4 CHAPTER CONCLUSIONS

Numerical simulations were used to study the effect of temperature changes on the fracturing of rocks in two different contexts. The extended finite element method (XFEM) was used to model the propagation of thermal fractures in the cooling experiment of rock salt. Under the low confining conditions of the cooling experiment, a temperature decrease of approximately 25 °C induced a fracture of more than 4 m long and more than 1 m deep. XFEM was able to capture the fracture propagation and fracture aperture without the need for mesh refinement or adapting the fracture geometry to the finite element mesh. This technique will become even more attractive in conditions where the fracture propagation direction is difficult to predict in

advance. This is the advantage of using XFEM compared to the classic modeling approach using finite element method, which is not able to model the fracture opening and is therefore limited to identifying the locations of first fractures.

The injection of cold water into a rock mass through a wellbore was shown to lead to the propagation of fractures, even under high compressive stresses. Under anisotropic stress conditions, the cooling of the wellbore leads to the initiation of multiple fractures but only fractures that are perpendicular to the minimum principal stress continue to propagate and become the dominant fractures. Under an isotropic stress state, all the initially induced fractures continue to grow radially in a symmetric manner. The study of the influence of the temperature of the injected fluid on the thermal fractures showed that the injected fluid temperature has a less pronounced effect due to the low thermal conductivity of the surrounding rock mass.

Chapter 4

Simulation of fracture propagation and fault slip due to hydraulic stimulation

RÉSUMÉ

Ce chapitre est consacré à l'étude de la propagation des fractures hydrauliques et du glissement des failles préexistantes dans les roches ignées de faible perméabilité dues à l'injection de fluide. Une partie de cette étude à fait l'objet de la publication (Ngo et al., 2019).

Le problème concerne les changements de température, l'écoulement des fluides dans l'espace poreux et dans les fractures hydrauliques ou failles, ainsi que la déformation du massif rocheuse. Les changements de température peuvent cependant avoir certains effets mais ne sont pas couplés à l'analyse et ne sont pas pris en compte ici en raison de la complexité qui en résulterait. Pour prendre en compte l'effet thermique, une procédure de simulation séquentielle telle que présentée au chapitre 3 peut être utilisée en première approximation. Dans ce chapitre, nous nous concentrons exclusivement sur les effets hydromécaniques. Toutes les simulations numériques présentées dans ce chapitre sont effectuées à l'aide du package d'éléments finis ABAQUS. Le modèle de zone cohésive en combinaison avec les éléments cohésifs est exclusivement utilisé pour modéliser les fractures hydrauliques et les failles préexistantes. Bien que le XFEM soit capable de faire le même travail, il requiert beaucoup plus d'efforts pour obtenir une solution précise et des problèmes de convergence se posent souvent.

Tout d'abord, je vais étudier des modèles de fracture hydraulique classique. Le modèle de déformation plane KGD et le modèle axisymétrique en forme de penny sont étudiés. Les

résultats des simulations sont ensuite comparés aux solutions analytiques présentées dans la sous-section 2.5.2 du chapitre 2. L'objectif principal de cette section est de démontrer la capacité de la technique de l'élément cohésif et de mieux comprendre tous les aspects numériques (par exemple, la technique de régularisation visqueuse, le maillage et paramètres numériques pour l'élément cohésif) à prendre en compte pour obtenir une solution précise au problème hydromécanique couplé.

Ensuite, j'étudierai la propagation d'une fracture hydraulique dans un milieu rocheux contenant une faille préexistante. Le comportement de glissement de la faille, après que la fracture hydraulique l'ait rencontrée, est soigneusement étudié. Ce scénario est une version simplifiée des conditions géologiques pouvant être rencontrées dans les substratums de roches ignées ciblés pour le développement des réservoirs géothermiques profonds. Certains des aspects les plus importants qui peuvent influencer le glissement de la faille sont examinés. Ceux-ci incluent le coefficient de frottement de la faille, le débit auquel le fluide est injecté ainsi que l'orientation de la faille par rapport aux contraintes in-situ initiales. Plusieurs conclusions générales sur le rôle de ces paramètres sont tirées.

Enfin, une configuration plus complexe dans laquelle sont présentées de multiples fractures hydrauliques et de plusieurs failles préexistantes est étudiée, afin d'étendre les conclusions obtenues pour le cas d'une fracture hydraulique et d'une faille unique à un cas plus général.

SUMMARY

This chapter is dedicated to the study of the propagation of hydraulic fractures and the slip of pre-existing faults in low-permeability igneous rocks due to fluid injection. The problem involves temperature changes, fluid flow both in the porous space and the hydraulic fractures/faults, and deformation of the rock mass. Temperature changes may exert some effects but are not coupled to the analysis and are not considered here because of the complexity that would be added. To account for the thermal effect, a sequential simulation procedure as presented in Chapter 3, which is used as a first approximation. In this chapter, the focus is exclusively on the hydro-mechanical effects. All the numerical simulations in this chapter were done using the ABAQUS finite element package. The cohesive zone model in combination with cohesive elements is exclusively used to model the hydraulic fractures and the pre-existing faults. Although the XFEM is able to do the same job, it requires much more effort to obtain an accurate solution and convergence issues often arise.

Firstly, the propagation of a single hydraulic fracture in a low-permeability poroelastic medium is simulated. Both the KGD plane strain model and the axisymmetric penny-shaped model are studied. The simulation results are then compared with the theoretical solutions presented in subsection 2.5.2 of Chapter 2. The main objective of this section is to demonstrate the capability of the cohesive element technique and to gain insight into all numerical aspects (e.g, viscous regularization technique, finite element mesh creation, and numerical parameters for the cohesive element) that require attention in order to obtain an accurate solution to the coupled hydro-mechanical problem.

Secondly, the propagation of a hydraulic fracture in rock medium that contains a pre-existing fault is studied. The slip behavior of the fault once it is intersected by the hydraulic fracture is carefully investigated. This scenario is a simplified version of the geological conditions that might be encountered in igneous basements targeted for the development of deep geothermal reservoirs. Some of the most important aspects that could influence the fault slip are examined. These include the fault friction coefficient, the rate at which fluid is injected, and the orientation of the fault with respect to the initial stresses. Several general conclusions on the role of these aspects are drawn.

Finally, a more complex configuration in which multiple hydraulic fractures and multiple pre-existing faults are present is studied to investigate whether the conclusions obtained for the case with a single hydraulic fracture and a single fault are an exception or a more general universal trend.

4.1 SIMULATION OF THE PROPAGATION OF A SINGLE HYDRAULIC FRACTURE

In this section, two single hydraulic fracture models, the KGD plane strain and the axisymmetric penny-shaped models, are studied. The numerical results are then compared with the analytical solutions presented in subsection 2.5.2 of Chapter 2. The cohesive zone model in combination with cohesive elements is used to model the fracture propagation. In order to make the numerical results comparable to the analytical solutions, the model dimensions and several material properties are chosen such that all the assumptions made to obtain the analytical solutions are satisfied. For instance, the dimensions of the model are much larger than the fracture dimensions (e.g., length and aperture) to limit the effect of model boundaries. The cohesive properties are selected such that the cohesive zone is small relative to the fracture length. This ensures that the fracture propagation modeled using the cohesive zone model is equivalent to that modeled in the analytical solutions using the theory of linear elastic fracture mechanics. The permeability is also defined to minimize the poroelastic effects since these effects are not considered in the analytical solutions. This section only analyzes and presents results for the toughness/storage-dominated regime of propagation (near vertex *K* in Figure 2.15). Models for the viscosity/storage-dominated regime (near vertex *M*) can be readily obtained based on the models for vertex *K* by adjusting the viscosity of the fluid.

4.1.1 Plane strain KGD model

4.1.1.1 Geometry and finite element mesh

The model studied consists of a vertical fracture that propagates in a poroelastic medium as illustrated in Figure 4.1a. As the fracture is under plane strain conditions, a 2D plane strain model, as shown Figure 4.1b, can be used for the simulation without compromising the accuracy.

The 2D domain has dimensions of width W and height B. These dimensions are chosen such that the maximum fracture length is expected to be less than one half of the width W. The numerical model also requires the presence of an initial crack in order to incorporate the physics for the fluid flow in the fracture. The model dimensions and the length of the initial crack are summarized in Table 4.1.

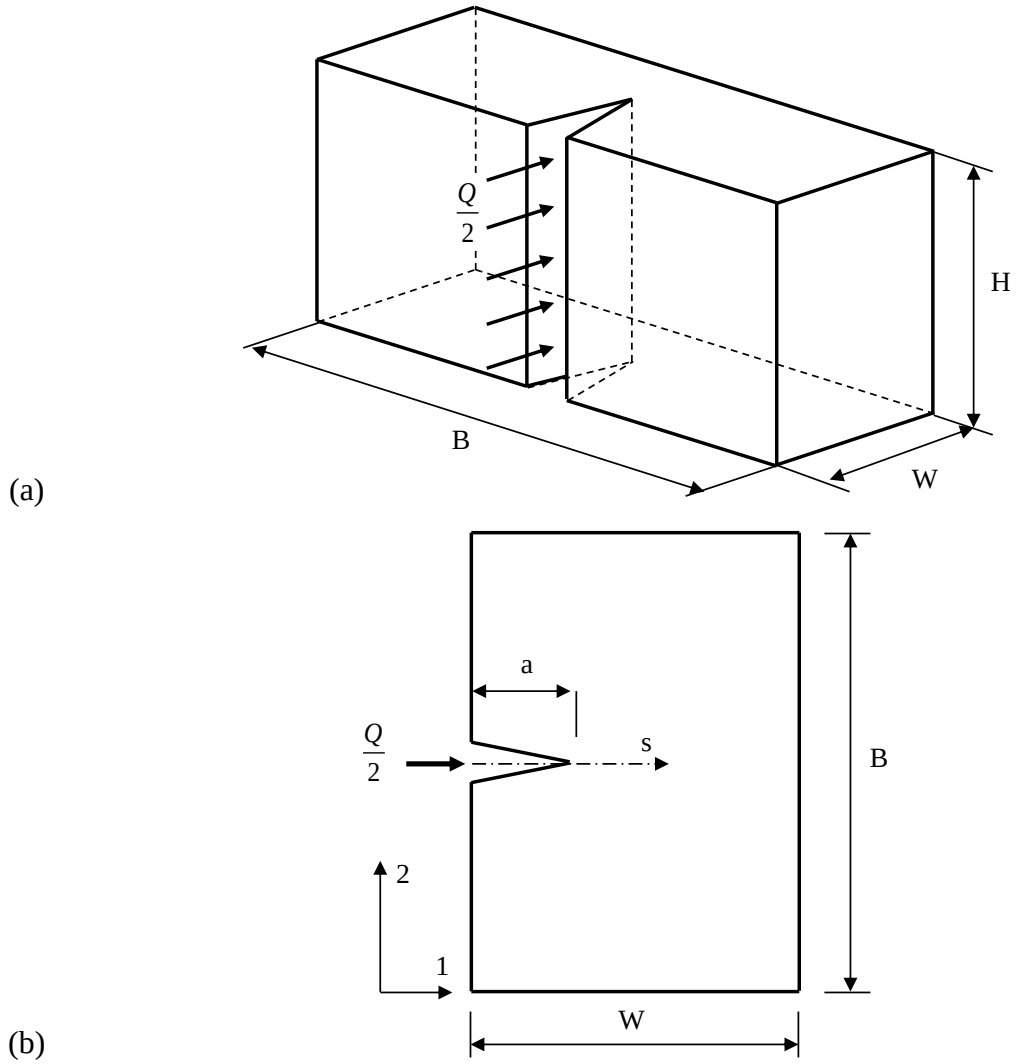

Figure 4.1 KGD model: (a) 3D domain with a vertical fracture, (b) 2D plane strain model used for simulation. *a* is the initial fracture length and *s* is the curvilinear coordinate along the fracture.

Table 4.1 Dimensions of the 2D plane strain KGD model

Dimension	**Value**
Width	W = 45 m
Height	B = 60 m
Initial crack length	a = 5 cm

The poroelastic medium is discretized by linear plane strain coupled pore fluid pressure/deformation continuum elements CPE4RP in ABAQUS (i.e., 4-node elements that

have both displacements and pore pressure as degree of freedom (DOF)), while the fracture is modeled by a thin layer of cohesive material that is discretized by coupled fluid pressure/deformation cohesive elements COH2D4P (i.e., elements with nodes at four corners that have both displacements and pore pressure as DOF and two mid-edge nodes that have only fluid pressure as DOF). The continuum elements and the cohesive elements are connected through shared nodes. Figure 4.2 illustrates the finite element mesh used.

The mesh is refined near the fracture plane where high gradients of stress and pore pressure are expected. In order to obtain accurate results when using cohesive elements, the traction in the cohesive zone ahead of the fracture tip must be properly represented. This requires the size of the cohesive elements to be small relative to the size of the cohesive zone. In other words, the cohesive zone must to be discretized into multiple cohesive elements. The length of the cohesive zone and the size of the cohesive element are defined as L_{cz} and L_e, respectively; the number of cohesive elements in the cohesive zone is:

$$N_e = \frac{L_{cz}}{L_e} \tag{4.1}$$

The length of the cohesive zone L_{cz} can be calculated from the properties of the cohesive material as (Turon et al., 2007):

$$L_{cz} = M \frac{EG_{IC}}{R_T^2} \tag{4.2}$$

where E is the Young's modulus of the rock mass; G_{IC} and R_T are the Mode I fracture energy and the tensile strength of the cohesive material, respectively; M is a constant. Several authors have proposed different values for M; in general, M can vary from 0.21 to 1 (Barenblatt, 1962; Hillerborg et al., 1976; Turon et al., 2007).

According to (Turon et al., 2007), three cohesive elements in the cohesive zone are sufficient to obtain accurate results. In all the simulations presented here, this suggestion is followed and a conservative value of M = 0.21 is used. In most cases, the cohesive zone is discretized with up to ten cohesive elements.

Following the guidance above and with the selected material properties presented in the next section, the finite element mesh was generated. Elements of size 5 cm are used close to the fracture, while elements of up to 5 m are used near the boundaries. In total, the mesh has 7076 nodes and 6603 elements.

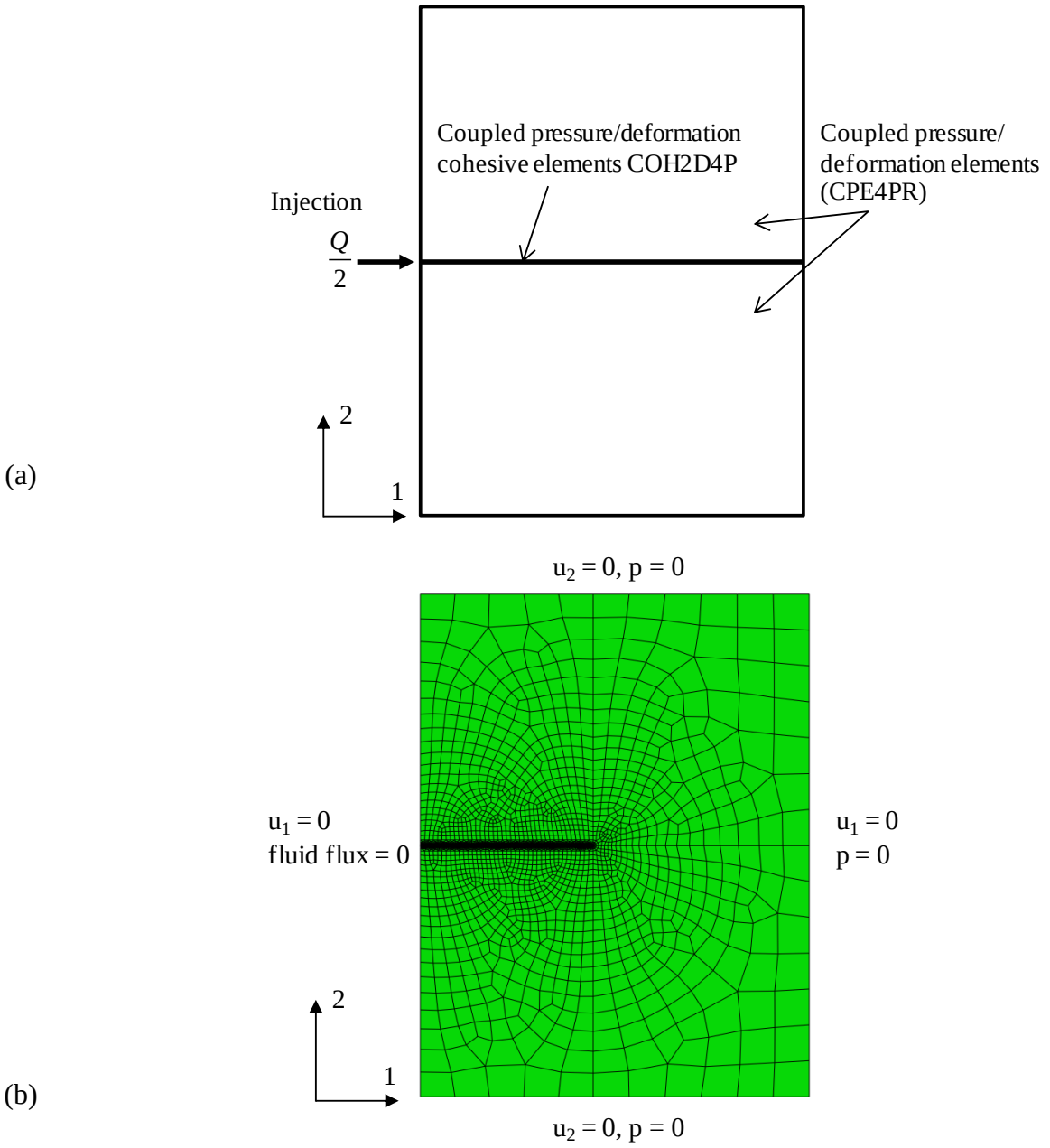

Figure 4.2 Finite element mesh for the KGD model: (a) Meshing scheme, (b) Actual finite element mesh with 7076 nodes and 6603 elements, and boundary conditions. Note: u_1 and u_2 are displacements in direction 1 and 2, respectively; p is the pore pressure

4.1.1.2 Material properties and injection rate

The material properties typical for granitic rock masses were chosen and are summarized in Table 4.2. The fluid is injected at a constant rate Q = 0.001 m^3/s over 20 seconds. The leakoff coefficient is set to zero, which ensures a storage-dominated regime of propagation.

Table 4.2 Material properties used for the KGD model

Property	**Value**	**Source / Comment**
Poroelastic medium		
Young's modulus	E = 30 GPa	Keshavarz (2009)
Poisson's ratio	$\nu = 0.22$	Keshavarz (2009)
Biot's coefficient	b = 0.9	Typical value
Biot's modulus	M = 90 MPa	Typical value
Porosity	$\phi = 0.01$	Keshavarz (2009)
Permeability	$k = 1.1 \times 10^{-16}$ m^2	Use very small value
Cohesive material		
Tensile strength	$R_T = 1.25$ MPa	Typical value
Critical stress intensity factor	$K_{IC} = 2.17$ MPa.$m^{0.5}$ ($G_{IC} = 150$ N/m)	Typical value
Fracturing fluid and fluid in the porous space		
Fluid viscosity	$\eta = 2 \times 10^{-5}$ Pa.s	Very small value
Fluid specific weight	$\gamma = 9800$ N/m^3	

Using the selected parameters, the dimensionless number *K* is calculated according to equation (2.80) as:

$$K = \frac{K'}{\left(E'^3 \mu' Q_0\right)^{1/4}} = \frac{4\left(\frac{2}{\pi}\right)^{0.5} \times 2.17 \times 10^6}{\left[\left(\frac{30 \times 10^9}{1-0.22^2}\right)^3 \times 12 \times 2 \times 10^{-5} \times 10^{-3}\right]^{1/4}} = 4.19$$

$K = 4.19 > 4$ ensures that the fracture will propagate in the toughness-dominated regime (see subsection 2.6.1.1).

4.1.1.3 Initial and boundary conditions

The poroelastic medium is assumed to be initially fully saturated with zero initial stress in all directions. The initial pore pressure can have an arbitrary value, but is set to zero in this simulation.

The boundary conditions are illustrated in Figure 4.2b. Constant pore pressure is maintained at the boundaries, except for the left boundary where a no fluid flow condition is enforced, which implies that the left edge of the model is a symmetric boundary. A zero-displacement condition is imposed for the normal direction of all boundaries.

4.1.1.4 Convergence issues and viscous regularization

Modeling fracture propagation using cohesive elements involves the progressive stiffness degradation and a softening response of the cohesive material, which are both known to lead to convergence difficulties. A common technique to avoid these problems and aid convergence is the use of viscous regularization of the constitutive equations, which allows the tangent stiffness matrix of the softening material to be positive for sufficiently small time increments.

The regularization process involves the use of a viscous stiffness degradation variable, D_v, which is defined as:

$$\dot{D}_v = \frac{1}{\mu}\left(D - D_v\right) \tag{4.3}$$

where μ is the numerical viscosity (s^{-1}) that represents the relaxation time of the viscous system and D is the actual damage variable evaluated in the backbone model (see equations (2.93)). The damaged cohesive response is then given by:

$$t = (1 - D_v)t_p \tag{4.4}$$

where t can be the normal or shear stresses of the damaged cohesive elements; t_p is the corresponding predictor that is estimated with the strain as if the cohesive material is undamaged.

Using this viscous regularization technique, the stresses on the damaged cohesive elements are allowed to be outside the limits set by the cohesive traction-separation law. However, these stresses will converge to those in the case without viscous regularization when $t/\mu \to \infty$, where t represents time.

Some of the energy of the system is dissipated due to the use of the viscous regularization. To ensure the accuracy of the solution results, the dissipated energy associated with the viscous regularization must be small compared to the damage energy of the cohesive elements. The final solution results may be altered if this criterion is not met. A numerical viscosity $\mu = 10^{-4}$ s^{-1} is used in this simulation.

4.1.1.5 Results and discussions

The time evolution of the hydraulic aperture at the injection point, the injection pressure, and the fracture length is presented in Figure 4.3, while the variation of the hydraulic aperture along the fracture at different times (5 s, 10 s, and 20 s) is presented in Figure 4.4. In these figures, the simulation results are compared with analytical solutions. Good agreement between the simulation results and the analytical solutions was found for all quantities. The final fracture length is approximately 20 m, which is less than one half of the width of the model as expected (the width of the model is W = 45 m).

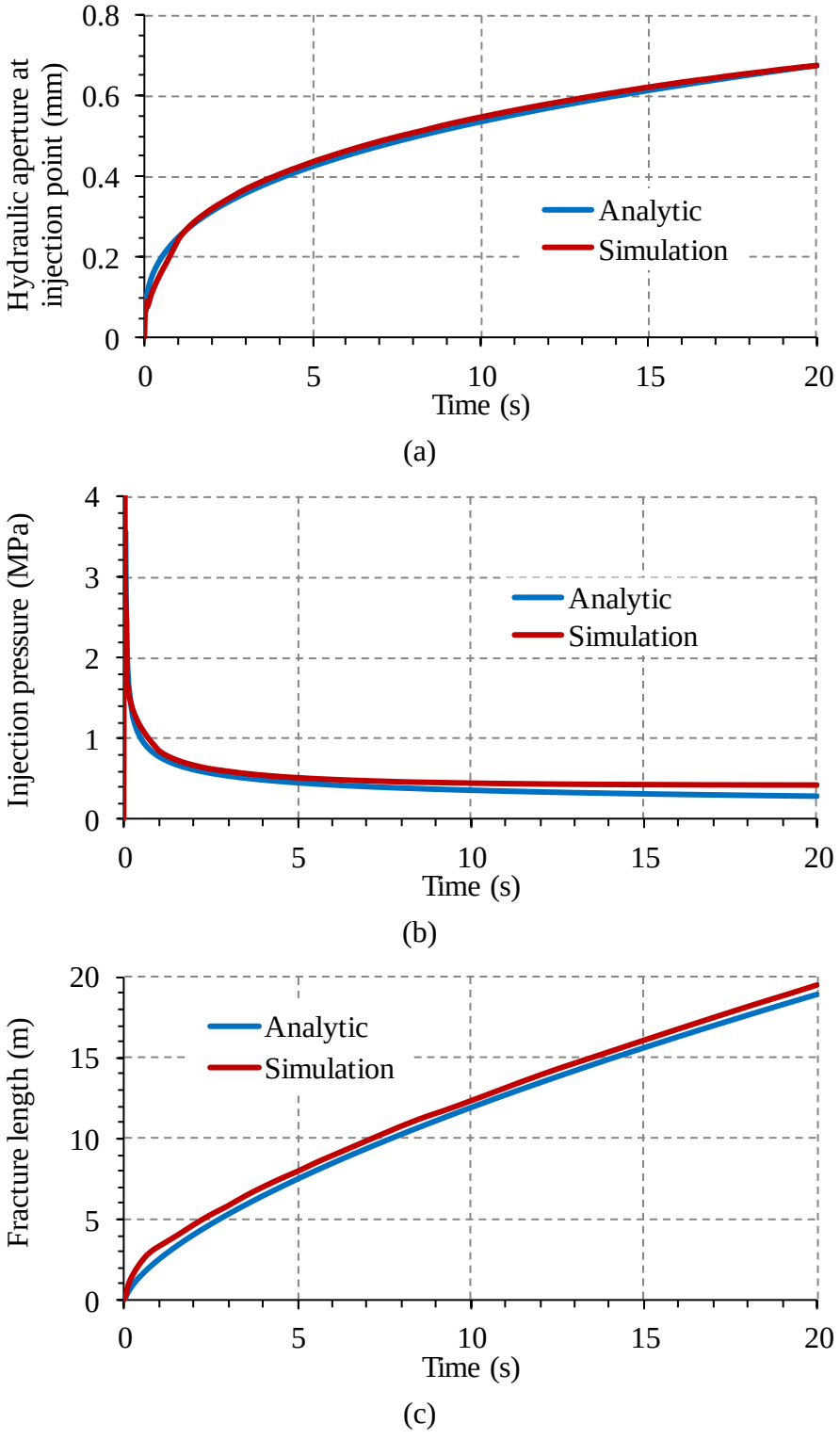

Figure 4.3 Time evolution of (a) hydraulic aperture at injection point, (b) injection pressure, and (c) fracture length

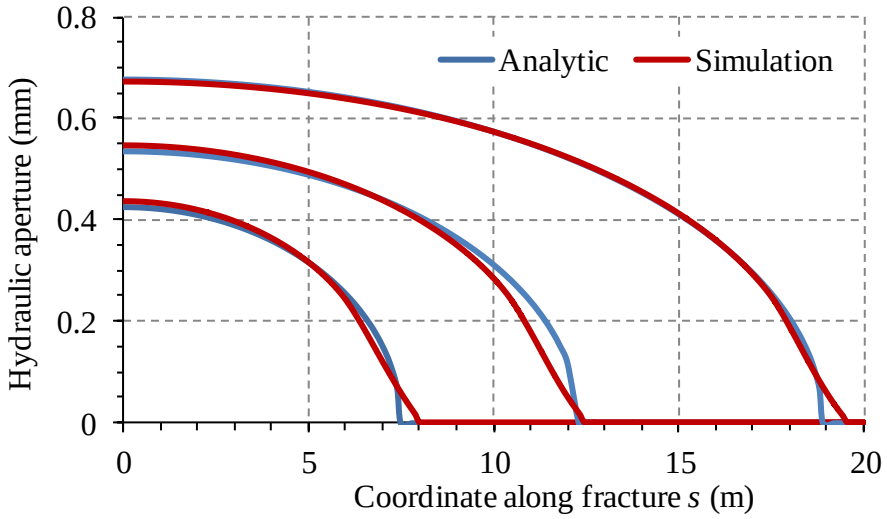

Figure 4.4 Variation of the hydraulic aperture along the fracture at 5 s, 10 s, and 20 s. The injection point is located at $s = 0$

Figure 4.5 displays the variation of the fluid pressure in the fracture and the stress normal to the fracture plane along the fracture. It can be seen in Figure 4.5a that the fluid pressure is nearly uniform along the fracture because the energy dissipated by the viscous flow of the fluid in the fracture is negligible. The effective normal stress (Figure 4.5b) is zero where the fracture has been created, gradually increases in the cohesive zone and peaks at the tip of the fracture with a peak value equal to the tensile strength of the cohesive material (i.e., 1.25 MPa). The effective normal stress then decreases rapidly with the distance from the fracture tip and eventually equals the in-situ stress, which is set to zero in this simulation. The length of the cohesive zone can be obtained from Figure 4.5b and is approximately 2 m. This value is larger than the value obtained by using equation (4.2), which is 0.6 m. This means that using equation (4.2) with the coefficient $M = 0.21$ to estimate the size of the cohesive zone is rather conservative. When a cohesive zone of 2 m long is discretized into 5-cm cohesive elements, there are 40 cohesive elements in the cohesive zone, which surpasses the requirement of three cohesive elements

The spatial distribution of pore pressure and effective stress in direction 2 is presented in Figure 4.6 and Figure 4.7, respectively. The uniform distribution of fluid pressure along the fracture and the stress concentration in the region near the tip of the fracture can be clearly observed.

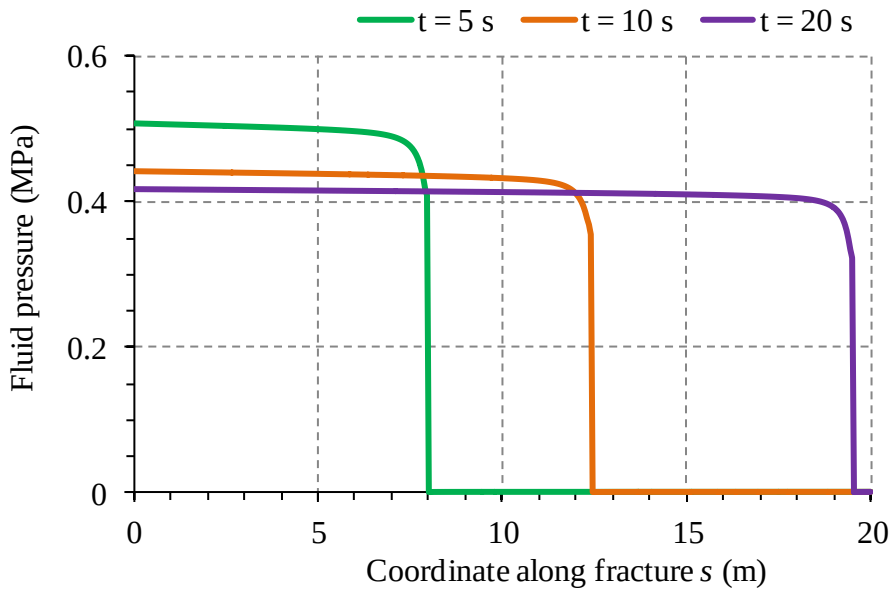

(a)

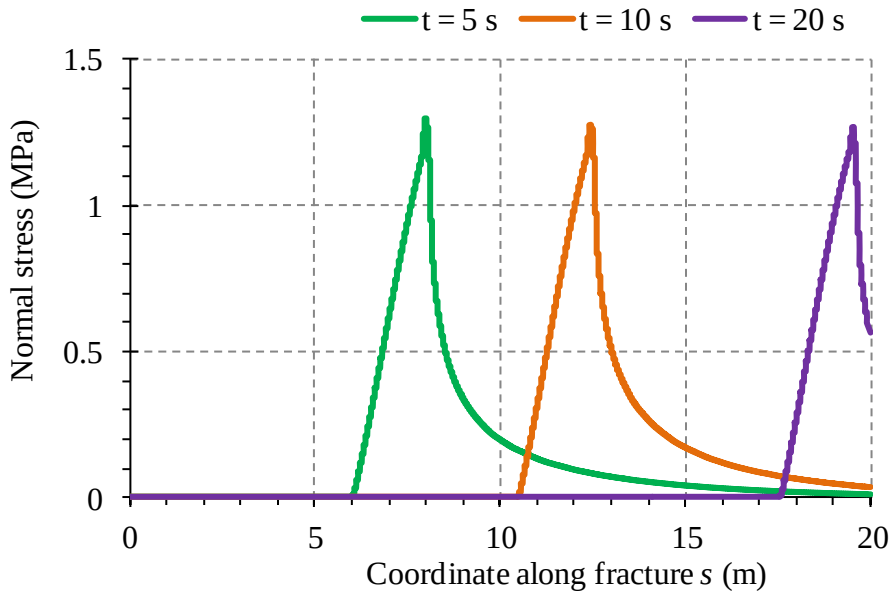

(b)

Figure 4.5 Simulated variation of (a) the fluid pressure inside the fracture and (b) the stress normal to the fracture plane at different times (The injection point is located at $s = 0$)

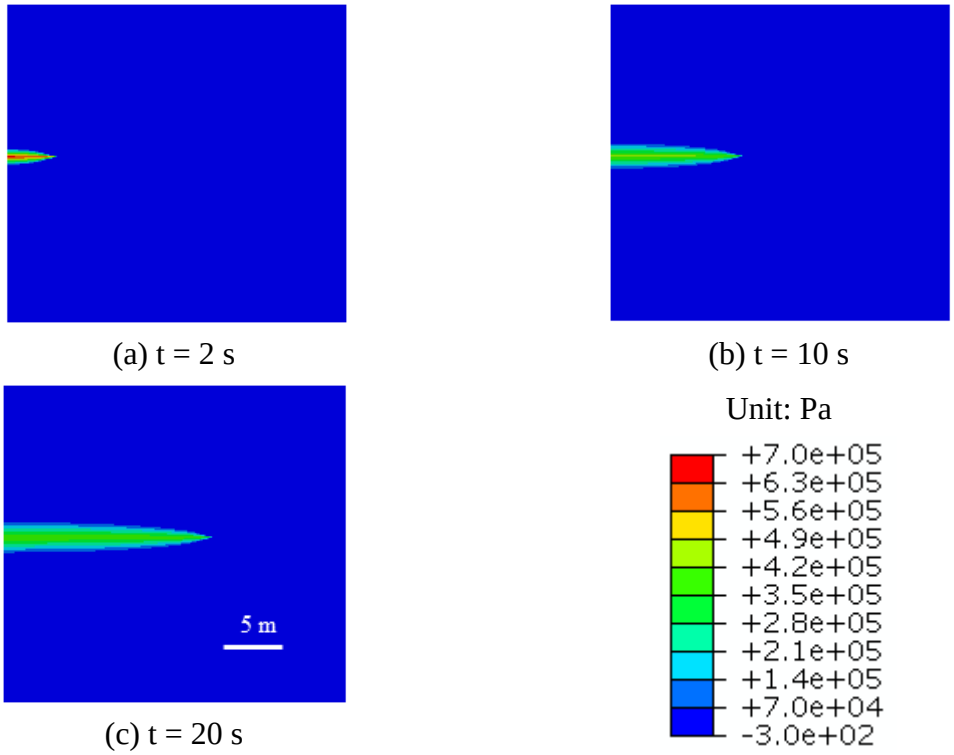

Figure 4.6 Simulated spatial distribution of pore pressure at different times

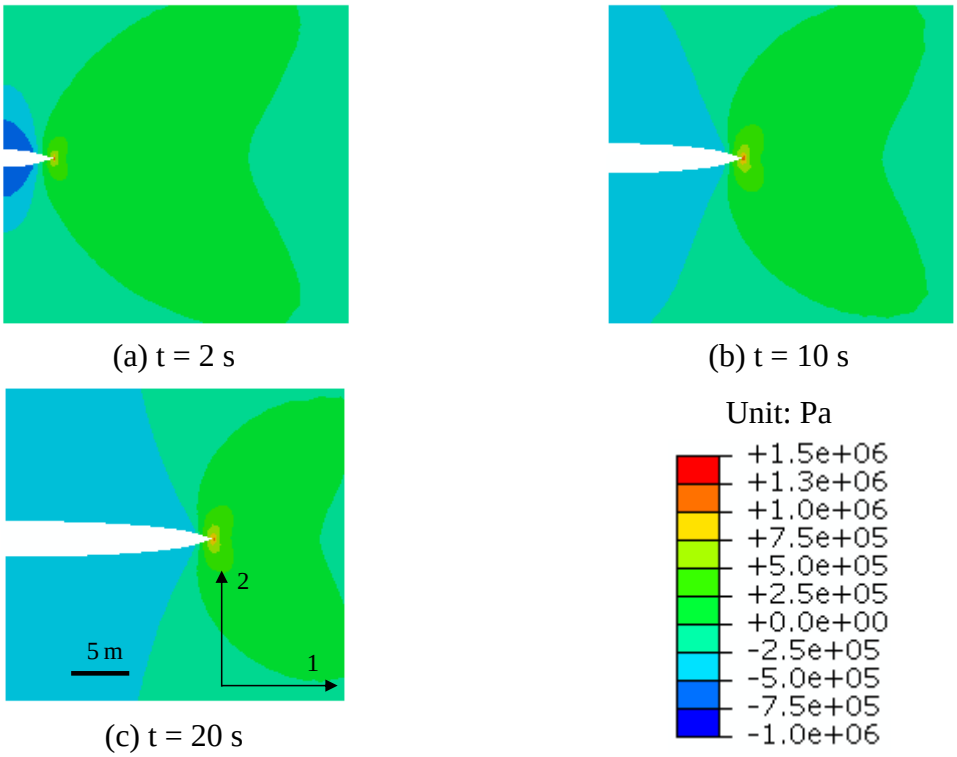

Figure 4.7 Simulated spatial distribution of effective normal stress in direction 2 at different times (Deformation in direction 2 was scaled up 5000 times)

The damage energy and the dissipated energy associated with the viscous regularization are presented in Figure 4.8. It can be seen that the viscous regularization dissipation is very small compared to the damage energy. The ratio between these two energies is approximately 1/150 at t = 20 s.

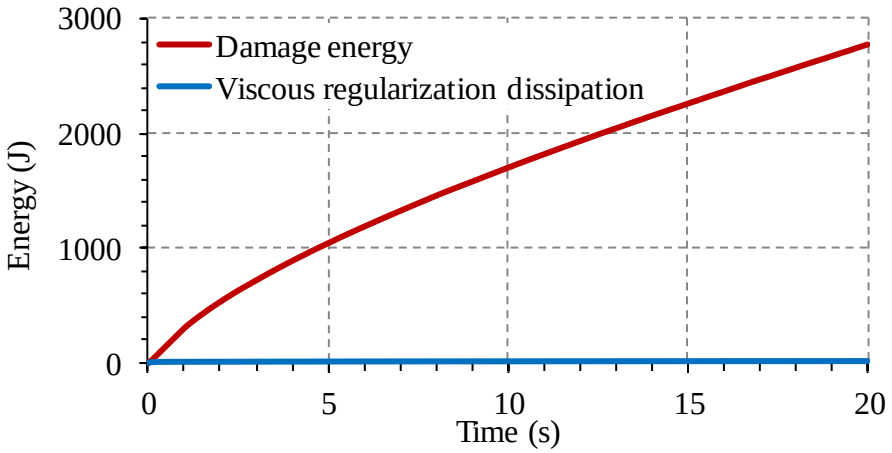

Figure 4.8 Damage energy and viscous regularization dissipation (for numerical viscosity $\mu = 10^{-4}$ s^{-1})

To assess the effect of the viscous regularization on the simulation results, the above simulation was re-run with a numerical viscosity $\mu = 10^{-2}$ s^{-1}. The results of the re-run simulation for damage energy – the dissipated energy associated with viscous regularization, and the hydraulic aperture at the injection point are presented in Figure 4.9. It can be seen that the dissipated energy associated with viscous regularization is approximately 17% of the damage energy (Figure 4.9a). The simulated hydraulic aperture is much higher than the analytical value. This shows that an over-large value for the numerical viscosity can alter the simulation results. Thus, care must be taken when viscous regularization is used. Simulations should start with a small numerical viscosity, e.g., 10^{-4} s^{-1}, and the ratio between the dissipated energy associated with viscous regularization and the damage energy should be relatively small.

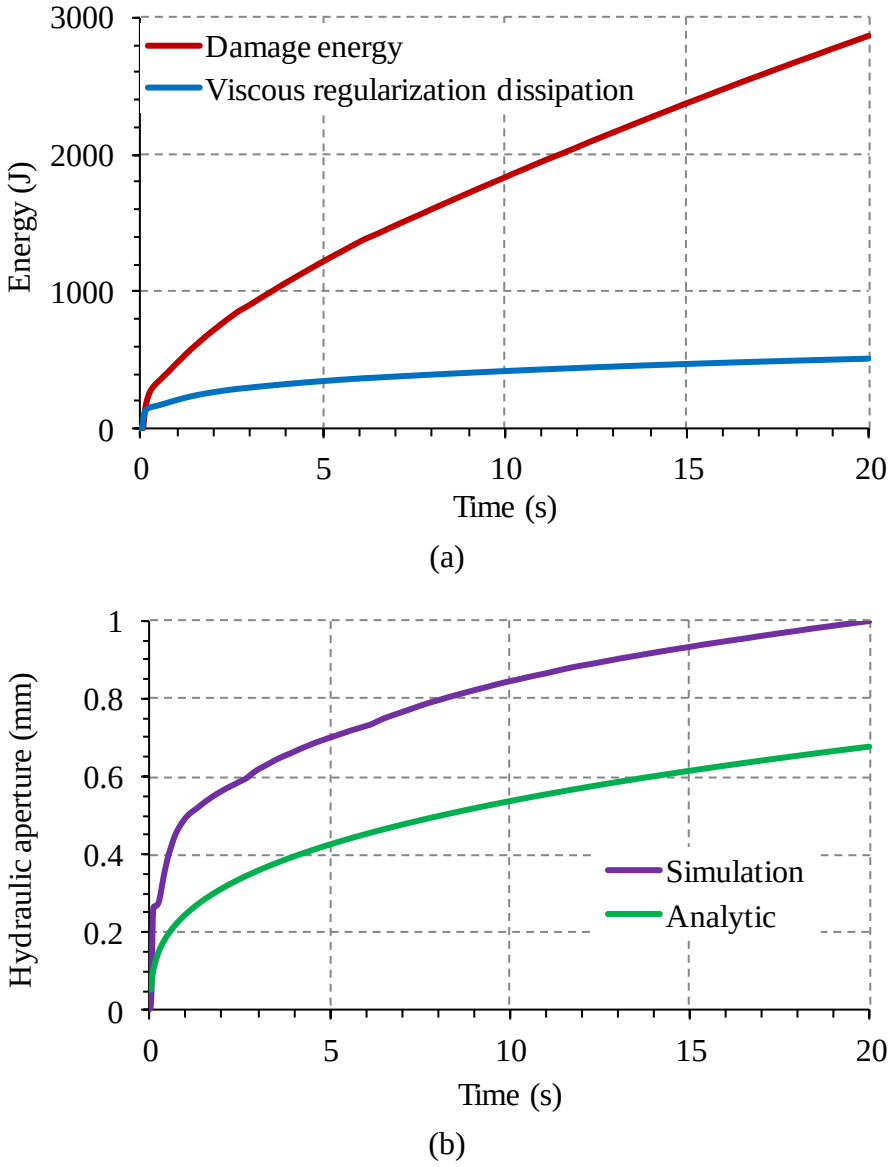

Figure 4.9 Simulation results with a numerical viscosity $\mu = 10^{-2}$ s^{-1}: (a) Damage energy and dissipated energy associated with viscous regularization, (b) Hydraulic aperture at injection point

4.1.2 Penny-shaped model

4.1.2.1 Model setup

The penny-shaped fracture model is a three-dimensional model in which the fracture grows radially due to the injection of fluid at the center of the fracture. Since the model is symmetric about an axis that passes through the injection point and is normal to the fracture plane, a two-dimensional axisymmetric model can be used for sake of simplicity. The 2D domain used has

dimensions of radius R and height H and is shown in Figure 4.10. A small initial crack is necessary to allow the resolution of the equation of fluid flow in the fracture. The dimensions of the model and the length of the initial crack are chosen so that the model boundaries have negligible effects on the fracture propagation. The selected dimensions are summarized in Table 4.3 and are identical to those used in the KDG model.

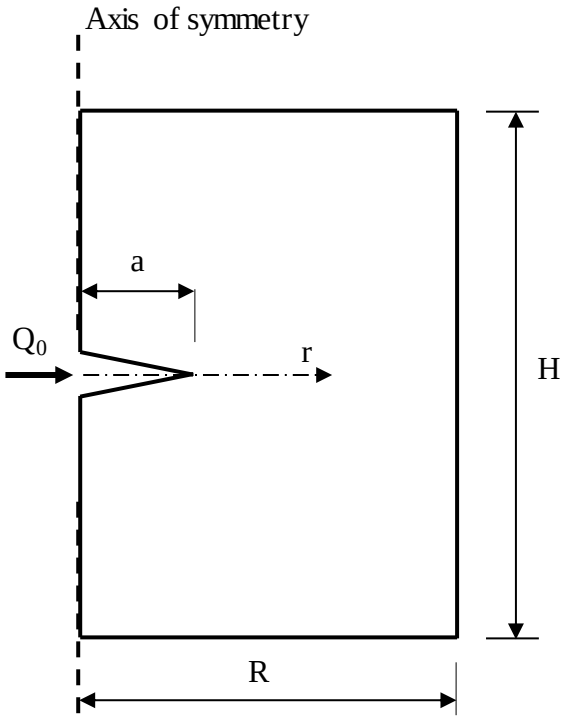

Figure 4.10 2D axisymmetric model used for simulation of penny-shaped fracture model

Table 4.3 Dimensions of the 2D axisymmetric model

Dimension	**Value**
Width	R = 45 m
Height	H = 60 m
Initial crack length	a = 5 cm

A finite element mesh identical to that of the KGD model is used (Figure 4.2b). However, in this case the poroelastic medium is discretized by linear axisymmetric coupled pore fluid pressure/deformation continuum elements CAX4RP and the fracture is modeled by axisymmetric coupled fluid pressure/deformation cohesive elements COHAX4P.

The material properties, initial conditions, and boundary conditions are identical to those previously used for the KGD model. The fluid is injected at constant rate of 0.001 m^3/s over 40 s. With the selected parameters, the dimensionless number K, calculated according to equation (2.86), is equal to 3.5 at t = 0.01 s. This ensures that the fracture will propagate in the toughness-dominated regime for most of the injection duration as intended. In fact, the viscosity-dominated and transition regimes only last 0.01 s from the beginning of the injection, which is negligible compared to the total injection time of 40 s. To aid convergence, a numerical viscosity $\mu = 10^{-4}$ s^{-1} is also used.

4.1.2.2 Results and discussions

Simulation results and analytical predictions for the hydraulic aperture at the injection point, the injection pressure, and the fracture radius are presented in Figure 4.11, with good agreement for all three quantities. The final fracture radius is approximately 6.8 m, which is much smaller than the radius of the model (R = 45 m), which ensures that the model boundaries have a negligible effect on the simulation results.

Figure 4.12 displays the variation of the fluid pressure in the fracture and the effective stress normal to the fracture plane along the fracture radius. As in the case of the KGD model, the fluid pressure is nearly uniform along the fracture radius due to the negligible viscous dissipation. The effective stress normal to the fracture plane is zero where the fracture has been created, increases in the cohesive zone and peaks at the tip of the fracture with a peak value approximately equal to the tensile strength of 1.25 MPa (Figure 4.12b).

The contour plots of pore pressure and the effective stress in direction 2 are presented in Figure 4.13 and Figure 4.14, respectively. These figures again confirm the uniform distribution of the fluid pressure in the fracture and the stress concentration in the region near the tip of the fracture.

The damage energy and the dissipated energy associated with viscous regularization are presented in Figure 4.15. It can be seen that the energy associated with viscous regularization is a tiny fraction of the damage energy.

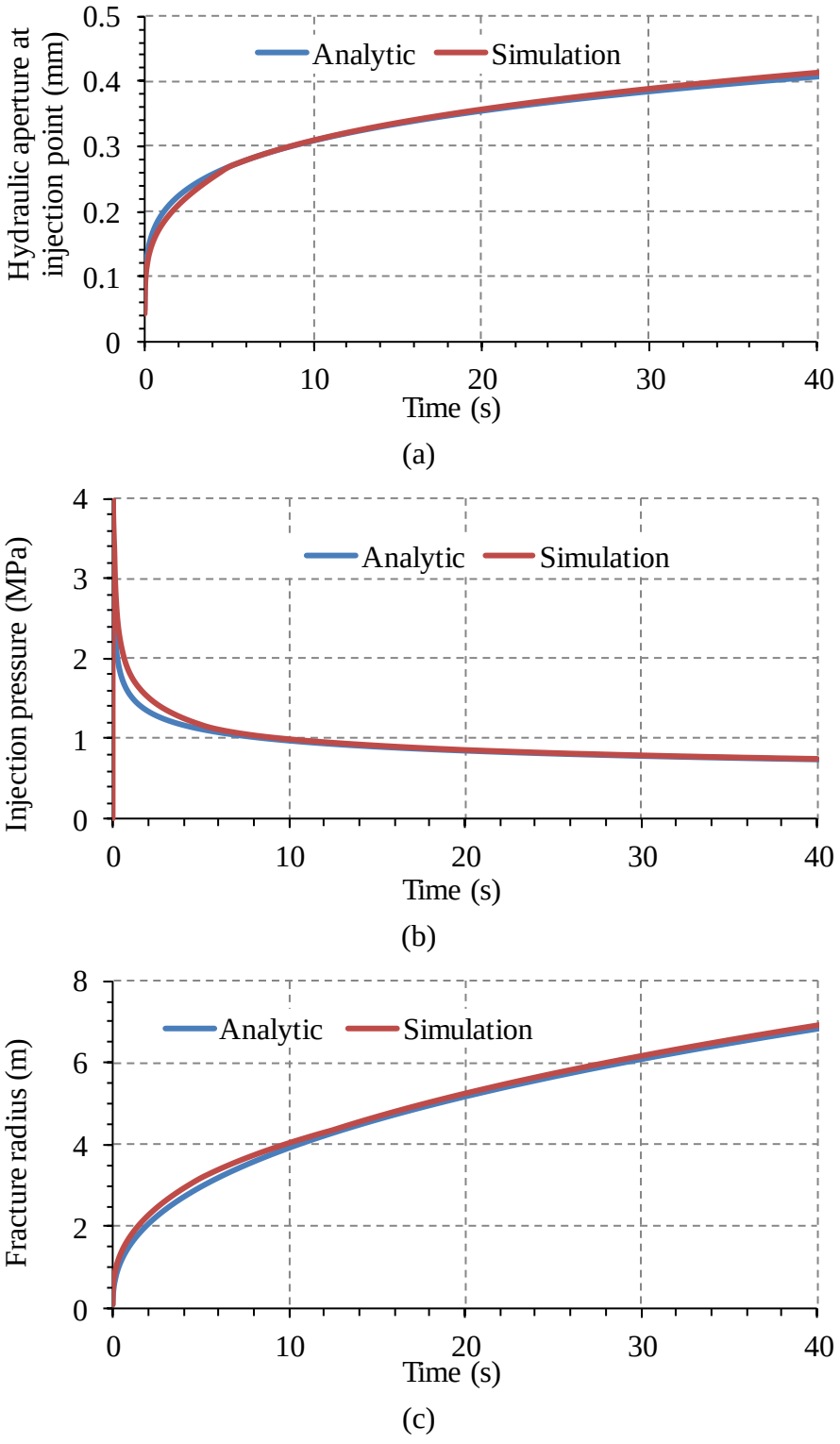

Figure 4.11 Time evolution of (a) hydraulic aperture at the injection point, (b) injection pressure, and (c) fracture radius

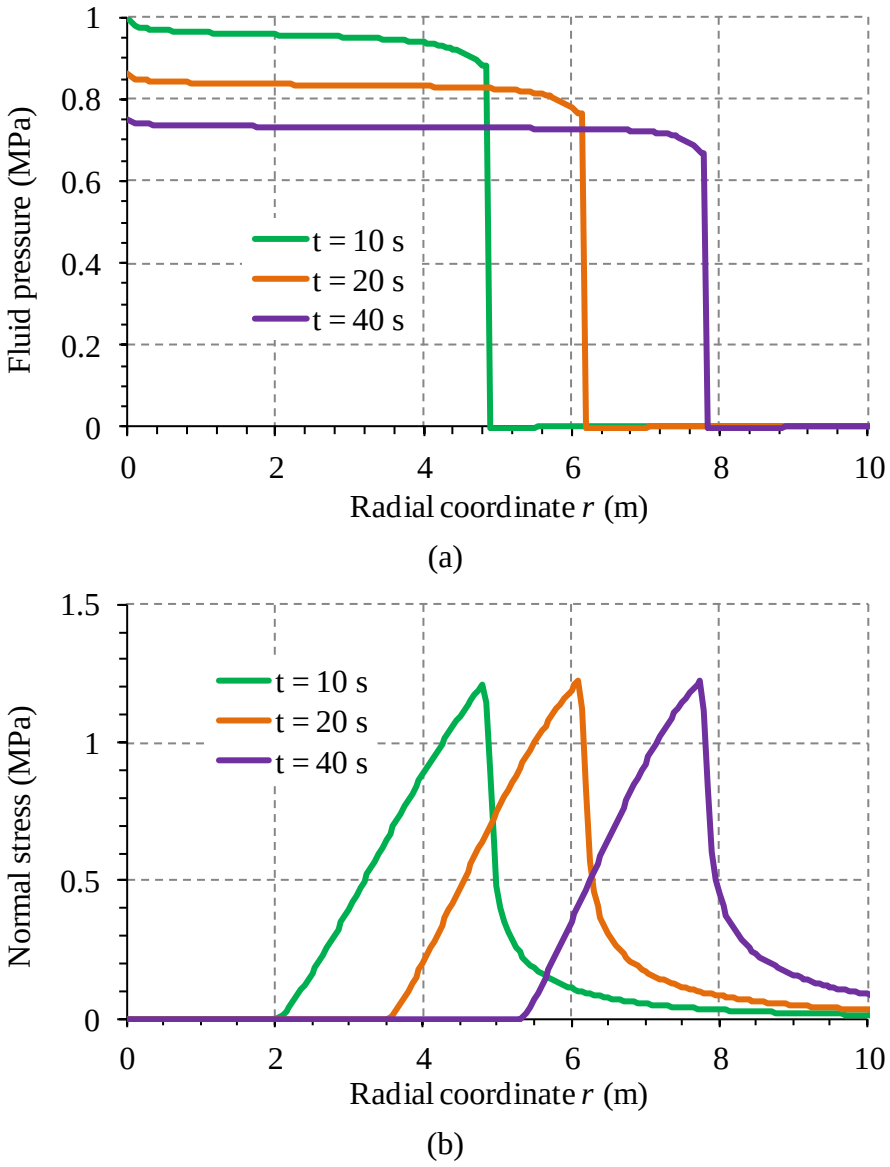

Figure 4.12 Simulated variation of (a) the fluid pressure in the fracture and (b) the stress normal to the fracture plane at 10 s, 20 s, and 40 s (The injection point is located at $r = 0$)

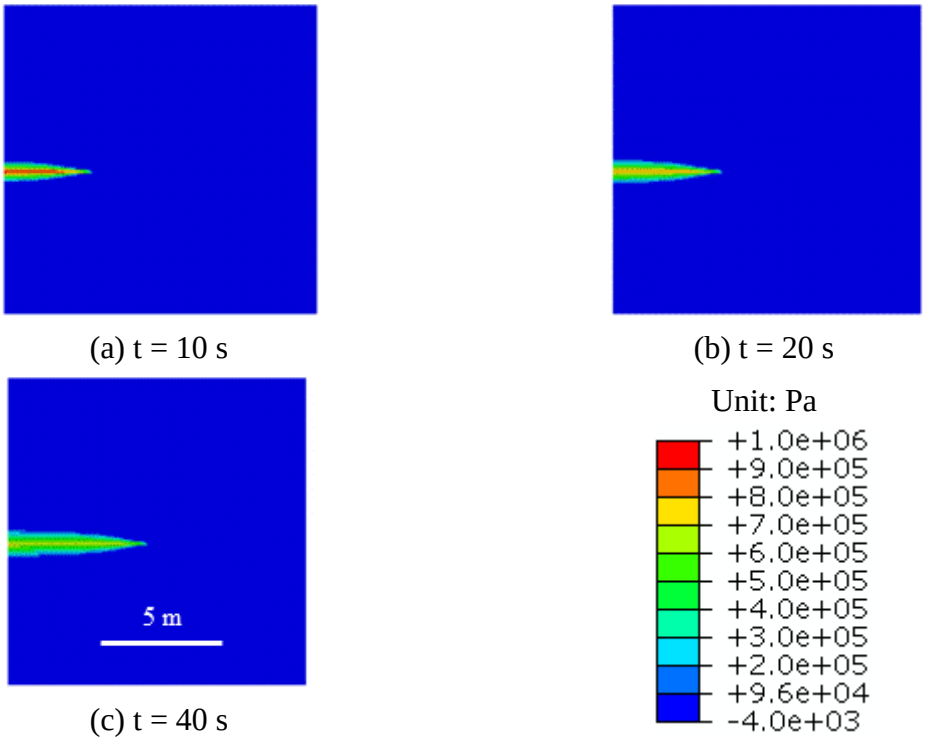

Figure 4.13 Simulated spatial distribution of pore pressure at different times

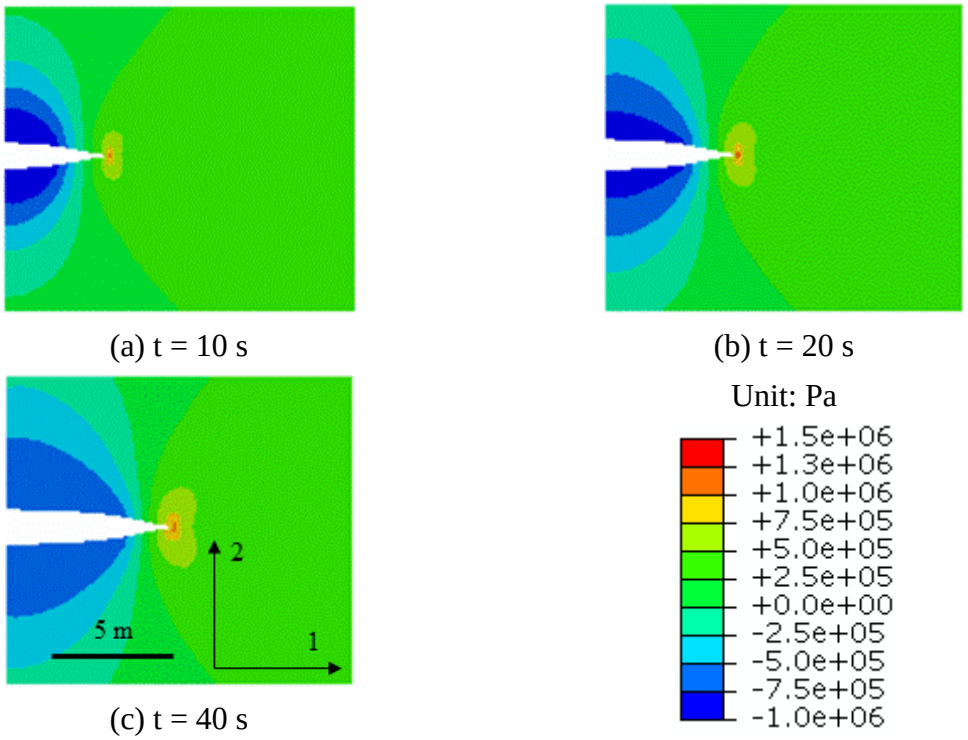

Figure 4.14 Simulated spatial distribution of effective stress in direction 2 at different times. Deformation in direction 2 was scaled up 4000 times.

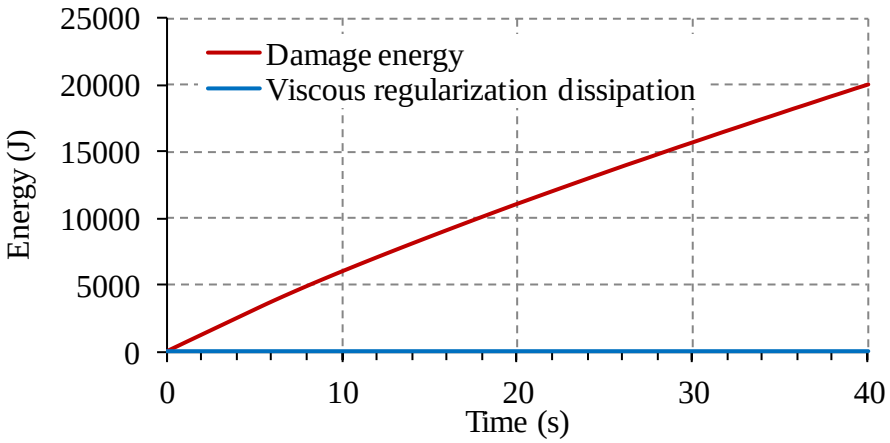

Figure 4.15 Time evolution of damage energy and viscous regularization dissipation

4.1.3 Concluding remarks

In section 4.1 simulations of the two most used hydraulic fracture models are presented - the KGD and the penny-shaped models - using the cohesive element technique. Good agreement between the numerical simulations and analytical predictions was obtained for both models.

Several numerical aspects associated with using cohesive elements for modeling fracture propagation were examined. These include viscous regularization and finite element size. When the viscous regularization technique is used to aid convergence, the dissipated energy associated with viscous regularization should be significantly smaller than the damage energy, while the size of the cohesive element should be small enough to properly characterize the stress in the cohesive zone.

4.2 PROPAGATION OF A HYDRAULIC FRACTURE AND SLIP OF A PRE-EXISTING FAULT

The propagation of a hydraulic fracture in a low-permeability granitic rock mass and the slip of a pre-existing fault are studied in this section. The slip behavior of a fault that has been intersected by a hydraulic fracture is carefully investigated. This scenario was chosen to mimic the geological conditions that may be encountered in igneous faulted basements targeted for the development of deep geothermal reservoirs; faulted areas are known to be a favorable control for geothermal upwelling (Faulds et al., 2010; Meixner et al., 2016). Some of the most

important aspects that may influence fault slip are examined. These include the fault friction coefficient, the rate at which fluid is injected, and the orientation of the fault with respect to the initial stresses (Aochi et al., 2013; Meller and Kohl, 2014; Meller and Ledésert, 2017).

4.2.1 Model setup

A 2D plane strain model is used, consisting of two potential hydraulic fractures HF1 and HF2 and one pre-existing fault F1 (Figure 4.16). This configuration is a simplification of a common pattern known as splay fracture, which results from a fluid driven nucleation and propagation process from a permeable fault (Zhang and Jeffrey, 2016). The model is 120 m wide and 200 m high. The length of fracture HF1 and fault F1 are 10 m and 30 m, respectively. The initial stress state consists of major and minor effective far-field stresses S_h and S_H, which act in directions 1 and 2, respectively. It is worth noting that two fractures HF1 and HF2 are perpendicular to the minor initial stress S_h and the fault F1 is oriented at an angle θ from the major initial stress S_H (hereafter called the orientation angle). The orientation angle is subjected to parametric study later (i.e., θ is changed from 10° to 45°).

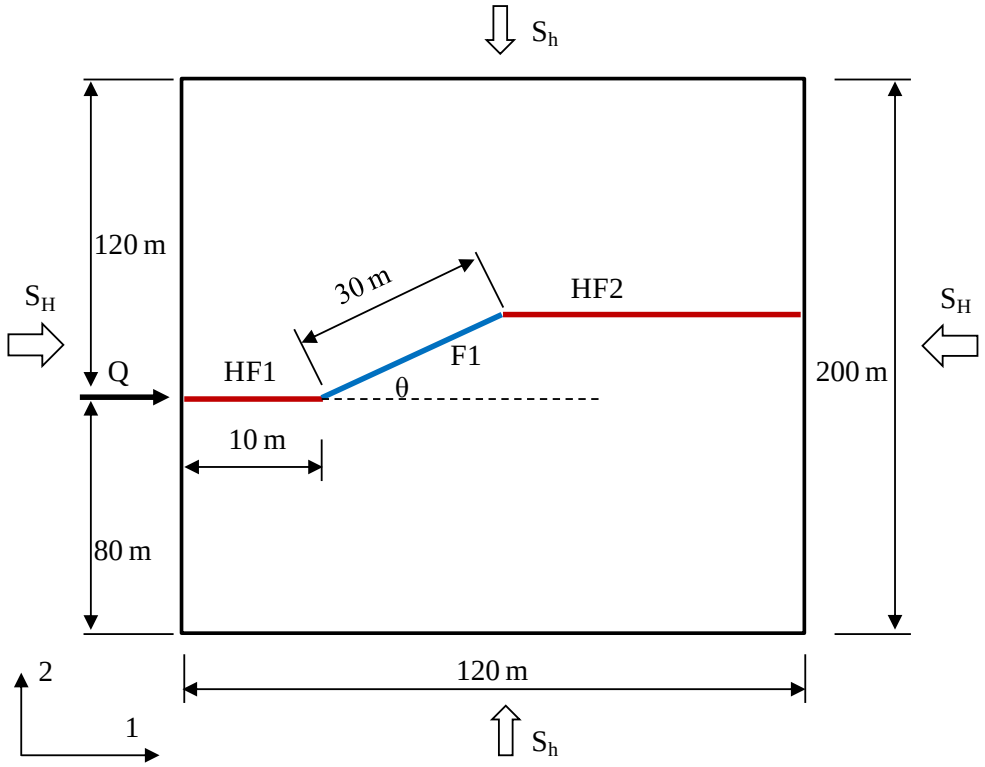

Figure 4.16 Single fault model. The model contains two hydraulic fractures HF1 and HF2 and one pre-existing fault F1. The sketch is not to scale.

The two Mode I fractures HF1 and HF2 are modeled by two layers of intact cohesive material that have similar fracture mechanics properties (i.e., tensile strength and fracture energy). The fault F1 is modeled as a cohesive layer that only has shear strength modeled using the Coulomb friction law. The rock mass has low permeability and is considered to be linear poroelastic.

The stimulation of the system of the fractures and fault is performed by injecting fluid on the left end of the model fracture HF1 (Figure 4.16). The fluid pressurization causes the fracture HF1 to be initiated and propagate. It is assumed that once the newly generated fracture HF1 intersects the fault F1, it is diverted into F1. The injected fluid is thus driven into the permeable fault F1 when intersection occurs, leading to an increase in the fluid pressure in the fault and eventually causing the fault to slip. As the fluid injection continues, a Mode I fracture, i.e., fracture HF2, is initiated from the opposite end of the fault F1. This new fracture might deviate slightly from the direction of the major initial stress S_H in the region near the end of the fault F1 due to stress disturbances caused by the fault but it will eventually align with S_H as it propagates away from the fault, much like tensile or wing cracks do in a strike-slip stress environment. This is the rationale for positioning fracture HF2 in alignement with the stress S_H.

The material properties used in the modeling (i.e., rock mass, cohesive materials, and fracturing fluid), initial stresses, and initial pore pressure are summarized in Table 4.4.

The boundary conditions for the single fault model are illustrated in Figure 4.17. The displacements normal to all the outer boundaries are constrained. The pore pressure is kept constant at its initial value of 23.7 MPa for all outer boundaries, except for the left boundary where no fluid flow condition is imposed. The poroelastic rock mass is assumed to be initially fully saturated (saturation degree equals 1) and remains saturated during the injection time.

To generate the finite element mesh, the rock mass is discretized by linear plane strain coupled pore fluid pressure/deformation continuum elements CPE4RP, while the cohesive layers are discretized by coupled fluid pressure/deformation cohesive elements COH2D4P. At the intersection of two cohesive layers (e.g., HF1 with F1 or F1 with HF2), a mid-edge node with pore pressure as a degree of freedom is shared between those cohesive elements to support

fluid flow continuity (see Section 2.7.2). The mesh is refined around the fractures and the fault (smallest size is 0.05 m) and gradually becomes coarser towards the boundaries (largest size is 10 m). A typical mesh, obtained with an orientation angle θ = 22°, is shown in Figure 4.17. The mesh has 16469 nodes and 15380 elements.

Table 4.4 Parameters used for the single fault model

Property	**Value**	**Source / Comment**
Rock mass		
Young's modulus	E = 30 GPa	Keshavarz (2009)
Poisson's ratio	ν = 0.22	Keshavarz (2009)
Biot's coefficient	b = 1.0	Incompressible solid and fluid
Porosity	ϕ = 0.01	Keshavarz (2009)
Hydraulic conductivity	k = 1.1x10^{-16} m^2	Stober and Bucher (2007)
Cohesive material for fractures HF1 and HF2		
Tensile strength	R_T = 2.0 MPa	Common value
Mode I fracture energy	G_{IC} = 62 N/m (K_{IC} = 1.4 MPa.m$^{0.5}$)	Common value Atkinson (1989)
Cohesive material for fault F1		
Hydraulic aperture	0.4 mm	After Meyer et al. (2017)
Friction coefficient	μ_f = 0.35	Subjected to sensitivity study
Fracturing and pore fluid		
Dynamic viscosity	η = 0.001 Pa	Common value for water
Density	ρ = 1000 kg/m^3	Common value for water
Initial conditions		
Initial stresses	S_h = -29, S_H = -36 MPa	Meyer et al. (2017)
Initial pore pressure	p_0 = 23.7 MPa	Meyer et al. (2017)
Injection rate	Q = 0.5 L/s per unit thickness	Subjected to sensitivity study

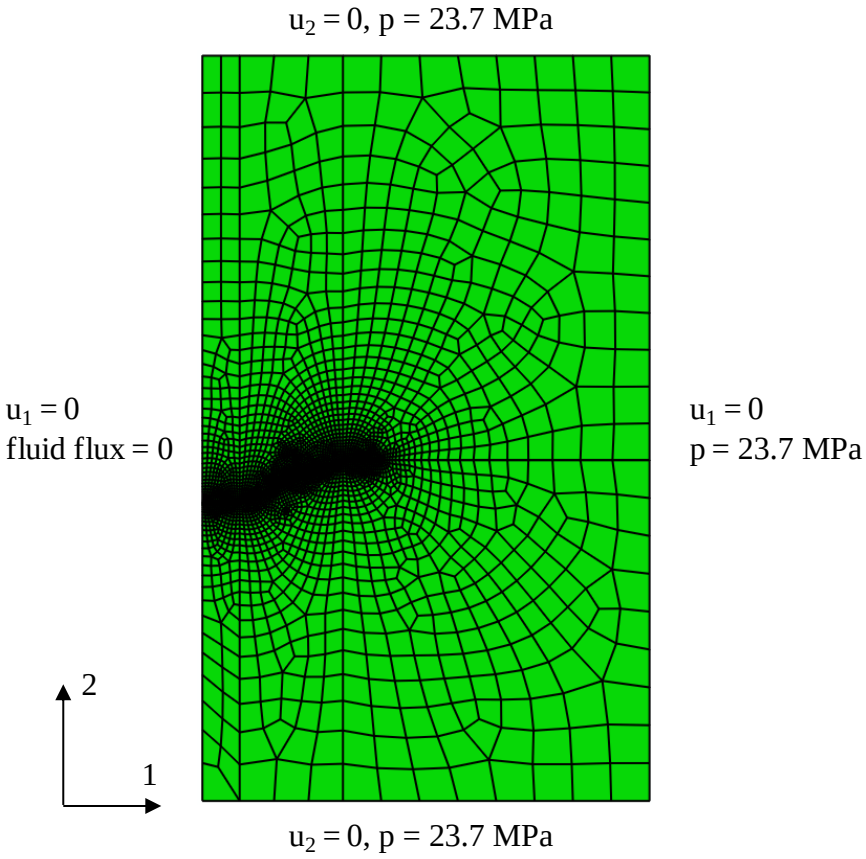

Figure 4.17 Finite element mesh and boundary conditions with an orientation angle θ = 22°. u_1 and u_2 are displacements in directions 1 and 2, p is pore pressure. The mesh has 16469 nodes and 15380 elements

The simulation strategy is as follows: In subsection 4.2.2, simulation with a fault friction coefficient μ_f = 0.35, an injection rate Q = 0.5 L/s, and an orientation angle θ = 22° is performed. The friction coefficient μ_f = 0.35 is lower than typical values for granitic rocks, which are from 0.6 to 0.65 (Jaeger et al., 2009). However, in faults that are filled with clay minerals or quartz, which are the main product of the hydrothermal alteration of rock, the friction coefficient can be reduced to as low as 0.3 (Morrow et al., 1992; Zoback et al., 2012). Thus, μ_f = 0.35 represents the lower range for the friction coefficient of faults. The results of the simulation are then presented and discussed in detail.

Parametric studies for the friction coefficient, the injection rate, and the orientation angle are presented in subsections 4.2.3, 4.2.4, and 4.2.5, respectively. The role of these parameters on the behavior of fault slip will then be discussed.

4.2.2 Simulation results for case S1 with μ_f = 0.35, Q = 0.5 L/s, and θ = 22°

The time evolution of the injection pressure, the fluid pressure at the center of the fault F1, and the hydraulic aperture at the injection point and at the center of fault F1 is presented in Figure 4.18. It can be seen that the injection pressure increases sharply from 23.7 MPa to 66.3 MPa after injection begins. Due to this fluid pressure increase, the fracture HF1 is initiated, accompanied by a sudden decrease in the injection pressure. As HF1 propagates the injection pressure continues to decrease and stabilizes at around 55 MPa (Figure 4.18a), which is approximately equal to the initial minor total stress plus the tensile strength of rock mass. The initial minor effective stress S_h and the initial pore pressure p_0 are S_h = 29 MPa and p_0 = 23.7 MPa (see Table 4.4). The initial minor total stress S_{hT} is $S_{hT} = S_h + p_0$ = 29 + 23.7= 52.7 MPa. The tensile strength of rock mass is R_T = 2 MPa. Thus, the summation of S_{hT} and R_T is 52.7 + 2 = 54.7 MPa, which is very close the stable fluid pressure 55 MPa.

When the fracture HF1 intersects the fault F1 at time 35.1 s, the injected fluid is suddenly driven into the fault, which leads to multiple events happening simultaneously:

(i) the injection pressure decreases suddenly by approximately 1.5 MPa (Figure 4.18a), which leads to a decrease of the hydraulic aperture at the injection point by 0.5 mm (Figure 4.18b)

(ii) the fluid pressure in the fault increases suddenly from the initial pressure to 53.3 MPa (Figure 4.18a), which leads to the opening of the fault F1. The hydraulic aperture at the center of fault F1 increases suddenly by roughly 0.3 mm from 0.4 mm to 0.7 mm (Figure 4.18b).

After the intersection between HF1 and F1, the fluid pressures at the injection point and in the fault are identical. This is because the fluid has a very small dynamic viscosity (i.e., dynamic viscosity of the fluid is 0.001 Pa.s) and the hydraulic aperture of fracture HF1 and fault F1 are relatively large. In fact, the fluid pressure is virtually uniform along both the fracture HF1 and the fault F1, as Figure 4.19 illustrates.

It should be noted that the pressure at the center of the fault F1 decreases slightly immediately before it intersects with the hydraulic fracture HF1 (Figure 4.18a). This pressure decrease is because the zone ahead of the tip of HF1 is in volumetric expansion due to the stress

concentrations, as shown in Figure 4.20a. As a consequence, the fluid in the nearby regions is sucked into this expansion zone (Figure 4.20b), which in turn causes a decrease in the fluid pressure in the nearby regions, including within the fault F1. If the volumetric fluid flow rate into this expansion zone is smaller than the volumetric expansion rate, the fluid in this zone may even undergo cavitation; in such cases the capillary effect needs to be considered.

The accumulative slip and the slip rate averaged over the length of the fault F1 are presented in Figure 4.21. The slip rate remains relatively close to zero during most of the injection time except in two instances. The first instance is at the onset of the hydraulic fracture HF1. The onset of HF1 is accompanied by a rapid decrease in the injection pressure. This induces stress disturbances in the whole model. If these stress disturbances exceed the shear strength of the fault F1, which is the case in this simulation, the fault will slip at a relatively high rate. The second instance is when HF1 intersects F1, during which the fault shear strength is lost by the rapid increase in fluid pressure within the fault. The slip rate is approximately 5.1 mm/s at the onset of HF1 and 6.2 mm/s when HF1 intersects F1. It should be noted that the fault slip can be stable (i.e., aseismic) or unstable (i.e., seismogenic). Usually a threshold of dynamic slip rate is used to distinguish these two slip regimes. This threshold can range from 5 mm/s to 0.1 m/s (Dublanchet et al., 2013; Gischig, 2015; McClure and Horne, 2014). When compared to these proposed thresholds of dynamic slip rates, the slip of fault F1 in this simulation is likely to be aseismic.

The contour plots of pore pressure at different times are presented in Figure 4.22. It can be seen that the fluid pressure inside the fracture HF1 and the fault F1 is nearly uniform and much higher than the pore pressure in the rock mass.

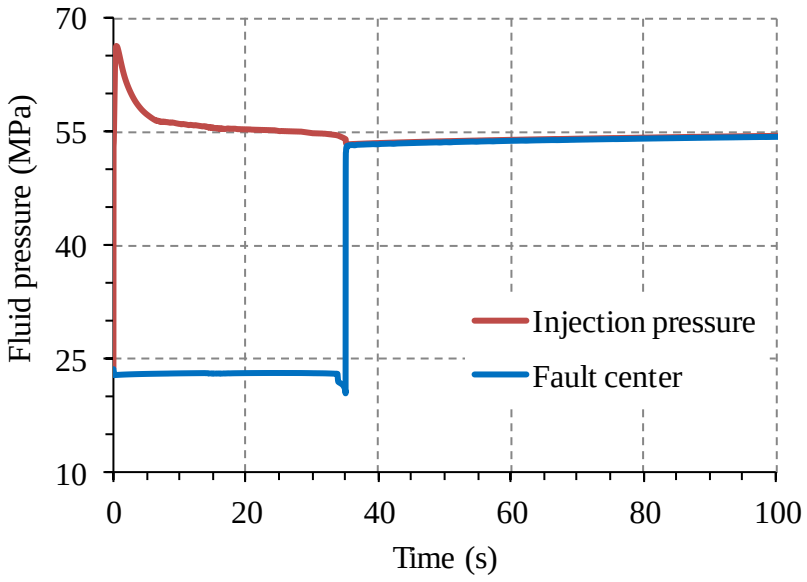

(a)

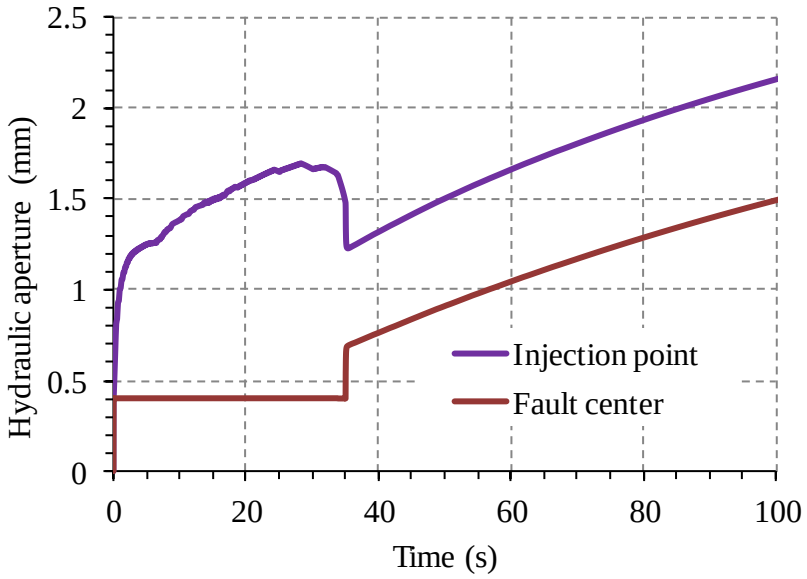

(b)

Figure 4.18 Time evolution of (a) injection pressure and fluid pressure at the center of the fault F1 and (b) hydraulic aperture at the injection point and at the center of the fault F1

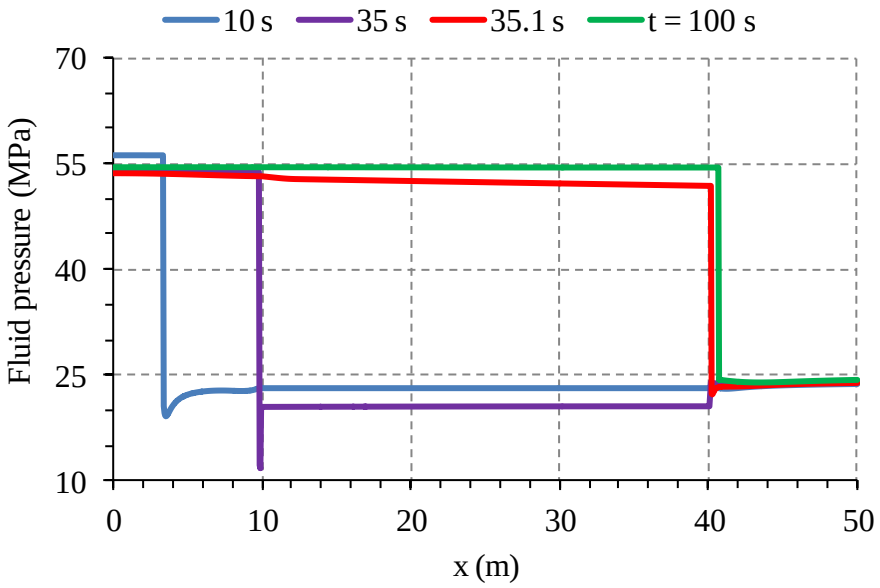

Figure 4.19 Distribution of fluid pressure along the path that consists of fracture HF1, fault F1, and fracture HF2 at different times. The injection point is located at x = 0. HF1, F1, and HF2 are determined by $0 \leq x \leq 10$, $10 \leq x \leq 40$, and $x > 40$, respectively.

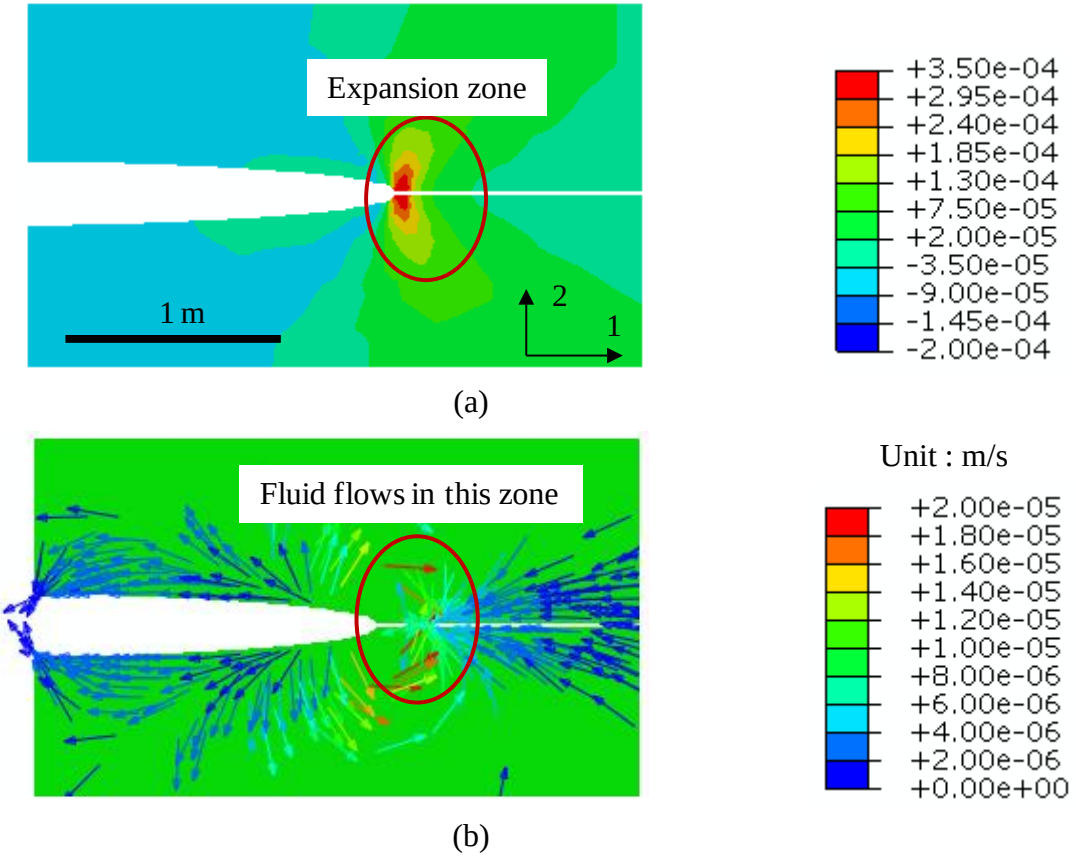

Figure 4.20 (a) Strain in direction 2 and (b) Fluid velocity vector at 4.4 s after injection

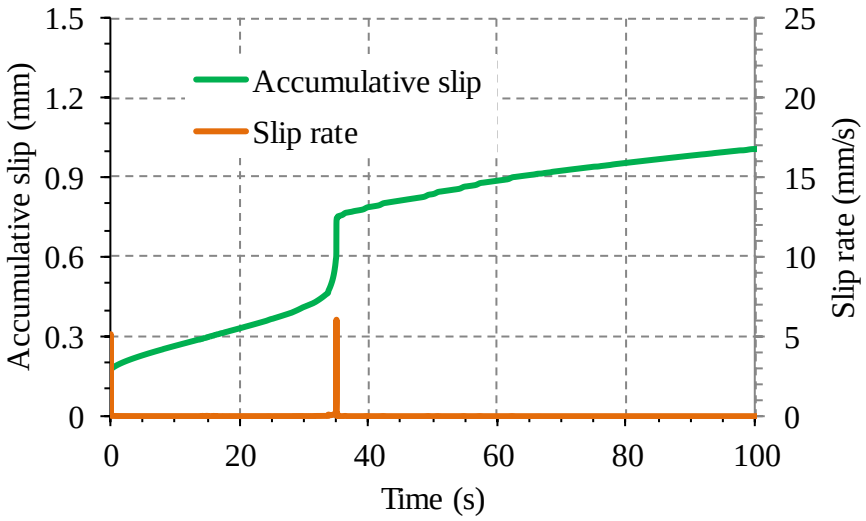

Figure 4.21 Time evolution of the accumulative slip and the slip rate of the fault F1

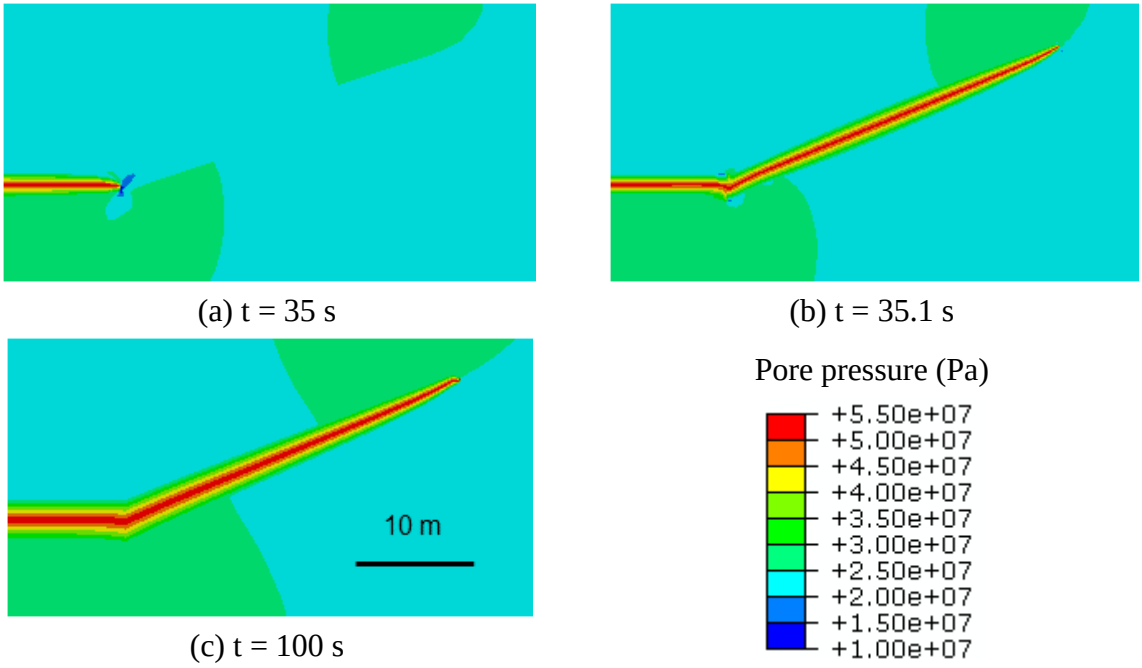

Figure 4.22 Contour plots of the pore pressure at different times

4.2.3 Effect of friction coefficient on fault slip

The influence of the friction coefficient on the slip of the fault F1 is investigated in this subsection. Three cases with different values of friction coefficient μ_f were studied and are listed in Table 4.5. The case S2, μ_f = 0.65 was chosen because it is typical of granitic rocks (Jaeger et al., 2009), while case S3 μ_f = 1.0, with a higher than normal friction coefficient, was

chosen only for the purpose of parametric study. The injection rate is Q = 0.5 L/s, fault orientation angle is θ = 22°. All the other material properties were given in Table 4.4.

Table 4.5 The friction coefficient values, cases S1, S2, and S3

Case	**Friction coefficient**
S1	0.35 (studied in section 4.2.2)
S2	0.65
S3	1.0

Simulation results and discussion:

The time evolution of fluid pressure (at the injection point and at the center of fault F1), accumulative slip and slip rate averaged over the length of the fault F1 is presented in Figure 4.23 and Figure 4.24 for cases S2 and S3, respectively. Similar patterns of evolution were observed in both cases:

1) The injection pressure increases immediately after injection commences and then decreases as the fracture HF1 starts to propagate
2) The fluid pressure in the fault F1 remains constant initially, decreases as the fracture HF1 approaches it, and then increases suddenly as HF1 intersects F1
3) The slip rate is very small for the majority of the injection time, including at the onset of HF1, while a high slip rate occurs only when the fracture HF1 intersects the fault F1.

Figure 4.25 shows the slip rate as function of the friction coefficient when the fracture HF1 is initiated and when it intersects the fault F1. It can be seen that the slip rate at the onset of the hydraulic fracture HF1 decreases as the friction coefficient increases, from 5.1 mm/s for case S1 (μ_f = 0.35) to almost zero for case S3 (μ_f = 1.0). This can be explained as follows. The fault F1 will slip at relatively high rates whenever the shear stress on the fault exceeds the shear strength of the fault. Otherwise, the fault will have elastic deformations, which results in lower slip rates. When the fault has a small friction coefficient (e.g., case S1 where μ_f = 0.35), the shear strength of the fault is also small. Thus, the shear stress caused by the onset of HF1 can exceed the small shear strength of the fault, causing the fault to slip. As the friction coefficient

increases, the shear strength also increases and becomes larger than the shear stress induced by the onset of HF1. This prevents the fault from slipping. In these cases the fault F1 only slips when it is intersected by HF1, which is when the fluid pressure in the fault increases suddenly, causing the shear strength to decrease significantly.

It is also noted from Figure 4.25 that the slip rate upon intersection of HF1 with F1 increases with the increase of friction coefficient, from 6.2 mm/s for case S1 to 19.2 mm/s for case S2 and to 23 mm/s for case S3. This can be interpreted as follows.

For a fault that has a small friction coefficient, the shear stress required to cause the fault to slip is also small. This means that the strain energy accumulated during the stress buildup process prior to the slip event, which is also the energy released during the slip event, is small. Consequently, the slip rate is small when slip occurs. Also, when the friction coefficient is small, the fault may slip multiple times during injection, but at a relatively small slip rate. In other words, the accumulated strain energy is released more evenly. This phenomenon is observed for case S1 where the fault F1 slips twice during fluid injection and both times the slip rate is relatively small (5.1 mm/s and 6.2 mm/s).

For a fault that has a higher friction coefficient, more strain energy is accumulated prior to the slip event because the fault shear strength is higher. This accumulated strain energy is all released at one time when the fault is intersected by the hydraulic fracture. Consequently, the slip is more violent with higher slip rates. For instance, the slip rate of fault F1 when it is intersected by the hydraulic fracture HF1 is 19.2 mm/s for case S2 (μ_f = 0.65) and 23 mm/s for case S3 (μ_f = 1). These slip rates are significantly higher than the lower threshold of the dynamic slip rate, which is from 5 mm/s to 10 mm/s (Dublanchet et al., 2013; McClure and Horne, 2011). Thus, these slip events are likely to be seismic.

Correlations between the friction coefficient of fractures/faults and their slip behavior were observed in lab experiments and in in-situ hydraulic stimulation tests. Through a series of lab tests on shale reservoir rocks, (Kohli and Zoback, 2013) found that: (1) the friction coefficient of a fault increases linearly with a decrease in the clay content; (2) faults with low clay contents, i.e., high friction coefficients, exhibit a velocity-weakening frictional behavior and the fault slip is unstable, whereas faults with high clay contents, i.e., low friction coefficients,

show a velocity-strengthening frictional behavior and the fault slip is stable. An experimental study by Ikari et al. (2011) also showed that weak faults (faults with a friction coefficient $\mu_f <$ 0.5) only exhibit increased friction with slip rate, which suppresses instable slip, while faults with higher friction coefficients can exhibit unstable slip behavior. Similar observations were obtained in 2000 during the hydraulic stimulation of two wellbores GKP1 and GKP3 at Soultz-sous-Forêts. Based on an analysis of the induced seismic events, (Meller and Kohl, 2014) showed that large-magnitude seismic events occurred on fractures that have no significant clay filling, i.e., fractures with high friction coefficients. Meanwhile, clay-rich fractures, i.e., fractures with lower friction coefficients, tend to produce smaller seismic events. They also concluded that clay inside the fractures reduces the friction on fractures, thus preventing large stress buildup and promoting aseismic slip.

The time evolution of the hydraulic aperture at the center of the fault F1 is presented in Figure 4.26 for all three cases S1, S2, and S3. It can be seen that in all cases the hydraulic aperture increases by approximately the same amount when intersection between HF1 and F1 occurs, even though the fault F1 slips at a much higher rate in cases 2 and 3 than in case 1.

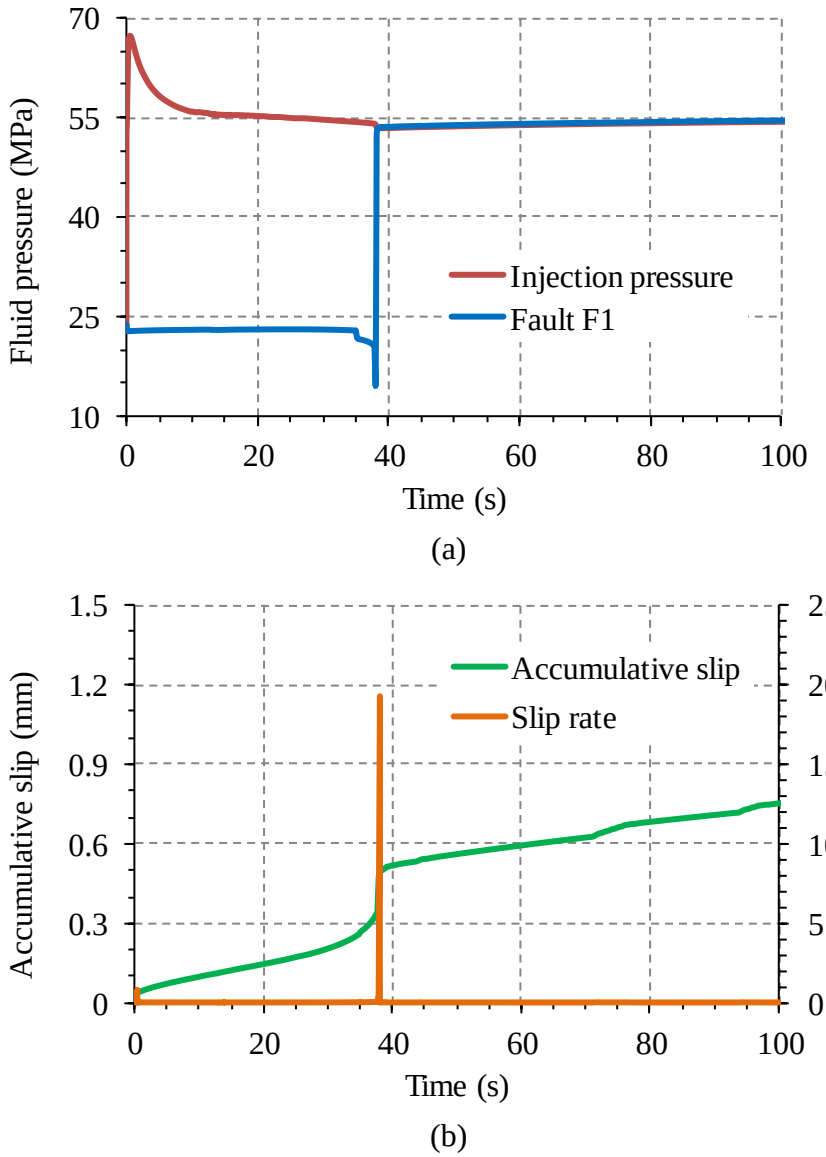

Figure 4.23 Results for case S2 (friction coefficient μ_f = 0.65): (a) time evolution of injection pressure and fluid pressure at the center of fault F1, (b) time evolution of accumulative slip and slip rate of fault F1

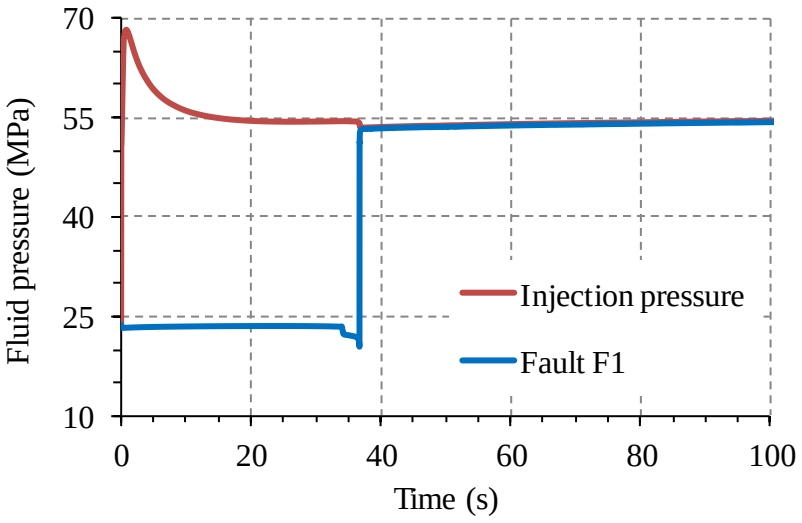

(a)

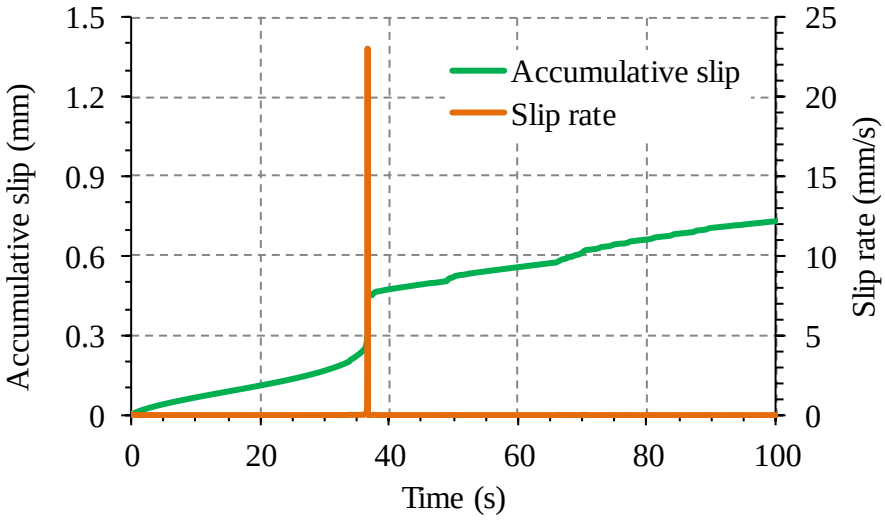

(b)

Figure 4.24 Results for case S3 (friction coefficient $\mu_f = 1$): (a) time evolution of injection pressure and fluid pressure at the center of fault F1, (b) time evolution of accumulative slip and slip rate of fault F1

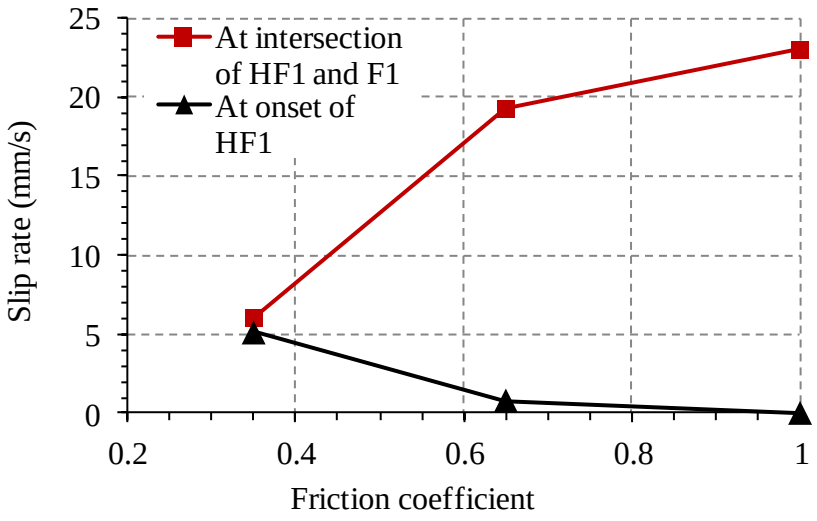

Figure 4.25 Slip rate of fault F1 at onset of fracture HF1 and at intersection of HF1 with fault F1 as function of the friction coefficient

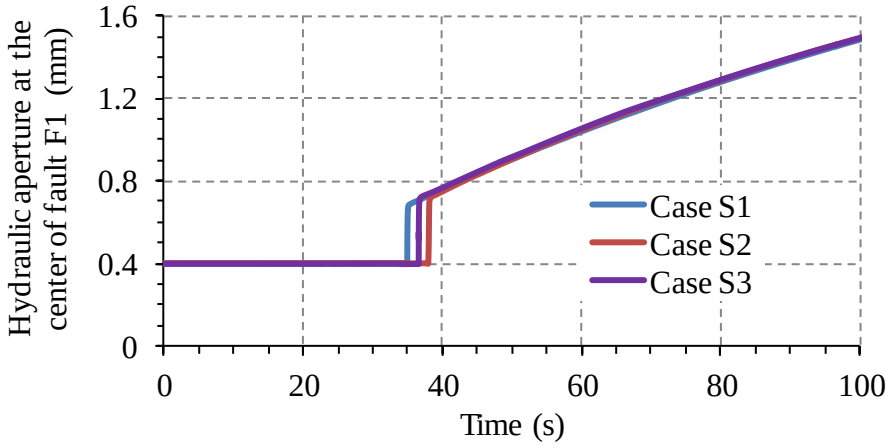

Figure 4.26 Time evolution of fault aperture for the 3 cases studied. The coefficient of friction for cases S1, S2, and S3 is 0.35, 0.65, and 1, respectively.

4.2.4 Effect of injection rate on fault slip

The effect of the injection rate on the fault slip is investigated in this subsection. Four cases with different injection rates were studied, ranging from 0.25 L/s to 3 L/s per unit thickness. The injection rates for these four cases, denoted by Q1 to Q4, are listed in Table 4.6. The fluid is injected over 100 s for cases Q1 to Q3. In case Q4, the higher injection rate (3 L/s) leads to fast propagation of the hydraulic fractures HF1 and HF2. Therefore, the injection is terminated after 53 s. The friction coefficient of the fault F1 was chosen as 0.65 for all cases; this friction

coefficient is typical of granitic rocks (Jaeger et al., 2009). The orientation angle of the fault F1 is $\theta = 22°$. Other material properties were given in Table 4.4.

Table 4.6 The injection rates for cases Q1 - Q4

Case	Injection rate Q (L/s per unit thickness)
Q1	0.25
Q2	0.5 (Case S2 in section 4.2.3)
Q3	1.0
Q4	3.0

Simulation results and discussion:

The time evolution of the injection pressure and the fluid pressure at the center of the fault F1 is presented in Figure 4.27 for all four cases Q1 to Q4. It can be seen that as the injection rate increases, the fracture propagates faster. For instance, the intersection between fracture HF1 and the fault F1 occurs after 77.5 s of injection when the injection rate is Q = 0.25 L/s. In case Q2 (Q = 0.5 L/s) the intersection occurs after 35.1 s, and is 18.5 s for case Q3 (Q = 1 L/s), and 8.1 s for case Q4 (Q = 3 L/s). The injection rate increases 12 times (3/0.25) between Q1 and Q4, while the propagation velocity of the fracture HF1 is increased by 77.5/8.1 = 9.6 times. This shows that the injection rate plays an important role on the propagation velocity of the hydraulic fracture HF1, but is not the only factor. Poroelastic effects and permeability of the rock mass also affect the fracture propagation velocity. The breakdown pressure, i.e., the maximum injection pressure, also increases with the injection rate, from 65.8 MPa for case Q1 to 74.5 MPa for case Q4 (Figure 4.29). Again, this is reflective of the influence of poroelastic effects. If poroelastic effects were not considered, the breakdown pressure would be the same for any injection rate.

The simulated accumulative slip and slip rate of the fault F1 are presented in Figure 4.28. It can be seen that the slip rate is close to zero during most of the injection time. A high slip rate only occurs upon the intersection of HF1 with F1. The slip rate of the fault F1 when it is intersected by the fracture HF1 and the breakdown pressure as function of the injection rate are presented in Figure 4.29. It can be seen that upon intersection the slip rate increases with

the injection rate. However, this effect of the injection rate on the slip rate is not significant as the slip rate only increases from 15.8 mm/s to 21.9 mm/s (less than 40% increase) when the injection rate is increased 12 times from 0.25 L/s to 3 L/s. The relatively small effect of the injection rate on the slip rate can be explained by the fluid pressure in the fault F1 as shown in Figure 4.27b. After intersection of HF1 with F1, the fluid pressure in the fault F1 is more or less similar for cases Q1, Q2, Q3, and Q4. The fluid pressure is the main factor that affects the shear strength, and thus the slip of the fault; small differences in the fluid pressure in the fault result in small differences in slip rate. Nonetheless, the slip rate in all four cases studied is higher than the 10 mm/s threshold of the dynamic slip rate, indicating that the slip is likely to be unstable (i.e., seismic). (Aochi et al., 2013) used a different model to study the fault slip; the fault is modeled as permeable zone of finite thickness but the authors came to similar conclusion that the induced seismicity, which is reflected by the fault slip, is self-induced and less sensitive to the injection rate. Rather, the injection rate delays the fault slip as the pressure buildup process at the injection point takes more time when the injection rate is small.

The hydraulic aperture at the center of the fault F1 after injecting 25 L of fluid as function of the injection rate is shown in Figure 4.30. It should be noted that unlike the breakdown pressure and the maximum slip rate that both increase with the injection rate, the hydraulic aperture of the fault F1 after injection of 25 L of fluid is relatively similar for all cases. This indicates that more unstable fault slip may not necessarily mean more permeability enhancement.

The contour plots of pore pressure at different times for all four cases are presented in Figure 4.31. The effect of the injection rate on the velocity of fracture propagation is clearly illustrated. For instance, after 40 s injection, the fracture in case Q1 is only approximately 5 m long, while for case Q4 the fracture HF1 (10 m long) is completely generated and the fracture HF2 has begun to propagate.

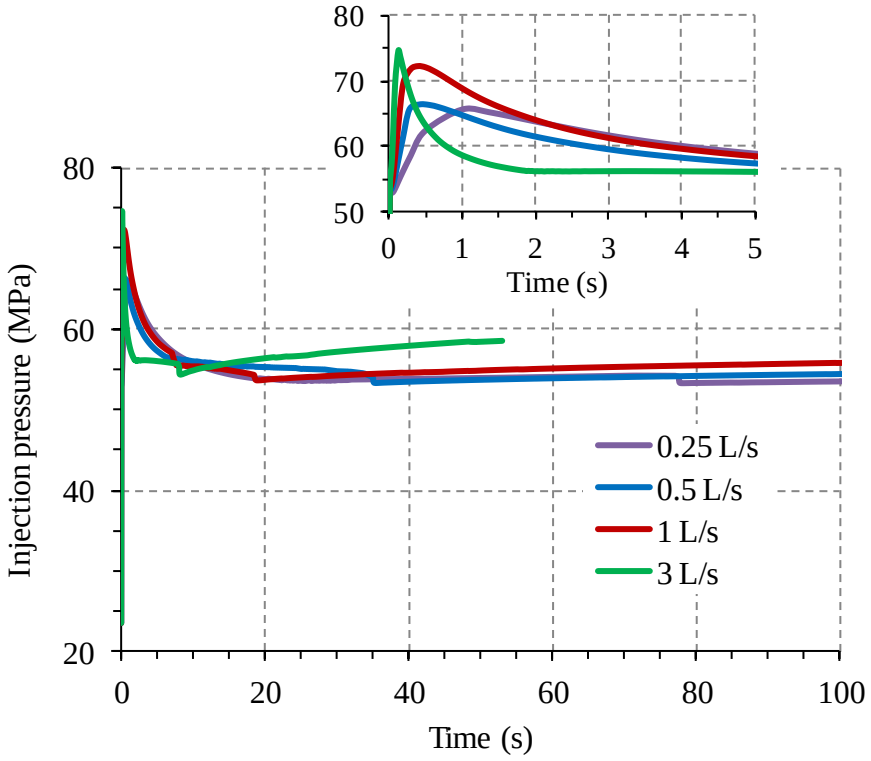

(a)

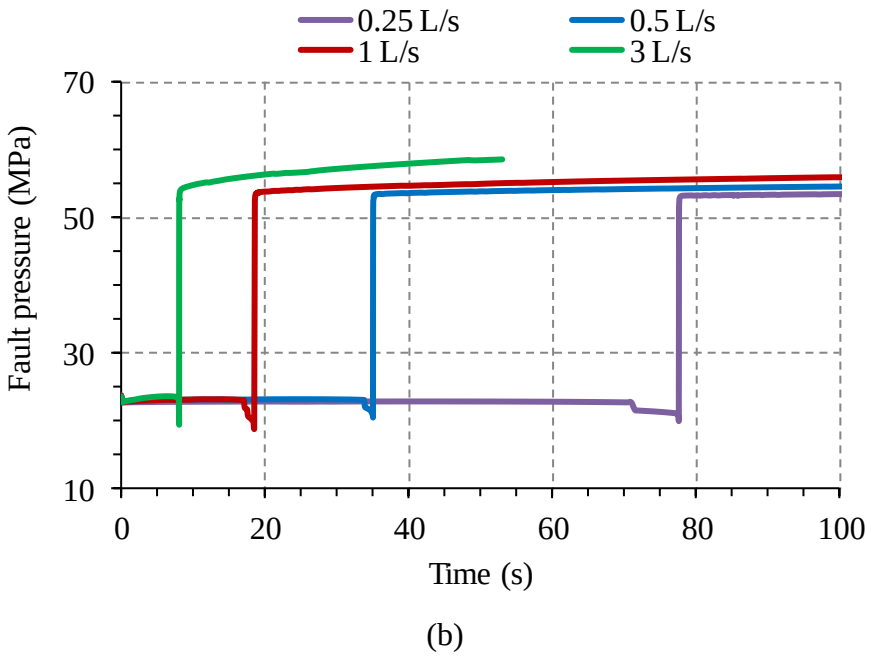

(b)

Figure 4.27 Time evolution of (a) breakdown pressure and (b) fluid pressure at the center of fault F1 for 4 cases Q1 to Q4; the injection rate for cases Q1, Q2, Q3, and Q4 is 0.25, 0.5, 1, and 3 L/s, respectively.

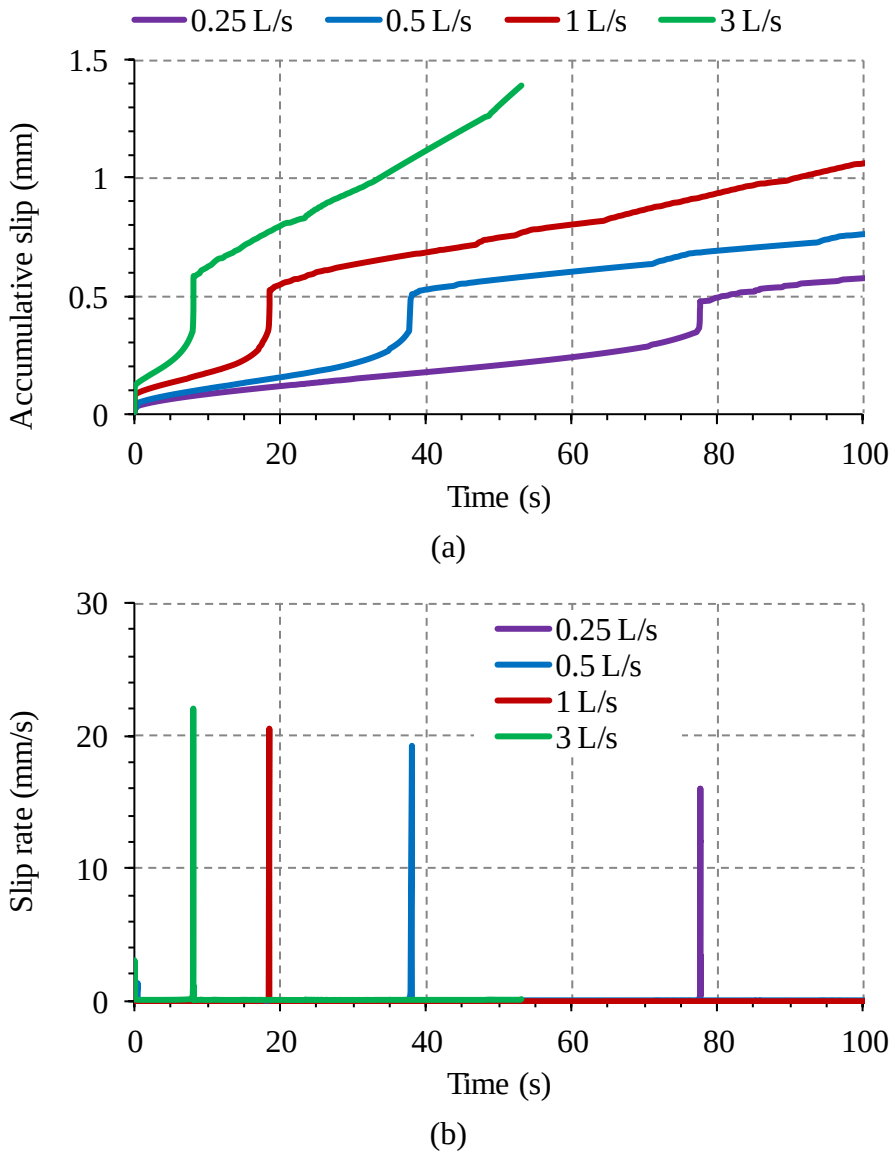

Figure 4.28 Time evolution of (a) accumulative slip and (b) slip rate of fault F1 for 4 cases Q1 to Q4; the injection rate for cases Q1, Q2, Q3, and Q4 is 0.25, 0.5, 1, and 3 L/s, respectively.

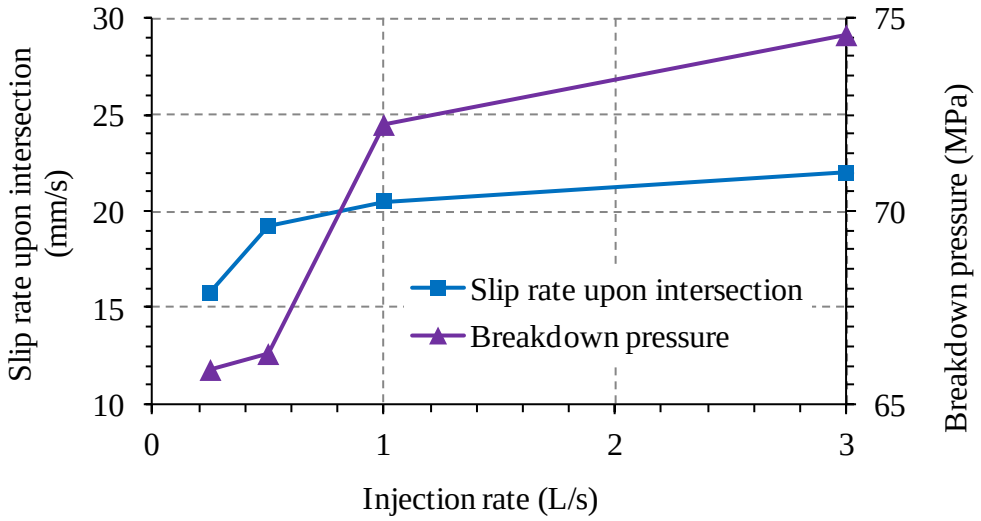

Figure 4.29 Slip rate of fault F1 when intersected by hydraulic fracture HF1 and breakdown pressure as a function of the injection rate

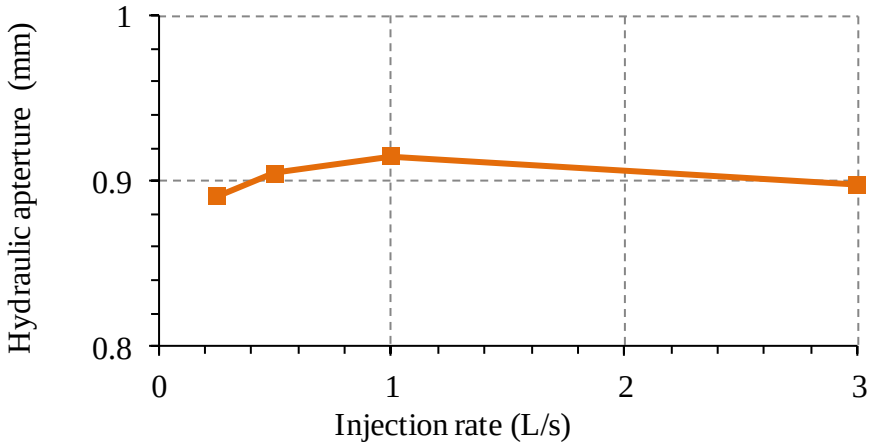

Figure 4.30 Hydraulic aperture at the center of fault F1 after injection of 25 L of fluid as a function of injection rate

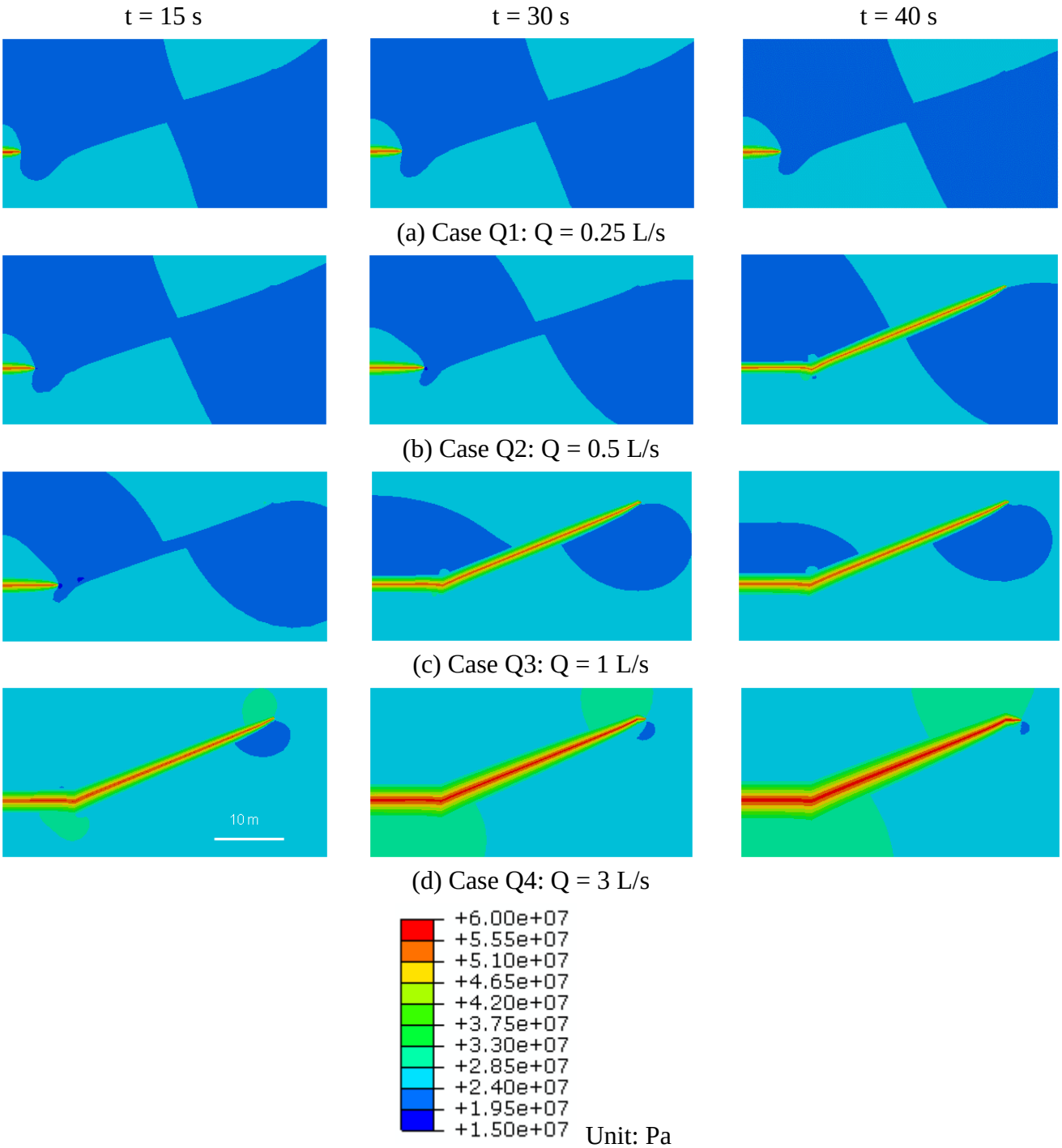

Figure 4.31 Contour plots of pore pressure for 4 cases Q1 to Q4 at 15 s, 30 s, and 40 s.

4.2.5 Effect of fault orientation on fault slip

The effect of the fault orientation with respect to initial stresses is studied in this subsection. Four cases with a different orientation angle θ ranging from 10° to 45° are examined. These

four cases, denoted by Z1 to Z4, are listed in Table 4.7. For all of these cases, the fluid is injected at 0.5 L/s in 100 s, while the friction coefficient of the fault F1 is μ_f = 0.65. Other material properties are unchanged and were given in Table 4.4.

Table 4.7 Fault orientation angle for the four cases studied

Case	**Orientation angle θ**
Z1	10°
Z2	22° (Case S2 in Section 4.2.3)
Z3	35°
Z4	45°

Simulation results and discussion:

The time evolution of the accumulative slip and the slip rate of the fault F1 is presented in Figure 4.32. The slip rate of the fault F1 when it is intersected by the hydraulic fracture HF1, as a function of the fault orientation angle, is shown in Figure 4.33. It can be seen from Figure 4.32b and Figure 4.33 that the maximum slip rate when the hydraulic fracture HF1 intersects with the fault F1 increases as the orientation angle increases. For instance, the slip rate increases from 4.1 mm/s for θ = 10° to 46.6 mm/s for θ = 45. It can also be seen from Figure 4.32b that the fracture propagation is faster as the orientation angle increases. For instance, the fracture HF1 intersects the fault F1 at a time of 50.9 s, 38.1 s, 35.4 s, and 27.1 s for θ = 10°, 22°, 35°, and 45°, respectively. This is counterintuitive because the orientation angle was expected to only affect the slip of the fault F1. The propagation velocity of the fracture HF1 is similar in all cases Z1 to Z4 as long as the fracture tip is far from the fault F1. This is illustrated on Figure 4.34, which shows the effective stress normal to the plane of the fracture HF1 (called stress S22) along the fracture HF1 for cases Z1 to Z4 after 10 s of fluid injection. The fracture tip is at the same location, approximately 3.7 m from the injection point. This shows that the fracture HF1 propagates at a similar velocity. However, it can also be seen in Figure 4.34 that the stress S22 near the intersection point between HF1 and F1 is disturbed differently for different orientation angles of the fault F1. S22 is reduced more (i.e., becoming

less compressive) when the fault orientation angle increases; a less compressive stress S22 favors fracture propagation, thus leading to faster propagation of HF1.

The contour plots of pore pressure at different times for cases Z1 to Z4 are presented in Figure 4.35. It can be seen that the fluid pressure is virtually uniform inside both the hydraulic fractures and the fault.

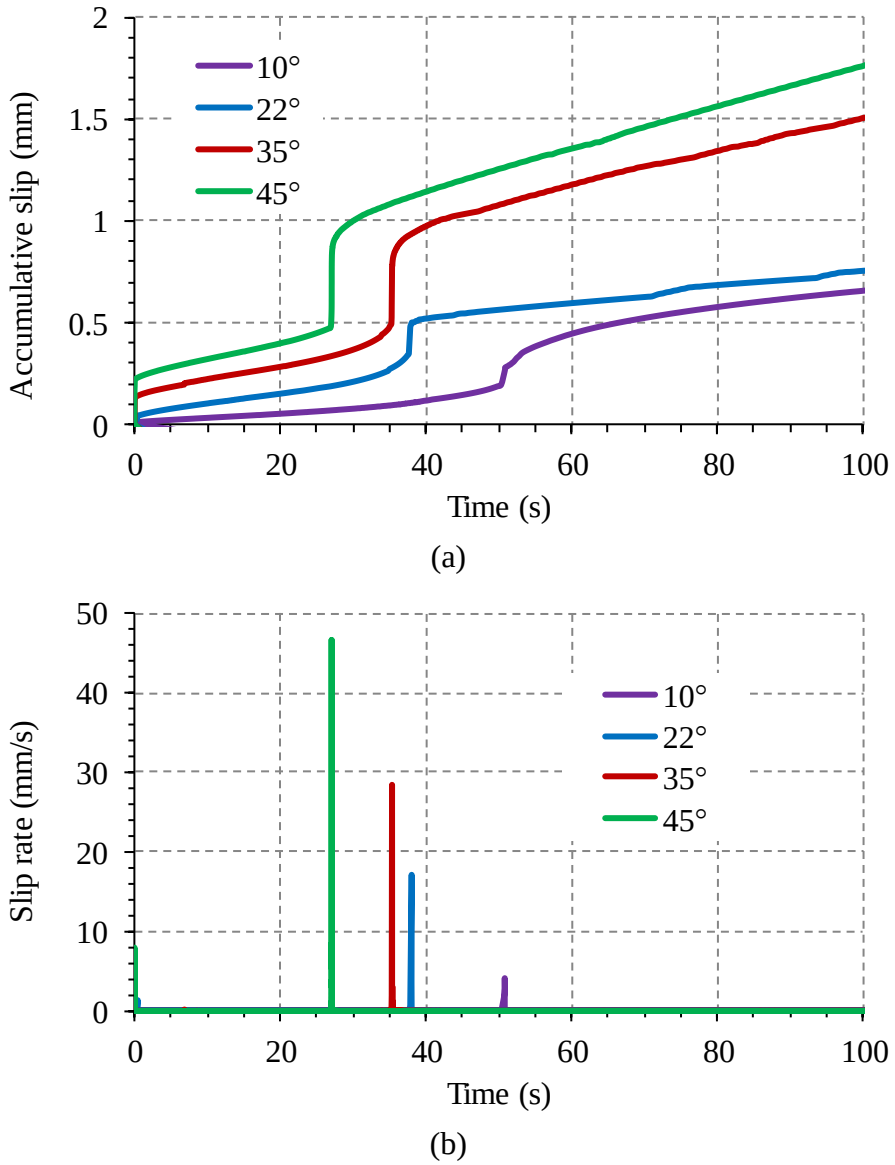

Figure 4.32 Time evolution of (a) the accumulative slip and (b) the slip rate of the fault F1 for cases Z1 to Z4 with different fault orientation angles ranging from 10° to 45°

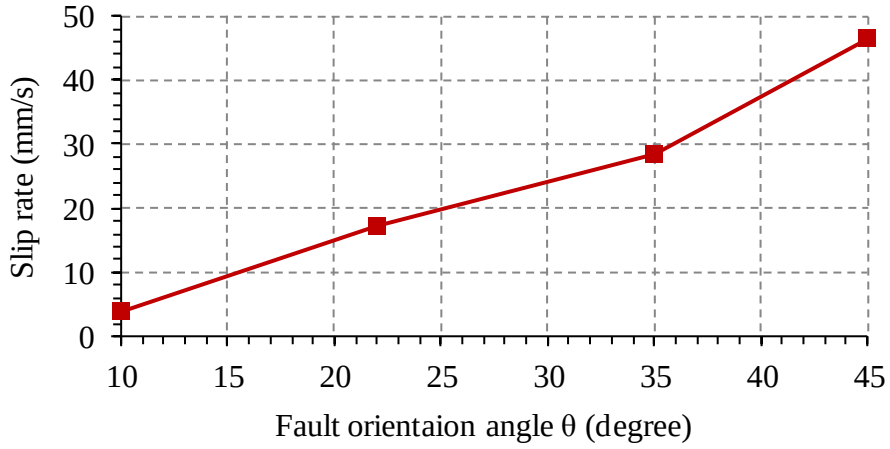

Figure 4.33 Slip rate of fault when intersected by the hydraulic fracture HF1 as a function of the orientation angle of the fault F1

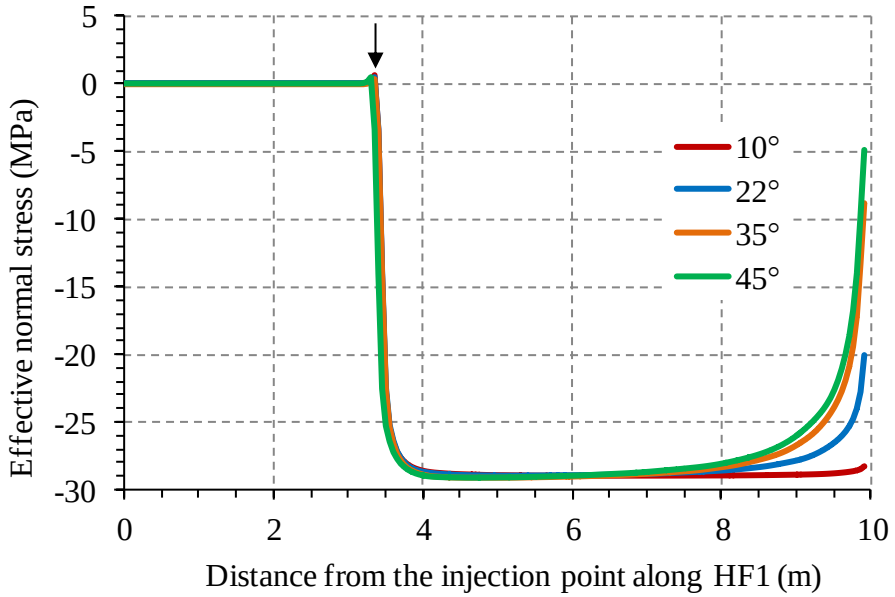

Figure 4.34 Effective stress normal to the plane of the fracture HF1 along the fracture HF1 at 10 s after injection for cases Z1 to Z4. The arrow indicates the location of the fracture tip. The initial stress in direction 2 is -29 MPa.

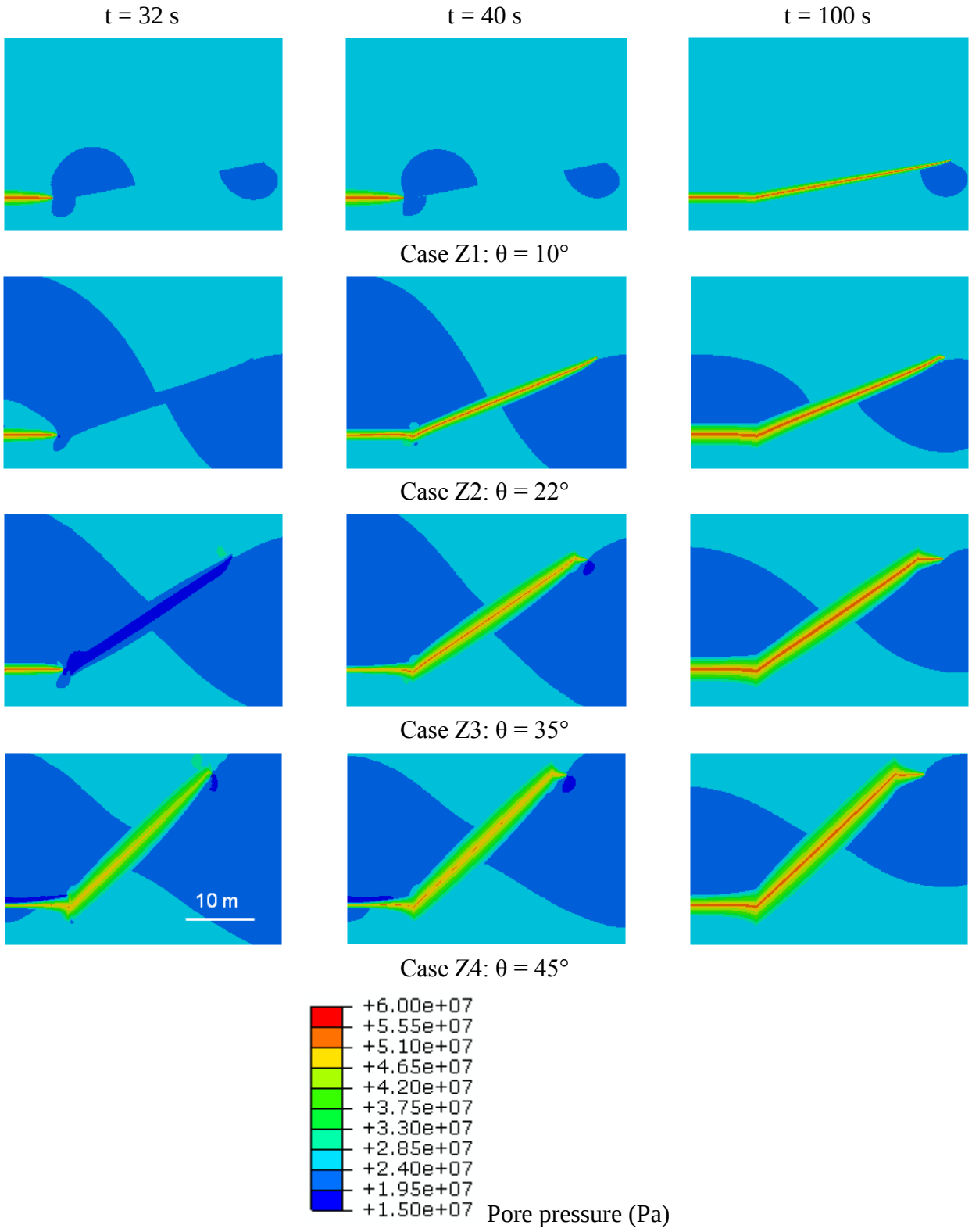

Figure 4.35 Contour plots of pore pressure at different times for 4 cases Z1 to Z4 with different fault orientation angles ranging from 10° to 45°

4.2.6 Concluding remarks

The propagation of a hydraulic fracture and the slip of a pre-existing fault were studied. The effect of several controlling parameters on the fault slip was investigated. These include the friction coefficient of the fault, the injection rate, and the orientation of the fault with respect to the initial stresses. The friction coefficient and the fault orientation were found to have a strong influence on the fault slip: the fault slip rate increases significantly with an increase in the fault friction coefficient or the fault orientation angle. While the injection rate also affects the fault slip, its effect is of a lesser extent.

4.3 PROPAGATION OF MULTIPLE HYDRAULIC FRACTURES AND INTERACTION WITH EXISTING FAULTS

The propagation of multiple hydraulic fractures and their intersection with pre-existing faults are studied. Specifically, the effect of the fault friction coefficient and the injection rate on the fault slip is examined in more detail. The model setup is presented in the next subsection. Then the results of the sensitivity studies for the fault friction coefficient and the injection rate are subsequently presented.

4.3.1 Model setup

The model studied is a 2D plane strain one that consists of four potential hydraulic fractures, denoted by HF1, HF2, HF3, and HF4, and three pre-existing faults, denoted by F1, F2, and F3 (Figure 4.36). The model is 120 m wide and 200 m high. The length of the fracture HF1 is 10 m, while HF2, HF3, and HF4 are 3 m long. All of the three faults are inclined at 22° with respect to the major principal stress S_H and are 10 m long. The initial stress state consists of major and minor effective far-field stresses S_h and S_H that act in directions 1 and 2, respectively. All hydraulic fractures HF1 to HF4 are perpendicular to the minor initial stress S_h.

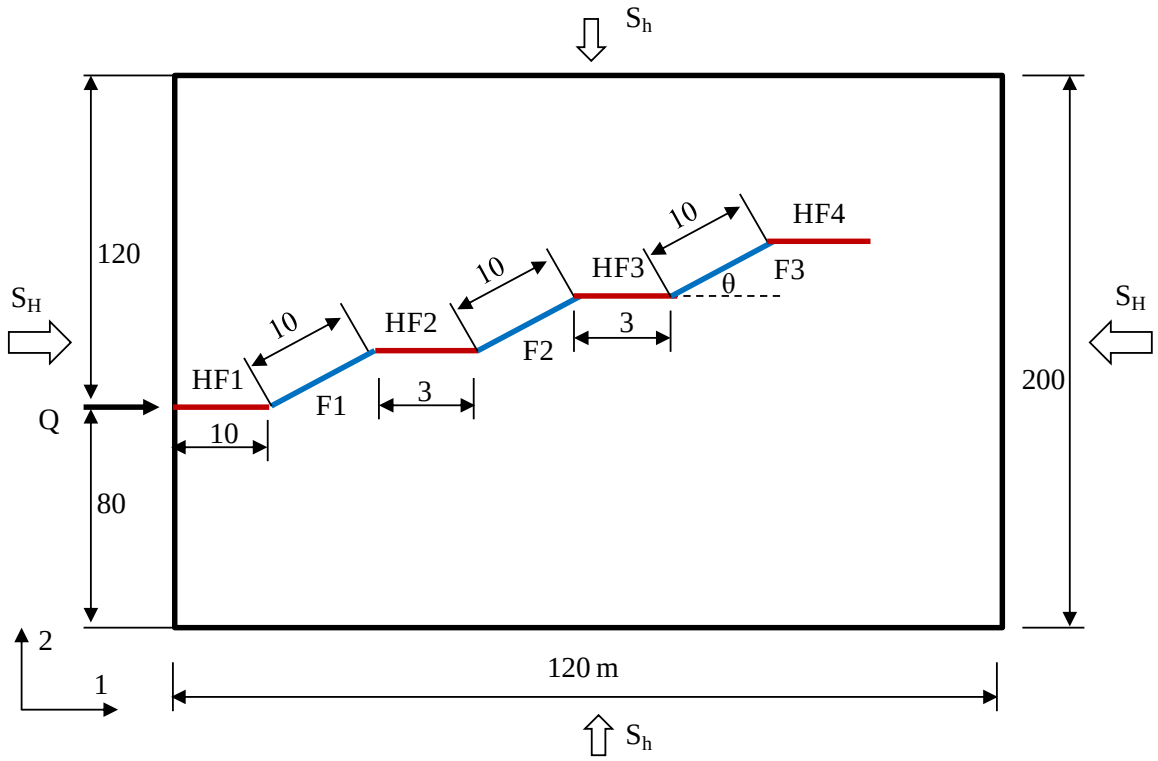

Figure 4.36 Multiple fault model. The model contains four hydraulic fractures HF1 to HF4 and three pre-existing faults F1, F2, and F3. S_h and S_H are the minor and major initial stresses. The unit of measurement is meters. The sketch is not to scale.

Four potential hydraulic fractures HF1 to HF4 are modeled by four layers of an intact cohesive material which have similar fracture mechanics properties (i.e., tensile strength and fracture energy). The three faults F1, F2, and F3 are modeled by three cohesive layers that are initially damaged. The shear strength of the faults is modeled using the Coulomb friction law with the same friction coefficient. The rock medium has low permeability and is considered to be linear poroelastic.

The stimulation of the system of fractures and faults is performed by injecting fluid at 0.5 L/s over 200 s through the left of the fracture HF1. When a hydraulic fracture intersects a pre-existing fault, it is assumed that the hydraulic fracture diverts into the fault. Thus, after the stimulation is completed a step like fracture system is obtained.

The properties of the materials (i.e., rock mass, cohesive materials, and fracturing fluid), initial stresses, and initial pore pressure are similar to those used in the previous section 4.2 and presented again in Table 4.8 for convenience.

Table 4.8 Parameters used for the multiple fault model

Property	**Value**	**Source / Comment**
Rock mass		
Young's modulus	E = 30 GPa	Keshavarz (2009)
Poisson's ratio	$\nu = 0.22$	Keshavarz (2009)
Biot coefficient	b = 1.0	Incompressible solid and fluid
Porosity	$\phi = 0.01$	Keshavarz (2009)
Hydraulic conductivity	$k = 1.1 \times 10^{-16}$ m^2	Stober and Bucher (2007)
Cohesive material for fractures HF1 to HF4		
Tensile strength	$R_T = 2.0$ MPa	Common value
Mode I fracture energy	$G_{IC} = 62$ N/m ($K_{IC} = 1.4$ MPa.m$^{0.5}$)	Common value, Atkinson (1989)
Faults F1 to F4		
Hydraulic aperture	0.4 mm	After Meyer et al. (2017)
Friction coefficient	$\mu_f = 0.35$ or 0.65 or 1.0	Subjected to sensitivity study
Fracturing and pore fluid		
Dynamic viscosity	$\eta = 0.001$ Pa	Common value
Density	$\rho = 1000$ kg/m^3	Common value
Initial conditions		
Initial stresses	$S_h = -29$, $S_H = -36$ MPa	Meyer et al. (2017)
Initial pore pressure	23.7 MPa	Meyer et al. (2017)
Injection rate	Q = 0.5 or 1 or 2 L/s per unit thickness	Subjected to sensitivity study

For the boundary conditions, the displacements normal to the outer boundaries are constrained for all of the outer boundaries. The pore pressure is kept constant at its initial value of 23.7 MPa for all outer boundaries, except for the left boundary where a no fluid flow condition is imposed. The poroelastic rock mass is assumed to be initially fully saturated (saturation degree equals 1) and remains fully saturated during the injection time.

For the finite element mesh, the rock mass is discretized by linear plane strain coupled pore fluid pressure/deformation continuum elements CPE4RP, while the cohesive layers are discretized by coupled fluid pressure/deformation cohesive elements COH2D4P. At the intersection of two cohesive layers, a mid-edge node that has the pore pressure as a degree of freedom is shared between those cohesive elements to support fluid flow continuity. The mesh is refined around the fractures and faults (smallest size is 0.05 m) and gradually becomes coarser towards the boundaries (largest size is 10 m). In total, the mesh has 21450 nodes and 20240 elements.

4.3.2 Sensitivity study of friction coefficient

The effect of the friction coefficient of the faults is studied in this subsection. All three faults F1, F2 and F3 have the same friction coefficient. However, the friction coefficient of these fault are changed to examine how it affects the slip of the faults. Three cases with different values of friction coefficient are studied and summarized in Table 4.9. The injection rate is fixed at 0.5 L/s for all of these cases.

Table 4.9 Friction coefficient for cases MS1, MS2, and MS3

Case	Friction coefficient
MS1	0.35
MS2	0.65
MS3	1.0

Simulation results and discussion:

The simulation results of case MS2 are presented in Figure 4.37, Figure 4.38, and Figure 4.39, while the results of the cases MS1 and MS3 are given in Appendix 2. It can be seen from Figure 4.37a that the injection pressure increases immediately after the start of fluid injection and then decreases as the fracture HF1 propagates. The fluid pressure in each of the three faults remains at the initial pore pressure before their intersection with the hydraulic fractures occurs and increases sharply upon the intersection (Figure 4.37a). For instance, the hydraulic

fracture HF1 intersects the fault F1 at 45.4 s. At the same time, the fluid pressure of fault F1 increases suddenly to approximately 54.2 MPa (Figure 4.37a).

The time evolution of hydraulic aperture was also investigated; the hydraulic aperture at the injection point of fracture HF1 increases during the propagation of fractures HF1, HF2 and HF3, and decreases suddenly each time a hydraulic fracture intersects a fault (Figure 4.37b). The decrease becomes smaller the farther the fault is from the injection point. For instance, the decrease in the hydraulic aperture at the injection point is approximately 0.33 mm when HF1 intersects F1, is 0.17 mm when HF2 intersects F2, and is 0.08 mm when HF3 intersects F3. Meanwhile, the hydraulic aperture of each fault increases suddenly when it is intersected by a hydraulic fracture and decreases upon subsequent intersections between the other faults and other hydraulic fractures (Figure 4.37b). For instance, the aperture of the fault F1 increases by nearly 0.44 mm when it is intersected by hydraulic fracture HF1, but decreases by 0.12 mm when the hydraulic fracture HF2 intersects fault F2, and decreases again by 0.06 mm when the hydraulic fracture HF3 intersects fault F3. The sudden increase in the hydraulic aperture of a fault when it is intersected by a hydraulic fracture is caused by the sudden increase in fluid pressure in the fault at the moment of intersection. Upon subsequent intersections between other hydraulic fractures and other faults, the injected fluid is driven into the additional faults, causing the aperture of the previously activated fault to decrease.

The contour plots of pore pressure at different times and the advancement of hydraulic fractures and pre-existing faults are presented in Figure 4.38. Again, it can be seen that the fluid pressure is almost constant along the hydraulic fractures and the pre-existing fractures, so that the whole structure extends at a pressure just below the minimum stress if the tensile strength is disregarded.

The slip rate of each fault, presented in Figure 4.39, remains small during most of the injection duration. High slip rates occur only when a hydraulic fracture intersects a fault. The slip rate of faults F1, F2, and F3 upon intersection with fractures HF1, HF2, and HF3 is 20.4 mm/s, 34.9 mm/s, and 6.1 mm/s, respectively. When compared to the threshold of the dynamic slip rate of 5 mm/s, all these intersection events are deemed to be seismic.

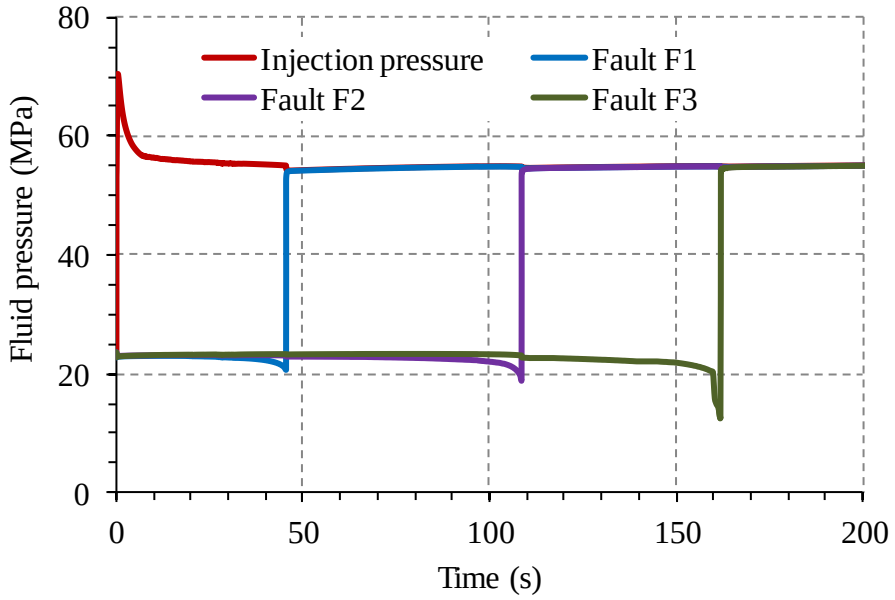

(a)

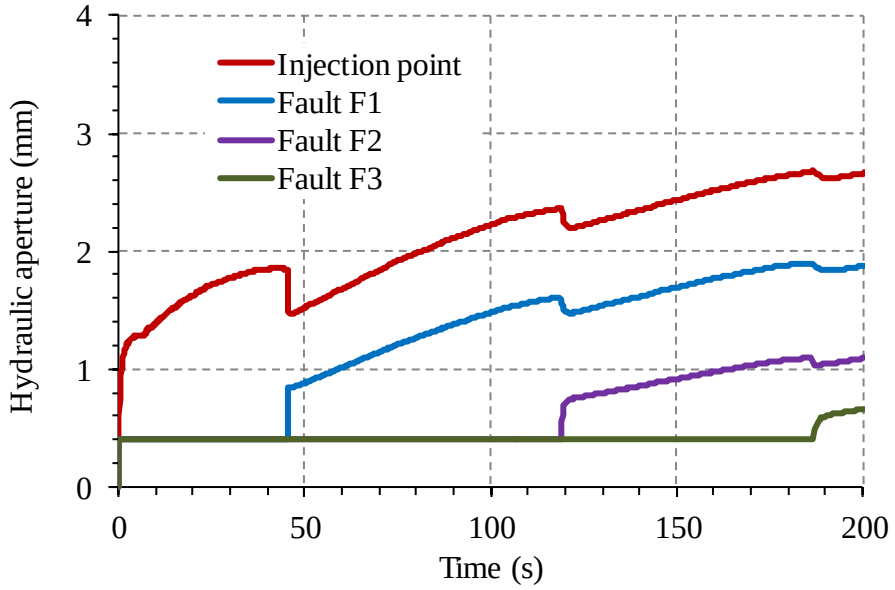

(b)

Figure 4.37 Simulation results of case MS2 (friction coefficient μ_f = 0.65): time evolution of (a) injection pressure and fluid pressure at the center of faults F1, F2, F3 and (b) hydraulic aperture at the injection point and at the center of faults F1, F2, F3

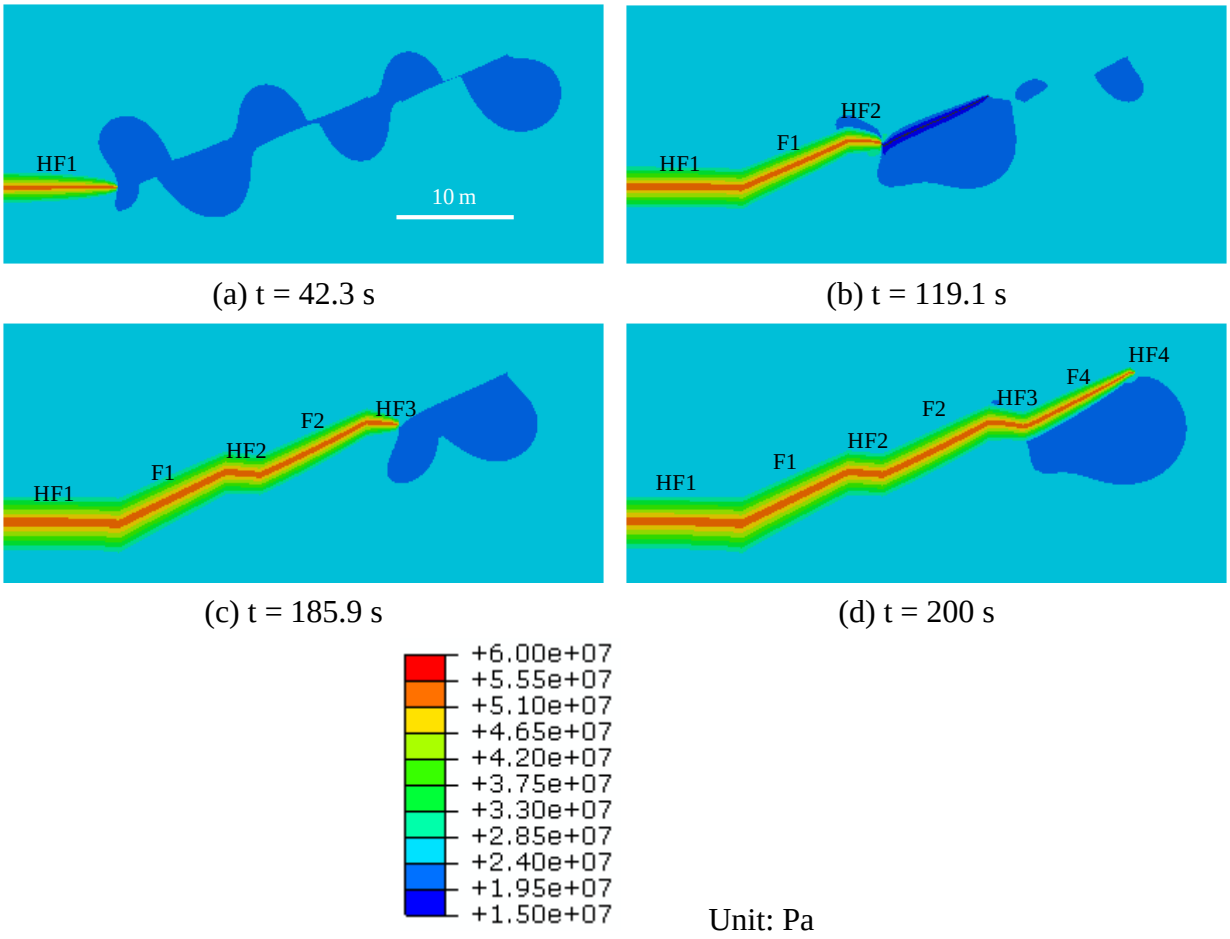

Figure 4.38 Contour plots of pore pressure at different times

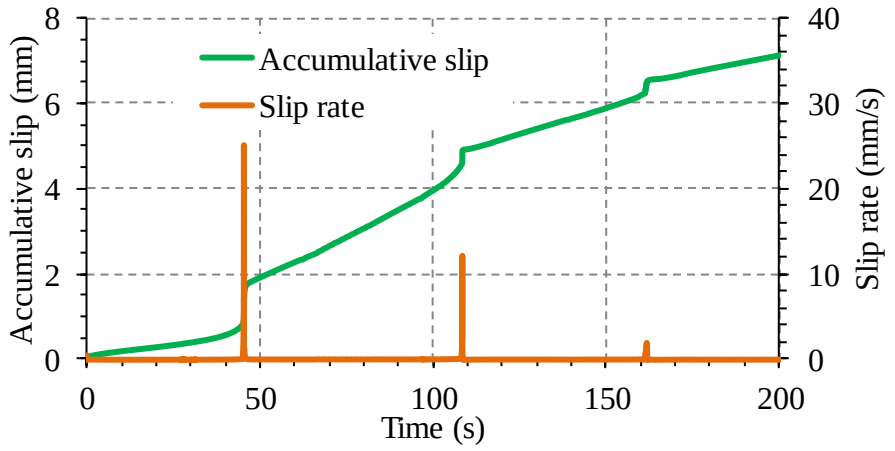

(a) Fault F1

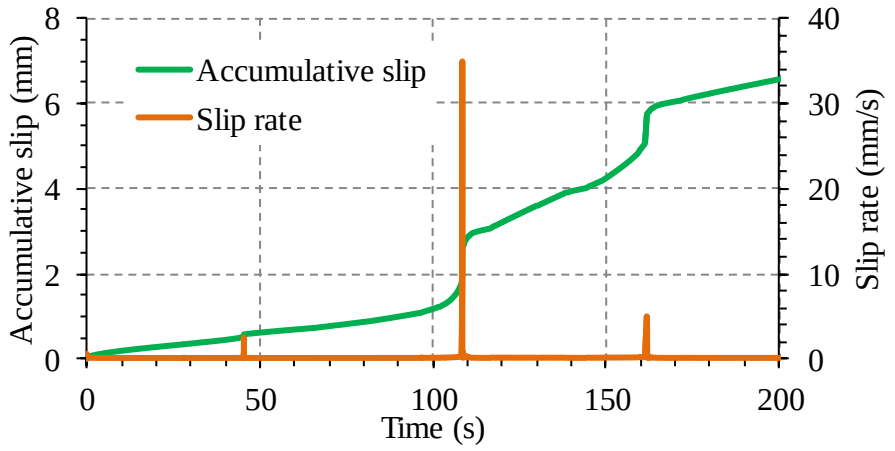

(b) Fault F2

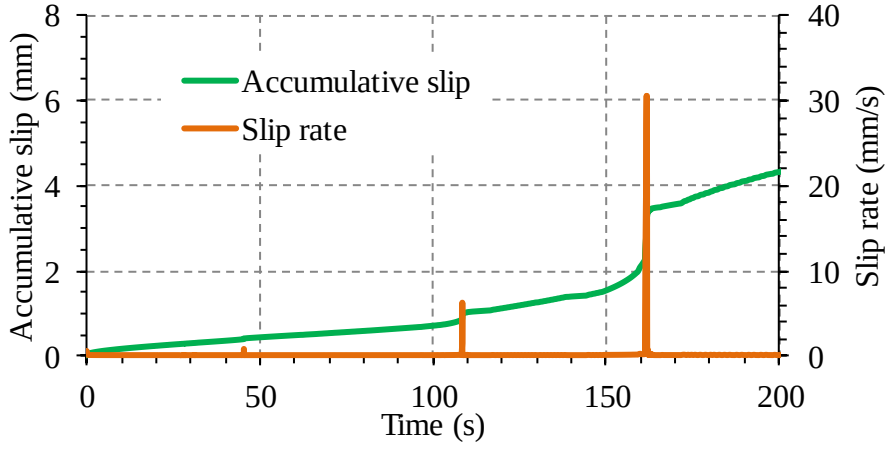

(c) Fault F3

Figure 4.39 Simulation results of case MS2 (friction coefficient μ_f = 0.65): time evolution of accumulative slip and slip rate of faults F1, F2, and F3

Evolution of slip rate as function of friction coefficient:

Detailed simulation results for cases MS1 and case MS3 are presented in Appendix 2. A summary of the results is presented in Figure 4.40, which shows the maximum slip rate of faults upon their intersection with hydraulic fractures as function of the fault friction coefficient. In general, the slip rate increases with the friction coefficient. Compared to the single fault model studied in subsection 4.2.3, the slip rate of faults in this multiple fault model is more sensitive to variations in the friction coefficient, especially for faults F2 and F3 whose slip rate increases from around 2 mm/s when the friction coefficient is 0.35 to around 100 mm/s when the friction coefficient is 1.

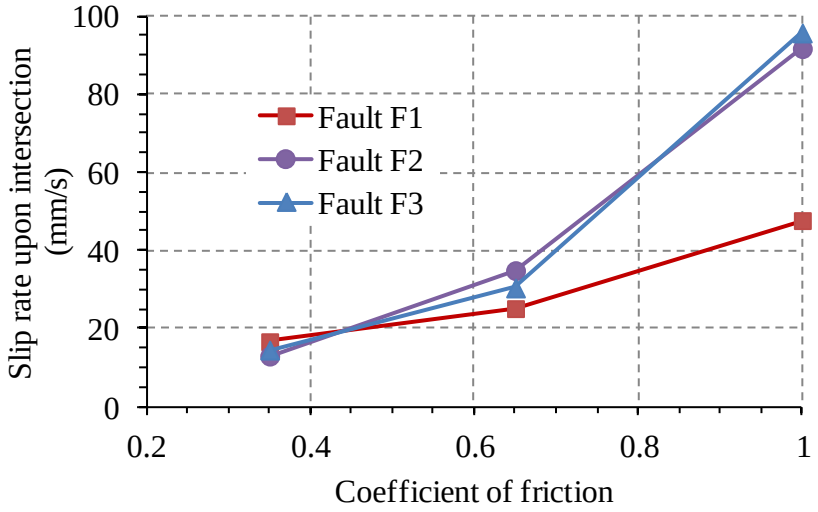

Figure 4.40 Maximum slip rate upon intersection as a function of the friction coefficient

4.3.3 Sensitivity study of injection rate

The effect of the injection rate is studied in this subsection. The injection rate is varied from 0.5 L/s to 2 L/s and the slip rate of the faults is examined. Three cases with different injection rates are listed in Table 4.10. The friction coefficient of all of the three faults is 0.65.

Table 4.10 Injection rates for cases MQ1, MQ2, and MQ3

Case	Injection rate Q (L/s per unit thickness)
MQ1	0.5 (Case MS2 in subsection 4.3.2)
MQ2	1.0
MQ3	2.0

Simulation results and discussion:

The time evolution of the injection pressure and the fluid pressure inside the faults F1, F2, and F3 for all three cases is presented in Figure 4.41. In this figure, the moment when the fluid pressure in a fault suddenly increases corresponds the moment when the fault intersects a hydraulic fracture. As can be seen in Figure 4.41, when the injection rate increases the fracture propagation is faster and intersection events between hydraulic fractures and faults happen earlier. For instance, HF1 intersects F1 at 45.4 s when the injection rate is 0.5 L/s, at 20.5 s when the injection rate is 1 L/s, and at 11.4 s when the injection rate is 2 L/s.

Detailed results of the time evolution of accumulative slip and slip rate of faults for two cases MQ2, and MQ3 are presented in Appendix 3, while results for case MQ1 are the same as the results for case MS2, which were presented in subsection 4.3.2. The slip rate of faults when they are intersected by the hydraulic fractures as function of the injection rate is summarized in Figure 4.42. In general, the maximum slip rate increases with the injection rate. However, it is worth noting that the maximum slip rate is more sensitive to the injection rate in the multiple fault model than in the single fault model studied in subsection 4.2.4. For the single fault model, the maximum slip rate increases less than 40% when the injection is increased 12 times from 0.25 L/s to 3 L/s. In the multiple fault model, for all three faults, the slip rate increases from 45 mm/s to 220 mm/s (an almost 5-fold increase) as the injection rate is raised from 0.5 L/s to 2 L/s (a 4-fold increase). This suggests that the slip of short faults is more sensitive to variations in the injection rate than for longer faults.

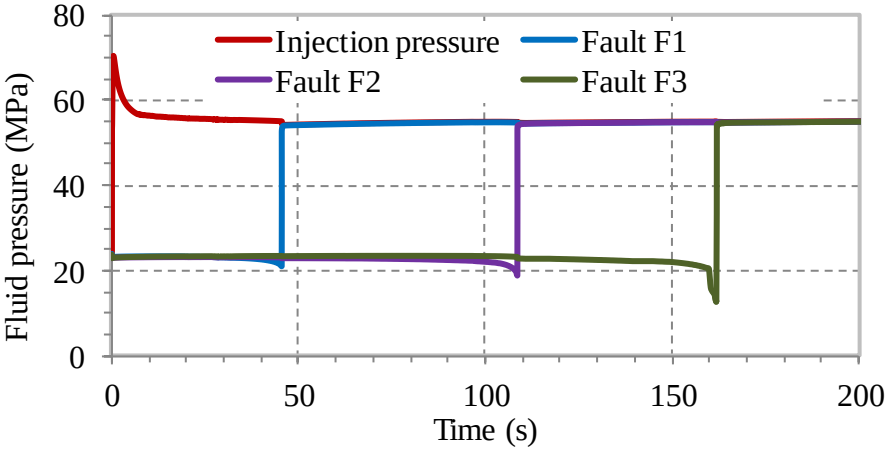

(a) Case MQ1: Q = 0.5 L/s

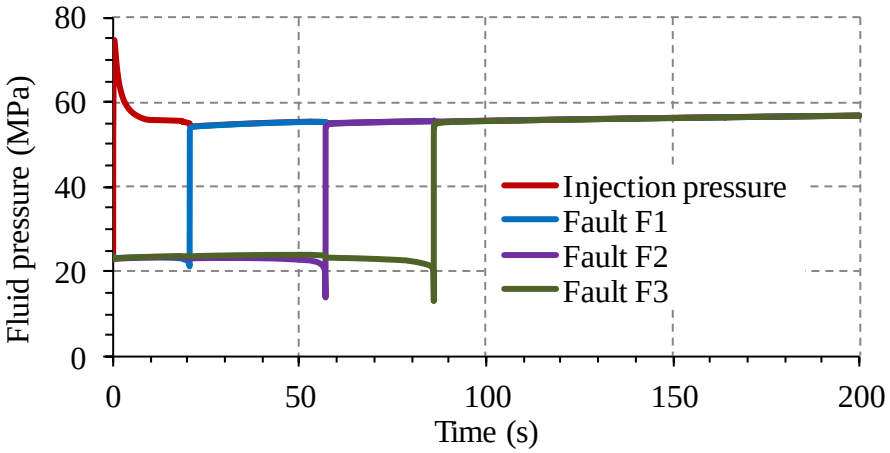

(b) Case MQ2: Q = 1 L/s

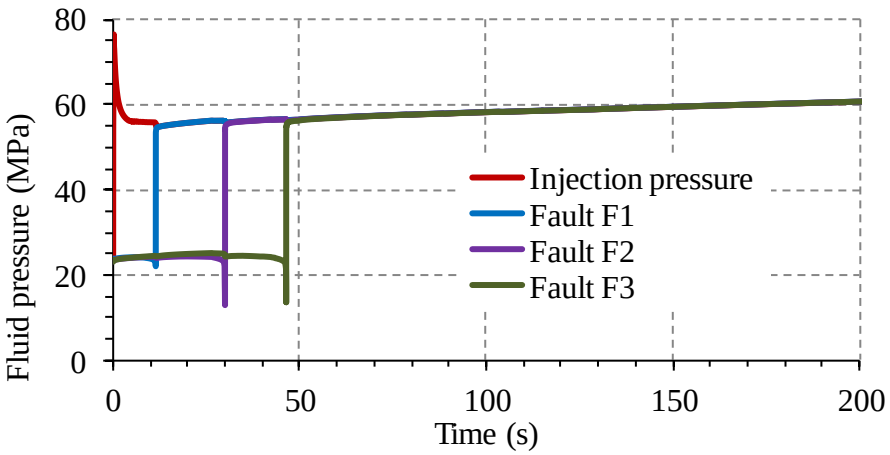

(c) Case MQ3: Q = 2 L/s

Figure 4.41 Time evolution of injection pressure and fluid pressure at the center of faults F1, F2, F3 for cases MQ1, MQ2, and MQ3. The moment when the pressure in a fault suddenly increases corresponds the moment of intersection of the fault with a hydraulic fracture.

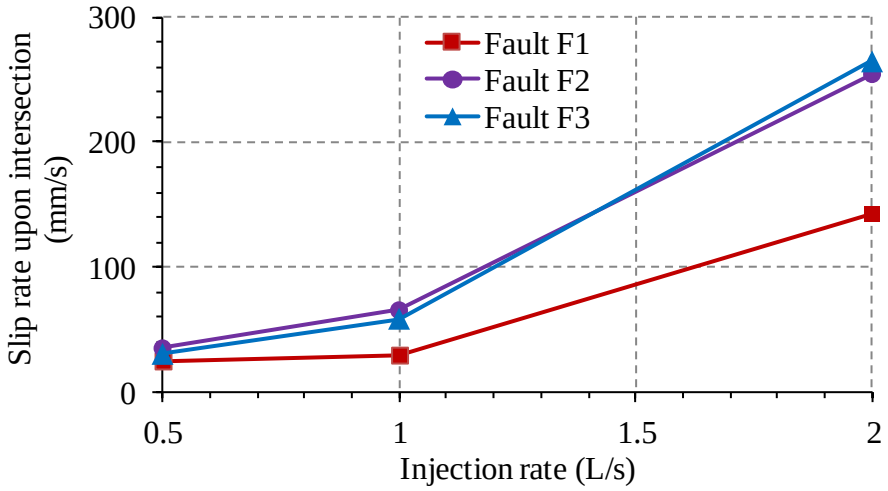

Figure 4.42 Slip rate of faults upon their intersection with hydraulic fractures

4.4 CHAPTER CONCLUSIONS

The propagation of hydraulic fractures and the slip of pre-existing faults in low-permeability poroelastic rock masses were studied. The hydraulic fractures are modeled using the cohesive zone model concept in combination with cohesive elements, while the shear strength of the pre-existing faults is modeled using the Coulomb friction law. It was found that the pre-existing faults slip at higher rates once they are intersected by the hydraulic fractures. This is because during the intersection, the fluid pressure inside the fault increases suddenly, causing the shear strength of the fault to decrease significantly and thus allowing the fault to slip. In most cases studied, the fault slip rate upon intersection is higher than the threshold of the dynamic slip rate, which indicates that the slip event is likely to be seismic.

The effect of the most important parameters on the slip of the pre-existing faults was investigated, including the fault friction coefficient, the injection rate, and the fault orientation with respect to the initial stresses. Faults that are more critically oriented with respect to the initial stresses slip at higher rates when they intersect with hydraulic fractures. Meanwhile, increasing the injection rate also increases the fault slip rate. However, short faults were found to be more sensitive to an increase in the injection rate. The friction coefficient was also found to have a strong influence on the fault slip. As the fault friction coefficient decreased, the fault slip rate upon intersection with hydraulic fracture also decreased. If the friction coefficient is low enough, the fault slip rate can be reduced to levels below the threshold of the dynamic slip

rate. This suggests that it is possible achieve the goal of stimulating a rock reservoir (i.e., activating pre-existing faults and connecting them together) while minimizing the risk of inducing seismic fault slip by reducing the friction coefficient of the pre-existing faults before hydraulic stimulation begins. This could be achieved by appropriate geochemical treatments according to a pre-identification of key minerals within the faulted zones.

At present, only the fault slip rate is used to characterize the dynamic nature of a slip event. However, it is worth noting that the fault slip rate does not provide direct information about the history of the induced seismic waves or the dominant frequency content, both of which are crucial in assessing human perception of the seismic waves and the damage potential to structures. In the next chapter, a modeling procedure to tackling these questions is proposed and a more in-depth analysis of fracture propagation/ fault slip-induced seismic waves is presented. This will provide a source model for induced micro earthquakes from small finite structures that experience shear and extend by developing wing cracks that grow in directions parallel to the most compressive stress (Johnson, 2014). However, contrary to Johnson (2014), who built a dynamic source tensor using the appropriate Green's function, the same dynamic mechanical concepts will be used to simulate seismograms at any location outside the source region.

Chapter 5

Simulation of induced dynamic effects

RÉSUMÉ

Ce chapitre est consacré à l'analyse et à la simulation de l'effet dynamique induit par la propagation de la fracture ou le glissement de la faille (c'est-à-dire les ondes élastiques induites). La toute première question que l'on se posera lorsqu'il s'agira de modéliser les ondes élastiques dynamiques induites par la propagation de fractures ou le glissement de failles est la suivante: comment les ondes élastiques dynamiques sont-elles induites par la propagation de fractures ou le glissement de failles, même lorsque les charges externes sont quasi-statiques? Cette question est plus difficile qu'il n'y paraît, même si la génération d'ondes élastiques dynamiques est un fait incontesté qui a été observé dans de nombreuses expériences quasi-statiques telles que l'essai de compression uniaxiale et l'essai brésilien. Pour apporter une réponse quantitative à ce phénomène, un modèle discret composé de ressorts et de masses élastiques est proposé, puis étendu à un modèle continu en utilisant le concept de matériau cohésif. La réponse à la question posée est progressivement dévoilée, de même que les principaux facteurs qui influent sur l'intensité des ondes élastiques induites.

Ensuite, je vais essayer de réaliser des simulations dynamiques de la propagation des ondes sismiques induites par le glissement de faille. Même s'il est démontré que le concept de matériau cohésif est capable de modéliser le processus de conversion d'énergie (énergie de déformation - énergie cinétique) et donc la génération d'ondes élastiques à partir de dommages matériels, une simulation hydromécanique entièrement couplée prenant en compte les forces d'inertie reste encore trop compliquée. Ainsi, une procédure de modélisation

séquentielle est adoptée pour modéliser les ondes élastiques induites par le glissement de faille en combinant deux simulations distinctes. La première simulation est une simulation de diffusion contrainte-transitoire quasi-statique dans laquelle la propagation de la fracture et le glissement de faille sont modélisés. Cependant, les forces d'inertie sont considérées comme négligeables dans la première simulation. Cette première simulation a été réalisée au chapitre 4, sections 4.2. La deuxième simulation est une simulation dynamique tenant compte des forces d'inertie et visant à modéliser la propagation des ondes élastiques induites par le glissement de la faille. À cette fin, les historiques temporels des déplacements des deux faces de la faille, obtenus à partir de la première simulation, sont considérés comme des charges externes pour la deuxième simulation. Les accélérations calculées à la surface du sol sont ensuite utilisées pour évaluer l'intensité du séisme en relation avec la a perception humaine des ondes sismiques et le potentiel d'endommagement des infrastructures.

SUMMARY

This chapter is focused on the explanation and the simulation of the dynamic effects induced by the fracture propagation or the fault slip (i.e., induced elastic waves). The initial question when it comes to modeling dynamic elastic waves that are induced by fracture propagation or fault slip is: how are dynamic elastic waves induced by the propagation of fractures or the slip of faults, even when the external loads are quasi-static? This question is more difficult than it appears even though the generation of dynamic elastic waves is an undisputed fact that has been observed in numerous quasi-static experiments such as the uniaxial compression test and the Brazilian test. Intuitively and experimentally, the answer is that material damage, such as fracture propagation or fault slip, is the source of the emission of elastic waves. This is true, but a more concrete and quantitative answer is required to model the induced dynamic elastic waves. By studying a discrete model made of elastic springs and masses and then a continuum model using the cohesive material concept, the answer to the fundamental question is gradually unveiled as well as the main factors that affect the intensity of the induced elastic waves

Next, dynamic simulations of the propagation of seismic waves induced by fault slip were performed. Even though the cohesive material concept is capable of modeling the energy conversion process (from strain energy to kinetic energy) and thus the generation of elastic waves resulting from material damage, a fully coupled hydro-mechanical simulation taking into account the inertia forces is still too complex. Thus, a modeling procedure is adopted where the elastic waves induced by fault slip are modeled by combining two sequential simulations. The first simulation, outlined in Chapter 4, sections 4.2, is a quasi-static stress-transient diffusion simulation in which both fracture propagation and fault slip are modeled. However, the inertia forces are considered to be negligible in the first simulation. The second simulation is a dynamic simulation in which the inertia forces are taken into account and it is aimed at modeling the propagation of the elastic waves induced by the fault slip. For this purpose, the time histories of the displacements of the two faces of the fault, obtained from the first simulation, are considered as the external loads for the second simulation. The radiation patterns can be obtained and the computed accelerations on the ground surface are then used to assess the human perception of the seismic waves and the damage potential to structures.

5.1 INTRODUCTION TO INDUCED MICROSEISMICITY

Induced microseismicity refers to the generation of seismic waves due to the slip of pre-existing faults or the propagation of brittle fractures (Hardy Jr, 2003; Swindlehurst, 1973). When a brittle material is loaded to some extent, atomic bonds between the atoms are broken, allowing the fracture to form and propagate. The strain energy of the system is altered and some of the strain energy is converted into kinetic energy in the form of elastic waves, which can be transmitted through the medium and recorded by seismic sensors. A schematic representation of the generation of seismic waves from fracture propagation is shown in Figure 5.1. The generation of seismic waves due to fault slip is somewhat similar: when the stress on fault exceeds the fault strength, either due to the reduction of the fault shear strength or an increase of the shear stress, the fault slips and a part of the strain energy is released in the form of seismic waves (Ellsworth, 2013).

The fault slip that occurs during hydraulic stimulation of geothermal reservoirs is typically tied to the reduction of shear strength of the fault due to an increase in the fluid pressure within the fault. It should be noted, however, that the slip of faults can be seismic (i.e., generating detectable seismic waves) or aseismic (i.e., not generating detectable seismic waves). In in-situ experiments, direct measurement of the ground motions (e.g., particle velocity or acceleration) during the fault slip can distinguish whether the fault slip is seismic or aseismic. In numerical simulation studies, the slip rate of the fault is generally accepted as a parameter to assess the dynamic character of the slip event (Cappa et al., 2018; Dublanchet et al., 2013; McClure and Horne, 2011, 2014).

Microseismic monitoring has been the only tool for assessing the development of enhanced geothermal reservoirs (Baria et al., 1989; Baria et al., 2004; Schill et al., 2017). The underlying idea behind the use of microseismic monitoring as a mapping tool is that the locations of the seismic events are considered to be a proxy for the presence of hydraulic fractures or the activation of pre-existing faults. Thus, the development of the seismic "cloud", also known as a swarm of events, provides information about the development and dimensions of the reservoir accessible to fluid. Microseismic source characteristics can also be inferred from the recorded waveforms (Gibowicz et al., 1991; Pearson, 1982; Wang and Tao, 2003).

Furthermore, real time monitoring of microseismicity can provide useful information for guiding the injection operation.

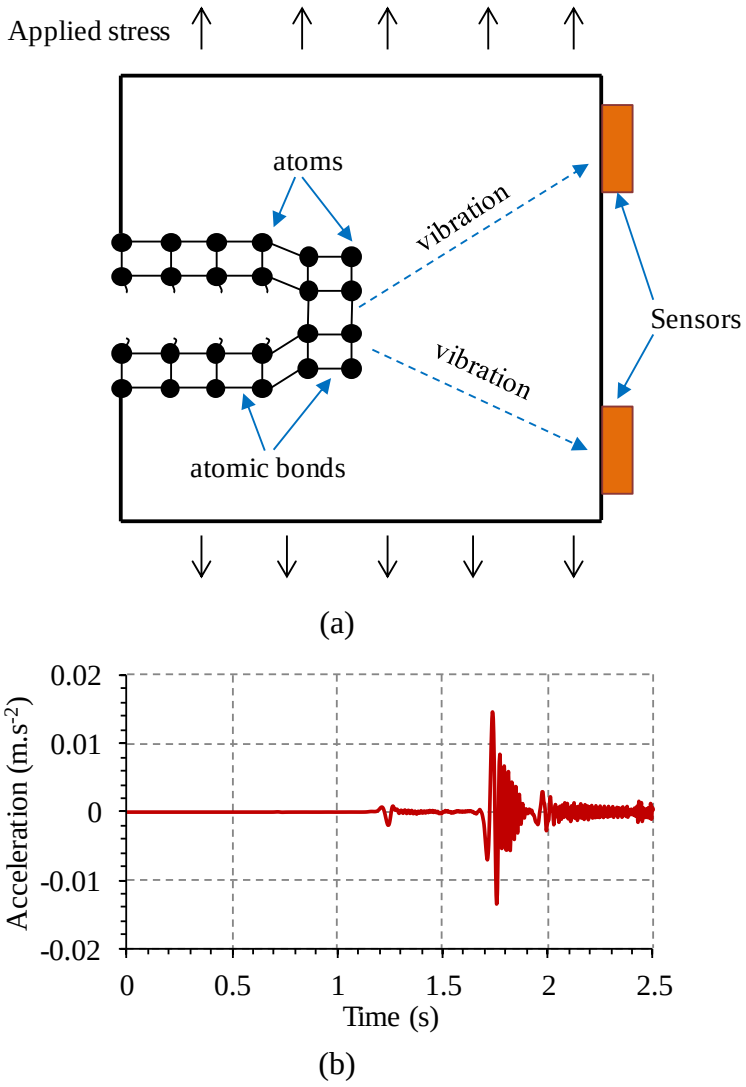

Figure 5.1 (a) Illustration of generation of elastic waves from fracture propagation, (b) Example of seismic signal (e.g., acceleration) recorded by sensors

In order to measure the "size" of a seismic event, various magnitude scales have been derived. Classical magnitude scales, which are calculated from the displacement amplitude of ground motion, include the local scale M_L for local seismic events and m_B or M_S for teleseismic events (Gutenberg and Richter, 1956; Richter, 1935). In 1977, the moment magnitude M_W was introduced by Kanamori (1977) and has since then been considered as the only well defined,

non-saturating magnitude scale and estimator of seismic events (Bormann and Di Giacomo, 2011). The moment magnitude is defined as:

$$M_W = \frac{2}{3}\left(\log_{10} M_0 - 9.1\right) \tag{5.1}$$

where M_0 is the seismic moment, which is related to the fundamental parameters of the faulting process including the average rigidity of the faulted rock μ, the rupture area S, and the average displacement on the fault D as:

$$M_0 = \mu SD \tag{5.2}$$

It should be noted that the seismic moment is the change in strain energy of the rock mass before and after the fault slips (i.e., strain energy release). Equation (5.2) was proposed by Kanamori (1977) based on analysis of the stress around a shear fracture embedded in an elastic medium by Knopoff (1958).

It is worth noting that not all of the strain energy release during fracture propagation or fault slip is converted into seismic waves. A large portion of the strain energy release goes into creating new surfaces and melting the rock. Thus, the use of the seismic moment (i.e., strain energy release) to estimate the seismic magnitude assumes that a proportion of the strain energy release is actually being released in the form of seismic waves. In fact, only a tiny fraction of the strain energy release, roughly about $5x10^{-5}$, is converted into seismic waves (Bormann and Di Giacomo, 2011; Kanamori, 1977).

Although the moment magnitude M_W has some advantage over the classical magnitude scales, it is still a static measure of the seismic event, i.e., based on the difference in strain energy before and after the fault slips. Thus, M_W does not provide direct information about the time history of the seismic waves, which is crucial in assessing the human perception of the seismic waves and the damage potential to structures.

The effect of the induced elastic waves on human perception and on structures on the ground surface can be quantified using the peak ground acceleration (PGA) or the peak ground velocity (PGV). By comparing horizontal peak ground motions to observed intensities for significant earthquakes in California, (Wald et al., 1999) proposed a regression relationship

between PGA or PGV and the Modified Mercalli intensity. The Modified Mercalli intensity scale was introduced by Wood and Neumann (1931) to quantify the shaking pattern and the potential damage of earthquakes. An abbreviated description of the levels of Modified Mercalli intensity and the corresponding PGA and PGV is given in Table 5.1.

Table 5.1 Modified Mercalli intensity scale and corresponding peak ground acceleration and peak ground velocity. Source: Wald et al. (1999), Wood and Neumann (1931)

Intensity	**Peak acceleration (%g)**	**Peak velocity (cm/s)**	**Perceived shaking**	**Potential damage**
I	< 0.17	< 0.1	Not felt	None
II–III	0.17 – 1.4	0.1 – 1.1	Weak	None
IV	1.4 –3.9	1.1 – 3.4	Light	None
V	3.9 – 9.2	3.4 – 8.1	Moderate	Very light
VI	9.2 –18	8.1 – 16	Strong	Light
VII	18 –34	16 – 31	Very strong	Moderate
VIII	34 –65	31 – 60	Severe	Moderate to heavy
IX	65 – 124	60 – 116	Violent	Heavy
X+	> 124	> 116	Extreme	Very heavy

5.2 MODELING OF INDUCED DYNAMIC EFFECTS

5.2.1 Introduction

Currently, three main numerical methods are used to model induced microseismicity: the finite element method in combination with damage mechanics, the discrete element method, and the combined finite-discrete element method.

In the finite element method, the fracturing process is modeled using damage mechanics (Kaiser and Tang, 1998; Tang, 1997; Tang and Kaiser, 1998). The material adopts a damageable constitutive law and microseismicity is simulated based on the assumption that

the number of induced seismic events is proportional to the number of elements that are damaged. The strain energy released in the damaged elements is considered analogous to seismic energy.

In discrete element models, the material is represented as an assemblage of particles that have the shape of a circular disc for 2D models or a sphere for 3D models (Cundall and Hart, 1992; Potyondy and Cundall, 2004). These particles are bonded together and interact with each other at contact points where constitutive contact laws are required to describe their normal and shear interactions. When the shear or tensile stress exceeds the shear or tensile strength of a contact bond, the contact bond is broken, allowing a crack to initiate and propagate. The magnitude of an induced seismic event is calculated based on the change in kinetic energy of particles before and after one or several bonds are broken. The method was used by Hazzard and Young (2000, 2004) to simulate triaxial compression tests and a mine-by tunnel experiment. The authors showed that the model was capable of reproducing the Gutenberg-Richter relationship between the magnitude and the number of induced seismic events with the numerical *b*-value situated within the range found in experiments. Note that the Gutenberg-Richter relationship is expressed as:

$$\log N = a - bM \tag{5.3}$$

where M is a magnitude scale, N is the number of events having a magnitude larger or equal to M, a and b are two positive constants. The constant b (i.e., the b-value), typically close to 1, is a parameter describing the relative abundance of large to smaller events (Okal and Romanowicz, 1994).

In the combined finite-discrete element method, the intact material is typically assumed to be linear elastic and is modeled by finite elements. Cohesive elements are inserted between the finite elements to model the fracture initiation and propagation (Munjiza, 2004). Once the fracture has occurred, the blocks of material are created and treated as discrete blocks. The kinetic energy that is induced by the fracture propagation is considered to be the seismic energy. This method has been used by Lisjak et al. (2013) to simulate induced seismic effects in an unconfined compression test on granite. The authors reported that the magnitudes of the

simulated events tended to display a power-law distribution, with *b* values in agreement with those reported in the literature for granitic rocks.

The three numerical methods briefly presented above have been successful to some extent in reproducing several features of the dynamic effects that are induced by fracture propagation (e.g., *b*-value in the range found in experiments). However, the following fundamental questions (FQ) have not been fully resolved in these simulations:

- FQ1: How are dynamic effects generated through fracture propagation even when the loading is quasi-static?
- FQ2: How much of the strain energy is converted into kinetic energy?
- FQ3: What are the most important parameters that influence the induced dynamic effects?

Some explanations can be found as answers to these questions. For question FQ1, the brittle nature of the fracture propagation can induce dynamic effects even when the loading rate is quasi-static. Many experiments have shown that microseismicity is induced by fracture propagation (Keshavarz et al., 2008; Moradian et al., 2016). For question FQ2, (Kanamori, 1977) proposed that a fraction, $2x10^{-5}$, of the strain energy change is converted into the kinetic energy of induced elastic waves. For the question FQ3, several authors have reported some relationship between the velocity of fracture propagation or fault slip rate and the intensity of the induced dynamic effects (Boudet et al., 1995; Fineberg et al., 1992). These explanations are plausible but they still have not answered the above questions in a concrete and quantitative way. In this section, I will attempt to quantitatively resolve these questions.

5.2.2 Explanations using discrete models

From an energy balance point of view, the generation of elastic waves from the fracture of a material is a process of conversion of strain energy into kinetic energy. A physics-based approach that models the induced elastic waves must be able to model this energy conversion process. The only model (that I know of so far) that illustratively explains the strain energy-kinetic energy conversion was proposed by Pollock (1973) and is presented in Figure 5.2. The model consists of a mass *m* suspended by two springs of stiffness *K*. The stiffness of the lower spring is assumed to instantaneously change by an amount δK. As the stiffness of the system

suddenly changes, the mass will move toward and vibrate around a new equilibrium position. The change in strain energy before and after the change in stiffness ΔE_s and the peak kinetic energy of the mass E_{kin} are, according to (Pollock, 1973):

$$\Delta E_s = \frac{1}{8}\delta K \cdot x^2 \quad ; \quad E_{kin} = \frac{1}{8}\frac{(\delta K)^2}{K}x^2 \tag{5.4}$$

where x is initial extension of the spring system due to the self weight of the mass m. From equation (5.4) the ratio between the kinetic energy and the change in strain energy can be obtained as $\Delta E_s / E_{kin} = \delta K / K$.

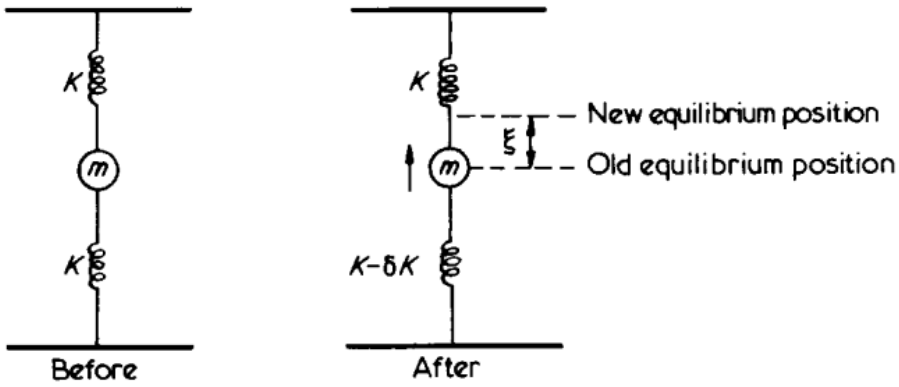

Figure 5.2 A spring-mass model. Source: Pollock (1973)

The model by Pollock shows that the amount of induced kinetic energy is proportional to the change in the stiffness of the system. For a continuum material, the stiffness change can originate from the propagation of fractures.

To more clearly illustrate the generation of dynamic effects from the damage regardless of the loading rate, I also use a mass-spring model as shown in Figure 5.3. The model consists of two masses M1 and M2, and two springs 1 and 2. Each spring is characterized by its stiffness and its tensile strength: K_1 and R_1 for spring 1, K_2 and R_2 for spring 2, with R_2 smaller than R_1 ($R_2 < R_1$). The system is loaded by controlling the displacement of the mass M2, as illustrated in Figure 5.3. As the mass M2 is slowly pulled downwards, internal forces of the same magnitude are generated in both the springs. At some point the internal force in the spring 2 reaches its tensile strength R_2, and spring 2 breaks. Assume that the damage of spring 2 is

instantaneous. At this time, the mass M1, displaced from its initial position a distance *a*, is free to move. The movement of the mass M1 after spring 2 is broken is a harmonic vibration with the following characteristics:

- Displacement of M1:

$$x = a\cos(\omega t) \tag{5.5}$$

- Velocity of M1:

$$v = -\omega a\sin(\omega t) \tag{5.6}$$

- Kinetic of M1:

$$E_k = \frac{1}{2}m_1 v^2 = \frac{1}{4}K_1 a^2\left[1-\cos(2\omega t)\right] \tag{5.7}$$

- Strain energy of spring 1:

$$E_p = \frac{1}{2}K_2 x^2 = \frac{1}{4}K_2 a^2\left[1+\cos(2\omega t)\right] \tag{5.8}$$

where ω is the angular frequency; and a is the displacement of the mass M1 when spring 2 is broken and is equal to R_2/K_1. Thus the maximum kinetic energy E_{kmax} of the mass M1 is:

$$E_{k\max} = \frac{1}{2}K_1 a^2 = \frac{1}{2}\frac{R_2^2}{K_1} \tag{5.9}$$

The time evolution of the kinetic and the strain energy is presented in Figure 5.4. From equations (5.5) to (5.9) and Figure 5.4, the following remarks can be made:

(i) The kinetic energy of the mass M1 is proportional to the tensile strength of the spring 2 and is inversely proportional to the stiffness of the spring 1 (equation (5.9))

(ii) There is a conversion between kinetic and strain energy: when the kinetic energy is zero the strain energy is a maximum, and vice versa (Figure 5.4)

(iii) The frequency of the kinetic energy and strain energy is double that of the frequency of the displacement or the velocity (equation (5.5) to (5.8) and Figure 5.4)

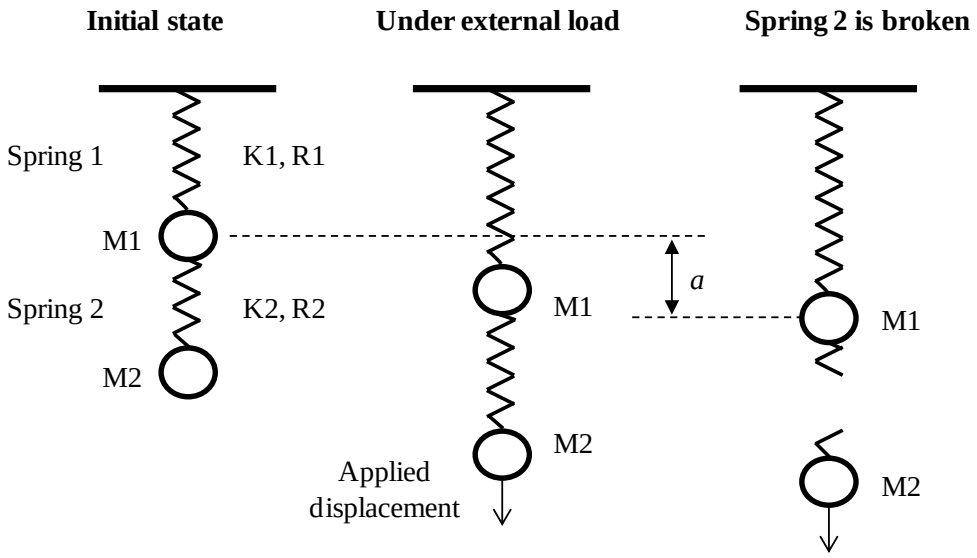

Figure 5.3 New spring-mass model. K1 and R1 are the stiffness and strength of spring 1, K2 and R2 are the stiffness and strength of spring 2.

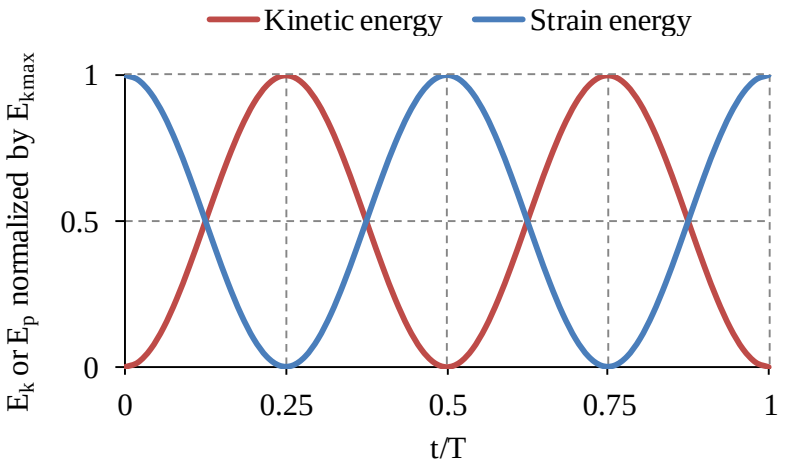

Figure 5.4 Time evolution of kinetic energy and strain energy. T is the period of the vibration of the mass M1

In the above calculation the strain energy of spring 2 and the energy loss due to the breakdown of the spring 2 are not included. For a discrete system of springs and masses, these simplifications are acceptable. The calculation shows clearly that the intensity of the induced dynamic effects, which is reflected by the maximum kinetic energy, depends on two factors: the strength and the stiffness of the system. Also, the kinetic energy of the mass M1 is shown to be independent of the rate of the applied displacement, which means that no matter how slowly the displacement is applied, the mass M1 will vibrate harmonically once spring 2 is

broken and the kinetic energy of the mass M1 will remain the same. By using this simple spring-mass model, the questions FQ1 and FQ3 are clearly and quantitatively resolved.

5.2.3 Explanations using continuum model: analytical calculation

Here the cohesive zone model is used to model the fracture in a uniaxial tension test of a plate and show that elastic waves can be induced even when the loading rate is quasi-static. The plate studied is shown in Figure 5.5. The height of the plate is L. The plate consists of two parts; the first part is a zero-thickness layer of cohesive material whose cohesive constitutive law is characterized by tensile strength R_T and fracture toughness G_{IC} (Figure 5.6). The second part is made of a linear elastic material, which is characterized by Young's modulus E and Poisson's ratio v. The loading is given by controlling the displacement rate of the top edge of the plate (Figure 5.5). As the applied displacement increases, the cohesive layer will be damaged and the separation rate of the cohesive layer is calculated. In this subsection, only the phase after damage initiation in the cohesive layer is considered, i.e., after the stress in the cohesive layer has reached the tensile strength and the two faces of the cohesive layer start to separate.

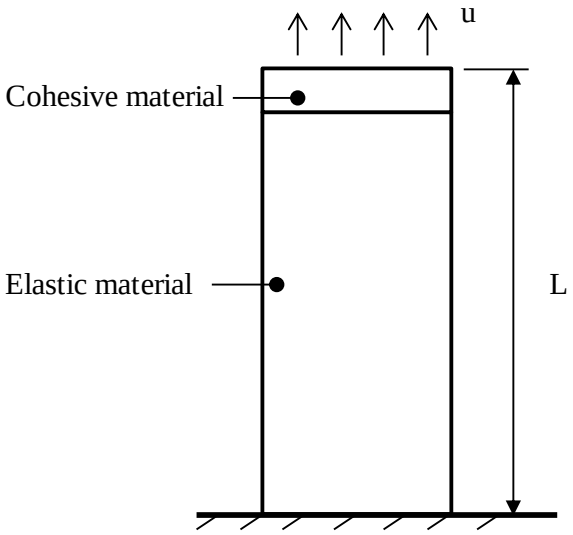

Figure 5.5 Plate model made of two materials. The cohesive layer has zero thickness. The sketch is not to scale

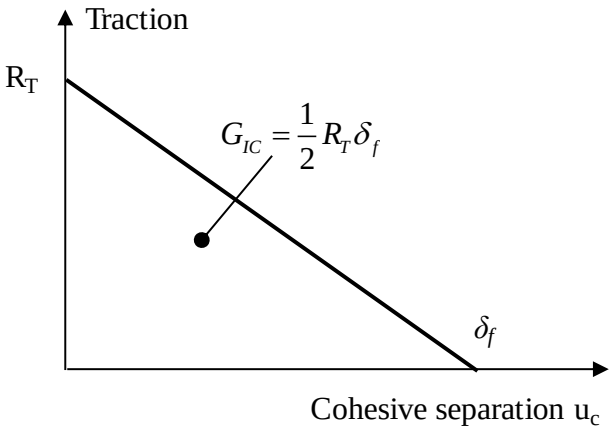

Figure 5.6 Cohesive traction-separation law

For each increment of stress in the cohesive layer $\Delta\sigma$ ($\Delta\sigma < 0$), the corresponding displacement increment at the top edge of the plate Δu consists of two components as follows:

$$\Delta u = \Delta u_c + \Delta u_s \tag{5.10}$$

where Δu_c is the separation increment of the cohesive layer and Δu_s is the change in length of the elastic part. Δu_c and Δu_s are determined by:

$$\begin{aligned} \Delta u_c &= \frac{\Delta\sigma}{K(u_c)} \\ \Delta u_s &= \frac{\Delta\sigma}{E} L \end{aligned} \tag{5.11}$$

where $K(u_c)$ is the slope of the cohesive traction – separation curve (Figure 5.6), which is $-R_T / \delta_f$ once the damage initiation occurs. Combining equations (5.10) and (5.11):

$$\Delta u_c = \frac{1}{1 - \frac{R_T}{E}\frac{L}{\delta_f}} \Delta u \tag{5.12}$$

Both sides of equation (5.12) are divided by Δt, the time increment during which the stress increment $\Delta\sigma$ takes place, which gives:

$$\dot{u}_c = \frac{1}{1 - \frac{R_T}{E}\frac{L}{\delta_f}} \dot{u} \tag{5.13}$$

Since $G_{IC} = 0.5 R_T \delta_f$, equation (5.13) can be rewritten as:

$$\dot{u}_c = \frac{1}{1 - \frac{R_T{}^2 L}{2 G_{IC} E}} \dot{u} \tag{5.14}$$

In equation(5.14), $\dot{u}_c$ and $\dot{u}$ are the separation rate of the cohesive layer and the applied displacement rate, respectively. Denote α as:

$$\alpha = \frac{R_T{}^2 L}{2 G_{IC} E} \tag{5.15}$$

And equation (5.14) then becomes:

$$\dot{u}_c = \frac{1}{1 - \alpha} \dot{u} \tag{5.16}$$

From equation (5.16), we can see that as $\alpha \rightarrow 1$ the separation rate of the cohesive layer $\dot{u}_c$ will become very large regardless of the applied displacement rate. A high separation rate for the cohesive layer means that elastic waves are generated.

It can also be seen that if the length of the plate is large enough, α can be larger than 1. In such cases $\dot{u}_c$ becomes negative. However, as the applied displacement continues to increase after damage initiation of the cohesive layer has occurred, the separation of the cohesive layer will increase with time and thus $\dot{u}_c$ must be positive. This leads to the realization that in cases where $\alpha > 1$ the calculation above is no longer valid. In fact, in the above calculation it is assumed that when the stress in the cohesive layer is changed by an increment $\Delta\sigma$, the whole plate experiences the same stress increment $\Delta\sigma$. This is indeed the case as long as $\alpha < 1$. When $\alpha > 1$, if the stress in the cohesive layer is changed by $\Delta\sigma$, it will not affect the whole plate instantaneously. Instead, the stress change will "propagate" as elastic "stress" waves from regions near the cohesive layer to outlying regions without dependence on the applied displacement rate. The length L of the plate can be seen as a characteristic length of the material. A closer look at α shows that α is in fact the ratio between the change in strain energy before damage initiation, $R_T{}^2 L / (2E)$, and the energy loss due fracture G_{IC}.

In conclusion, if the strain energy that is released during the fracture propagation is larger than the energy needed to create new fracture surfaces (i.e., the fracture energy), elastic waves will be generated regardless of the loading rate. The intensity of the induced elastic waves is proportional to the ratio between the strain energy release and the fracture energy.

5.2.4 Explanations using a continuum model: numerical simulation

The model presented in subsection 5.2.3 is numerically investigated. Again, the objective is to model the elastic waves induced by the fracture and investigate the factors that influence the intensity of the induced elastic waves. The following points will be demonstrated using the numerical simulations:

(i) Elastic waves are induced if α, i.e., the ratio between the change in strain energy E_S before and after fracture occurs and the energy loss due to the fracture E_F, is larger than 1 (subsection 5.2.4.1)

(ii) The loading rate does not affect the induced elastic waves (subsection 5.2.4.2)

(iii) The intensity of the induced elastic waves also increases if α increases (subsection 5.2.4.3)

5.2.4.1 Reference simulation when $\alpha > 1$

The plate studied has a width W = 0.2 m and length L = 1 m. The top edge of the plate is pulled upwards at a constant and relatively small rate such that the loading does not introduce any dynamic effects. In this simulation, a displacement rate of 9 mm/s, which corresponds to a strain rate 0.009 s^{-1}, is chosen. This loading rate may seem too high, but as shown later this displacement rate actually does not cause any significant dynamic effect on the system.

The three other edges of the plate are fixed. An illustration of the model with boundary conditions and loading is given in Figure 5.**7**. With these boundary conditions and loading, the problem is equivalent to a 1D problem and only the displacement, velocity, and acceleration in direction 2 are non-zero. Thus, in the following the words displacement, velocity, and acceleration are used to describe the displacement, velocity, and acceleration in direction 2. Parameters for the cohesive material and the linear elastic material are presented in Table 5.2.

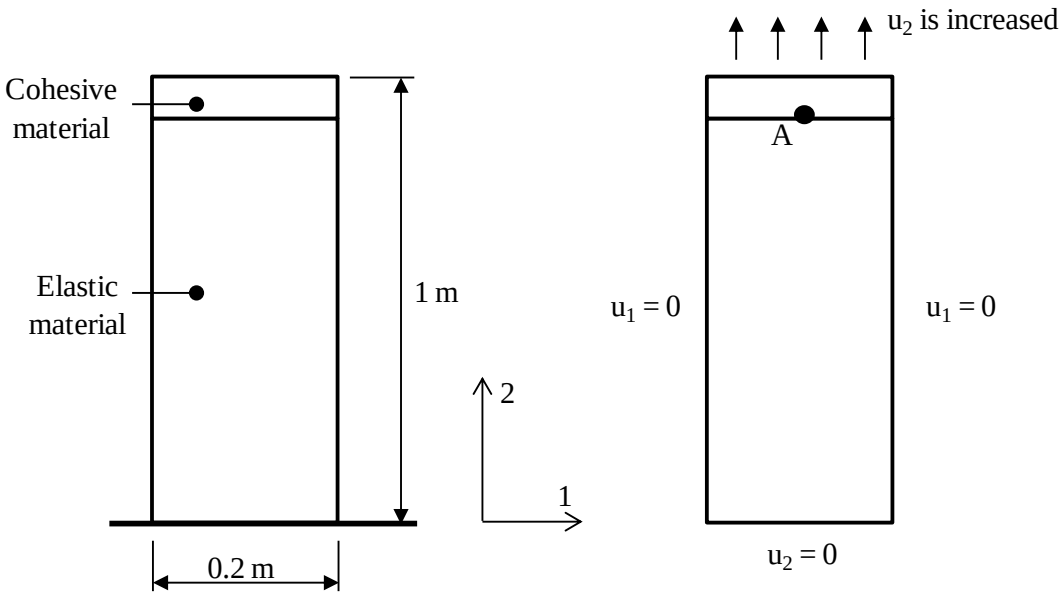

Figure 5.7 Dimensions of the plate, boundary conditions and loading

Table 5.2 Material properties

Property	**Value**
Cohesive material	
Tensile strength	R_T = 2.6 MPa
Fracture toughness	G_{IC} = 25 J/m^2
Linear elastic material	
Young's modulus	E = 30 GPa
Poisson's ratio	ν = 0.22
Density	ρ = 2500 kg/m^3
P-wave speed	C_p = 3464 m/s

With these selected parameters, the following can be calculated:

- The maximum strain energy available for release is:

$$E_S = \frac{R_T{}^2 L}{2E} W = \frac{(2.6\times10^6)^2 \times 1}{2\times30\times10^9} \times 0.2 = 22.5 \text{ J} \tag{5.17}$$

- The energy loss due to fracture is:

$$E_F = G_{IC} \times W = 25 \times 0.2 = 5 \text{ J} \tag{5.18}$$

From equations (5.17) and (5.18), α is calculated as:

$$\alpha = \frac{E_S}{E_F} = \frac{22.5}{5} = 4.5 \tag{5.19}$$

Since α is larger than 1, elastic waves are expected to be induced after damage to the cohesive layer has occurred.

Simulation results:

A contour plot of the normal stress S22 in direction 2 during one period from the beginning of damage to the cohesive layer is presented in Figure 5.8. Here, one period is defined as the time it takes the induced elastic waves to propagate from the top edge of the plate to the bottom edge, reflect off this edge and propagate back to the top edge. The damage of the cohesive layer begins at approximately 8 ms when the tensile stress is equal to the tensile strength (Figure 5.8a). Then, the stress in the region near the cohesive layer begins to decrease (Figure 5.8b). The stress decrease propagates toward the bottom of the plate as stress waves. Once the stress waves reach the bottom edge (Figure 5.8c), they are reflected back (Figure 5.8d) and move toward the top edge (Figure 5.8e, f). It can also be seen that the sign of the stress changes from positive to negative as the stress waves are reflected of the bottom edge (Figure 5.8d, e). The distribution of stress in direction 2, S22, along the length of the plate at times corresponding to those in Figure 5.8 is presented in Figure 5.9. The propagation of the stress decrease and the reflection of the stress waves are clearly observed.

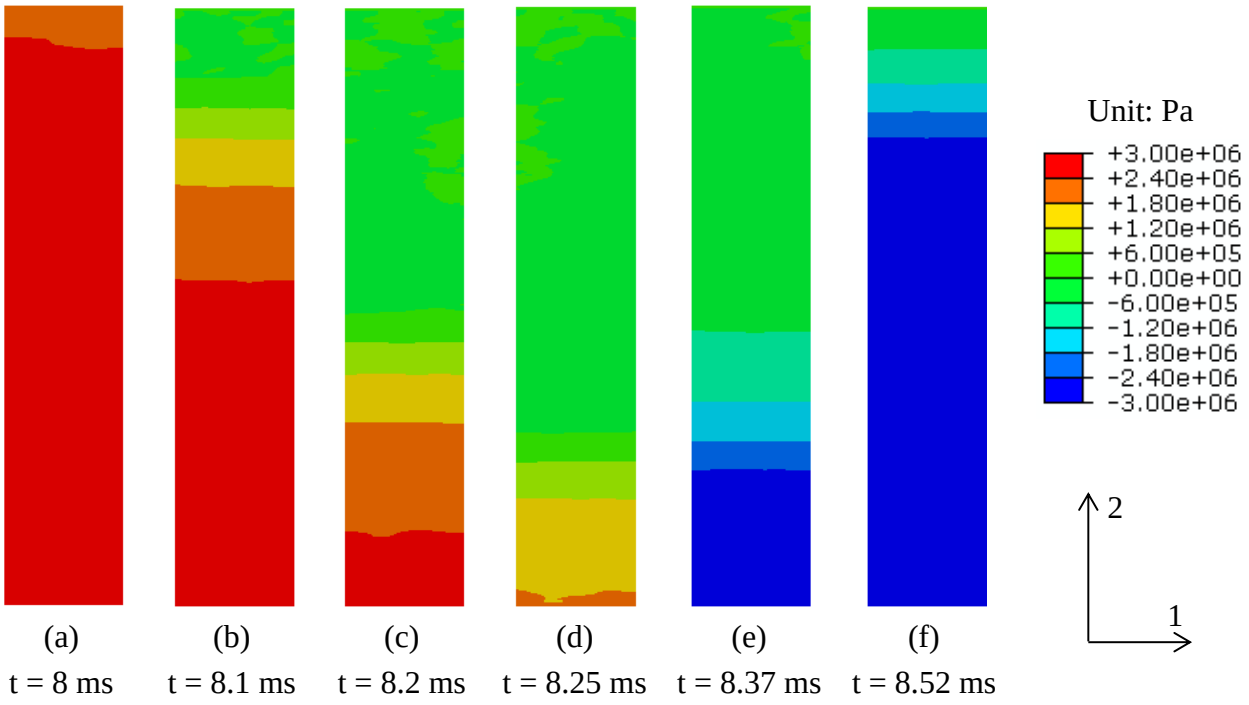

Figure 5.8 Normal stress S22 in direction 2 during one period after the damage to the cohesive layer. The damage begins at time t = 8 ms

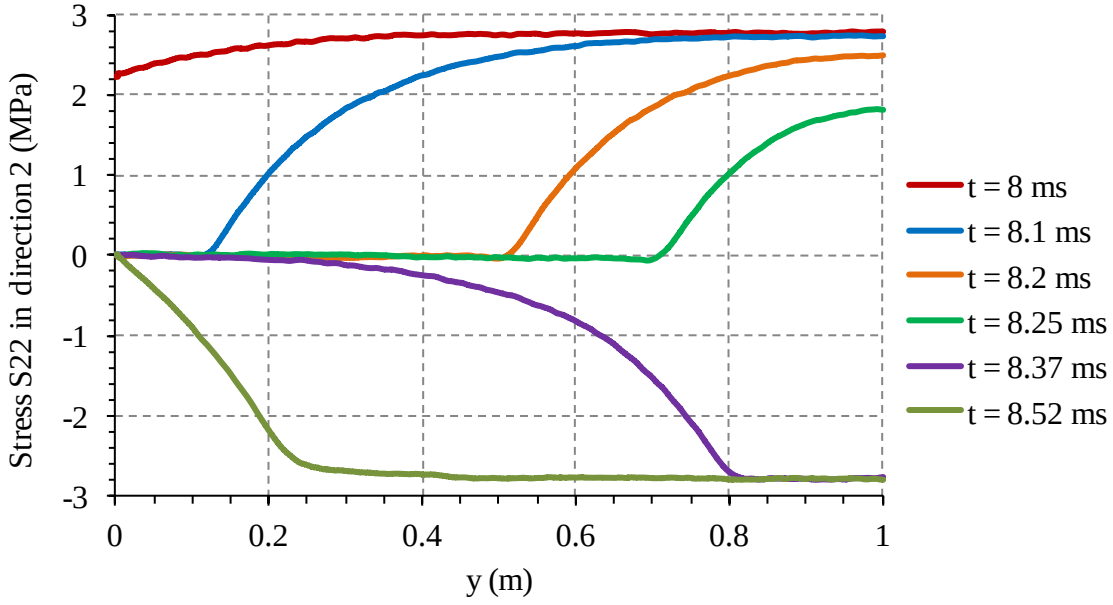

Figure 5.9 Stress S22 along the length of the plate at different times corresponding to those of Figure 5.8. The damage begins at time t = 8 ms. The top and bottom edges of the plate are located at y = 0 and y = 1, respectively.

The computed time evolution of displacement and velocity of the point A (Figure 5.**7**) is presented in Figure 5.10. It can be seen that the displacement increases linearly at first, and then starts to decrease as the cohesive layer is damaged. But instead of decreasing to zero, it oscillates around the zero-position. A similar evolution pattern is observed for the velocity: the velocity is relatively small before the damage of the cohesive layer, but starts to increase once the cohesive damage occurs and oscillates afterward. The maximum velocity of the point A is 0.32 m/s, which is 35.5 times the applied displacement rate. Both the displacement and the velocity oscillate with the same period of approximately 1.6 ms.

The time evolution of the different types of energy in the whole model (strain energy, kinetic energy, and fracture energy) is presented in Figure 5.11. The strain energy increases at first and then starts to decrease when cohesive damage occurs, while the kinetic energy remains close to zero before the cohesive damage and starts to increase when the cohesive damage occurs. The fact that the kinetic energy is close to zero before cohesive damage insures that the relatively high applied displacement rate used in the simulation has a negligible effect on the solution. After cohesive damage, both the strain energy and the kinetic energy oscillate harmonically with the same period of approximately 0.8 ms. These two types of energy are also converted back and forth into each other: when the kinetic energy is zero the strain energy is largest and vice versa. The maximum value of the kinetic energy after damage to the cohesive material is approximately 17.5 J. The energy dissipated due to the damage of the cohesive layer, i.e., the fracture energy, increases suddenly from 0 to 5 J upon the damage of the cohesive layer. This value of fracture energy is equal to the predicted value in equation (5.18).

It is worth noting that the oscillation period of the displacement and the velocity (T = 1.6 ms) is double that of the kinetic and strain energies (T = 0.8 ms). This observation, also obtained in discrete spring-mass model, is clearly illustrated in Figure 5.12.

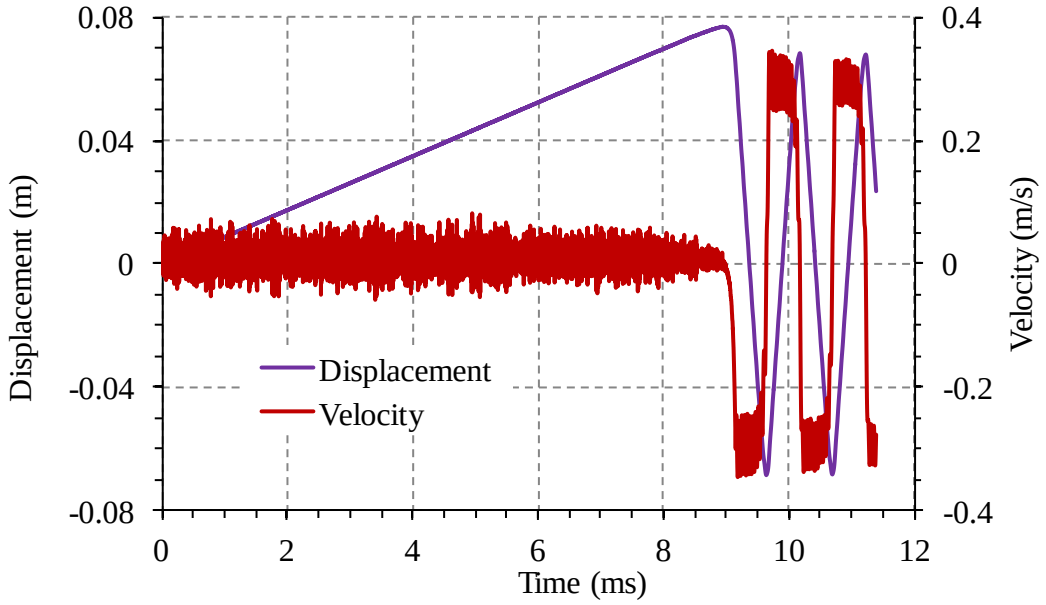

Figure 5.10 Time evolution of displacement and velocity of point A

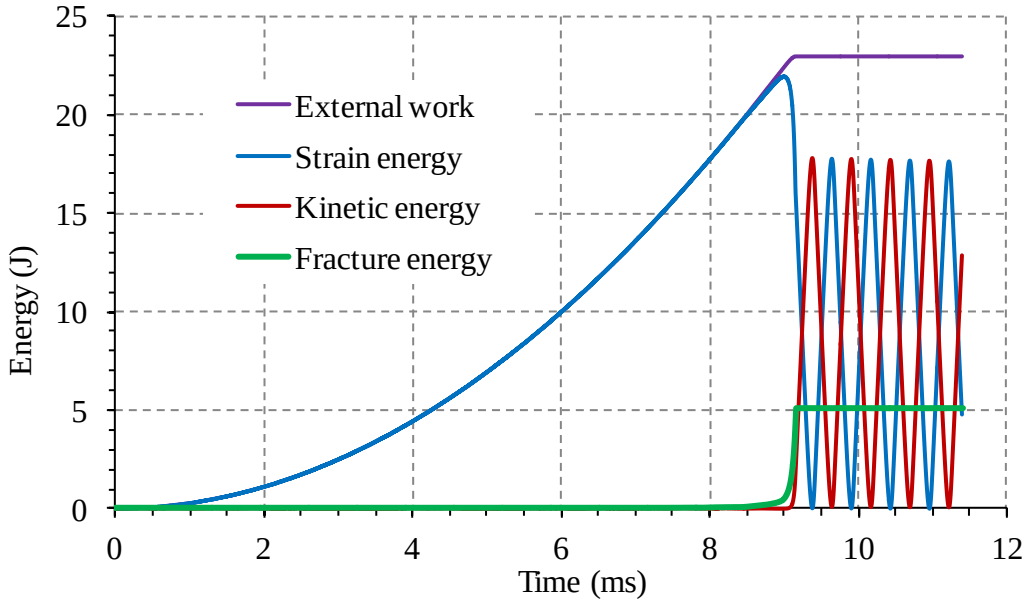

Figure 5.11 Time evolution of different types of energy in the model

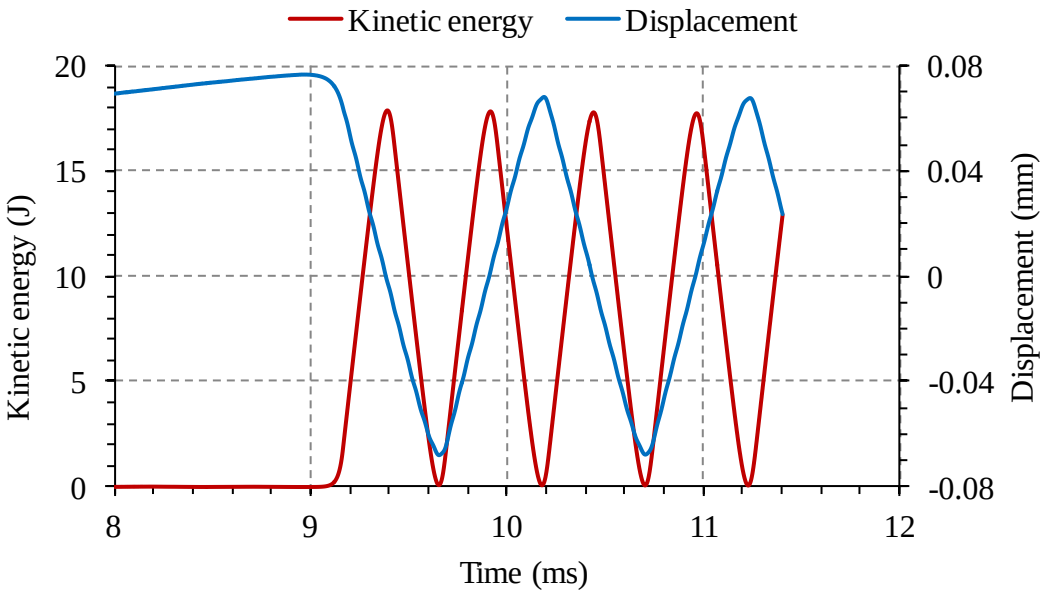

Figure 5.12 Time evolution of the kinetic energy and displacement showing that the oscillation period of the displacement is double that of the kinetic energy

5.2.4.2 Influence of the applied displacement rate

In the previous numerical simulation (subsection 5.2.4.1), the applied displacement rate is increased so that the loading duration can be reduced, which in turn reduces the computation time. To demonstrate that the increase of the applied displacement rate has a negligible effect on the final results, the simulation is re-run with a displacement rate of 0.9 mm/s, which is ten times smaller than in the previous case.

The simulation results are presented in Figure 5.13 for the time evolution of displacement and velocity of the point A and in Figure 5.14 for the time evolution of different types of energy. The damage of the cohesive material occurs at around 77 ms. After that, trends for the time evolution are seen to be identical to the previous case. For instance, after damage to the cohesive material, the displacement and the velocity of the point A and kinetic and strain energies oscillate. The oscillation period of the kinetic and strain energies is approximately 0.8 s (Figure 5.14b), while the displacement and velocity of the point A oscillate with a period of approximately 1.6 s (Figure 5.13b). These periods are identical to those that were obtained in the previous case. The maximum velocity of the point A is 0.32 m/s and the maximum kinetic energy is 17.5 J, which are again identical to those obtained in the previous case. Thus, the simulation shows that the reduced applied displacement rate only expands the elastic

deformation phase and delays the damage of the cohesive layer. After the cohesive layer is damaged, the behavior of the model is identical to the previous case.

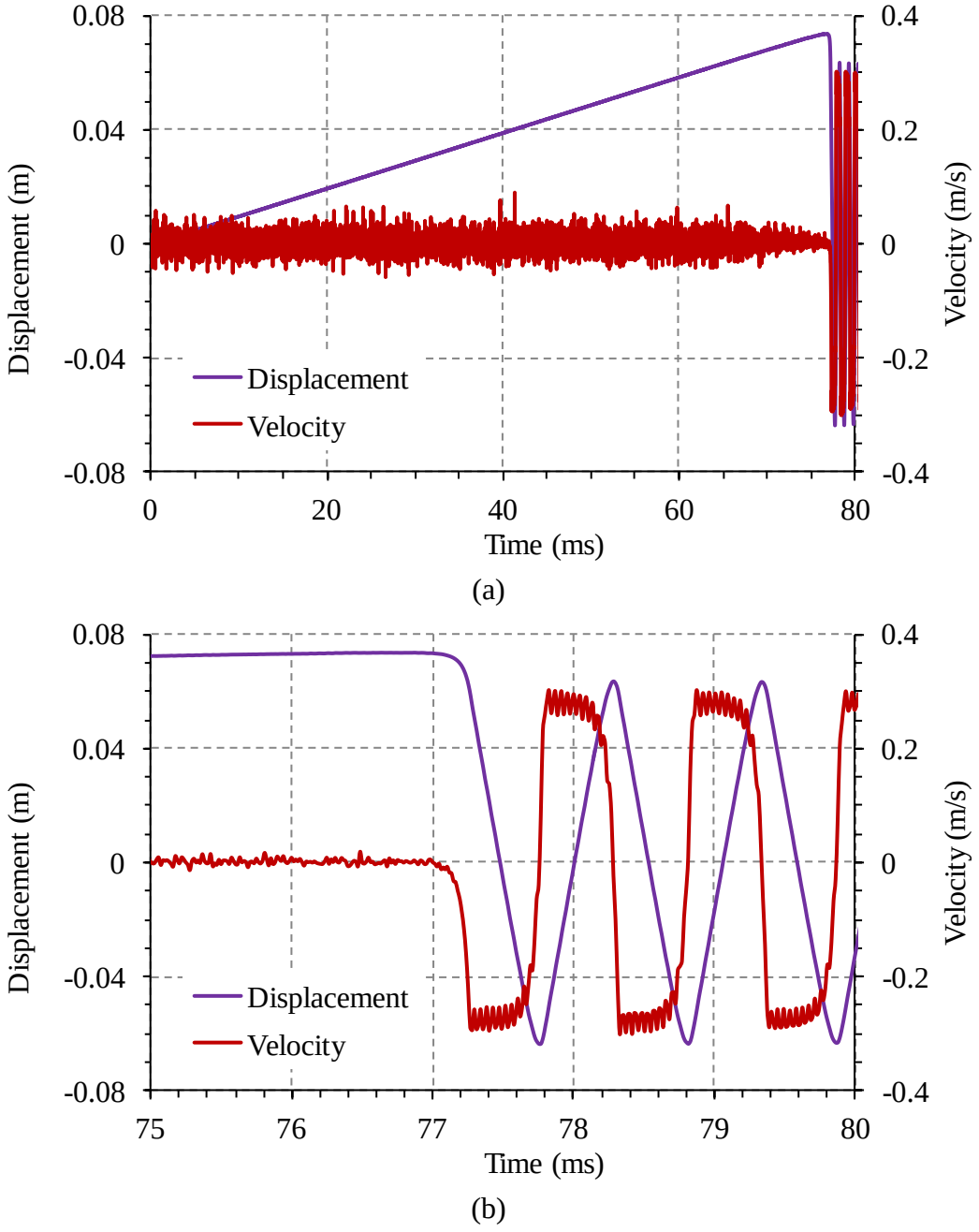

Figure 5.13 Time evolution of the displacement and the velocity of point A: (a) from the outset, (b) a zoom-in during and after damage to the cohesive layer

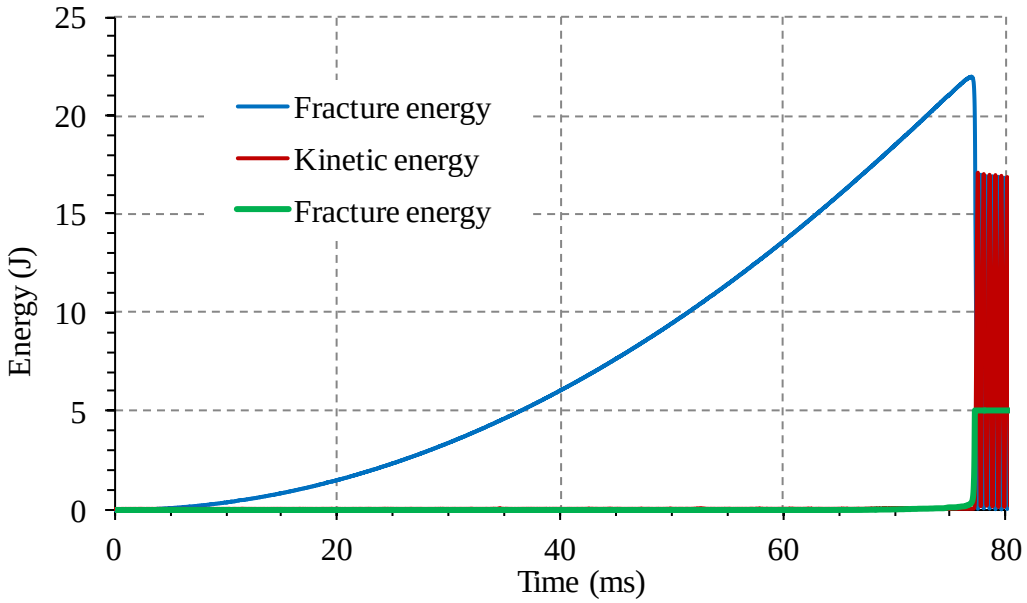

(a)

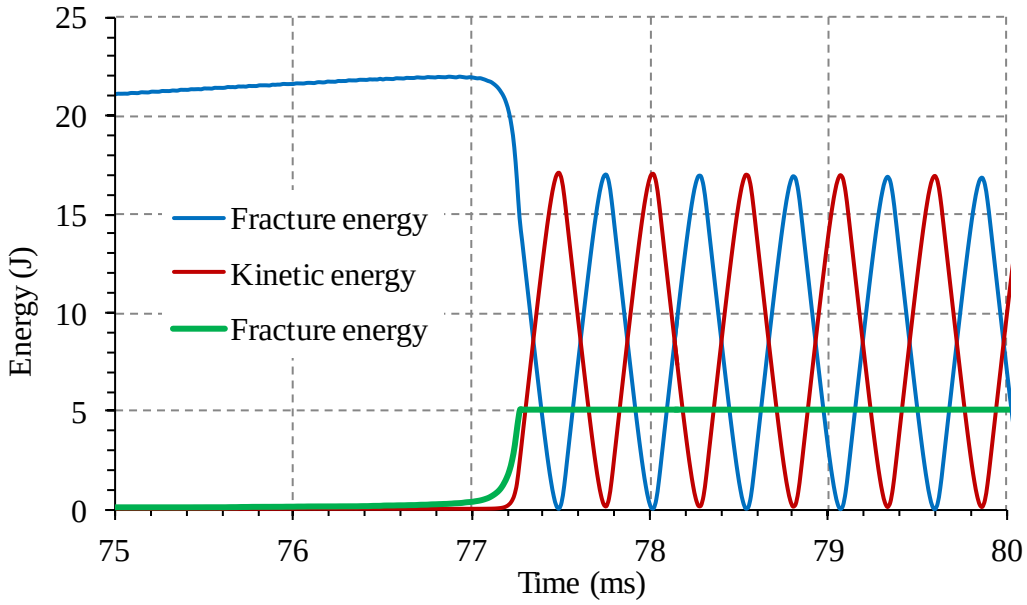

(b)

Figure 5.14 Time evolution of different types of energy in the whole model: (a) from the outset, (b) a zoom-in during and after damage to the cohesive layer

5.2.4.3 Influence of tensile strength on the intensity of induced elastic waves

In this section, the influence of the ratio α on the intensity of the induced elastic waves, which is reflected by the maximum velocity of the point A, is investigated. The expression for α, as presented in equation (5.15), is repeated here for convenience:

$$\alpha = \frac{R_T{}^2 L}{2 G_{IC} E}$$

As can be seen in the above expression α can be varied by changing either the tensile strength R_T, the length of the specimen L, the fracture toughness G_{IC}, or the Young's modulus E. Here, the tensile strength is change. The change in tensile strength for a Mode I fracture is equivalent to the change in shear strength for a Mode II fracture. Thus, conclusions obtained in this simulation are also valid for Mode II fractures.

Five cases with different tensile strengths are considered. These are listed in Table 5.3. Since the applied displacement rate has been proven to have negligible effect on the response of the system after the damage of the cohesive material, a displacement rate of 9 mm/s is used. For all of these five cases the loading rate is applied within 20 ms.

Table 5.3 Tensile strength and the corresponding α for simulation cases 1 – 5

Case	**Tensile strength R_T (MPa)**	**α**
1	0.6	0.24
2	1.9	2.4
3	2.6	4.5 (studied in subsection 5.2.4.1)
4	3.5	8.2
5	4.6	14.1

Simulation results:

The time evolution of the displacement and the velocity of the point A are presented in Figure 5.15 and Figure 5.16, respectively. As can be seen in Figure 5.15, for case 1 (α = 0.24) the velocity of the point A is virtually zero the whole time, both before and after damage to the cohesive material. As predicted by equation (5.16), the velocity of the point A after the damage of the cohesive material is:

$$\dot{u}_A = \frac{1}{1-\alpha}\dot{u} = \frac{1}{1-0.24} \times 9 = 11.8 \text{ mm/s}$$

This velocity is of the same magnitude as the applied displacement rate.

As α is increased from 2.4 in case 2 to 14.1 in case 5 (Figure 5.15), which corresponds to an increase in the tensile strength from 1.9 MPa to 4.6 MPa, the damage to the cohesive material, which corresponds to the moment when the velocity of the point A changes significantly, is delayed, as expected. The dynamic behavior of the system after cohesive damage, which is reflected by the time evolution of the point A in Figure 5.15, is similar for all cases: the velocity of the point A oscillates with similar period of approximately 1.6 ms. However, as α is increased from 2.4 to 14.1, the maximum velocity of the point A increases from 0.19 m/s (21 times the applied displacement rate) to 0.99 m/s (111 times the applied displacement rate). The maximum velocity of the point A is plotted in Figure 5.17a as a function of the coefficient α. An increasing linear relationship between these two quantities, which is represented as a straight line passing through the origin, is observed. Figure 5.17b shows the maximum velocity as a function of the tensile strength. Again, it is noted that the maximum velocity tends to zero for a small tensile strength and increases rapidly as the tensile strength increases.

The above observations are consistent with the conclusions regarding the role of the ratio between the strain energy release and the fracture energy, which is represented through the coefficient α, that as the ratio between the strain energy release and the fracture energy increases the intensity of the induced elastic waves will also increase.

The above results can be interpolated to a Mode II fracture (shear-mode): as the shear strength of the Mode II fracture increases the intensity of the elastic waves that are induced when the fracture slips will also increase. And for a Mode II fracture and a given stress state, the shear strength of the fracture is solely proportional to the friction coefficient of the fracture. In other words, if the friction coefficient of the fracture can be reduced, which will lead to a reduction in the shear strength of the fracture, the intensity of the induced elastic waves will be reduced.

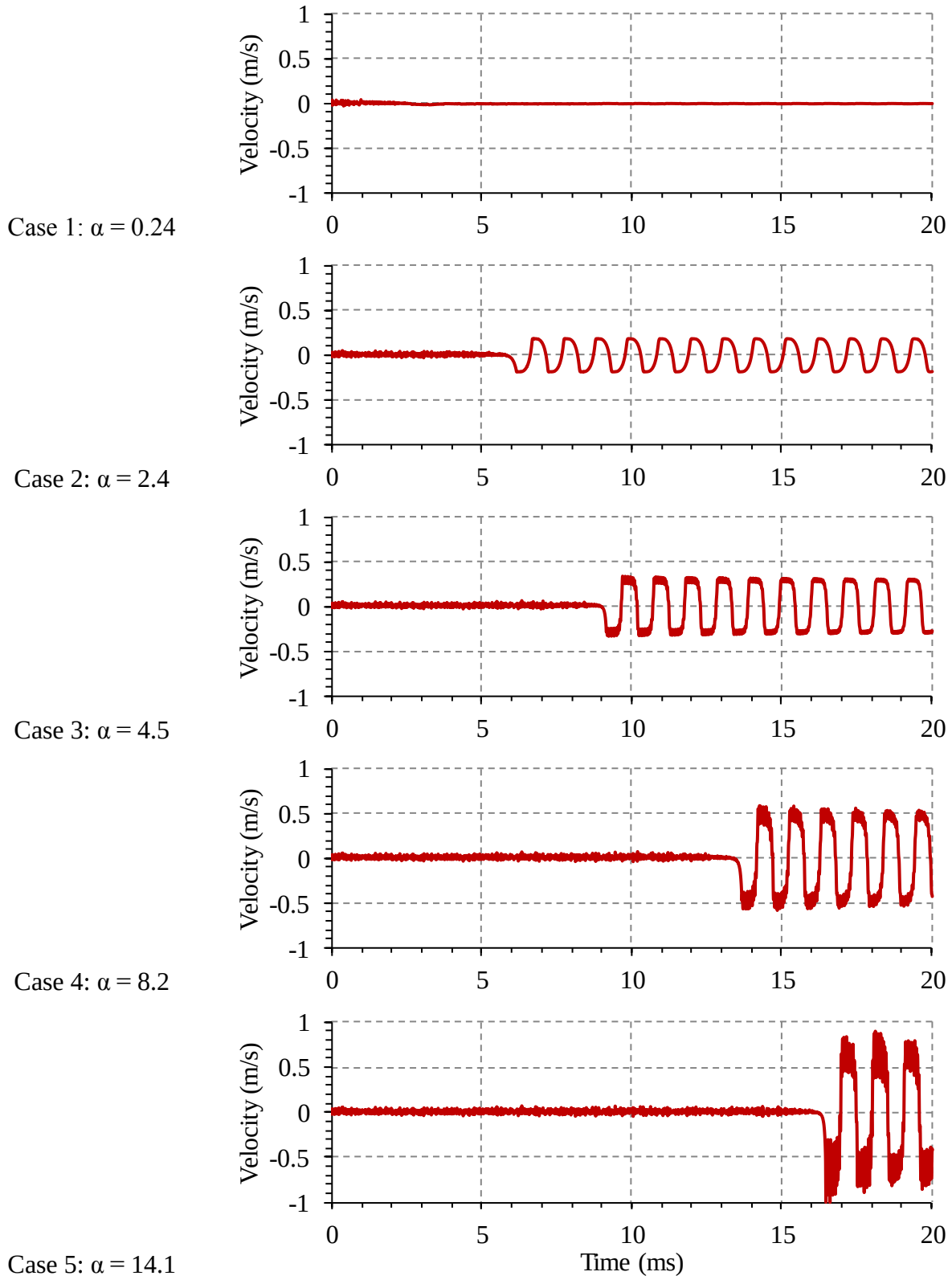

Figure 5.15 Time evolution of the velocity of the point A in direction 2 for the 5 cases studied

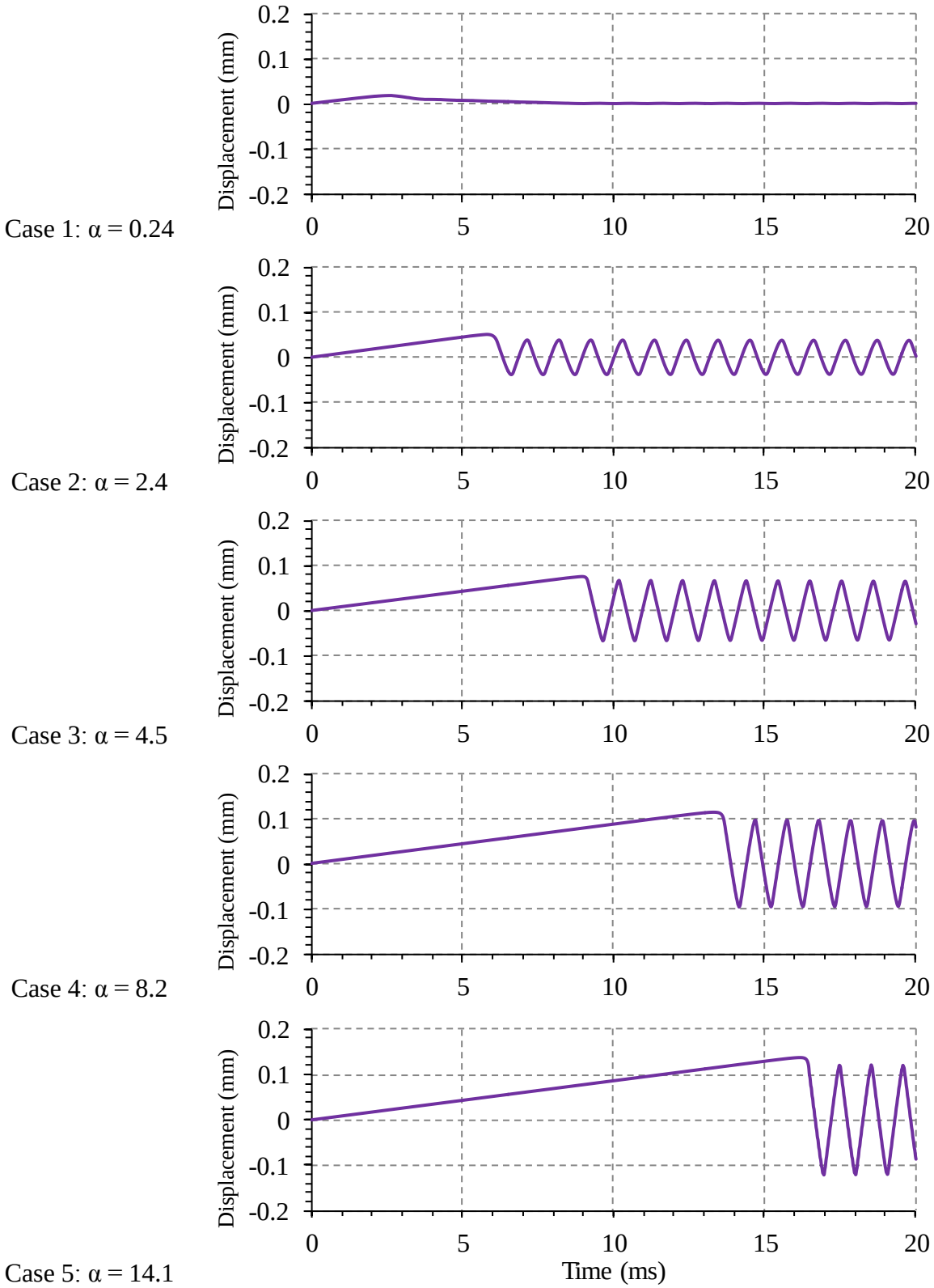

Figure 5.16 Time evolution of the displacement of the point A in direction 2 for the 5 cases studied

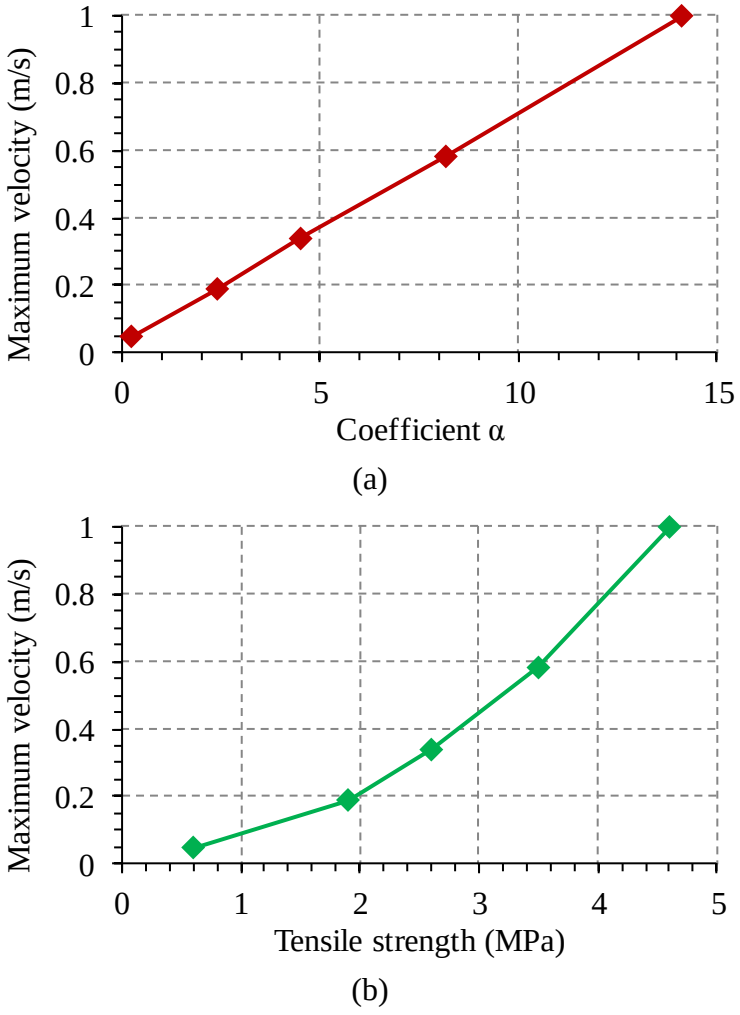

Figure 5.17 Maximum velocity of the point A as a function of (a) the coefficient α and (b) the tensile strength

5.3 ESTIMATION OF ACCELERATION INDUCED BY FAULT SLIP

As mentioned previously, the fault slip rate is generally used as the main parameter to assess the dynamic character of the fault slip. If the slip rate is higher than a certain threshold, the slip event is considered to be seismic. Otherwise, the slip event is aseismic. The magnitude of the slip event can also be obtained by using the slip rate in combination with the seismic moment. However, the most important question that remains unanswered is: what is the effect of the induced seismic waves on human perception and structural systems at a specific location? In this section, dynamic simulations of the propagation of seismic waves induced by the fault slip

are preformed to estimate the potential effects on humans and structural systems by using simplified 2D models.

5.3.1 Model setup

The model studied is similar to the model used in section 4.2, except that the dimensions of the model are now real dimensions, as shown in Figure 5.18. Specifically, the model is a 2D plane strain one that contains only one existing 30 m long fault F1, i.e., similar to the case given in section 4.2 of Chapter 4. The fault is located at 2.5 km from the ground level and is oriented at angle θ from direction 1.

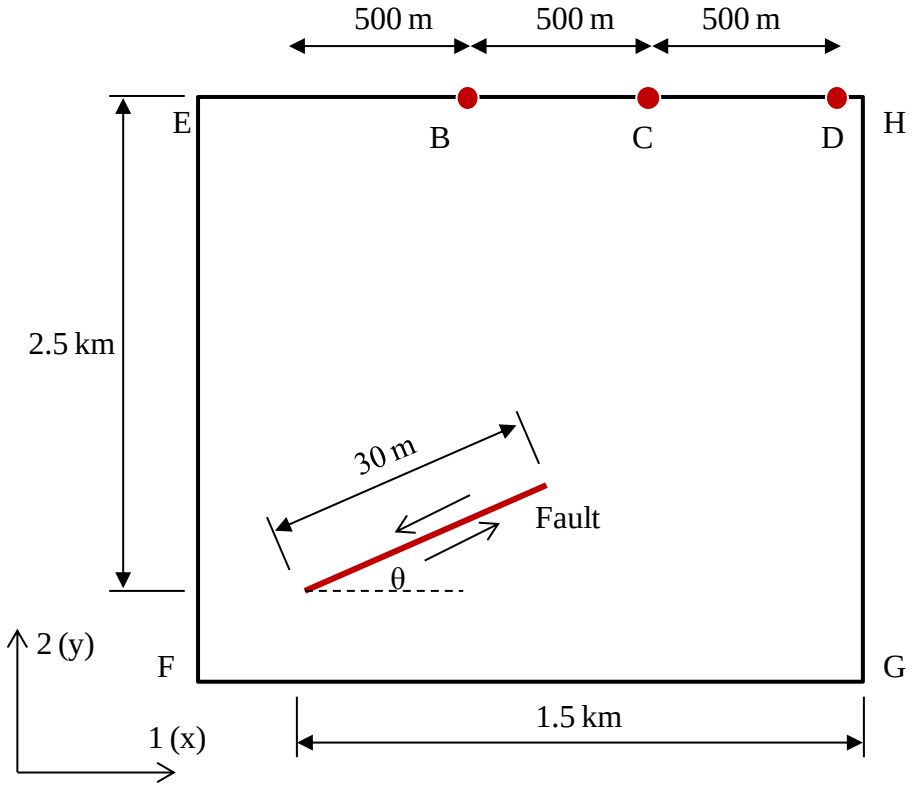

Figure 5.18 Model for dynamic simulation

The objective is to calculate the time evolution of the accelerations on the ground surface that are induced by the slip of the fault. Here, the accelerations at three locations B, C, and D are tracked. For this purpose, the time history of the displacements of all the nodes on two faces of the fault, which were obtained by quasi-static simulations in Chapter 4, are prescribed and inertia effects are also taken into consideration. Only the time during which the hydraulic

fracture intersects the fault is considered because during this time the slip rate of the fault is largest and thus the induced dynamic effects are expected to be most pronounced.

The material is assumed to be linear elastic and the whole domain is composed of only one material. This assumption is not altogether realistic as real formations can be made of multiple layers of different materials. However, the objective is only to demonstrate the methodology and the simulation procedure. Additionally, undrained conditions are also assumed since high slip rates occur only during a short time period. The so-called undrained Poisson's ratio is assumed to be v_u = 0.3 (Jin, 2018). The undrained Young's modulus can be found by using the condition that the shear modulus is similar in both the drained and undrained conditions:

$$E_u = \frac{1+\nu_u}{1+\nu} E \tag{5.20}$$

where E and v are Young's modulus and Poisson's ratio of the rock mass in the drained condition. When E = 30 GPa and v = 0.22, E_u is 31.96 GPa. The saturated density of the rock mass is assumed to be 2700 kg/m^3. The speed of dilatational waves and shear waves are calculated using equation (2.62). All the material parameters are listed in Table 5.4.

Table 5.4 Material parameters for the dynamic simulation

Property	**Value**
Undrained Young's modulus	E_u = 31.96 GPa
Undrained Poisson's ratio	ν_u = 0.3
Dilatational wave speed	C_p = 3992 m/s
Shear wave speed	C_s = 2133 m/s
Saturated density	ρ = 2600 kg/m^3

For boundary conditions, the fault is assumed to be located in an infinite medium. The ground surface (edge EH in Figure 5.18) is the only free surface. The model used in this simulation has finite dimensions. Thus, to eliminate the reflection of waves from the outer boundaries of the finite model, "quiet" boundary conditions must be used. In ABAQUS, the quiet boundary is assigned using infinite elements CINPE4.

For the finite element mesh, the 2D domain is uniformly discretized with elements that have a characteristic size of 0.25 m.

We have the relationship between the wavelength λ, wave speed C_p, and the wave frequency f as:

$$f = \frac{C_p}{\lambda} \tag{5.21}$$

In order to accurately model the propagation of elastic waves, one wavelength should be discretized into a number of finite elements, i.e.:

$$\lambda = N \times L_e \tag{5.22}$$

where L_e is the size of the finite element and N is the number of finite elements used to discretize one wavelength.

Combining equations (5.21) and (5.22) gives the following relationship:

$$f = \frac{C_p}{N \times L_e} \tag{5.23}$$

with C_p = 3992 m/s, L_e = 0.25 m, and N = 5, f is 3193 Hz. This means that the finite element mesh is capable of accurately modeling the propagation of waves that have frequencies up to approximately 3193 Hz. It should be noted that seismic events in the field typically have frequencies from 1 to 5 kHz (Hardy Jr, 2003). Thus, the finite element mesh used is considered appropriate.

Dynamic simulations were run for all cases that have been studied in subsections 4.2.3 (Effect of friction coefficient on fault slip) and 4.2.4 (Effect of injection rate on fault slip), and are repeated again in Table 5.5 and Table 5.6 for convenience. The time histories of the displacements of all nodes on two surfaces of the pre-existing fault are prescribed using the results from the quasi-static simulations done in subsections 4.2.3 and 4.2.4. The simulation results for these cases are presented in the next sections.

Table 5.5 Friction coefficient for cases S1, S2, and S3

Case	Friction coefficient
S1	0.35 (studied in section 4.2.2)
S2	0.65
S3	1.0

Table 5.6 Injection rate for cases Q1 to Q4

Case	Injection rate Q (L/s per unit thickness)
Q1	0.25
Q2	0.5 (Case S2 in section 4.2.3)
Q3	1.0
Q4	3.0

5.3.2 Results of dynamic simulation to assess the effect of friction coefficient (cases S1, S2, and S3)

Results of case S1:

Detailed results for case S1 are presented in this subsection, while those for cases S2 and S3 are presented in Appendix 4.

Figure 5.19 and Figure 5.20 show the contour plots of accelerations in directions 1 and 2 during the arrival of the dilatational waves to the top surface of the model. Note that only the upper part of the model containing the top surface is presented. The dilatational waves arrive at the top surface of the model at time t = 1.15 s (Figure 5.19a and Figure 5.20a). After that, surface waves are induced and propagate along the top surface (Figure 5.19b,c and Figure 5.20b,c); a part the incident dilatational waves are reflected off the top surface back into the model and interfere with the incident waves (Figure 5.19d and Figure 5.20d).

Figure 5.21 and Figure 5.22 give the contour plots of accelerations in directions 1 and 2 during the arrival of the shear waves to the top surface of the model. The shear waves arrive at the top

surface of the model at time t = 1.65 s (Figure 5.21a and Figure 5.22a). Surface waves are then induced and propagate along the top surface (Figure 5.21b and Figure 5.22b). The propagation of the reflected waves and their interference with the incident waves are also seen in Figure 5.21c and Figure 5.22c.

The accelerations in directions 1 and 2 at points B, C, and D are presented in Figure 5.23 and Figure 5.24, respectively. The arrival of the dilatational and shear waves is clearly observed in these accelerograms. The dilatational waves arrive first, followed by the shear waves. For instance, at the point B the dilatational and shear waves arrive at approximately t = 1.15 s and t = 1.65 s, respectively (Figure 5.23a or Figure 5.24a). The time lag between the first arrival and the second arrival is $\Delta t \approx 1.65 - 1.15 = 0.5$ s. This is consistent with the theoretical prediction, which is given by:

$$\Delta t = d\left(\frac{1}{C_S} - \frac{1}{C_P}\right) = 2500\left(\frac{1}{2174} - \frac{1}{3767}\right) = 0.49\ s$$

where d is the distance from the source to the observation point, which is roughly 2500 m.

It can also be seen that point C is farther from the wave-emitting source (i.e., the pre-existing fault) than the point B and the point D is the most distant (see Figure 5.18). Therefore, the incident waves (both dilatational and shear waves) arrive at point B earlier than point C, and arrive last at point D.

The maximum acceleration in directions 1 and 2 at points B, C, and D are plotted against the distance from the points to the projection of the pre-existing fault on the top surface in Figure 5.25. Among these three points, the accelerations at B are highest in both directions with A_{1max} = 0.015 m/s^2 (maximum acceleration in direction 1) and A_{2max} = 0.007 m/s^2 (maximum acceleration in direction 1). The total acceleration at this point B is:

$$A = \sqrt{A_{1\max}^2 + A_{2\max}^2} = \sqrt{0.015^2 + 0.007^2} = 0.016\ \text{m/s}^2 = 0.17\%\ \text{g}$$

where g is the gravitational acceleration which is approximately equal to 9.8 m/s^2.

Compared to intensity levels presented in Table 5.1, this peak acceleration (A = 0.17% g) would not be felt by human beings and is not capable of causing any structural damage.

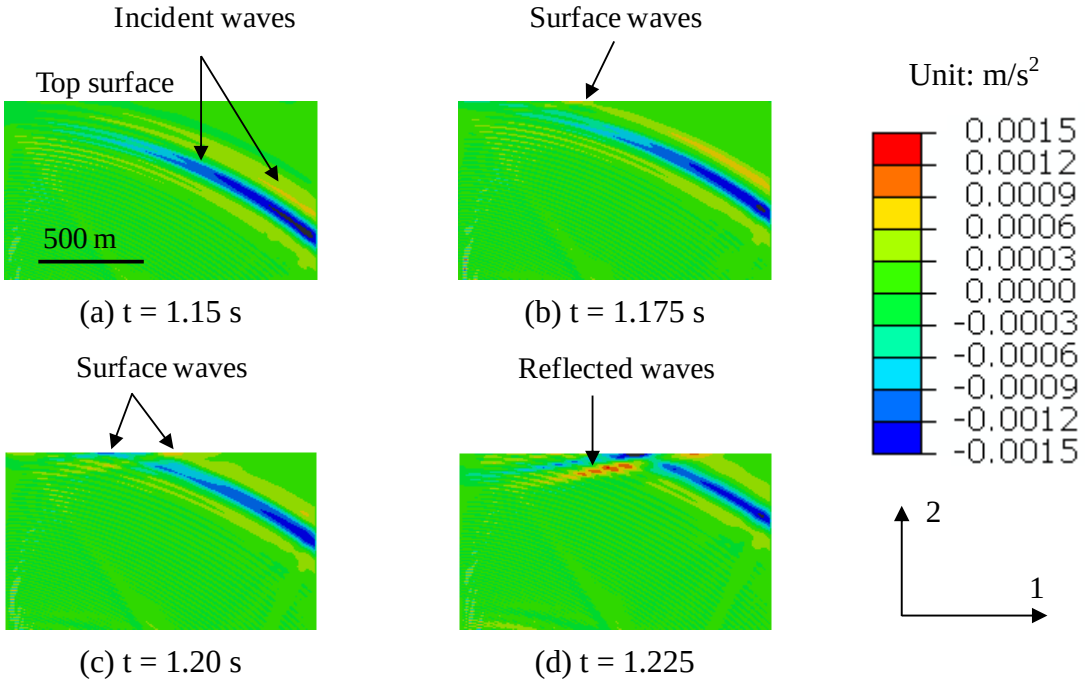

Figure 5.19 Contour plots of acceleration in direction 1 at different times (Only the upper part of the model is presented)

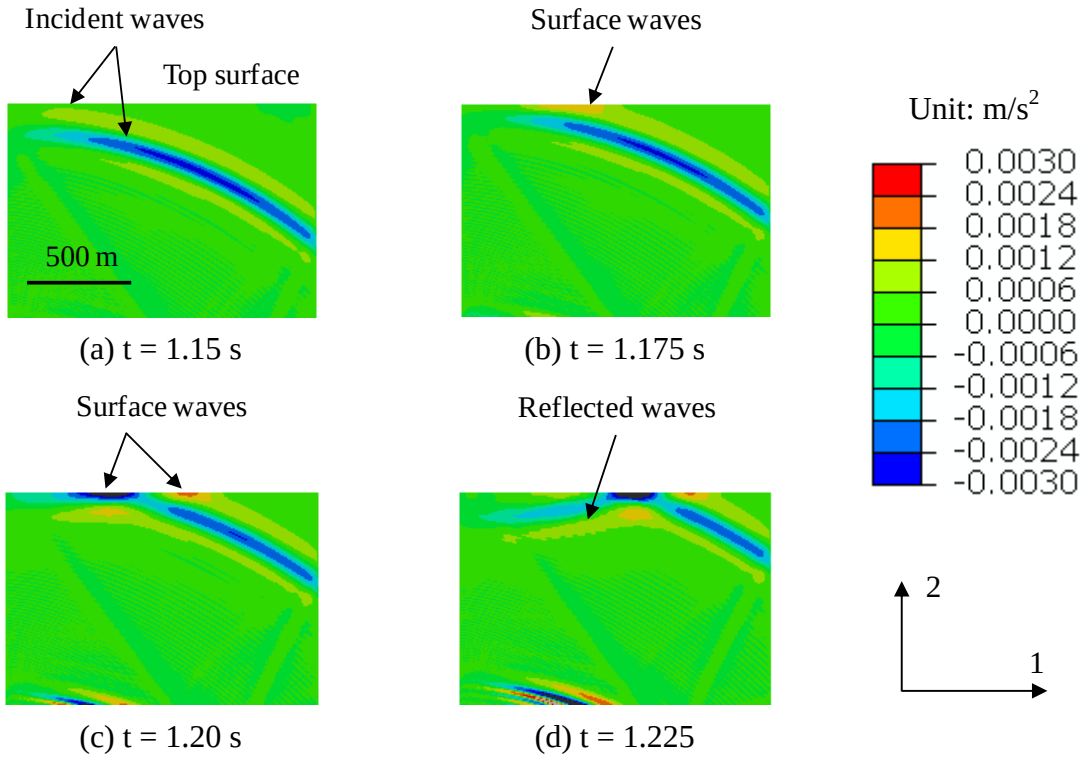

Figure 5.20 Arrival of dilatational waves in direction 2 at the top surface and generation of surface waves (Only the upper part of the model is presented)

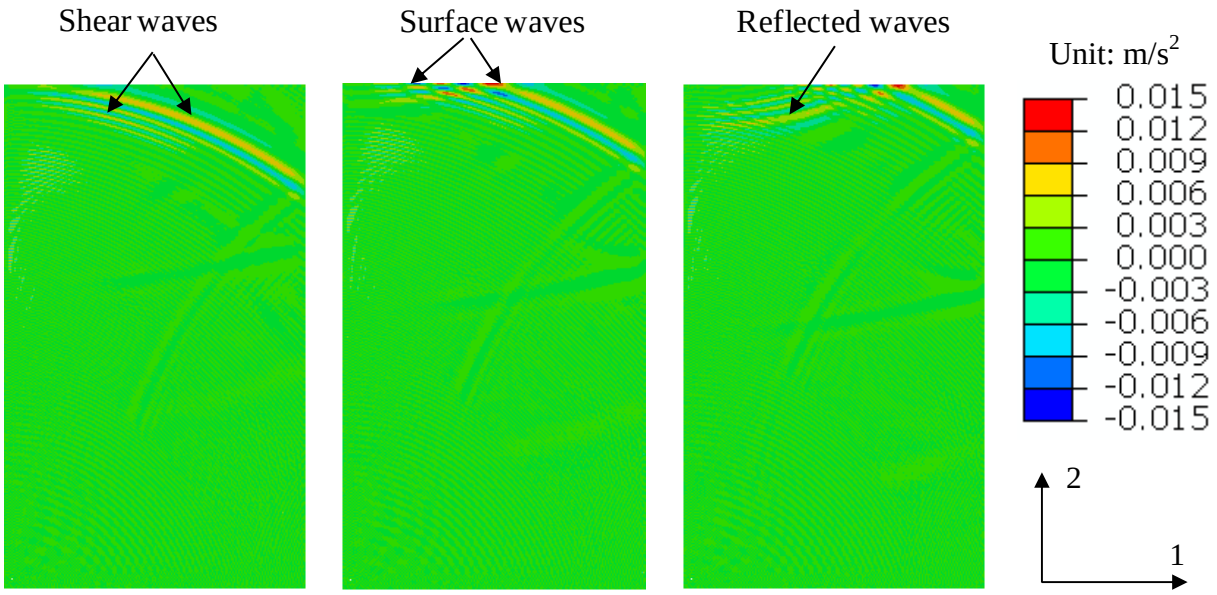

(a) t = 1.65 s (b) t = 1.70 s (c) t = 1.75 s

Figure 5.21 Arrival of transverse waves in direction 1 at the top surface and generation of surface waves (The whole model is presented)

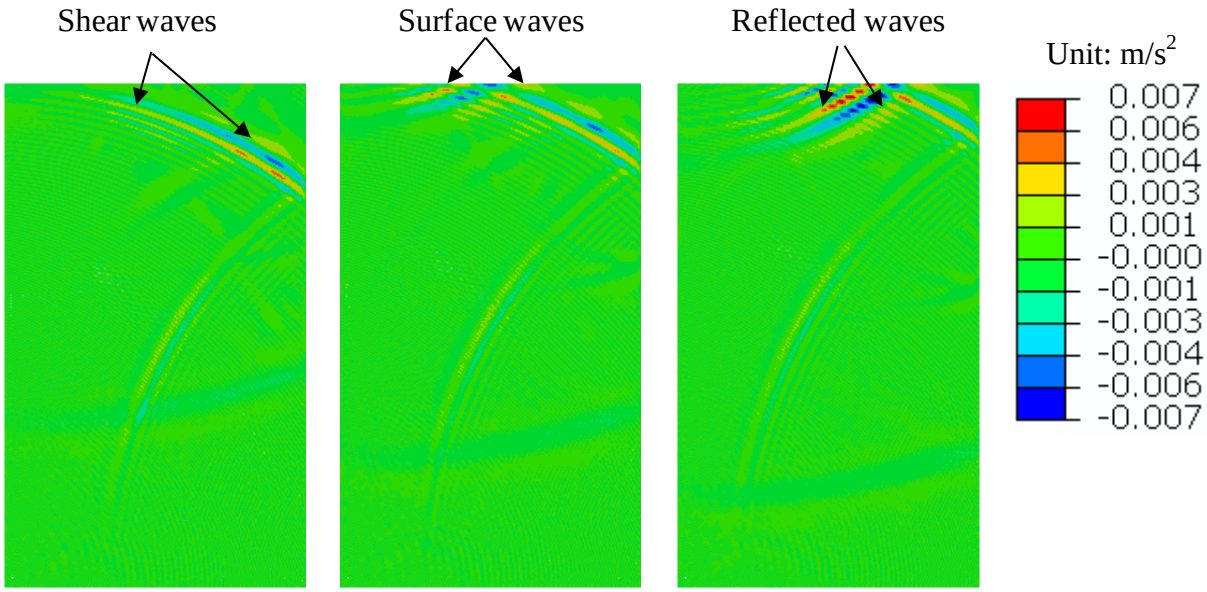

(a) t = 1.65 s (b) t = 1.70 s (c) t = 1.75 s

Figure 5.22 Arrival of shear waves in direction 2 at the top surface and generation of surface waves (The whole model is presented)

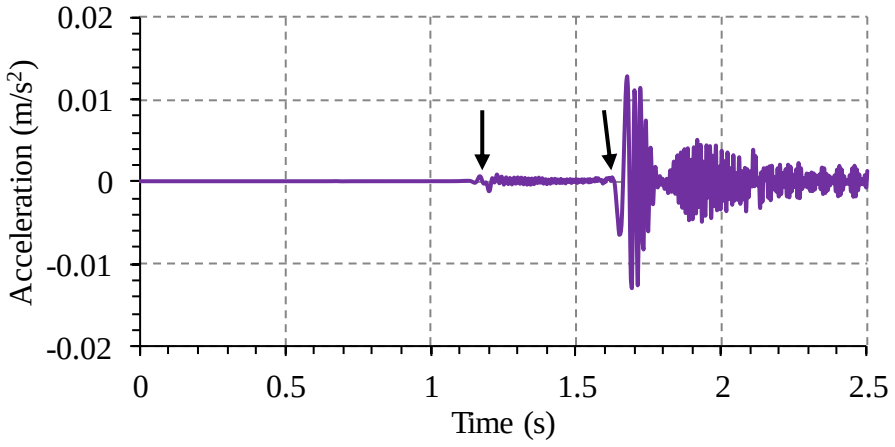

(a) Point B

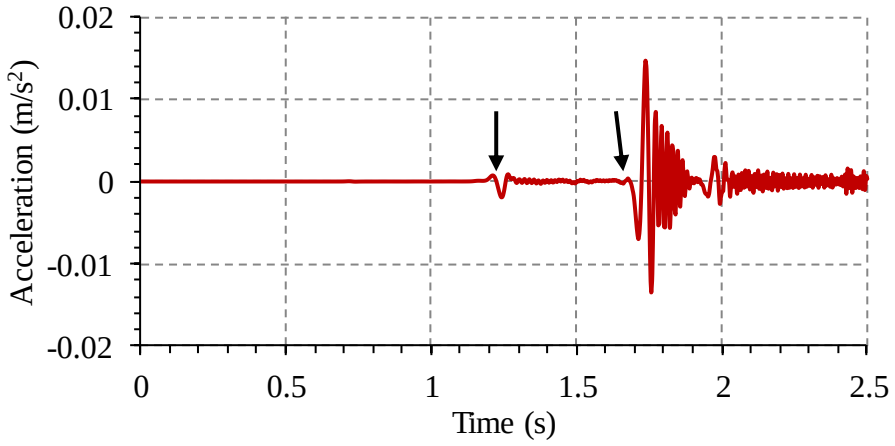

(b) Point C

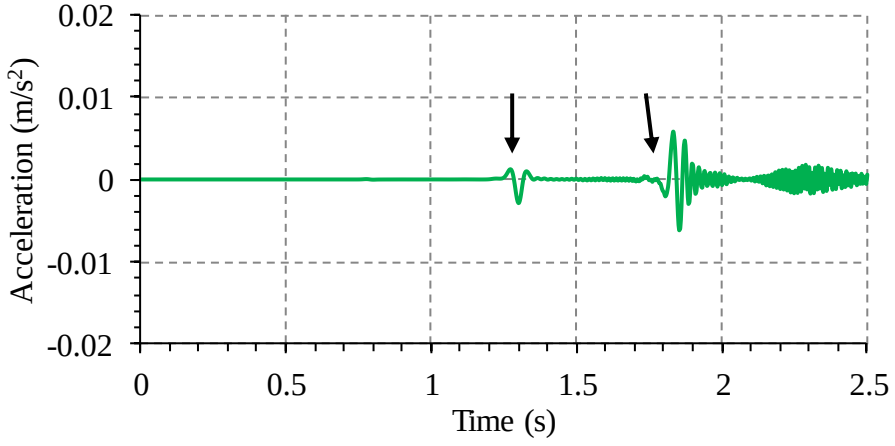

(c) Point D

Figure 5.23 Time evolution of acceleration in direction 1 at three points B, C, and D. The arrows indicate the arrivals of elastic waves: left arrow shows the arrival of dilatational waves and dilatational-wave-induced surface waves; right arrow shows the arrival of shear waves and shear-wave-induced surface waves

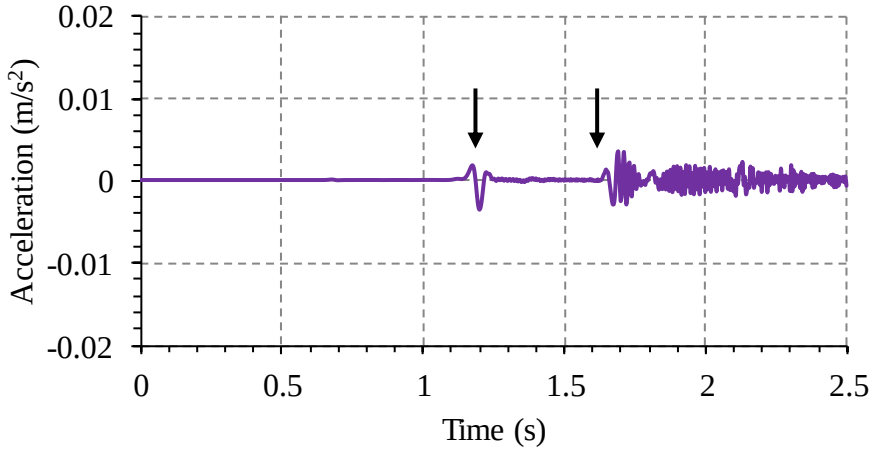

(a) Point B

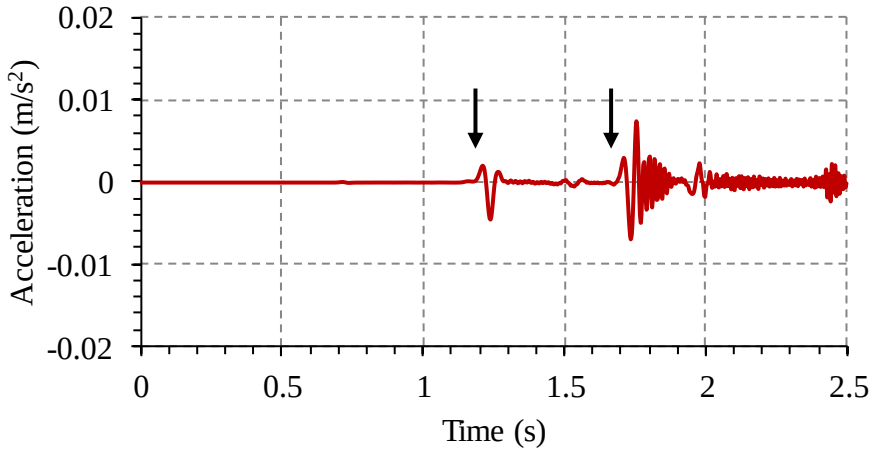

(b) Point C

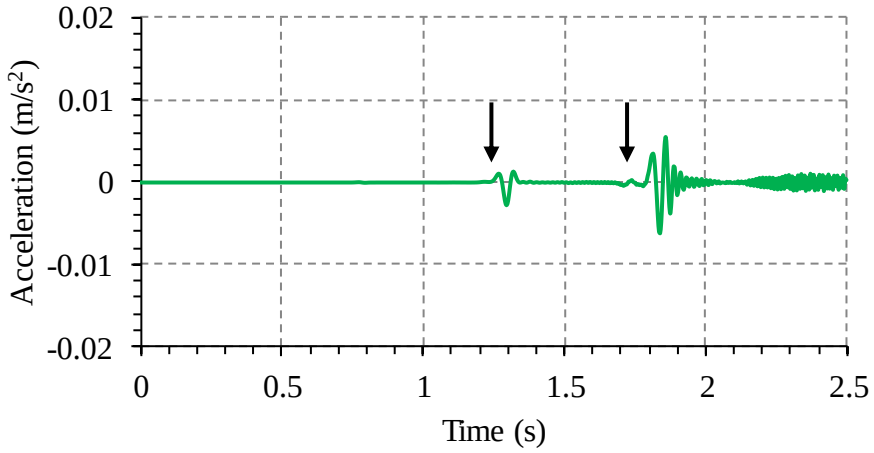

(c) Point D

Figure 5.24 Time evolution of acceleration in direction 2 at three points B, C, and D. The arrows indicate the arrivals of elastic waves: left arrow for the arrival of dilatational waves and dilatational-wave-induced surface waves; right arrow for the arrival of shear waves and shear-wave-induced surface waves

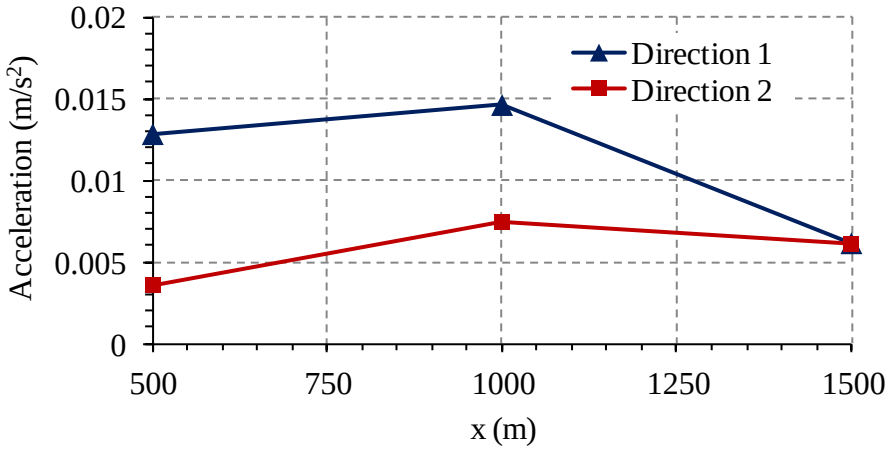

Figure 5.25 Maximum accelerations in directions 1 and 2 along the top surface. Points B, C, and D correspond to x = 500, 1000, and 1500 m, respectively

PGA as a function of friction coefficient:

The peak ground acceleration (PGA) in directions 1 and 2 and the total PGA at points B, C, and D for all three cases are presented in Table 5.7, Table 5.8, and Table 5.9, respectively. These results are plotted against the friction coefficient of the pre-existing fault and are presented in Figure 5.26. In general, for all three points B, C, and D, the PGA increases with an increase in the friction coefficient.

For case S1 with a friction coefficient μ_f = 0.35, the total PGA, measured in %g, is maximum at point C with a value of 0.167, which corresponds to the intensity level I (Table 5.1), i.e., the induced elastic waves may not be perceived by human beings and there is no potential for damage to structural systems. However, for the case S2 where friction coefficient μ_f = 0.65, which is a normal value for a fault friction coefficient, the total PGA measured in %g at points B, C, and D is 0.44, 0.53, and 0.27, respectively. When compared to the Modified Mercalli intensity scale figures given in Table 5.1, these PGA values correspond to an intensity level II-III (0.17% g $\leq$ PGA $\leq$ 1.4% g), which again means that the induced elastic waves are not capable of causing any structural damage but can be "weakly" perceived by humans.

For case S3 with a higher-than-normal friction coefficient, the total PGA increases up to 1.68% g at point B, which corresponds to the intensity level IV. Human perception of the induced elastic waves is greater than case S2 (human perception of induced elastic waves from

"weak" in case S2 to "light" in case S3, Table 5.1). However, there is still no potential for structural damage.

Table 5.7 PGA at point B for cases S1, S2, and S3

Case	Friction coefficient	PGA in direction 1 (m/s^2)	PGA in direction 2 (m/s^2)	Total PGA (m/s^2)	Total PGA (%g)
S1	0.35	0.013	0.004	0.013	0.14
S2	0.65	0.042	0.011	0.043	0.44
S3	1	0.159	0.042	0.164	1.68

Table 5.8 PGA at point C for cases S1, S2, and S3

Case	Friction coefficient	PGA in direction 1 (m/s^2)	PGA in direction 2 (m/s^2)	Total PGA (m/s^2)	Total PGA (%g)
S1	0.35	0.015	0.007	0.016	0.17
S2	0.65	0.046	0.025	0.052	0.53
S3	1	0.084	0.045	0.095	0.97

Table 5.9 PGA at point D for cases S1, S2, and S3

Case	Friction coefficient	PGA in direction 1 (m/s^2)	PGA in direction 2 (m/s^2)	Total PGA (m/s^2)	Total PGA (%g)
S1	0.35	0.006	0.006	0.009	0.09
S2	0.65	0.019	0.018	0.026	0.27
S3	1	0.037	0.030	0.048	0.49

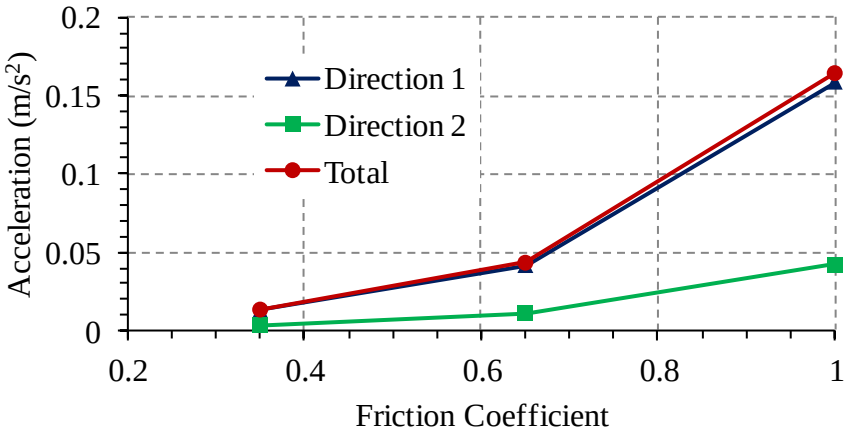

(a) Point B

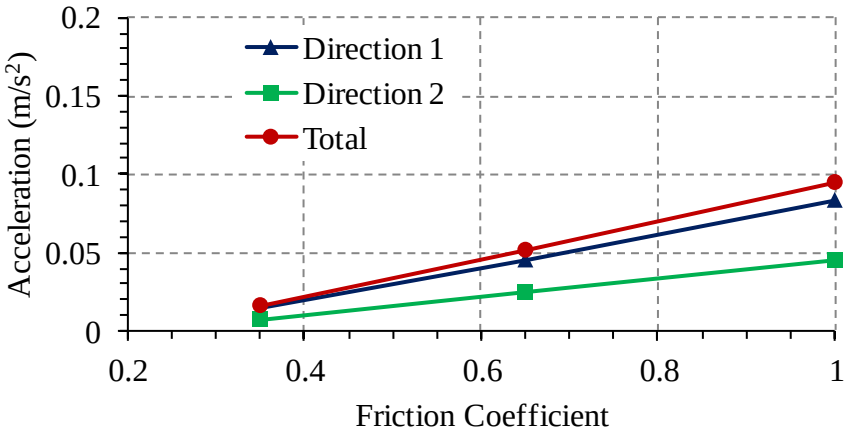

(b) Point C

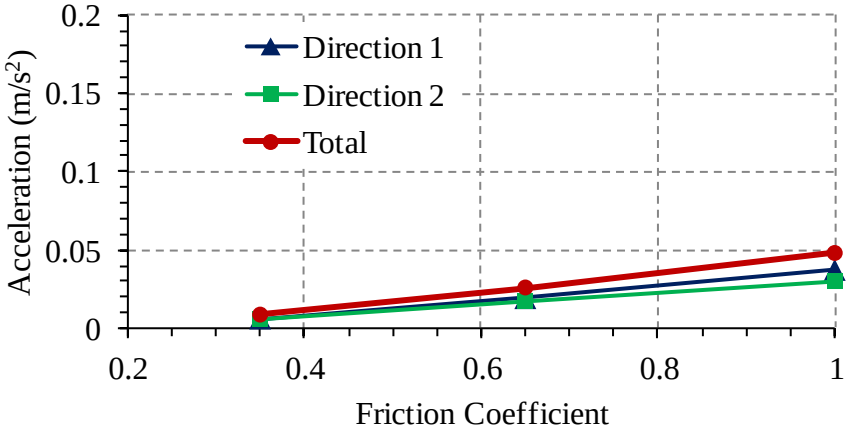

(c) Point D

Figure 5.26 PGA in directions 1 and 2 and total PGA at points B, C, and D as a function of the friction coefficient

5.3.3 Results of dynamic simulation to assess the effect of the injection rate (cases Q1, Q2, Q3, and Q4)

Detailed results of the dynamic simulations for cases Q1 to Q4 are presented in Appendix 5. A summary of the results are presented in Table 5.10, Table 5.11, and Table 5.12, which show the PGA in all cases for points B, C, and D, respectively. These results are plotted against the injection rate in Figure 5.27. Note that for all four cases, the friction coefficient of the fault is 0.65.

As can be seen from Figure 5.27 the PGA increases with the increase of the injection rate. However, the increase rate of the PGA is faster when the injection rate increases from 0.25 L/s to 1 L/s than when the injection increases from 1 L/s to 3 L/s.

The total PGA at all three points B, C, and D for all four cases is in the range from 0.17% g to 1.4% g, which means the induced elastic waves may be felt the human beings but only weakly and there is no damage potential for structural systems.

Table 5.10 PGA at point B for cases Q1, Q2, Q3, and Q4

Case	Injection rate (L/s)	PGA in direction 1 (m/s^2)	PGA in direction 2 (m/s^2)	Total PGA (m/s^2)	Total PGA (%g)
Q1	0.25	0.030	0.008	0.031	0.32
Q2	0.55	0.042	0.011	0.043	0.44
Q3	1	0.100	0.030	0.105	1.07
Q4	3	0.156	0.044	0.162	1.65

Table 5.11 PGA at point C for cases Q1, Q2, Q3, and Q4

Case	Injection rate (L/s)	PGA in direction 1 (m/s^2)	PGA in direction 2 (m/s^2)	Total PGA (m/s^2)	Total PGA (%g)
Q1	0.25	0.037	0.022	0.043	0.44
Q2	0.55	0.046	0.025	0.052	0.53
Q3	1	0.067	0.035	0.076	0.77
Q4	3	0.074	0.056	0.093	0.95

Table 5.12 PGA at point D for cases Q1, Q2, Q3, and Q4

Case	Injection rate (L/s)	PGA in direction 1 (m/s^2)	PGA in direction 2 (m/s^2)	Total PGA (m/s^2)	Total PGA (%g)
Q1	0.25	0.019	0.016	0.024	0.25
Q2	0.55	0.019	0.018	0.026	0.27
Q3	1	0.032	0.024	0.040	0.41
Q4	3	0.054	0.026	0.060	0.61

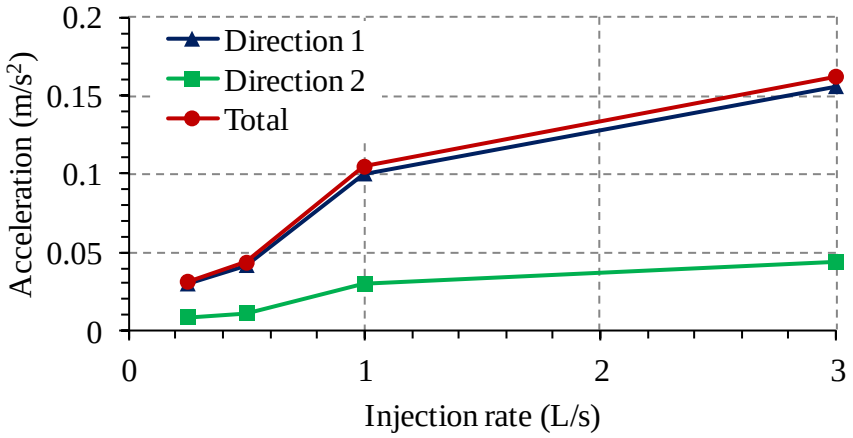

(a) Point B

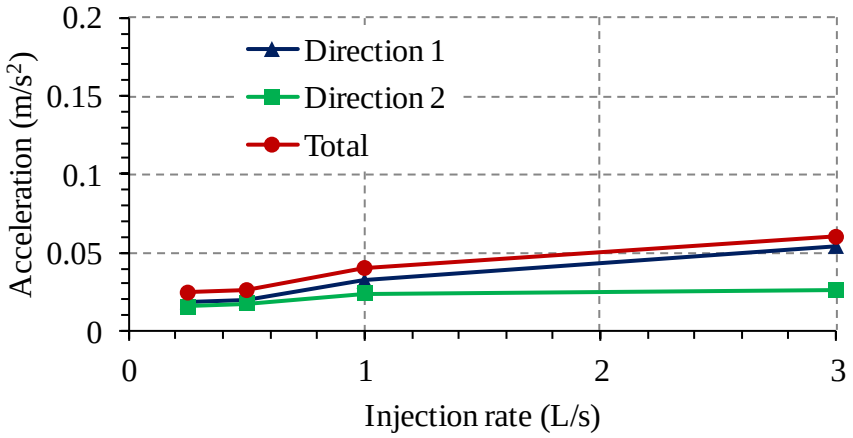

(b) Point C

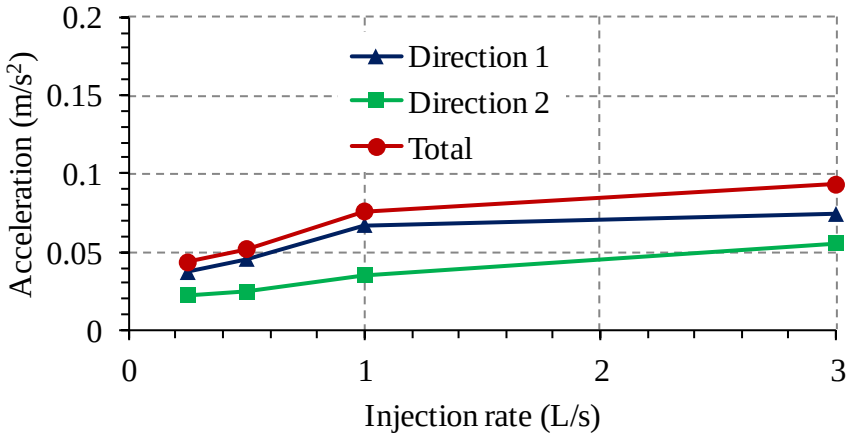

(c) Point D

Figure 5.27 PGA in directions 1 and 2 and total PGA at points B, C, and D as function of the injection rate

5.4 CHAPTER CONCLUSIONS

In this chapter 5, the generation of elastic waves from the material damage is studied using a discrete model (mass-spring model) and a cohesive material model. It is shown that when a material is damaged the main reason leading to the generation of elastic waves is the excess strain energy that is released during material damage, which is greater than the energy that can be dissipated through the material damage (e.g., energy consumed to create new surfaces). The intensity of the induced elastic waves is dependent on the amount of the excess strain energy, or, put another way, is dependent on the ratio between the strain energy release and the energy dissipated through damage. It is also shown that as long as the loading does not introduce significant dynamic effects to the system (i.e., the loading is still considered as quasi-static), the dynamic response of the system that is induced by the material damage is independent of the loading rate.

The propagation of elastic waves induced by the fault slip is simulated by a modeling procedure. The effect of the induced elastic waves on human perception and structural systems is quantified using the peak ground acceleration. The simulation results show that lower fault friction coefficients or lower injection rates result in smaller peak ground accelerations. For the studied configuration, it has been shown that the induced elastic waves may be "weakly" or "lightly" felt by human beings but are not capable of posing any concern to the structural systems on the ground.

Chapter 6

Conclusions and perspectives

6.1 CONCLUSIONS

This research is a part of the major project GEOTREF whose aim is to improve the understanding of fractured geothermal reservoirs in order to reduce geothermal geological risk and to ensure sustainable exploitation of the reservoir during the production phase. The principal objective of this research is to build numerical models to simulate the fracture propagation and the slip of pre-existing faults during hydraulic stimulation of deep geothermal reservoirs and to propose a procedure to model the induced seismicity. The main results can be summarized in the following:

1. **The effect of thermal cooling on fracture propagation:**

Thermal cooling effects are shown to be able to cause fracture propagation. These thermal fractures can contribute to an increase in the reservoir permeability. Numerical models based on the extended finite element method or cohesive element concepts were performed and were shown to be able to capture the main characteristics of thermal fracture propagation. The low thermal conductivity of the rock reduced heat transfer process; thus, the thermal cooling effect is more pronounced over the long term.

2. **Modeling of the propagation of hydraulic fractures and the slip of pre-existing faults during the stimulation phase**

The hydraulic fractures are modeled using the cohesive zone model concept, while the shear strength of the pre-existing faults is modeled using the Coulomb friction law. It was observed

that the slip rate of the pre-existing faults increases suddenly when they are intersected by the newly created hydraulic fractures. The main reason for this is that during intersection the fluid pressure inside the faults increases suddenly due to fluid flow from the hydraulic fractures into the faults, causing a significant decrease in the shear strength of the faults, allowing the faults to slip at higher rate. In most cases studied, the fault slip rate upon intersection with the newly created hydraulic fractures is higher than the threshold of the dynamic slip rate, which indicates that the slip event is likely seismic.

3. **The effect of the fault orientation, fault friction coefficient, and the injection rate on the fault slip**

Through parametric studies, it was found that:

- Faults that are more critically oriented with respect to the initial stresses show higher slip rates when they are intersected with hydraulic fractures
- Increasing the fluid injection rate also increases the fault slip rate. However, short faults are more sensitive to an increase in the injection rate than longer faults.
- The friction coefficient was also found to have a strong influence on the fault slip. As the fault friction coefficient decreases, the fault slip rate upon intersection with hydraulic fractures also decreases. If the friction coefficient is low enough, the fault slip rate can be reduced to levels below the threshold of the dynamic slip rate. This suggests that one can still achieve the goal of stimulating a rock reservoir (i.e., activation of the pre-existing faults and connecting them together) while minimizing the risk of inducing seismic fault slip by reducing the friction coefficient of the pre-existing faults before the hydraulic stimulation begins.

4. **The generation of elastic waves from fracture propagation and fault slip**

- It was theoretically shown (see chapter 5) that the main mechanism leading to the generation of elastic waves when the material is damaged (e.g., fracture propagation or fault slip) is that, during the material damage process the amount of strain energy released is larger than the amount of energy that can be dissipated through the material damage (e.g., energy consumed to create new fracture surfaces). Thus, the excess strain energy is converted into kinetic energy in the form of elastic waves.

- The intensity of the induced elastic waves is dependent on the amount of the excess strain energy, or in other words, is dependent on the ratio between the strain energy release and the energy dissipated through damage.
- It is also shown that as long as the external loads do not introduce significant dynamic effects into the system (i.e., the external loads are still considered to be quasi-static), the dynamic response of the system that results from the induced material damage is independent of the loading rate.

5. **The methodology for computing peak ground accelerations (PGAs) induced by fault slip**
   - A numerical modeling approach is proposed to compute the ground accelerations induced by fault slip. The sequential approach combines quasi-static coupled hydromechanical simulations with dynamic simulations.
   - For the configurations studied in this research, the estimated PGAs may be felt by the public but will not cause damage to structural systems or the built environment. For instance, the maximum PGA for all studied cases is approximately 2 %g, which is smaller than the 4 %g limit specified by the Building code Eurocode 1998 above which seismic designs must be implemented (Clause 3.2.1 (5)P of the Eurocode 1998 - part 1).

6.2 RECOMMENDATION FOR FUTURE RESEARCH

- The main results of the numerical models (chapter 4), with respect to the relationship between the friction conditions of the faults, the injection rate, and fault orientation with its slip behavior, are qualitatively supported by in-situ observations. New laboratory experiments under controlled conditions analogous to shear-faulting reservoirs need to be done in order to quantitatively validate and calibrate the numerical models. Using the methodological developments in chapter 5 it is possible to analyze the responses recorded by micro-seismic sensors used in laboratory experiments, which are usually in the form of electrical signals (piezoelectric sensors), and calibrate the waveforms with geometrical and mechanical parameters of the shearing and/or opening zone. A similar analysis can be carried out for in-situ

situations to find out possible relationships between the responses at seismometers and the source mechanism and mechanical properties of the source.

- The behavior of fractured geothermal reservoirs during the stimulation phase is the main focus of this research. The reservoir behavior during the production phase still requires further research as the production phase is expected to last as long as 30 to 50 years. The models that have been built for the stimulation phase can be modified to study the behavior of the reservoirs during the production phase, e.g., adding physical couplings such as thermal processes.
- The thermal effects have been evaluated separately from fluid processes in chapter 3. The cooling experiment using rock salt showed that a temperature decrease of 25 °C was able to create a 10 m long, 1 m deep, and 1 mm wide fracture. In deep geothermal reservoirs, temperature changes may be of the order of hundreds of °C. Therefore, it is expected that the thermal cooling effects in geothermal reservoirs will be more significant. The first well-known effect is the increase over time in the injectivity at the reinjection borehole, which is linked to the contraction of the rock mass. The second possible effect is the risk of thermal breakthrough, i.e., the injected fluid concentrates in a more direct flow path linking directly the two boreholes. The thermal breakthrough, if occurs, will be detrimental to the sustainability of any geothermal project. Several studies have also suggested that thermal contraction of the geothermal reservoirs is responsible for the settlements observed on the ground surface above the reservoir. Thus, the thermal cooling effects may require further research at a larger scale and over long time scales with respect to its impact on the reservoir permeability enhancement and possible delayed seismic fault slip. Our conclusions on the potential effect of a change in the friction behavior lead us to recommend additional research on the possibility of friction reduction with time due to delayed effects of hydro-thermo-chemical processes in geothermal reservoirs. This effect would be of the utmost importance for CO2 underground storage reservoirs/caverns having undetected sub-seismic faults as the injected fluids would have become more acid than native fluids.

Appendix 1: List of publications

Publications in peer-reviewed journals:

1) Dac Thuong Ngo, Frederic L. Pellet (2018). Numerical modeling of thermally-induced fractures in a large rock salt mass. Journal of Rock Mechanics and Geotechnical Engineering 10, 844-855 (doi.org/10.1016/j.jrmge.2018.04.008)
2) Dac Thuong Ngo, Frederic L. Pellet, Dominique Bruel (2019). Modeling of fault slip during hydraulic stimulation in a naturally fractured medium. Geomechanics and Geophysics for Geo-Energy and Geo-Resources (doi.org/10.1007/s40948-019-00108-1)

Publications in international conferences:

1) Dac Thuong Ngo, Frédéric L. Pellet, Dominique Bruel. Modeling of dynamic crack propagation under quasi-static loading. *15th International Conference of the International Association for Computer Methods and Advances in Geomechanics, Wuhan, China, October 2017*
2) Dac Thuong Ngo, Frédéric L. Pellet, Dominique Bruel. Numerical modeling of rock fracturing in geothermal systems. *6th International Conference on Coupled THMC Processes in Geosystems, Paris, France, July 2017*

Appendix 2: Simulation results for cases MS1 and MS3 of Section 4.3.2

Simulation results for case MS1 (friction coefficient μ_f = 0.35):

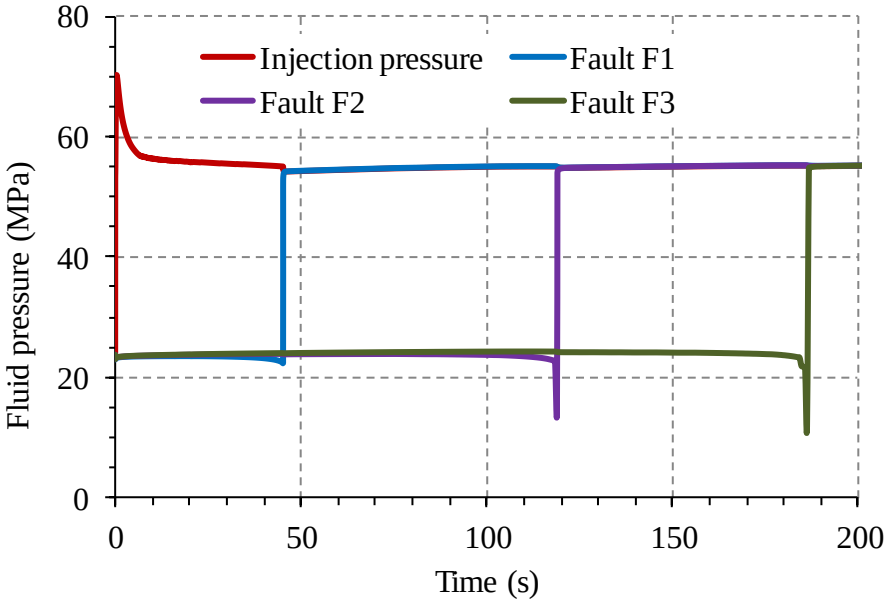

Figure AN-1 Time evolution of injection pressure and fluid pressure at the center of faults F1, F2, and F3 (case MS1)

(a) Fault F1

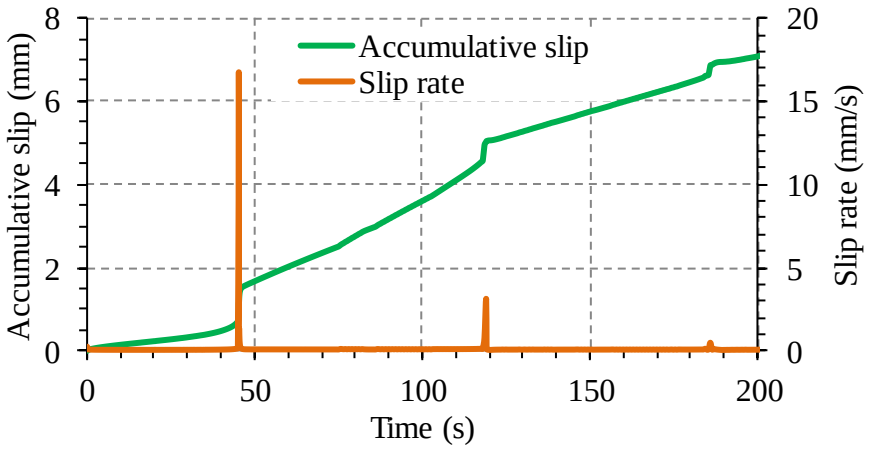

(b) Fault F2

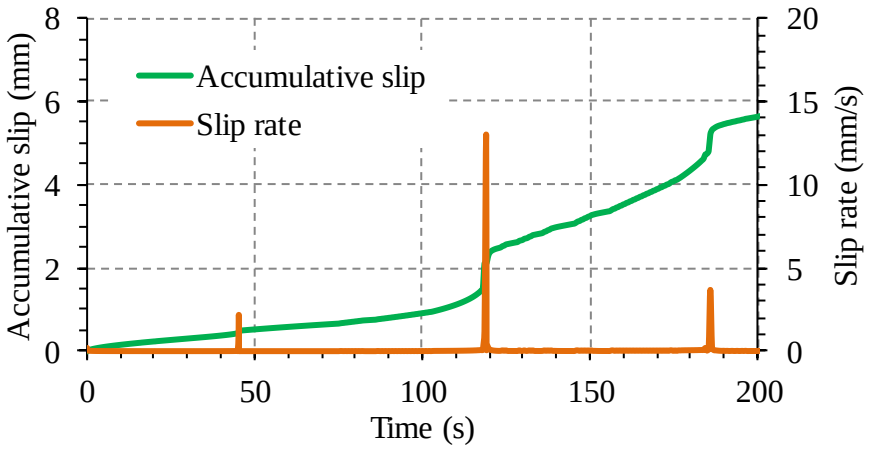

(c) Fault F3

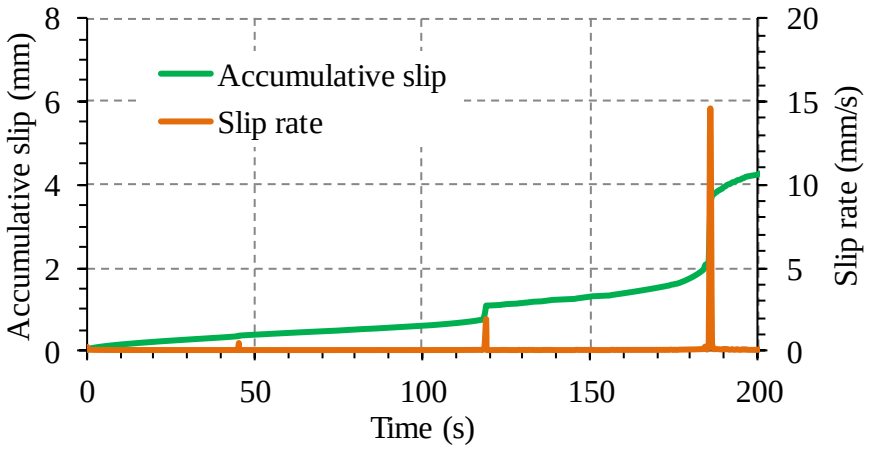

Figure AN-2 Time evolution of accumulative slip and slip rate for faults F1, F2, and F3 (case MS1)

Simulation results for case MS3 (friction coefficient μ_f = 1.0):

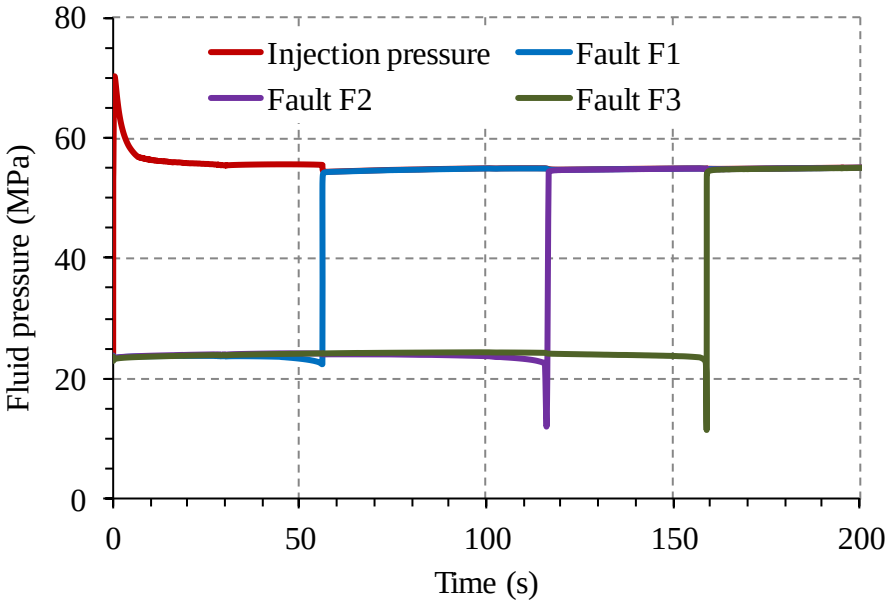

Figure AN-3 Time evolution of injection pressure and fluid pressure at the center of faults F1, F2, and F3 (case MS3)

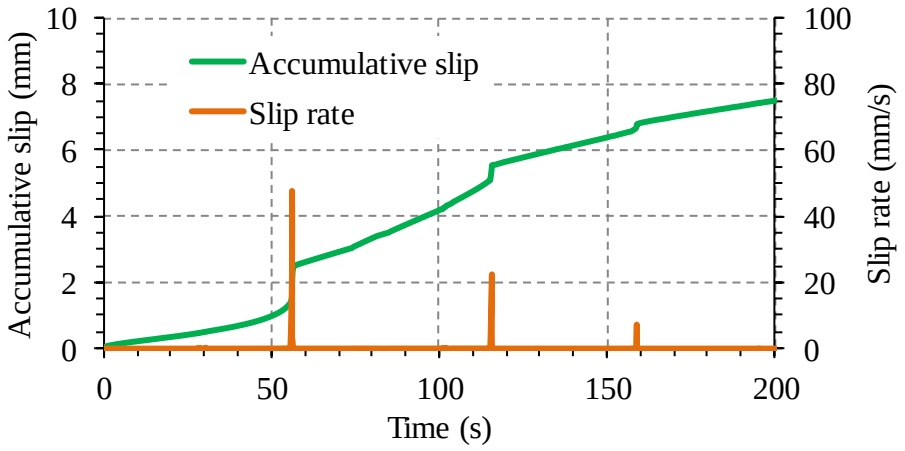

(a) Fault F1

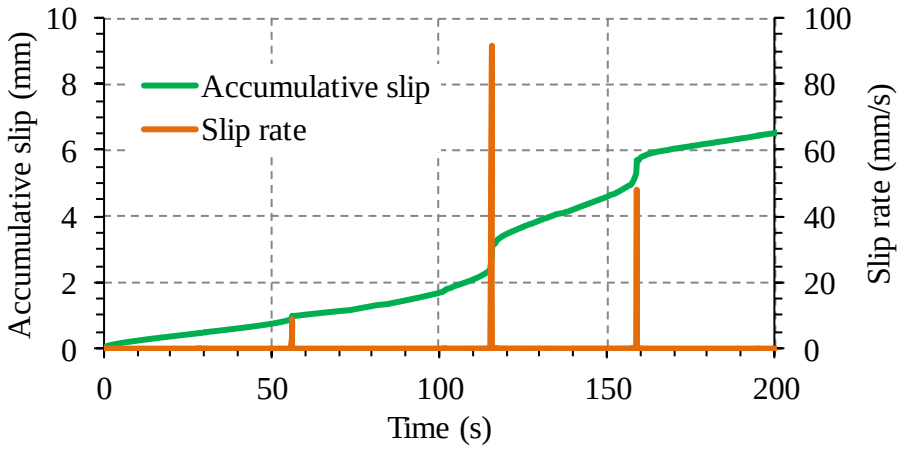

(b) Fault F2

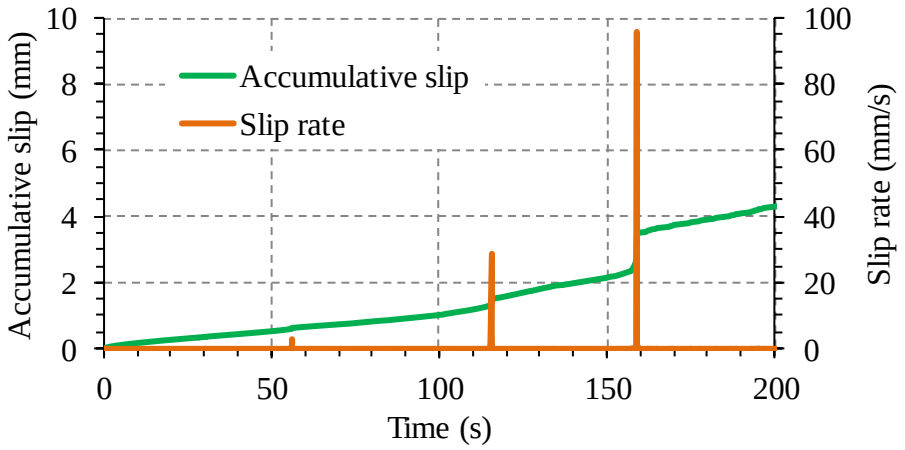

(c) Fault F3

Figure AN-4 Time evolution of accumulative slip and slip rate for faults F1, F2, and F3 (case MS3)

Appendix 3: Simulation results for cases MQ2, and MQ3 of Section 4.3.3

Simulation results for case MQ2 (injection rate Q = 1 L/s):

(a) Fault F1

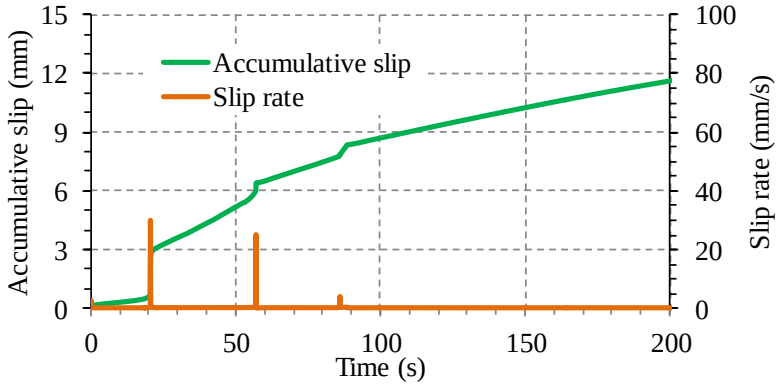

(b) Fault F2

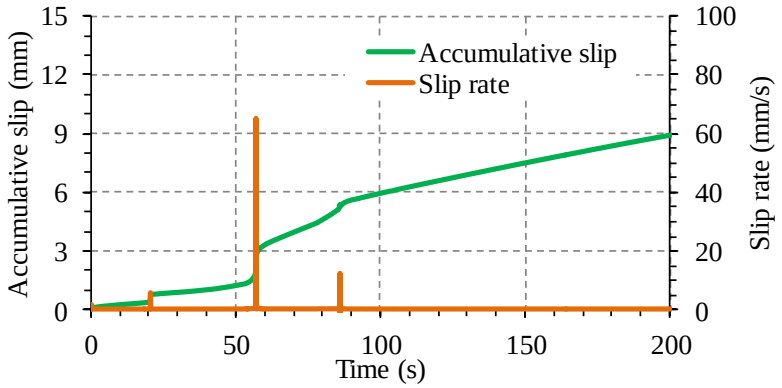

(c) Fault F3

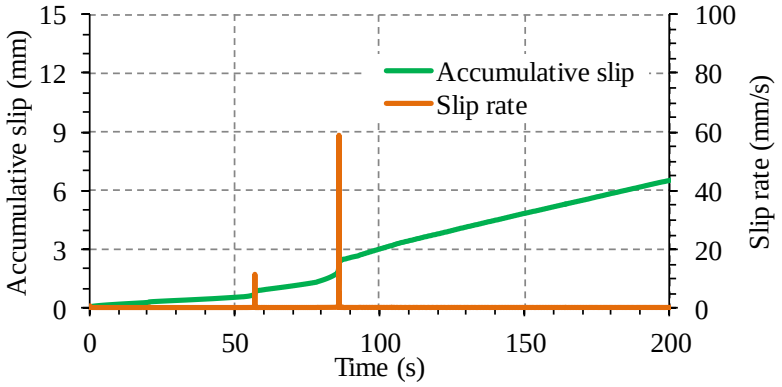

Figure AN-5 Time evolution of accumulative slip and slip rate for faults F1, F2, and F3 (case MQ2)

Simulation results for case MQ3 (injection rate Q = 2 L/s):

(a) Fault F1

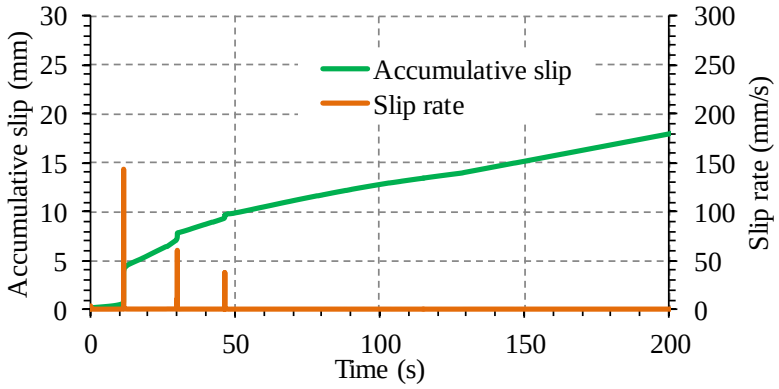

(b) Fault F2

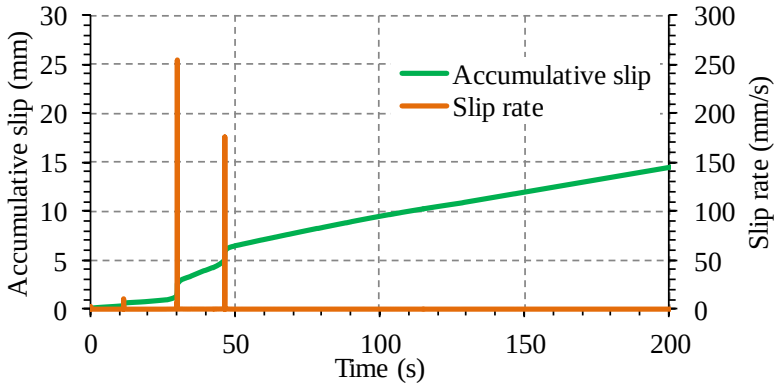

(c) Fault F3

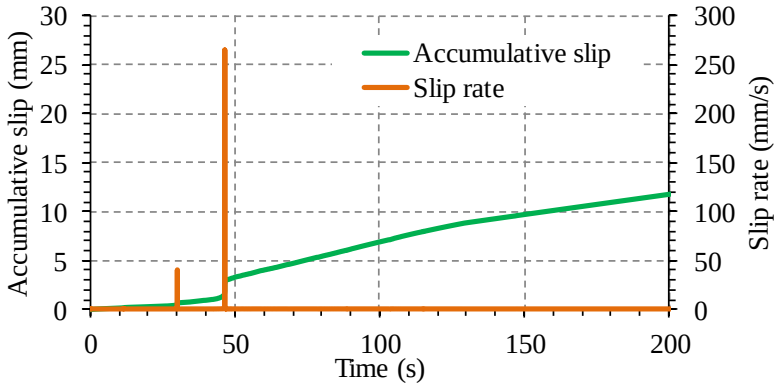

Figure AN-6 Time evolution of accumulative slip and slip rate for faults F1, F2, and F3 (case MQ3)

Appendix 4: Results of dynamic simulation for cases S2 and S3 of Section 5.3.2

Results of dynamic simulation for case S2:

(a) Point B

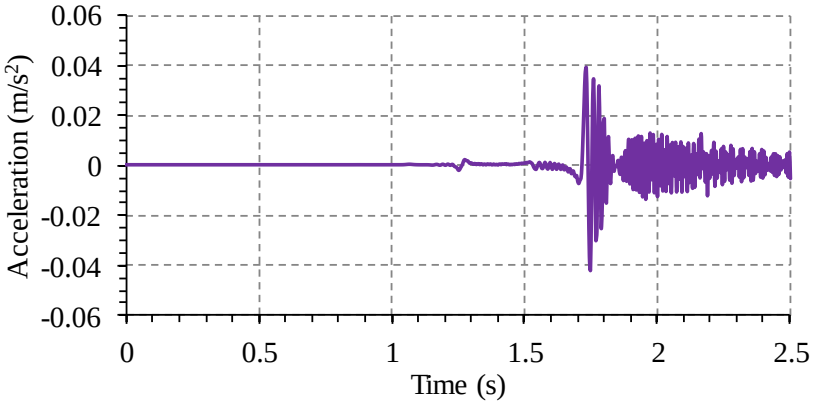

(b) Point C

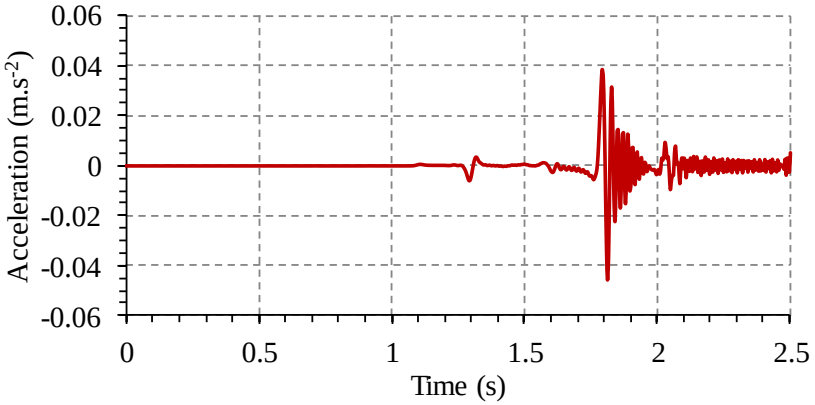

(c) Point D

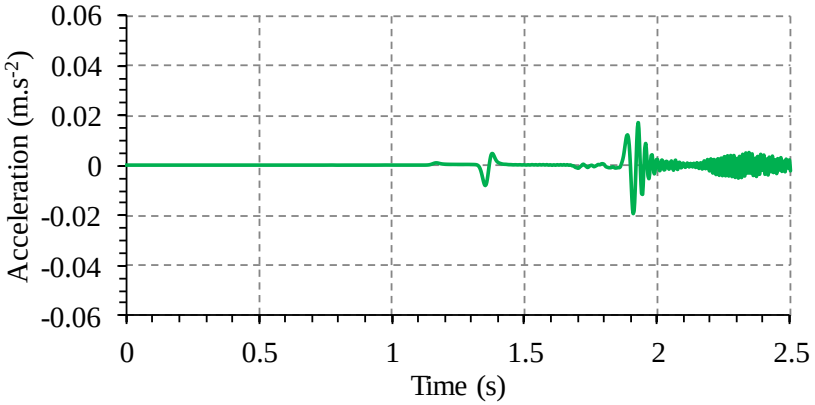

Figure AN-7 Time evolution of acceleration in direction 1 at points B, C, and D (case S2)

(a) Point B

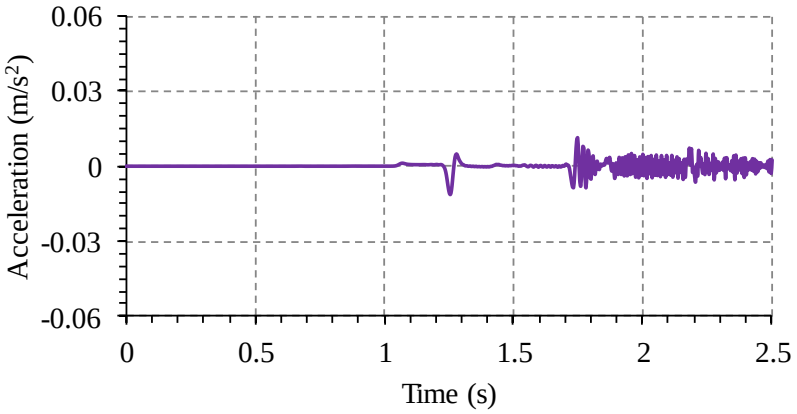

(b) Point C

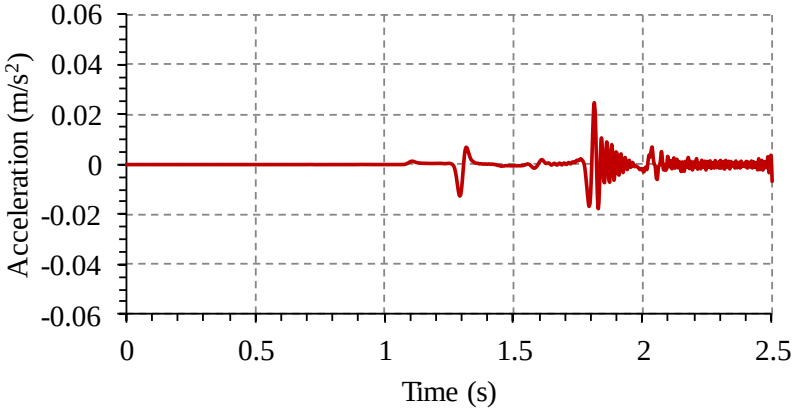

(c) Point D

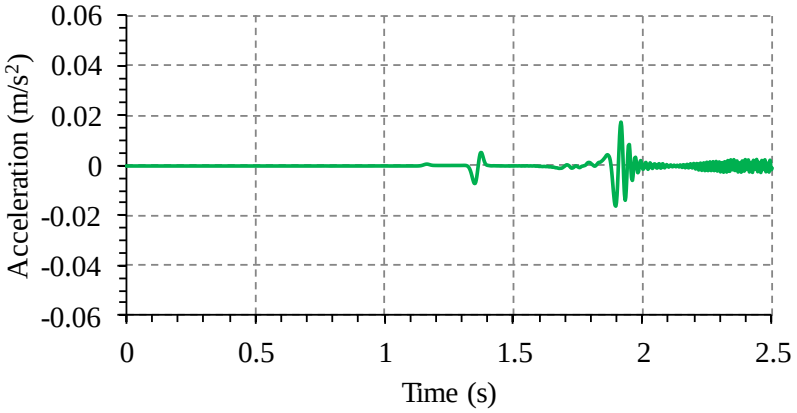

Figure AN-8 Time evolution of acceleration in direction 2 at points B, C, and D (case S2)

Results of dynamic simulation for case S3:

(a) Point B

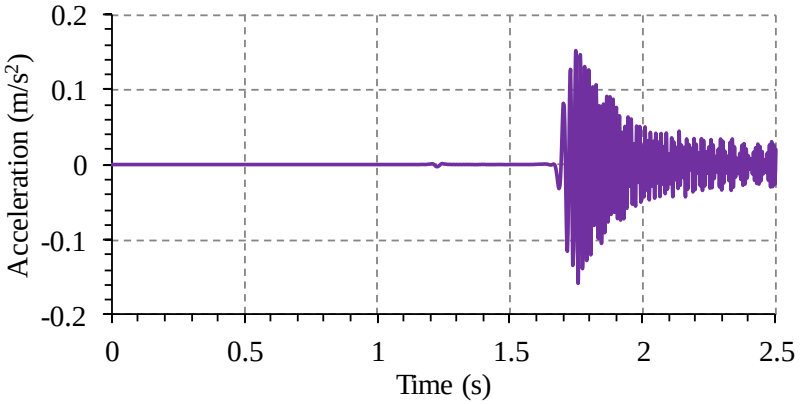

(b) Point C

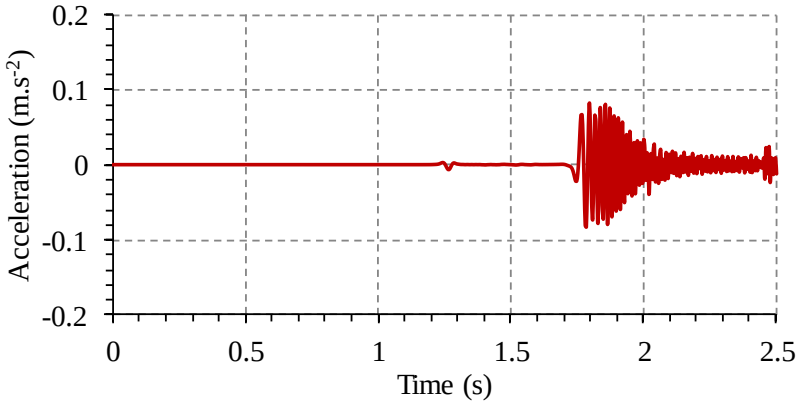

(c) Point D

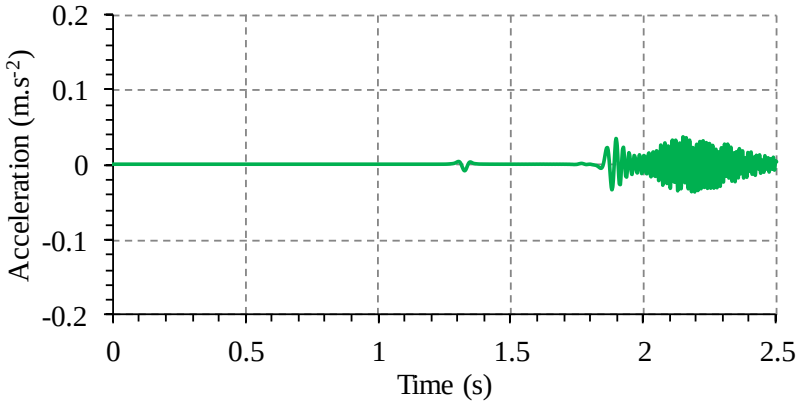

Figure AN-9 Time evolution of acceleration in direction 1 at points B, C, and D (case S3)

(a) Point B

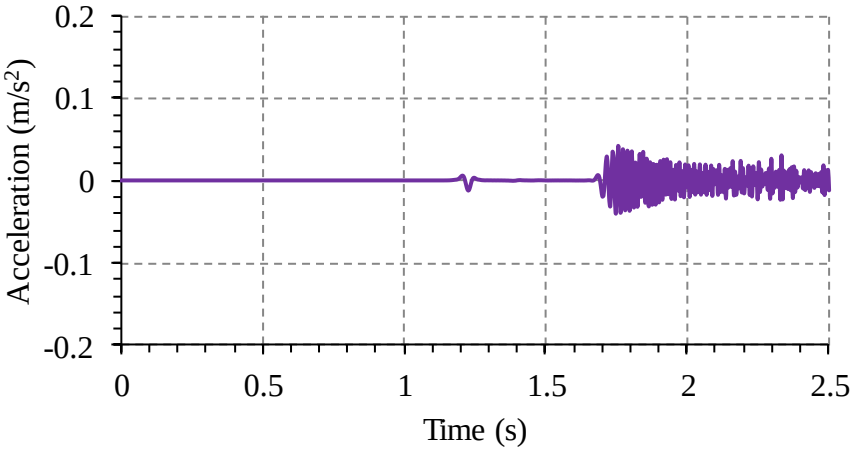

(b) Point C

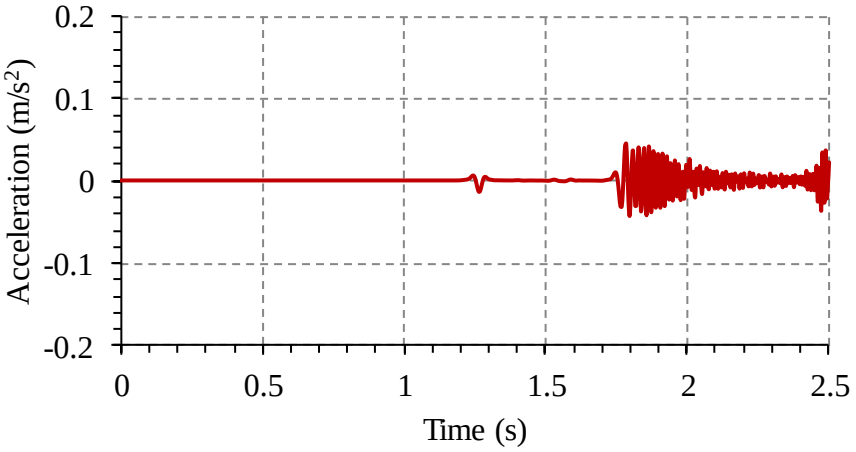

(c) Point D

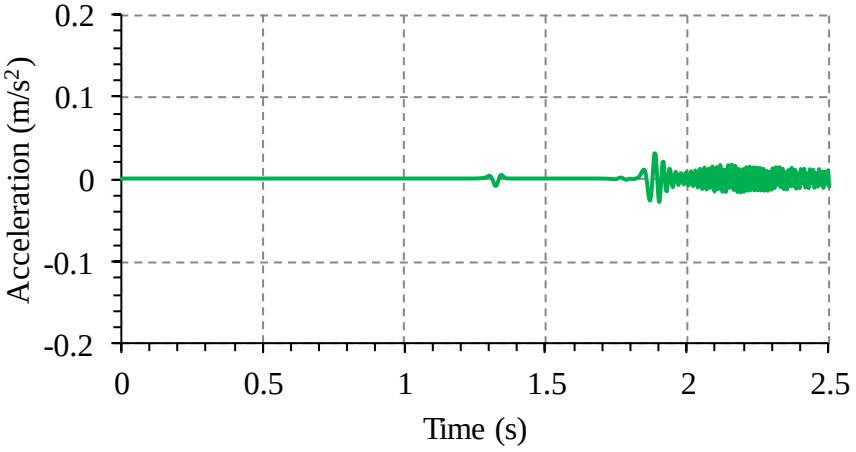

Figure AN-10 Time evolution of acceleration in direction 2 at points B, C, and D (case S3)

Appendix 5: Results of dynamic simulation for cases Q1 to Q4 of Section 5.3.3

Results of dynamic simulation for case Q1 (injection rate = 0.25 L/s):

(a) Point B

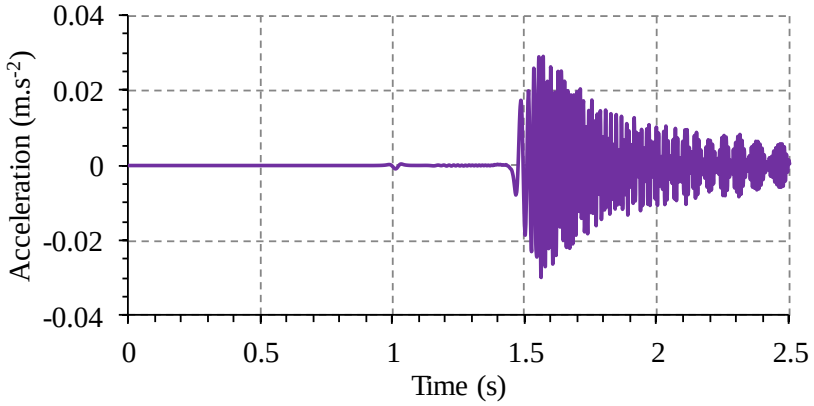

(b) Point C

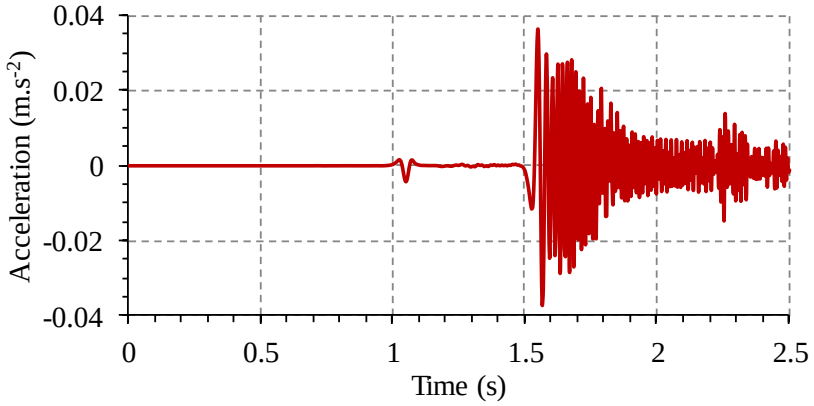

(c) Point D

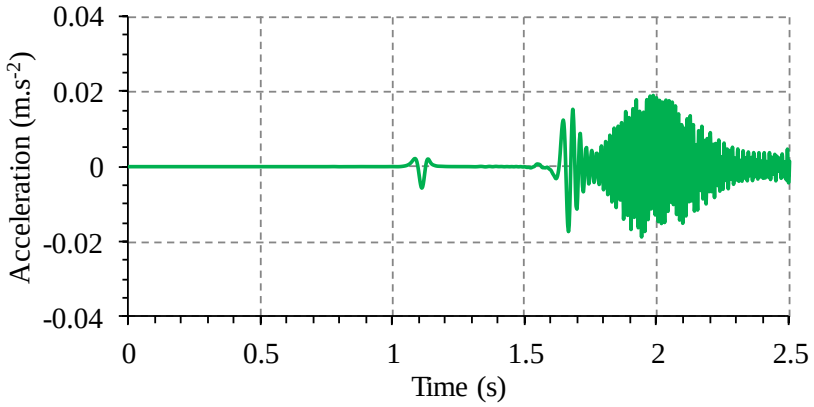

Figure AN-11 Time evolution of acceleration in direction 1 at points B, C, and D (case Q1)

(a) Point B

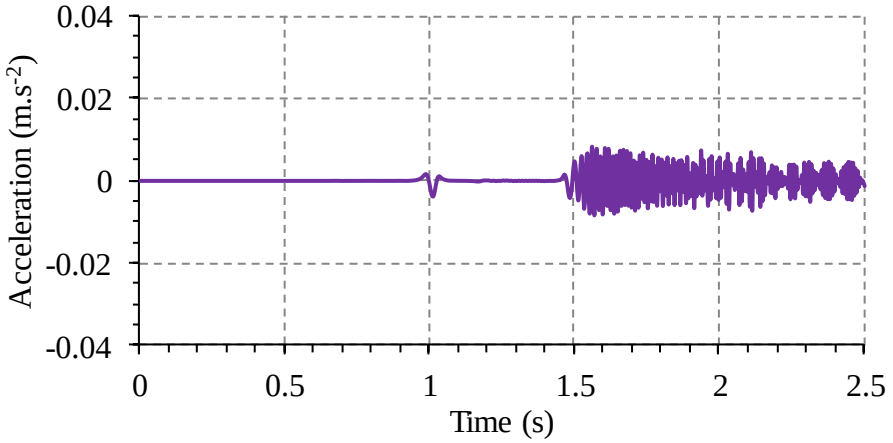

(b) Point C

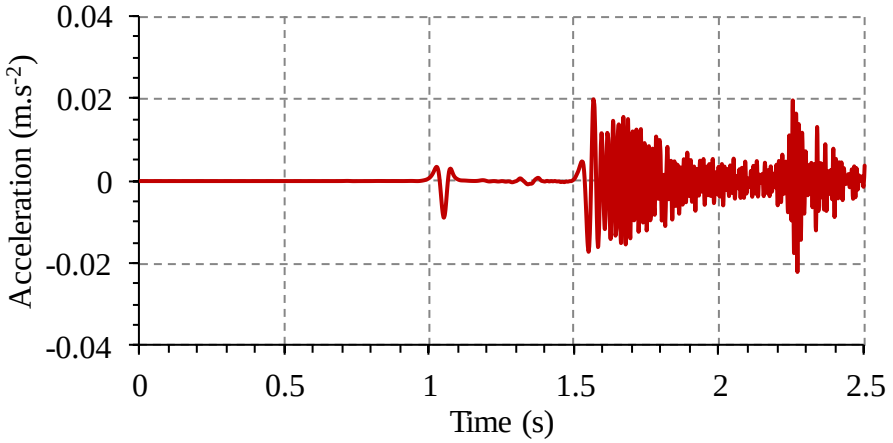

(c) Point D

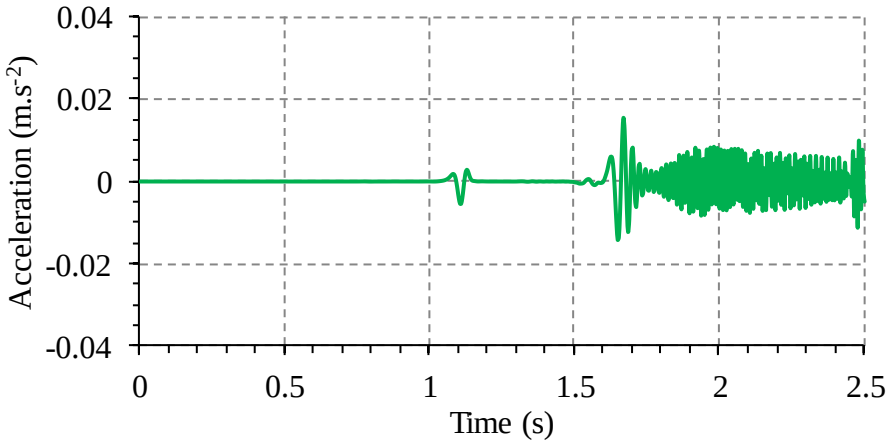

Figure AN-12 Time evolution of acceleration in direction 2 at points B, C, and D (case Q1)

Results of dynamic simulation for case Q2 (injection rate = 0.5 L/s):

(a) Point B

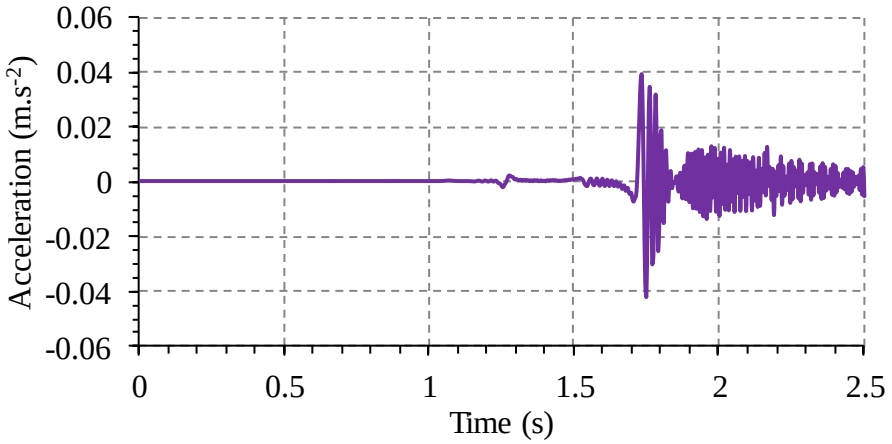

(b) Point C

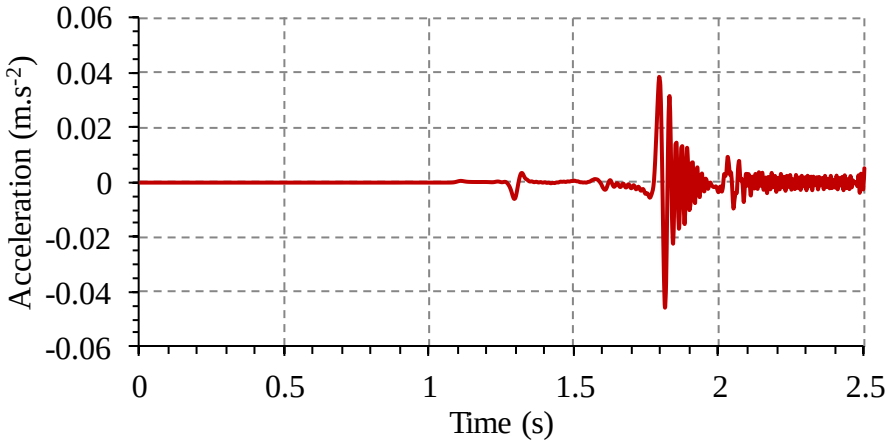

(c) Point D

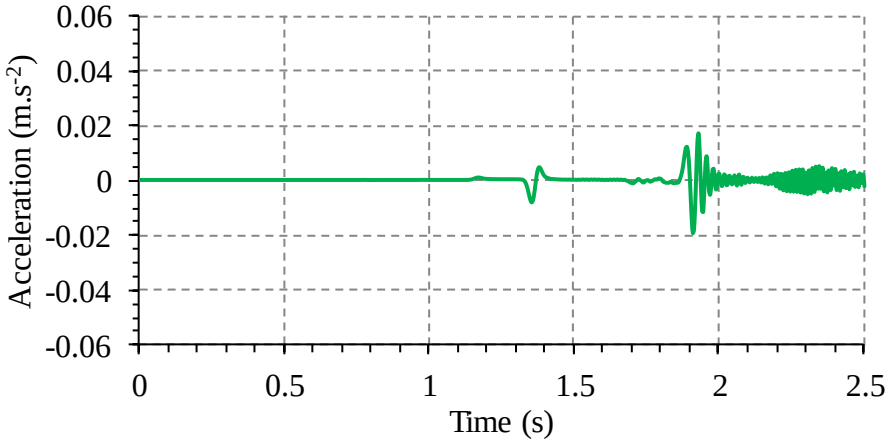

Figure AN-13 Time evolution of acceleration in direction 1 at points B, C, and D (case Q2)

(a) Point B

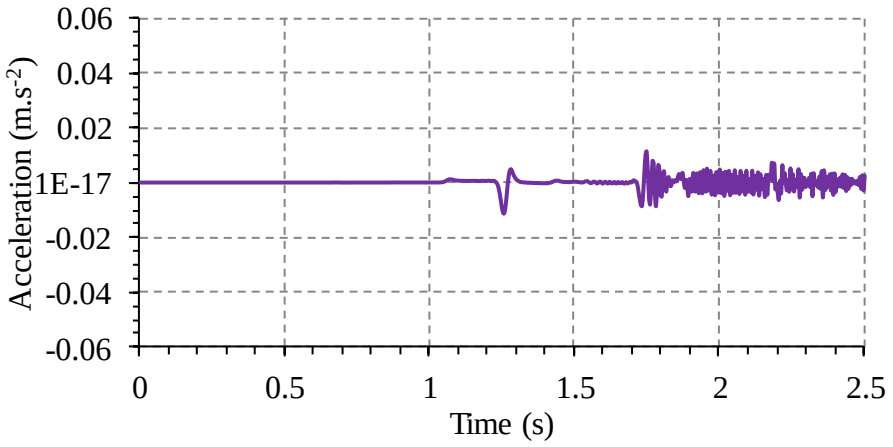

(b) Point C

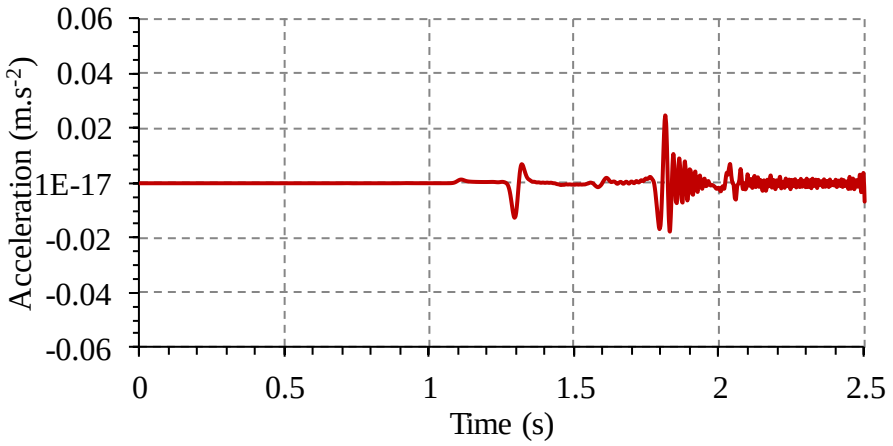

(c) Point D

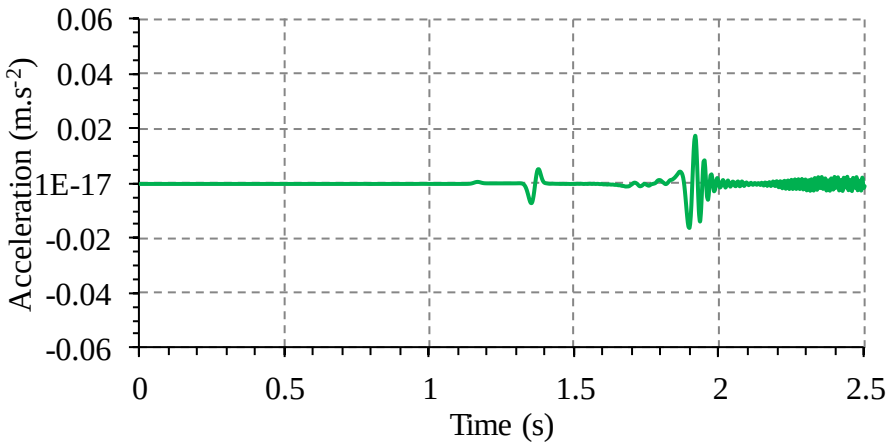

Figure AN-14 Time evolution of acceleration in direction 2 at points B, C, and D (case Q2)

Results of dynamic simulation for case Q3 (injection rate = 1 L/s):

(a) Point B

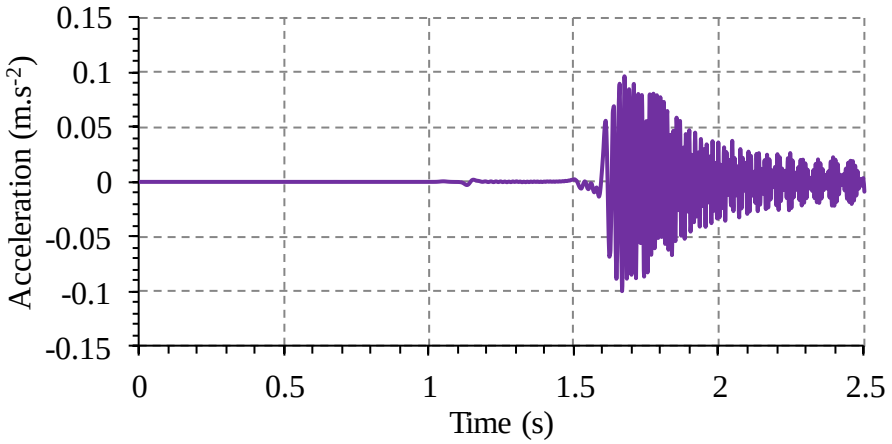

(b) Point C

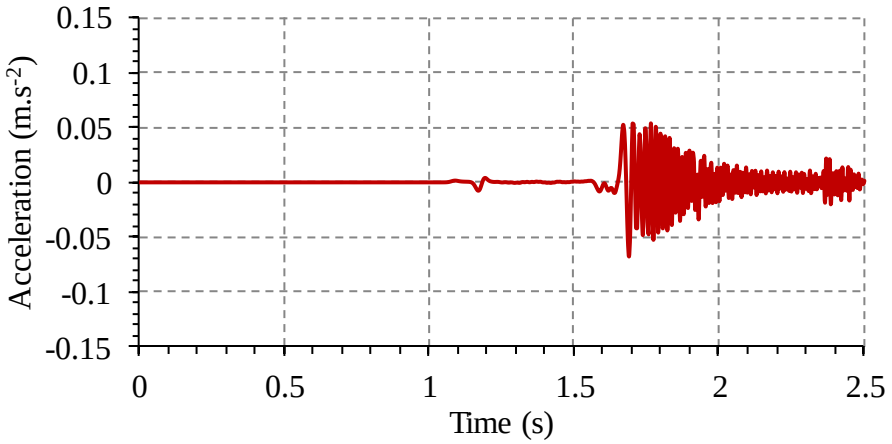

(c) Point D

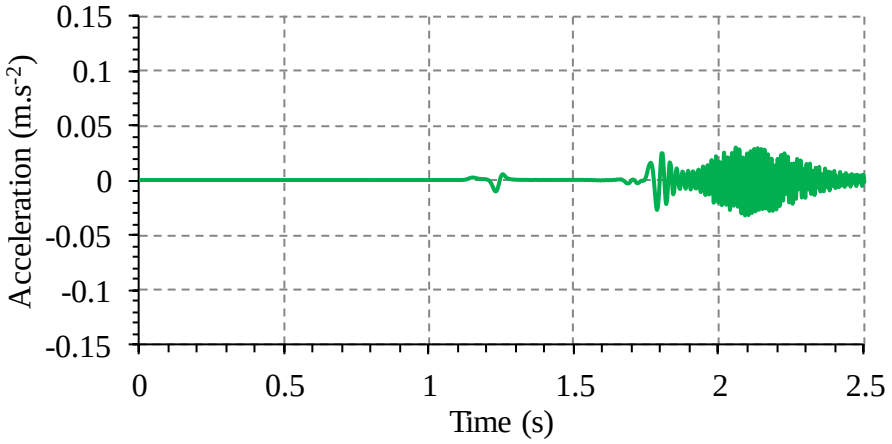

Figure AN-15 Time evolution of acceleration in direction 1 at points B, C, and D (case Q3)

(a) Point B

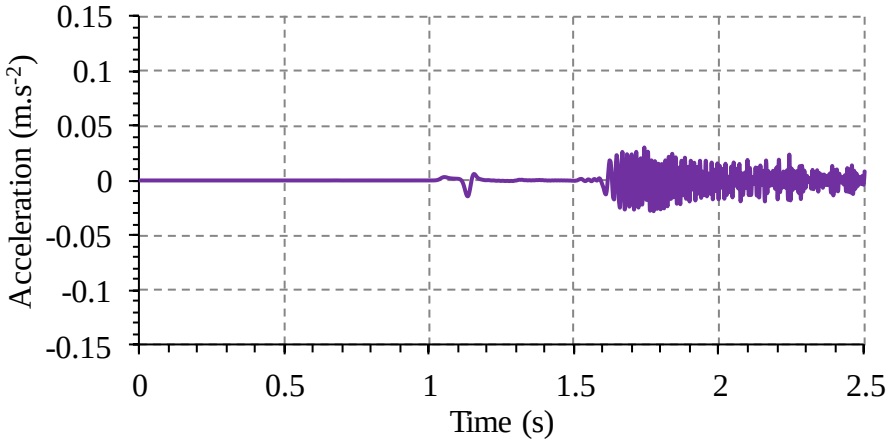

(b) Point C

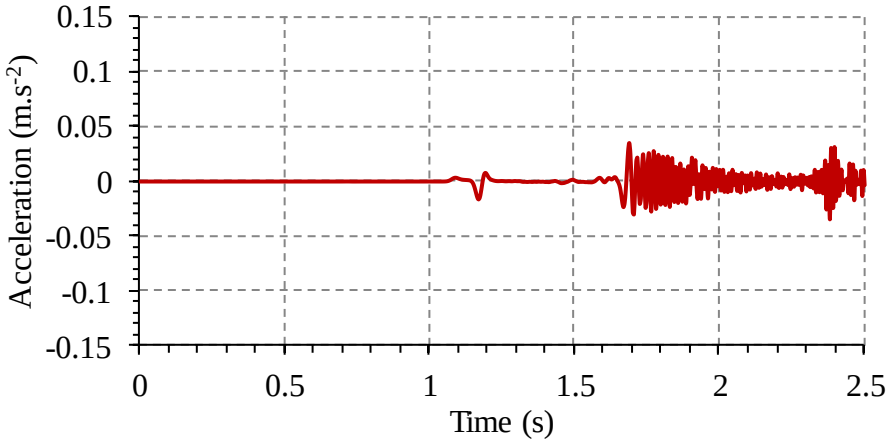

(c) Point D

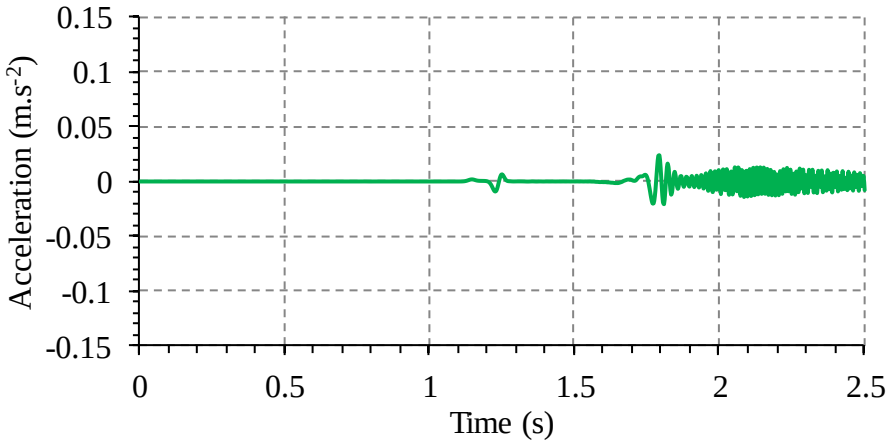

Figure AN-16 Time evolution of acceleration in direction 2 at points B, C, and D (case Q3)

Results of dynamic simulation for case Q4 (injection rate = 3 L/s):

(a) Point B

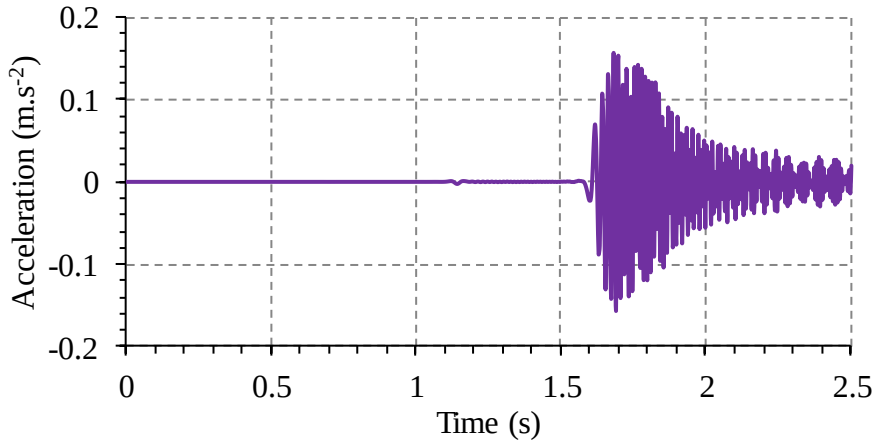

(b) Point C

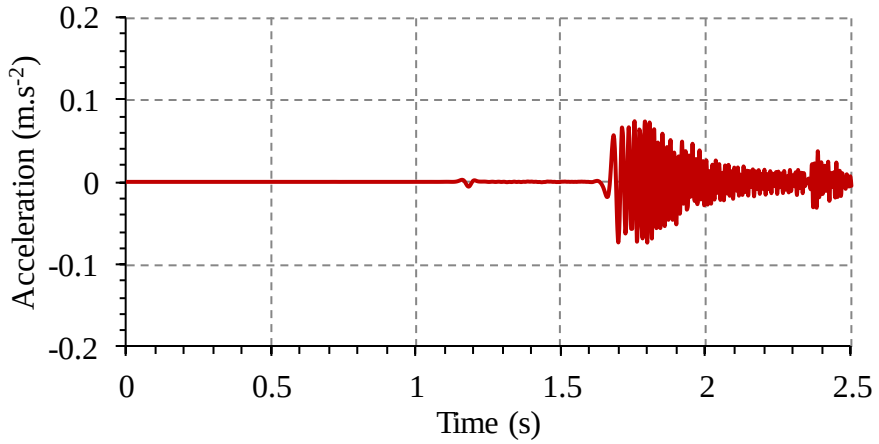

(c) Point D

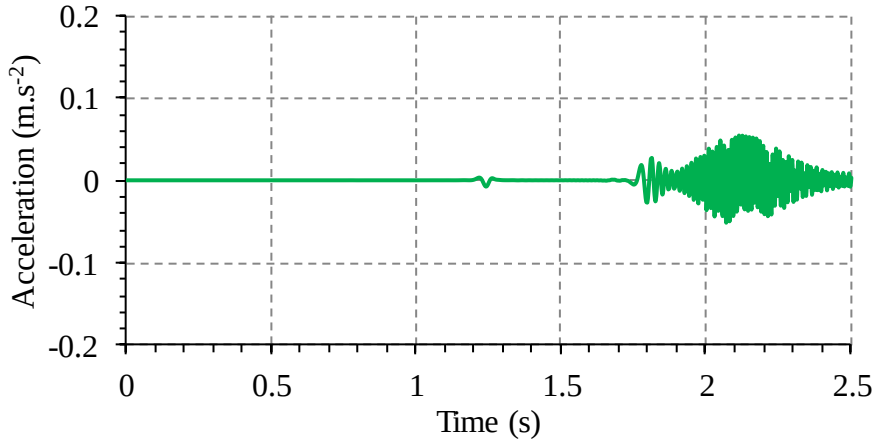

Figure AN-17 Time evolution of acceleration in direction 1 at points B, C, and D (case Q4)

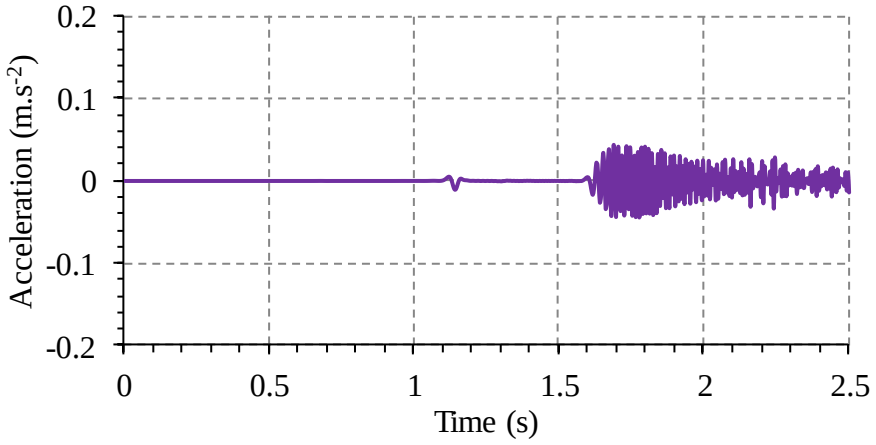

(a) Point B

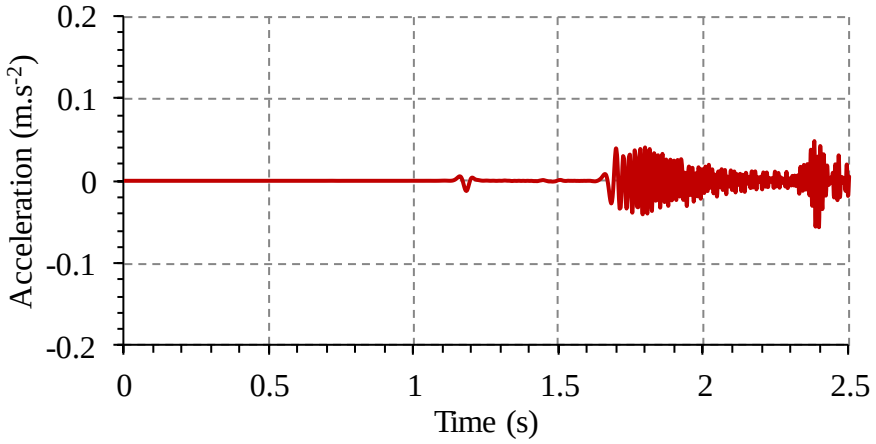

(b) Point C

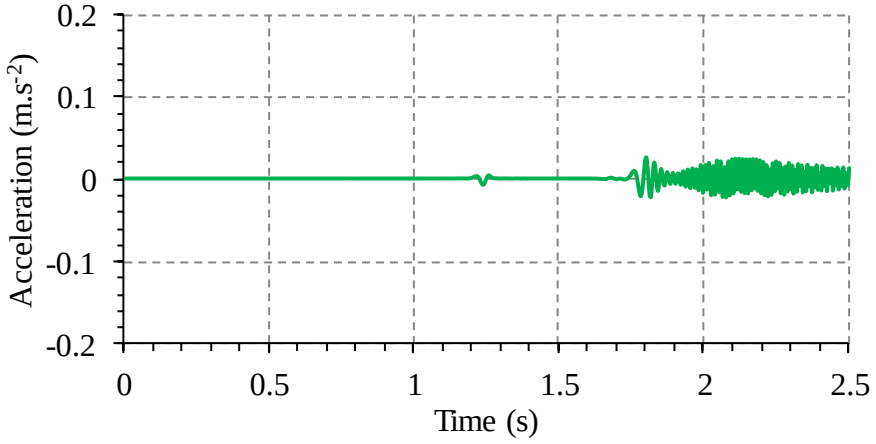

(c) Point D

Figure AN-18 Time evolution of acceleration in direction 2 at points B, C, and D (case Q4)

Appendix 6: Effect of the finite element mesh

The influence of the finite element mesh on the results of the hydromechanical simulation of fracture propagation is investigated and presented here. For this purpose, the KGD fracture model, which was studied in section 4.1.1, is chosen. Three different meshes are tested. These meshes are presented in Figure AN-19. The minimum size of these meshes is 0.05 m, 0.3 m, and 1 m.

The material properties, the boundary and loading conditions are similar to what were used in section 4.1.1.

The simulation results for hydraulic aperture and injection pressure for these meshes are compared to the analytical solution and presented in Figure AN-20. It can be seen that as the mesh size decreases, the simulation results approach closer to the analytical solution. The mesh A, which has the minimum size of 0.05 m, gives the best results. Meanwhile, for the mesh C, which has the minimum size of 1 m, oscillations are observed in the time evolution of both the hydraulic aperture at the injection point and the injection pressure.

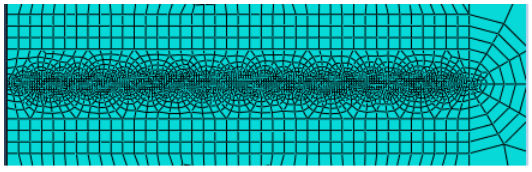

(a) Mesh A

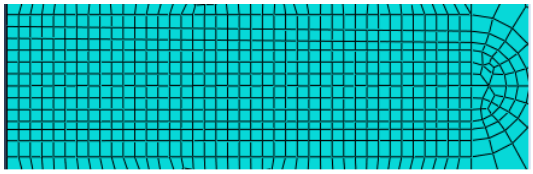

(b) Mesh B

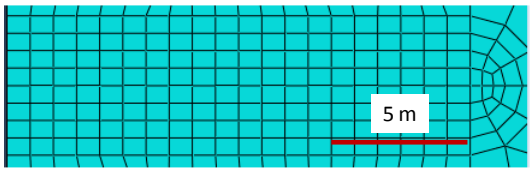

(c) Mesh C

Figure AN-19 Different finite element meshes. The minimum size for mesh A, B, and C is 0.05 m, 0.3 m, and 1 m, respectively.

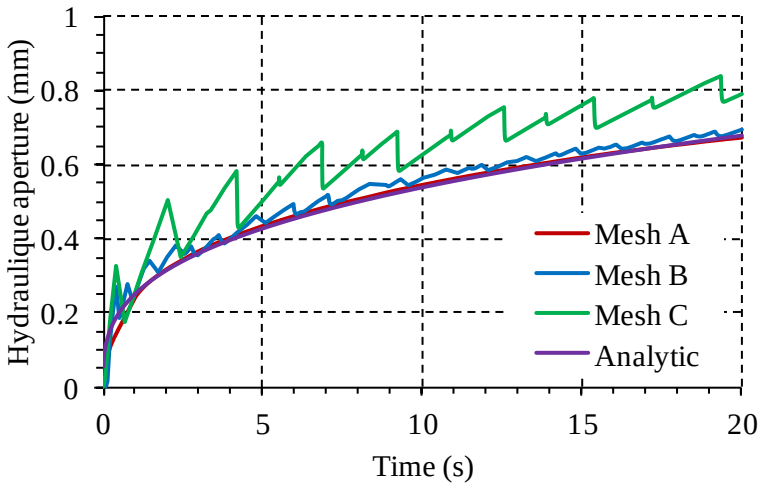

(a)

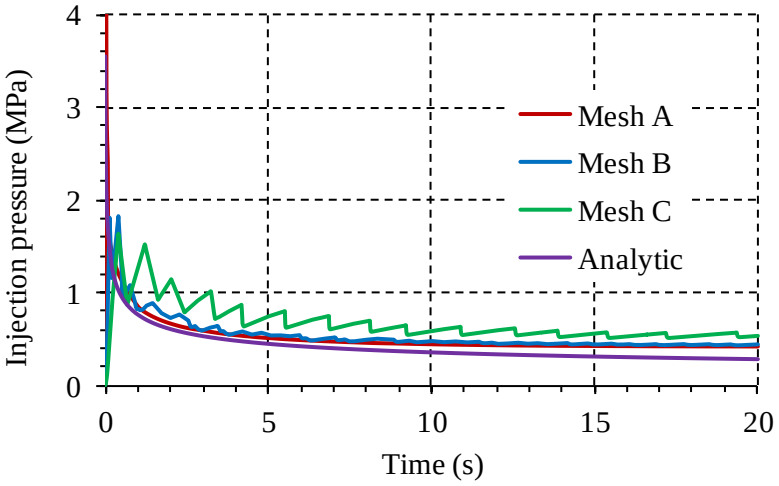

(b)

Figure AN-20 Time evolution of (a) Hydraulic aperture at the injection point and (b) Injection pressure

References

ABAQUS, 2016. Analysis User's Manual Version R2016, Dassault Système.

Abé, H., 1992. Fundamentals of design concept and design methodology for artificial geothermal reservoir systems. GRC Bulletin, 149-155.

Adachi, J., Detournay, E., 2002. Self-similar solution of a plane-strain fracture driven by a power-law fluid. International Journal for Numerical and Analytical Methods in Geomechanics 26, 579-604.

Anderson, T.L., 2005. Fracture Mechanics: Fundamentals and Applications. CRC Press.

Aochi, H., Poisson, B., Schmittbuhl, J., Toussaint, R., Rachez, X., 2013. Self-induced seismicity due to fluid circulation along faults. Geophysical Journal International 196, 1544-1563.

Asanuma, H., Soma, N., Kaieda, H., Kumano, Y., Izumi, T., Tezuka, K., Niitsuma, H., Wyborn, D., 2005. Microseismic monitoring of hydraulic stimulation at the Australian HDR project in Cooper Basin, Proceedings World Geothermal Congress, Antalya, Turkey, pp. 24-29.

Atkinson, B.K., 1989. Fracture Mechanics of Rock. Academic Press.

Atkinson, C., Craster, R., 1991. Plane strain fracture in poroelastic media. Proceedings of the Royal Society of London. Series A: Mathematical and Physical Sciences 434, 605-633.

Baisch, S., Weidler, R., Vörös, R., Wyborn, D., de Graaf, L., 2006. Induced seismicity during the stimulation of a geothermal HFR reservoir in the Cooper Basin, Australia. Bulletin of the Seismological Society of America 96, 2242-2256.

Banks, D., 2012. An Introduction to Thermogeology: Ground Source Heating and Cooling. John Wiley & Sons.

Barbier, E., 1997. Nature and technology of geothermal energy: A review. Renewable and Sustainable Energy Reviews 1, 1-69.

Barenblatt, G.I., 1962. The mathematical theory of equilibrium cracks in brittle fracture. Advances in Applied Mechanics 7, 55-129.

Baria, R., Green, A.S.P., Hearn, K.C., 1989. Phase 2B Final Report of the Camborne School of Mines Project (Part 5 Sesmics. Section 1 Microseismic results). Camborne School of Mines, Penryn, UK, pp. 682-740.

Baria, R., Michelet, S., Baumgärtner, J., Dyer, B., Gerard, A., Nicholls, J., Hettkamp, T., Teza, D., Soma, N., Asanuma, H., 2004. Microseismic monitoring of the world's largest potential HDR reservoir, Proceedings, Twenty-Ninth Workshop on Geothermal Reservoir Engineering.

Batchelor, A., 1989a. The creation of hot dry rock systems by combined explosive and hydraulic fracturing. Camborne School of Mines.

Batchelor, A., 1989b. Phase 2B Final Report of the Camborne School of Mines Project (Part 2 The drilling and stimulation of the third well (RH15). Section 1 The role of the third well in the CSM HDR project). Camborne School of Mines, Penryn, UK, pp. 185-200.

Beckers, K.F., Lukawski, M.Z., Anderson, B.J., Moore, M.C., Tester, J.W., 2014. Levelized costs of electricity and direct-use heat from Enhanced Geothermal Systems. Journal of Renewable and Sustainable Energy 6, 013141.

Belytschko, T., Black, T., 1999. Elastic crack growth in finite elements with minimal remeshing. International Journal for Numerical Methods in Engineering 45, 601-620.

Benzeggagh, M.L., Kenane, M., 1996. Measurement of mixed-mode delamination fracture toughness of unidirectional glass/epoxy composites with mixed-mode bending apparatus. Composites Science and Technology 56, 439-449.

Blanton, T.L., 1982. An Experimental Study of Interaction Between Hydraulically Induced and Pre-Existing Fractures, SPE Unconventional Gas Recovery Symposium. Society of Petroleum Engineers, Pittsburgh, Pennsylvania, p. 13.

Bormann, P., Di Giacomo, D., 2011. The moment magnitude Mw and the energy magnitude Me: common roots and differences. Journal of Seismology 15, 411-427.

Boudet, J., Ciliberto, S., Steinberg, V., 1995. Experimental study of the instability of crack propagation in brittle materials. EPL (Europhysics Letters) 30, 337.

Boyle, G., 2004. Renewable energy. Oxford University Press.

Brace, W., Byerlee, J., 1966. Stick-slip as a mechanism for earthquakes. Science 153, 990-992.

Broberg, K.B., 1999. Cracks and Fracture. Academic Press, San Diego.

Brown, D.W., 2009. Hot dry rock geothermal energy: important lessons from Fenton Hill, 34th Workshop on Geothermal Reservoir Engineering, Stanford University, California, USA.

Brown, D.W., Duchane, D.V., 1999. Scientific progress on the Fenton Hill HDR project since 1983. Geothermics 28, 591-601.

Brown, D.W., Duchane, D.V., Heiken, G., Hriscu, V.T., 2012. Mining the earth's heat: hot dry rock geothermal energy. Springer Science & Business Media.

Bruel, D., 1995. Heat extraction modelling from forced fluid flow through stimulated fractured rock masses: application to the Rosemanowes hot dry rock reservoir. Geothermics 24, 361-374.

Bruel, D., 2002. Impact of induced thermal stresses during circulation tests in an engineered fractured geothermal reservoir: example of the Soultz-sous-Forets European hot fractured rock geothermal project, Rhine Graben, France. Oil & Gas Science and Technology 57, 459-470.

Bunger, A.P., Detournay, E., Garagash, D.I., 2005. Toughness-dominated hydraulic fracture with leak-off. International Journal of Fracture 134, 175-190.

Byerlee, J., 1978. Friction of rocks. Pure and Applied Geophysics 116, 615-626.

Byerlee, J.D., Brace, W., 1968. Stick slip, stable sliding, and earthquakes—effect of rock type, pressure, strain rate, and stiffness. Journal of Geophysical Research 73, 6031-6037.

Calò, M., Dorbath, C., Frogneux, M., 2014. Injection tests at the EGS reservoir of Soultz-sous-Forêts. Seismic response of the GPK4 stimulations. Geothermics 52, 50-58.

Cappa, F., Guglielmi, Y., Nussbaum, C., Birkholzer, J., 2018. On the relationship between fault permeability increases, induced Stress perturbation, and the growth of aseismic slip during fluid injection. Geophysical Research Letters 45, 11,012-011,020.

Carter, E., 1957. Optimum fluid characteristics for fracture extension, in: Howard, G.C., Fast, C. (Eds.), Drilling and Production Practice. American Petroleum Institute.

Cha, M., Alqahtani, N.B., Yin, X., Kneafsey, T.J., Yao, B., Wu, Y.-S., 2017. Laboratory system for studying cryogenic thermal rock fracturing for well stimulation. Journal of Petroleum Science and Engineering 156, 780-789.

Cornet, F., 1989. Experimental investigations of forced fluid flow through a granite rock mass, Proceedings 4th Int. Seminar on the results of EC Geothermal Energy Demonstration, Florence, Italy, pp. 189-204.

Cornet, F., Bérard, T., Bourouis, S., 2007. How close to failure is a granite rock mass at a 5 km depth? International Journal of Rock Mechanics and Mining Sciences 44, 47-66.

Cornet, F.H., 2015. Elements of Crustal Geomechanics. Cambridge University Press, Cambridge.

Coussy, O., 2004. Poromechanics. John Wiley & Sons.

Cuenot, N., Dorbath, C., Dorbath, L., 2008. Analysis of the Microseismicity Induced by Fluid Injections at the EGS Site of Soultz-sous-Forêts (Alsace, France): Implications for the Characterization of the Geothermal Reservoir Properties. Pure and Applied Geophysics 165, 797-828.

Cueto-Felgueroso, L., Santillán, D., Mosquera, J.C., 2017. Stick-slip dynamics of flow-induced seismicity on rate and state faults. Geophysical Research Letters 44, 4098-4106.

Cundall, P.A., Hart, R.D., 1992. Numerical modelling of discontinua. Engineering Computations 9, 101-113.

Dahi Taleghani, A., Olson, J.E., 2013. How natural fractures could affect hydraulic-fracture geometry. SPE journal 19, 161-171.

De Simone, S., Vilarrasa, V., Carrera, J., Alcolea, A., Meier, P., 2013. Thermal coupling may control mechanical stability of geothermal reservoirs during cold water injection. Physics and Chemistry of the Earth, Parts A/B/C 64, 117-126.

Deichmann, N., Giardini, D., 2009. Earthquakes induced by the stimulation of an enhanced geothermal system below Basel (Switzerland). Seismological Research Letters 80, 784-798.

Detournay, E., 2004. Propagation regimes of fluid-driven fractures in impermeable rocks. International Journal of Geomechanics 4, 35-45.

Dèzes, P., Schmid, S., Ziegler, P., 2004. Evolution of the European Cenozoic Rift System: interaction of the Alpine and Pyrenean orogens with their foreland lithosphere. Tectonophysics 389, 1-33.

Dieterich, J.H., 1972. Time-dependent friction in rocks. Journal of Geophysical Research 77, 3690-3697.

DiPippo, R., 1988. International Developments in Geothermal Power Production. Geothermal Resources Council Bulletin, 8-19.

DOE, 2015. Geothermal Technologies Program, US Department of Energy.

Dorbath, L., Cuenot, N., Genter, A., Frogneux, M., 2009. Seismic response of the fractured and faulted granite of Soultz-sous-Forêts (France) to 5 km deep massive water injections. Geophysical Journal International 177, 653-675.

Dublanchet, P., Bernard, P., Favreau, P., 2013. Interactions and triggering in a 3-D rate-and-state asperity model. Journal of Geophysical Research: Solid Earth 118, 2225-2245.

Duchane, D., Brown, D., 2002. Hot dry rock (HDR) geothermal energy research and development at Fenton Hill, New Mexico. GHC Bulletin, 13-19.

Dugdale, D.S., 1960. Yielding of steel sheets containing slits. Journal of the Mechanics and Physics of Solids 8, 100-104.

Edwards, L.M., Chilingar, G.V., Rieke, H.H., Fertl, W.H., 1982. Handbook of geothermal energy. Gulf Publishing Company.

Ellsworth, W.L., 2013. Injection-Induced Earthquakes. Science 341, 1225942.

Engelder, J.T., Scholz, C.H., 1976. The role of asperity indentation and ploughing in rock friction—II: Influence of relative hardness and normal load. International Journal of Rock Mechanics and Mining Sciences & Geomechanics Abstracts 13, 155-163.

Erdogan, F., Sih, G., 1963. On the crack extension in plates under plane loading and transverse shear. Journal of Basic Engineering 85, 519-525.

Evans, K.F., Cornet, F.H., Hashida, T., Hayashi, K., Ito, T., Matsuki, K., Wallroth, T., 1999. Stress and rock mechanics issues of relevance to HDR/HWR engineered geothermal systems: Review of developments during the past 15 years. Geothermics 28, 455-474.

Evans, K.F., Zappone, A., Kraft, T., Deichmann, N., Moia, F., 2012. A survey of the induced seismic responses to fluid injection in geothermal and CO2 reservoirs in Europe. Geothermics 41, 30-54.

Faulds, J., Coolbaugh, M., Bouchot, V., Moek, I., Oguz, K., 2010. Characterizing structural controls of geothermal reservoirs in the Great Basin, USA, and Western Turkey: Developing successful exploration strategies in extended terranes, World Geothermal Congress 2010, p. 11

Fineberg, J., Gross, S.P., Marder, M., Swinney, H.L., 1992. Instability in the propagation of fast cracks. Physical Review B 45, 5146.

Flóvenz, O., Ágústsson, K., Guðnason, E.Á., Kristjánsdóttir, S., 2015. Reinjection and induced seismicity in geothermal fields in Iceland, Proceedings of World Geothermal Congress.

Freund, L.B., 1998. Dynamic Facture Mechanics. Cambridge University Press.

Freymark, J., Sippel, J., Scheck-Wenderoth, M., Bär, K., Stiller, M., Fritsche, J.-G., Kracht, M., 2017. The deep thermal field of the Upper Rhine Graben. Tectonophysics 694, 114-129.

Garagash, D.I., 2006. Plane-strain propagation of a fluid-driven fracture during injection and shut-in: Asymptotics of large toughness. Engineering Facture Mechanics 73, 456-481.

Gaucher, E., Schoenball, M., Heidbach, O., Zang, A., Fokker, P.A., van Wees, J.-D., Kohl, T., 2015. Induced seismicity in geothermal reservoirs: A review of forecasting approaches. Renewable and Sustainable Energy Reviews 52, 1473-1490.

Geertsma, J., de Klerk, F., 1969. A rapid method of predicting width and extent of hydraulically induced fractures. Journal of Petroleum Technology 21, 1,571-571,581.

Geertsma, J., Haafkens, R., 1979. A Comparison of the Theories for Predicting Width and Extent of Vertical Hydraulically Induced Fractures. Journal of Energy Resources Technology 101, 8-19.

Genter, A., Evans, K., Cuenot, N., Fritsch, D., Sanjuan, B., 2010. The Soultz geothermal adventure: 20 years of research and exploration of deep crystalline fractured rocks for EGS development. Comptes Rendus Geoscience 342, 502-516.

Genter, A., Traineau, H., 1996. Analysis of macroscopic fractures in granite in the HDR geothermal well EPS-1, Soultz-sous-Forêts, France. Journal of Volcanology and Geothermal Research 72, 121-142.

Geodynamics, 2015. Annual report 2014–2015. Geodynamics Limited 2015.

Ghassemi, A., 2012. A Review of Some Rock Mechanics Issues in Geothermal Reservoir Development. Geotechnical and Geological Engineering 30, 647-664.

Ghassemi, A., Tao, Q., 2016. Thermo-poroelastic effects on reservoir seismicity and permeability change. Geothermics 63, 210-224.

Ghassemi, A., Tarasovs, S., 2015. Analysis of Fracture Propagation under Thermal Stress in Geothermal Reservoirs, Proceedings World Geothermal Congress 2015, Melbourne, Australia.

Ghassemi, A., Zhang, Q., 2004. Poro-thermoelastic mechanisms in wellbore stability and reservoir stimulation, Proceedings of the 29th Workshop on Geothermal Reservoir Engineering, Stanford University, CA.

Gibowicz, S., Young, R., Talebi, S., Rawlence, D., 1991. Source parameters of seismic events at the Underground Research Laboratory in Manitoba, Canada: Scaling relations for events with moment magnitude smaller than− 2. Bulletin of the Seismological Society of America 81, 1157-1182.

Gischig, V.S., 2015. Rupture propagation behavior and the largest possible earthquake induced by fluid injection into deep reservoirs. Geophysical Research Letters 42, 7420-7428.

Glaser, S.D., Selvadurai, P.A., 2016. Asperity generation and its relationship to seismicity on a planar fault: a laboratory simulation. Geophysical Journal International 208, 1009-1025.

Green, A.S.P., Baria, R., 1989. Phase 2B Final Report of the Camborne School of Mines Project (Part 5 Sesmics. Section 2 Crosshole seismic results). Camborne School of Mines, Penryn, UK, pp. 741-838.

Griffith, A.A., 1920. The phenomenon of rupture and flow in solids. Philosophical Transactions of the Royal Socieity London, A 221, 163-198.

Grigoli, F., Cesca, S., Rinaldi, A., Manconi, A., López-Comino, J., Clinton, J., Westaway, R., Cauzzi, C., Dahm, T., Wiemer, S., 2018. The November 2017 Mw 5.5 Pohang earthquake: A possible case of induced seismicity in South Korea. Science 360, 1003-1006.

Grigsby, C.O., Tester, J.W., Trujillo, P.E., Counce, D.A., 1989. Rock-water interactions in the Fenton Hill, new Mexico, hot dry rock geothermal systems I. fluid mixing and chemical geothermometry. Geothermics 18, 629-656.

Gu, H., Weng, X., 2010. Criterion For Fractures Crossing Frictional Interfaces At Non-orthogonal Angles, 44th U.S. Rock Mechanics Symposium and 5th U.S.-Canada Rock Mechanics Symposium. American Rock Mechanics Association, Salt Lake City, Utah, p. 6.

Gu, H., Weng, X., Lund, J.B., Mack, M.G., Ganguly, U., Suarez-Rivera, R., 2012. Hydraulic Fracture Crossing Natural Fracture at Nonorthogonal Angles: A Criterion and Its Validation. SPE-139984-PA 27, 20-26.

Gutenberg, B., Richter, C.F., 1956. Earthquake magnitude, intensity, energy, and acceleration: (Second paper). Bulletin of the Seismological society of America 46, 105-145.

Hardy Jr, H.R., 2003. Acoustic Emission/Microseismic Activity: volume 1: Principles, Techniques and Geotechnical Applications. CRC Press.

Häring, M.O., Schanz, U., Ladner, F., Dyer, B.C., 2008. Characterisation of the Basel 1 enhanced geothermal system. Geothermics 37, 469-495.

Hazzard, J., Young, R., 2000. Simulating acoustic emissions in bonded-particle models of rock. International Journal of Rock Mechanics and Mining Sciences 37, 867-872.

Hazzard, J., Young, R., 2004. Dynamic modelling of induced seismicity. International Journal of Rock Mechanics and Mining Sciences 41, 1365-1376.

Hébert, R.L., Ledésert, B., Bartier, D., Dezayes, C., Genter, A., Grall, C., 2010. The Enhanced Geothermal System of Soultz-sous-Forêts: A study of the relationships between fracture zones and calcite content. Journal of Volcanology and Geothermal Research 196, 126-133.

Held, S., Genter, A., Kohl, T., Kölbel, T., Sausse, J., Schoenball, M., 2014. Economic evaluation of geothermal reservoir performance through modeling the complexity of the operating EGS in Soultz-sous-Forêts. Geothermics 51, 270-280.

Hettkamp, T., Baumgärtner, J., Baria, R., Gerard, A., Gandy, T., Michelet, S., Teza, D., 2004. Electricity production from hot rocks, Proceedings, 29th Workshop on Geothermal Reservoir Engineering, Stanford University, California, USA.

Hévin, G., Charnavel, Y., Balland, C., Bigarré, P., Billiotte, J., Hadj-Hassen, F., BrunoTessier, Rouabhi, A., Pellet, F., Blanco-Martin, L., Bonnard, C., Thelier, N., Hertz, E., Tribout, D., Staudtmeister, K., Leuger, B., Zapf, D., 2016. Perform a Thermo-mechanical Test in a Salt

Mine, as part of SMRI's Research Program on High Frequency Cycling of Salt Storage Caverns.

Hillerborg, A., Modéer, M., Petersson, P.E., 1976. Analysis of crack formation and crack growth in concrete by means of fracture mechanics and finite elements. Cement and Concrete Research 6, 773-781.

Hoskins, E., Jaeger, J., Rosengren, K., 1968. A medium-scale direct friction experiment, International Journal of Rock Mechanics and Mining Sciences & Geomechanics Abstracts. Elsevier, pp. 143-152.

Huang, K., Ghassemi, A., 2016. Modeling 3D thermal fracture propagation by transient cooling using virtual multidimensional internal bonds. International Journal for Numerical and Analytical Methods in Geomechanics 40, 2293-2311.

Ikari, M.J., Marone, C., Saffer, D.M., 2011. On the relation between fault strength and frictional stability. Geology 39, 83-86.

Inglis, C.E., 1913. Stresses in a plate due to the presence of cracks and sharp corners. Transactions of the Institute of Naval Architects 55, 219-241.

Irwin, G.R., 1957. Analysis of stresses and strains near the end of a crack traversing a plate. Journal of Applied Mechanics 24, 361-364.

Jaeger, J.C., Cook, N.G., Zimmerman, R., 2009. Fundamentals of Rock Mechanics. John Wiley & Sons.

Jafari, M.K., Amini Hosseini, K., Pellet, F., Boulon, M., Buzzi, O., 2003. Evaluation of shear strength of rock joints subjected to cyclic loading. Soil Dynamics and Earthquake Engineering 23, 619-630.

Jin, L., 2018. Fluid-induced seismicity and fully dynamic earthquake rupture in fractured poroelastic media : models, discretization and computation, Department of Geophysics. Stanford University, Stanford, California, p. 235.

Johnson, L.R., 2014. A source model for induced earthquakes at The Geysers geothermal reservoir. Pure and Applied Geophysics 171, 1625-1640.

Juncu, D., Árnadóttir, T., Geirsson, H., Guðmundsson, G.B., Lund, B., Gunnarsson, G., Hooper, A., Hreinsdóttir, S., Michalczewska, K., 2018. Injection-induced surface deformation and seismicity at the Hellisheidi geothermal field, Iceland. Journal of Volcanology and Geothermal Research.

Jung, R., 2013. EGS —Goodbye or Back to the Future, ISRM International Conference for Effective and Sustainable Hydraulic Fracturing. International Society for Rock Mechanics and Rock Engineering, Brisbane, Australia, p. 28.

Kaiser, P., Tang, C., 1998. Numerical simulation of damage accumulation and seismic energy release during brittle rock failure—Part II: Rib pillar collapse. International Journal of Rock Mechanics and Mining Sciences 35, 123-134.

Kanamori, H., 1977. The energy release in great earthquakes. Journal of Geophysical Research 82, 2981-2987.

Keshavarz, M., 2009. Contribution to experimental study of mechanical and thermal damage in crystalline hard rocks. PhD dissertaion. Université Joseph Fourier-Grenoble I.

Keshavarz, M., Pellet, F., Rousseau, C., Hosseini, K.A., 2008. Comparing the results of acoustic emission monitoring in Brazilian and uniaxial compression tests, ISRM International Symposium-5th Asian Rock Mechanics Symposium. International Society for Rock Mechanics.

Keshavarz, M., Pellet, F.L., Loret, B., 2010. Damage and changes in mechanical properties of a Gabbro thermally loaded up to 1,000°C. Pure and Applied Geophysics 167, 1511-1523.

Knopoff, L., 1958. Energy release in earthquakes. Geophysical Journal International 1, 44-52.

Kohli, A.H., Zoback, M.D., 2013. Frictional properties of shale reservoir rocks. Journal of Geophysical Research: Solid Earth 118, 5109-5125.

Ledésert, B., Dubois, J., Genter, A., Meunier, A., 1993. Fractal analysis of fractures applied to Soultz-sous-Forets hot dry rock geothermal program. Journal of Volcanology and Geothermal Research 57, 1-17.

Ledésert, B., Hebert, R., Genter, A., Bartier, D., Clauer, N., Grall, C., 2010. Fractures, hydrothermal alterations and permeability in the Soultz Enhanced Geothermal System. Comptes Rendus Geoscience 342, 607-615.

Lisjak, A., Liu, Q., Zhao, Q., Mahabadi, O., Grasselli, G., 2013. Numerical simulation of acoustic emission in brittle rocks by two-dimensional finite-discrete element analysis. Geophysical Journal International 195, 423-443.

Mahyari, A., Selvadurai, A., 1998. Enhanced consolidation in brittle geomaterials susceptible to damage. Mechanics of Cohesive-frictional Materials 3, 291-303.

McClure, M.W., Horne, R.N., 2011. Investigation of injection-induced seismicity using a coupled fluid flow and rate/state friction model. Geophysics 76, WC181-WC198.

McClure, M.W., Horne, R.N., 2014. An investigation of stimulation mechanisms in Enhanced Geothermal Systems. International Journal of Rock Mechanics and Mining Sciences 72, 242-260.

Meixner, J., Schill, E., Grimmer, J.C., Gaucher, E., Kohl, T., Klingler, P., 2016. Structural control of geothermal reservoirs in extensional tectonic settings: An example from the Upper Rhine Graben. Journal of Structural Geology 82, 1-15.

Meller, C., Kohl, T., 2014. The significance of hydrothermal alteration zones for the mechanical behavior of a geothermal reservoir. Geothermal Energy 2, 12.

Meller, C., Ledésert, B., 2017. Is there a link between mineralogy, petrophysics, and the hydraulic and seismic behaviors of the Soultz-sous-Forêts granite during stimulation? A review and reinterpretation of petro-hydromechanical data toward a Better Understanding of Induced Seismicity and Fluid Flow. Journal of Geophysical Research: Solid Earth 122, 9755-9774.

Meyer, G., Baujard, C., Hehn, R., Genter, A., McClure, M., 2017. Analysis and numerical modelling of pressure drops observed during hydraulic stimulation of GRT-1 geothermal well (Rittershoffen, France), Proceedings 42nd Workshop on Geothermal Reservoir Engineering.

Mock, J.E., Tester, J.W., Wright, P.M., 1997. Geothermal energy from the earth: its potential impact as an environmentally sustainable resource. Annual Review of Energy and the Environment 22, 305-356.

Moës, N., Dolbow, J., Belytschko, T., 1999. A finite element method for crack growth without remeshing. International Journal for Numerical Methods in Engineering 46, 131-150.

Moradian, Z., Einstein, H.H., Ballivy, G., 2016. Detection of cracking levels in brittle rocks by parametric analysis of the acoustic emission signals. Rock Mechanics and Rock Engineering 49, 785-800.

Morrow, C., Radney, B., Byerlee, J., 1992. Chapter 3 Frictional Strength and the Effective Pressure Law of Montmorillonite and lllite Clays, in: Evans, B., Wong, T.-F. (Eds.), International Geophysics. Academic Press, pp. 69-88.

Munjiza, A.A., 2004. The Combined Finite-Discrete Element Method. John Wiley & Sons.

Murphy, H., Keppler, H., Dash, Z., 1983. Does hydraulic-fracturing theory work in jointed rock masses?, Geothermal Resources Council's annual meeting, Portland, OR, USA, 24 Oct 1983 p. 7.

Murphy, H.D., 1978. Thermal stress cracking and the enhancement of heat extraction from fractured geothermal reservoirs. Los Alamos Scientific Lab., N. Mex.(USA).

Ngo, D.T., Pellet, F.L., 2018. Numerical modeling of thermally-induced fractures in a large rock salt mass. Journal of Rock Mechanics and Geotechnical Engineering 10, 844-855.

Ngo, D.T., Pellet, F.L., Bruel, D., 2019. Modeling of fault slip during hydraulic stimulation in a naturally fractured medium. Geomechanics and Geophysics for Geo-Energy and Geo-Resources (https://doi.org/10.1007/s40948-019-00108-1).

Nicol, D.A.C., Robinson, B.A., 1990. Modelling the heat extraction from the Rosemanowes HDR reservoir. Geothermics 19, 247-257.

Nordgren, R., 1972. Propagation of a vertical hydraulic fracture. Society of Petroleum Engineers Journal 12, 306-314.

O'Keeffe, N.J., Huppert, H.E., Linden, P.F., 2018. Experimental exploration of fluid-driven cracks in brittle hydrogels. Journal of Fluid Mechanics 844, 435-458.

Okal, E.A., Romanowicz, B.A., 1994. On the variation of b-values with earthquake size. Physics of the Earth and Planetary Interiors 87, 55-76.

Parker, R.H., 1989. Overview, Hot Dry Rock geothermal energy, Phase 2B final report of the Camborne School of Mines Project, pp. 1-38.

Pearson, C., 1981. The relationship between microseismicity and high pore pressures during hydraulic stimulation experiments in low permeability granitic rocks. Journal of Geophysical Research: Solid Earth 86, 7855-7864.

Pearson, C., 1982. Parameters and a magnitude moment relationship from small earthquakes observed during hydraulic fracturing experiments in crystalline rocks. Geophysical Research Letters 9, 404-407.

Pellet, F., 2017. Rock mechanics is meeting the challenges of geo-energies. Procedia Engineering 191, 1104-1107.

Pollock, A.A., 1973. Acoustic emission - 2: Acoustic emission amplitudes. Non-Destructive Testing 6, 264-269.

Potter, R., Robinson, E., Smith, M., 1974. Method of extracting heat from dry geothermal reservoirs. US Atomic Energy Commission. Patent #3,786,858, United States.

Potyondy, D.O., Cundall, P.A., 2004. A bonded-particle model for rock. International Journal of Rock Mechanics and Mining Sciences 41, 1329-1364.

Qian, J., Fatemi, A., 1996. Mixed mode fatigue crack growth: a literature survey. Engineering Fracture Mechanics 55, 969-990.

Rattez, H., Stefanou, I., Sulem, J., 2017. Effect of Thermo-Poro-Mechanical Properties on the Stability of Faults, Poromechanics VI : Proceedings of the Sixth Biot Conference on Poromechanics, pp. 1858-1865.

Reeder, J., Song, K., Chunchu, P., Ambur, D., 2002. Postbuckling and growth of delaminations in composite plates subjected to axial compression, 43rd AIAA/ASME/ASCE/AHS/ASC Structures, Structural Dynamics, and Materials Conference, Denver, Corolado, p. 1746.

Renshaw, C., Pollard, D., 1995. An experimentally verified criterion for propagation across unbounded frictional interfaces in brittle, linear elastic materials. International Journal of Rock Mechanics and Mining Sciences & Geomechanics Abstracts 32, 237-249.

Rice, J.R., 1968. A path independent integral and the approximate analysis of strain concentration by notches and cracks. Journal of Applied Mechanics 35, 379-386.

Richards, H.G., Parker, R.H., Green, A.S.P., Jones, R.H., Nicholls, J.D.M., Nicol, D.A.C., Randall, M.M., Richards, S., Stewart, R.C., Willis-Richards, J., 1994. The performance and characteristics of the experimental hot dry rock geothermal reservoir at Rosemanowes, Cornwall (1985–1988). Geothermics 23, 73-109.

Richter, C.F., 1935. An instrumental earthquake magnitude scale. Bulletin of the Seismological Society of America 25, 1-32.

Rutqvist, J., Cappa, F., Rinaldi, A.P., Godano, M., 2014. Modeling of induced seismicity and ground vibrations associated with geologic CO2 storage, and assessing their effects on surface structures and human perception. International Journal of Greenhouse Gas Control 24, 64-77.

Rybach, L., 2010. The future of geothermal energy" and its challenges, Proceedings World Geothermal Congress, Bali, Indonesia, 25-29 April 2010 pp. 1-4.

Sausse, J., 2002. Hydromechanical properties and alteration of natural fracture surfaces in the Soultz granite (Bas-Rhin, France). Tectonophysics 348, 169-185.

Sausse, J., Genter, A., 2005. Types of permeable fractures in granite. Geological Society, London, Special Publications 240, 1-14.

Savitski, A., Detournay, E., 2002. Propagation of a penny-shaped fluid-driven fracture in an impermeable rock: asymptotic solutions. International Journal of Solids and Structures 39, 6311-6337.

Schill, E., Genter, A., Cuenot, N., Kohl, T., 2017. Hydraulic performance history at the Soultz EGS reservoirs from stimulation and long-term circulation tests. Geothermics 70, 110-124.

Scholz, C., 1968. Experimental study of the fracturing process in brittle rock. Journal of Geophysical Research 73, 1447-1454.

Scholz, C.H., 2002. The Mechanics of Earthquakes and Faulting. Cambridge University Press.

Scuderi, M.M., Collettini, C., Marone, C., 2017. Frictional stability and earthquake triggering during fluid pressure stimulation of an experimental fault. Earth and Planetary Science Letters 477, 84-96.

Segall, P., 2010. Earthquake and Volcano Deformation. Princeton University Press.

Segall, P., Fitzgerald, S.D., 1998. A note on induced stress changes in hydrocarbon and geothermal reservoirs. Tectonophysics 289, 117-128.

Selvadurai, A., Mahyari, A., 1997. Computational modeling of the indentation of a cracked poroelastic half-space. International Journal of Fracture 86, 59-74.

Selvadurai, A.P.S., Suvorov, A.P., 2016. Thermo-poroelasticity and Geomechanics. Cambridge University Press.

Selvadurai, P.A., Glaser, S.D., 2015. Laboratory-developed contact models controlling instability on frictional faults. Journal of Geophysical Research: Solid Earth 120, 4208-4236.

Sih, G., Barthelemy, B., 1980. Mixed mode fatigue crack growth predictions. Engineering Fracture Mechanics 13, 439-451.

Smith, M.C., 1975. The Los Alamos scientific laboratory dry hot rock geothermal project (LASL Group Q-22). Geothermics 4, 27-39.

Sneddon, I.N., 1946. The distribution of stress in the neighbourhood of a crack in an elastic solid. Proceedings of the Royal Society London A 187, 229-260.

Spence, D., Sharp, P., 1985. Self-similar solutions for elastohydrodynamic cavity flow. Proceedings of the Royal Society of London A 400, 289-313.

Stober, I., Bucher, K., 2007. Hydraulic properties of the crystalline basement. Hydrogeology Journal 15, 213-224.

Sulem, J., Stefanou, I., 2015. Multiphysics Couplings and Stability of Fault Zones, 13th ISRM International Congress of Rock Mechanics. International Society for Rock Mechanics and Rock Engineering.

Swenson, D., Hardeman, B., 1997. The effects of thermal deformation on flow in a jointed geothermal reservoir. International Journal of Rock Mechanics and Mining Sciences 34, 308.e301-308.e320.

Swindlehurst, W., 1973. Acoustic emission - 1 Introduction. Non-Destructive Testing 6, 152-158.

Taleghani, A.D., Gonzalez, M., Shojaei, A., 2016. Overview of numerical models for interactions between hydraulic fractures and natural fractures: Challenges and limitations. Computers and Geotechnics 71, 361-368.

Tang, C., 1997. Numerical simulation of progressive rock failure and associated seismicity. International Journal of Rock Mechanics and Mining Sciences 34, 249-261.

Tang, C.A., Kaiser, P.K., 1998. Numerical simulation of sumulative damage and seismic energy release during brittle rock failure—Part I: Fundamentals. International Journal of Rock Mechanics and Mining Sciences 35, 113-121.

Tester, J.W., 1989. Hot dry rock geothermal energy-a new energy agenda for the 21st century. LANL Report, LA-11514-MS. Los Alamos National Laboratory, pp. 1-6.

Thomas, R.N., Paluszny, A., Zimmerman, R.W., 2017. Quantification of fracture interaction using stress intensity factor variation maps. Journal of Geophysical Research: Solid Earth 122, 7698-7717.

Turon, A., Dávila, C.G., Camanho, P.P., Costa, J., 2007. An engineering solution for mesh size effects in the simulation of delamination using cohesive zone models. Engineering Fracture Mechanics 74, 1665-1682.

Vallier, F., Mitani, Y., Boulon, M., Esaki, T., Pellet, F., 2010. A shear model accounting scale effect in rock joints behavior. Rock Mechanics and Rock Engineering 43, 581-595.

Wald, D.J., Quitoriano, V., Heaton, T.H., Kanamori, H., 1999. Relationships between peak ground acceleration, peak ground velocity, and modified Mercalli intensity in California. Earthquake Spectra 15, 557-564.

Wang, H., Tao, X., 2003. Relationships between moment magnitude and fault parameters: theoretical and semi-empirical relationships. Earthquake Engineering and Engineering Vibration 2, 201-211.

Wang, W., Wang, M., Liu, X., 2016. Study on mechanical features of brazilian splitting fatigue tests of salt rock. Advances in Civil Engineering 2016, 1-10.

Warpinski, N.R., Teufel, L.W., 1987. Influence of Geologic Discontinuities on Hydraulic Fracture Propagation (includes associated papers 17011 and 17074). Journal of Petroleum Technology 39, 209-220.

Weng, X., Cohen, C.-E., Kresse, O., 2016. Impact of Preexisting Natural Fractures on Hydraulic Fracture Simulation, Unconventional Oil and Gas Resources Handbook. Elsevier, pp. 289-331.

Wohlenberg, J., Keppler, H., 1987. Monitoring and interpretation of seismic observations in hot dry rock geothermal energy systems. Geothermics 16, 441-445.

Wong, T.-F., Brace, W.F., 1979. Thermal expansion of rocks: some measurements at high pressure. Tectonophysics 57, 95-117.

Wood, H.O., Neumann, F., 1931. Modified Mercalli intensity scale of 1931. Bulletin of the Seismological Society of America 21, 277-283.

Wu, E.M., Reuter Jr, R., 1965. Crack extension in fiberglass reinforced plastics. University of Illinois.

Zang, A., Oye, V., Jousset, P., Deichmann, N., Gritto, R., McGarr, A., Majer, E., Bruhn, D., 2014. Analysis of induced seismicity in geothermal reservoirs – An overview. Geothermics 52, 6-21.

Zhang, S., Huang, Z., Wang, H., Zhang, H., Zhang, C., Xiong, C., 2018a. Thermal characteristics analysis with local thermal non-equilibrium model during liquid nitrogen jet fracturing for HDR reservoirs. Applied Thermal Engineering 143, 482-492.

Zhang, S., Huang, Z., Zhang, H., Guo, Z., Wu, X., Wang, T., Zhang, C., Xiong, C., 2018b. Experimental study of thermal-crack characteristics on hot dry rock impacted by liquid nitrogen jet. Geothermics 76, 253-260.

Zhang, X., Jeffrey, R.G., 2016. Fluid-driven nucleation and propagation of splay fractures from a permeable fault. Journal of Geophysical Research: Solid Earth 121, 5257-5277.

Zhao, Y., Feng, Z., Zhao, Y., Wan, Z., 2017. Experimental investigation on thermal cracking, permeability under HTHP and application for geothermal mining of HDR. Energy 132, 305-314.

Zhou, C., Wan, Z., Zhang, Y., Gu, B., 2018. Experimental study on hydraulic fracturing of granite under thermal shock. Geothermics 71, 146-155.

Zhou, J., Xue, C., 2011. Experimental Investigation of Fracture Interaction between Natural Fractures and Hydraulic Fracture in Naturally Fractured Reservoirs, SPE EUROPEC/EAGE Annual Conference and Exhibition. Society of Petroleum Engineers, Vienna, Austria, p. 12.

Ziegler, P.A., 1992. European Cenozoic rift system. Tectonophysics 208, 91-111.

Zielonka, M., Searles, K., Ning, J., Buechler, S., 2014. Development and validation of fully-coupled hydraulic fracturing simulation capabilities, Proceedings of the SIMULIA community conference, SCC2014, pp. 19-21.

Zoback, M.D., Kohli, A., Das, I., Mcclure, M.W., 2012. The importance of slow slip on faults during hydraulic fracturing stimulation of shale gas reservoirs, SPE Americas Unconventional Resources Conference. Society of Petroleum Engineers.

RÉSUMÉ

Le développement et l'exploitation de réservoirs géothermiques profonds s'accompagnent généralement d'une sismicité induite - un effet secondaire indésirable. Cette recherche est axée sur l'utilisation de simulations numériques pour étudier la propagation des fractures hydrauliques et la réactivation de failles préexistantes lors de la stimulation hydraulique des réservoirs afin de mieux comprendre le comportement du réservoir fracturé et de réduire le risque potentiel de sismicité induite.

La sismicité induite est d'abord étudiée du point de vue de l'utilisation de la loi de conservation de l'énergie afin d'expliquer le mécanisme de génération d'ondes élastiques à partir d'une rupture de roche. Ensuite, une approche approximative est proposée pour calculer les accélérations de pointe de pointe (PGA) induites par le glissement de faille. Les PGA calculés à la surface du sol servent à évaluer la perception humaine des ondes sismiques et le potentiel de dégradation des structures.

MOTS CLÉS

Géothermie, stimulation hydraulique, modélisation numérique, sismicité induite, mécanique de la rupture, FEM

ABSTRACT

The development and the exploitation of deep geothermal reservoirs are usually accompanied with induced seismicity – an unwanted side effect. This research is focused on using numerical simulations to investigate the propagation of hydraulic fractures and the reactivation of pre-existing faults during the hydraulic stimulation of the reservoirs in an effort to better understand the fractured reservoir behavior and to reduce the potential risk of induced seismicity.

The induced seismicity is studied first from the standpoint of using the law of energy conservation in order to explain the mechanism of generating elastic waves from rock failure. Then an approximate approach is proposed to calculate the peak ground accelerations (PGAs) that are induced by the fault slip. The computed PGAs on ground surface are used to assess the human perception of the seismic waves and the damage potential to structures.

KEYWORDS

Geothermal energy, hydraulic stimulation, numerical modeling, induced seismicity, fracture mechanics, FEM